Studies of Adsorption of Organic Macromolecules on Oxide and Perfluorinated Surfaces

by

Peiling Sun

A thesis submitted to the Department of Chemistry

In conformity with the requirements for

the degree of Doctor of Philosophy

Queen's University

Kingston, Ontario, Canada

October, 2011

Abstract

Humic-based organic compounds containing phenol or benzoic acid groups strongly compete with phosphates for specific binding sites on the surface of these colloidal particles. To study the interactions between phenol groups and the surface binding sites of unmodified or modified colloidal particles, chemical force spectrometry (CFS) was used as a tool to measure the adhesion force between an atomic force microscopy (AFM) tip terminated with a phenol self-assembled monolayer and colloidal particles under varying pH conditions. Two modification methods, co-precipitation and post-precipitation, were used to simulate the naturally-occurring phosphate and humic-acid adsorption process. The pH dependence of adhesion forces between phenol-terminated tip and colloidal particles could be explained by an interplay of electrostatic forces, the surface loading of the modifying phosphate or humic acid species and ionic hydrogen bonding.

Polydimethylsiloxane (PDMS) is a widely-used polymer in microfluidic devices. PDMS surfaces are commonly modified to make it suitable for specific microfluidic devices. We studied the surface modification of PDMS using four perfluoroalkyl-triethoxysilane molecules of differing length of perfluorinated alkyl chain. The results show that the length of fluorinated alkyl chain has important effects on the density of surface modifying molecules, surface topography and surface zeta potential. The perfluorinated overlayer makes PDMS more efficient at supporting electroosmotic flow, which has potential applications in microfluidic devices.

The kinetic study of RNase A, lysozyme C, α-lactalbumin and myoglobin at different concentrations adsorbed on the self-assembled monolayers of 1-octanethiol (OT-Au) and 1H, 1H, 2H, 2H-perfluorooctyl-1-thiol (FOT-Au) has been carried out. The results show a positive relationship between the lower protein concentration and the increased adsorption rate constant (k_a) on both surfaces. At low concentrations, the protein adsorption on an OT-Au surface has

greater k_a than it on a FOT-Au surface. Comparing k_a values for four proteins on OT-Au and FOT-Au surface demonstrates that hard proteins (lysozyme and RNase A) have larger k_a than soft proteins (α-lactalbumin and myoglobin) on both surfaces. The discussion is based on the hydrophobicity of OT-Au and FOT-Au surfaces, as well as average superficial hydrophobicity, flexibility, size, stability, and surface induced conformation change of proteins.

Acknowledgements

I would like to sincerely thank my research supervisor, Dr. J. Hugh Horton, and my supervisory committee members, Dr. Gary W. VanLoon and Dr. Robert P. Lemieux, for their support and encouragement. Thanks also to our group members who were always willing to offer help and suggestions.

I would also like to thank all those in the Department of Chemistry who have helped me in various ways in my research. My thanks and appreciations are also dedicated to Mr. Kim Munro from the Protein Function Discovery facility at the Department of Biochemistry.

My special thanks to all of my friends. Your smiles brighten up my life. I am really grateful that I have you in my life.

I express my deepest thanks to my family with all of my heart for your many forms of love, trust, support, patience and understanding while I completed my Ph.D degree. I love you Mom!

Statement of Originality

I hereby certify that all of the work described within this thesis is the original work of the author. Any published (or unpublished) ideas and/or techniques from the work of others are fully acknowledged in accordance with the standard referencing practices.

Peiling Sun

August, 2011

Table of Contents

List of Figures

List of Tables

Chapter 1
Introduction

The fundamental understanding of the interactions between molecules and an interface in solution is crucial since many molecular phenomena in chemistry, physics and biology are interfacial in nature. The various interaction forces include hydrophobic effects, electrostatic repulsion, ionic hydrogen bonding, hydrogen bonding, and van der Waals forces. Indeed, modification of a surface with as little as a monolayer, e.g. a self-assembled monolayer, can completely change material properties on the macroscopic scale such as wetting, lubrication, and surface zeta potential. In this thesis, I report on three projects, which are respectively involved in the study of molecule-surface interactions and surface modification. While disparate in nature, the two chemical systems studied – metal oxides and perfluorinated hydrocarbons – exemplify the importance of interaction forces in surface chemistry.

The first project is a study of phenol interactions with hydrous iron and aluminum oxide colloids. The reason we are interested in this system is that iron and aluminum oxide colloids are important components in soil systems and efficient coagulants in water treatment processes: phenol is one of the predominant functional groups of humic-based organic compounds, which may occupy specific Fe-OH and Al-OH binding sites on the surfaces of these two colloids. At the same time carboxylates, another predominant functional groups associated with humic-based organic compounds, and phosphate anions, compete with the phenol for similar surface binding sites on these metal oxide colloidal particles.[1-9] This competitive adsorption from soil or solution onto surfaces of hydrous iron and aluminum oxide colloidal particles is relevant to some essential environmental issues such as eutrophication, contaminant transport, particle coagulation, and mineral weathering.[10-14]

The unique part of my research is the study of the interaction of phenol and hydrous iron and aluminum oxide colloidal particles at the molecular level using chemical force spectrometry (CFS). Chemical force spectrometry (CFS) has the ability to measure interfacial forces at the pN to nN scale over atomic scale distances using the nanometre scale tip of an atomic force microscope (AFM).[15] In this research, a gold coated AFM tip was modified with the phenol compound (4-(12-mercaptododecyl) phenol,), which forms a self-assembled monolayer on the gold coated AFM tip with the phenol groups facing outward. Then AFM was used to measure the adhesion force between phenol terminated tip and bare or modified colloidal particles as a function pH (3-12), effectively a chemical force titration (CFT). As the surface roughness and the surface heterogeneity may also impact the adhesion force during each measurement, CFT data were collected at several different locations on the substrate. The colloidal particles were modified using two different protocols by potassium hydrophosphate, gallic acid (GA) or tannic acid (TA) to simulate the naturally-occurring adsorption process. Here, GA and TA were used as relatively simple models of humic-based organic compounds. The post-precipitation process is one in which a stoichiometric excess of the modifying agents (KH_2PO_4, GA or TA) were added in aqueous solution after colloidal particles were formed. For the co-precipitation process, excess trivalent aluminum and iron cations were added to the modifying agents, which then formed insoluble aluminum and iron phosphate salts or soluble organic-metal complexes that subsequently formed colloidal particles. The soluble organic metal complexes adsorb on the surface of iron and aluminum hydroxide through unsaturated carboxyl and phenolic sites. GA is a subunit of complex humic acid with both phenolic (pK_{a1}=8.70, pK_{a2}=11.45) and benzoic groups (pK_a=4.26). [15] TA, representing a more complex model of humic substances than GA, contains a mixture of related compounds, such as saccharide and aromatic as well as benzoic and phenolic groups. It has been used as a model compound for soluble organic matter in studies on water

treatment as well as in studies on soil science as it is similar in some ways to soluble fulvic acid. [16, 17] Its weak acidity ($pK_a \approx 10$) is due to the predominance of phenol groups in the structure.

Since phenol, phosphate, GA, TA, Fe-OH and Al-OH surface binding sites are all ionizable in the pH range of 3-12, the interactions taking place on the surfaces was expected to be dominated by acid-base chemistry, particularly the formation of ionic hydrogen bonds. Such bonds formed between ions and neutral protic species have bonds strengths of up to a third of those associated with covalent bonds. An ionic H-bond has been shown to be 10-30 times stronger than a neutral H-bond. [18] In this case, the ionic hydrogen bonds $OH_2^+ \cdot O$ and $O^- \cdot HO$ may form and have bond energies on the order of 30 kcal/mol. [19, 20] On the other hand, the number of interacting molecules are usually on the order of tens to hundreds. However, the quantitative study of interaction is difficult in this case since the number of surface binding sites is difficult to determine due to the amorphous surface colloid surfaces used.

Electrostatic forces also play an important role in the interaction so that understanding the surface charge status on both the surfaces of tip and colloidal particles under different pH solutions becomes crucial. The isoelectric points of various colloidal particles were measured by potentiometry and the surface pK_a of phenol groups was determined by CFT between surface phenol-phenol groups.

Before adhesion force measurement were carried out on the colloids, the phenol SAM on gold-mica surface was well characterized using X-ray photoelectron spectroscopy (XPS) and attenuated total reflection fourier transform infrared (ATR-FTIR) to respectively explore the surface composition and the molecular orientation at the surface. Meanwhile, the composition and topography of the surface of colloidal particle substrates were respectively tested by XPS and AFM.

The second project consists of a study of fluorinated polydimethylsiloxane (PDMS) surface.

The study was focused on the effects of surface zeta potential following modification and nonspecific binding of globular proteins on the fluorinated PDMS. The ζ-potential between the modified PDMS surface and an aqueous solution under varying pH is the main parameter we were curious about, as it is an indispensable requirement for electroosmotic flow (EOF), key to electrokinetic pumping in microfluidic devices. The reason that we have interests in this study is that PDMS is a promising polymer material used in the fabrication of microfluidic devices, instead of traditional glass and silicon. Previous work from our group has demonstrated that fluorinated PDMS has a larger surface zeta potential compared to unmodified PDMS, which more effectively supports electro-osmotic flow in the microchannel and allows the specific adsorption of fluorous-tagged protein, although some non-specific adsorption of proteins does take place on the fluorinated PDMS surface.[21, 22] However, the mechanism of the surface zeta potential enhancement and nonspecific protein binding was not explored in depth. Here, we describe the use of perfluoroalkyl-triethoxysilane molecules of varying perfluorinated alkyl chain length to modify the surface of PDMS and we observed the surface topography after each modification using AFM. The current-time monitoring method was used to measure the ζ-potential values for this work. We also correlated ζ-potential values to their relative chemical composition and surface morphology information, which were acquired with X-Ray photoelectron spectroscopy (XPS) and atomic force microscope (AFM), respectively.

The third project consisted of a study of nonspecific protein adsorption on the fluorinated self-assembled monolayer of 1H, 1H, 2H, 2H-perfluorooctyl-1-thiol using surface plasmon resonance. The self-assembled monolayer was used instead of fluorinated PDMS or glass because the structures of polymer and glass are mostly undefined at the molecular level [23] and the self-assembled monolayers provide well defined surface composition and properties, which are suitable for the study of protein adsorption. A fluorinated surface is more hydrophobic than an

alkyl surface. The hydrophobic force is one of the main forces acting in the protein-surface adsorption. Here, we carried out a kinetic study of RNase A, Lysozyme C, α-Lactalbumin and Myoglobin at different concentrations adsorbed on the self-assembled monolayer of 1-octanethiol (OT-Au) and 1H, 1H, 2H, 2H-perfluorooctyl-1-thiol (FOT-Au). The experimental results showed that a positive relationship among the lower protein concentration, the lower surface coverage of protein and an increased adsorption rate constant k_a on both surfaces of OT-Au and FOT-Au. In addition, at low concentration, the protein adsorption rate constants for protein adsorption on FOT-Au surface were less than for the same protein on an OT-Au surface. Comparing the protein adsorption rate constant (k_a) of the four proteins lysozyme, RNase A, lactalbumin and myoglobin on OT-Au and FOT-Au surfaces, demonstrated that hard proteins (lysozyme and RNase A) have larger k_a than soft proteins (lactalbumin and myoglobin) for both surfaces. The adsorption of two proteins (cytochrome c and ubiquitin) on the self-assembled monolayer of 1-octanethiol (OT-Au), 1H, 1H, 2H, 2H-perfluorooctyl-1-thiol (FOT-Au) and 8-mercapto-1-octanol (MOT-Au) were studied in the pH range 4.5 to 8.5. For an MOT-Au surface, the quantity of cytochrome c adsorbed increased as pH increased from 4.5 to 8.5, which is consistent with the reduction of lateral electrostatic repulsion among the adsorbed proteins as the pH approaches the protein's isoelectric point (pI). However, we did not observe the maximum adsorption at pH 6.5 for ubiquitin (pI 6.5). The adsorptions of cytochrome c and ubiquitin on OT-Au and FOT-Au surfaces show the same trend as a function of pH, but the adsorption of proteins on OT-Au is greater than FOT-Au. We explained the results based on the calculated average superficial hydrophobicity, flexibility of protein, protein size, protein stability, and surface induced conformation change of proteins.

Chapter 2
Literature Review

2.1 Iron/aluminum (hydr)oxide colloids in soil colloids

Soil colloids, one solid phase component of soils, make an important contribution to the mobility of both limiting nutrients and contaminant species in ecosystems. This is due not only to their large surface area, but also due to the exchange of aqueous species on various binding sites. [24] Many contaminants strongly adsorb on the soil solid phase even though these contaminants are soluble in water. The diameter of colloidal particles usually is between approximately 5 and 200 nanometers. [25]

The three most important and abundant components in soil colloids are clays, humic substances and (hydr)oxides. In addition, (hydr)oxides are highly important due to their large reactive surfaces, which have the ability to immobilize anionic species, especially phosphate ions and soil organic compounds such as polysaccharides and humic substances. When aqueous solutions contact the oxides, the surfaces of oxides are hydrolyzed. These species have much in common with the surface of hydroxides, so here the term, "(hydr)oxides" is used to refer to both of hydrolyzed oxides and hydroxides.

Aluminum, iron, and manganese are the most important (hydr)oxides due to their great abundance in soils and their low solubility. Here, we focus on the study of the first two metal oxide colloids. Iron oxide colloids are one of the smallest particles of soil with dimensions in the range of 10 to 100 nm, so it has an important effect in the surface area of soil and soil color. [26] Goethite is the most stable crystalline form of iron oxides. Ferrihydrite and hematite are less

stable and will finally transform to goethite. Gibbsite is the most important stable crystalline form of aluminum oxides.

2.2 The surface hydroxyl of iron/aluminum (hydr)oxide

Hydrous metal oxide surfaces contain three different types of sites. The O anions can act as electron-donating Lewis base sites; incompletely coordinated cations can act as electron-accepting Lewis acid sites; OH^- anions can act as not only Lewis base or acid but also Brønsted-Lowry base or acid.[27] The most abundant and reactive surface functional group in soil is the hydroxyl group, which is found on metal oxides and (hydr)oxides. The hydroxyl groups can coordinate a hydroxide anion at high pH and coordinate a proton at low pH. In addition, hydroxyl groups can form outer-sphere surface complexes or inner-sphere surface complexes with metal anions.

In this research, the surface properties of iron (hydr)oxide and aluminum (hydr)oxide play a crucial role in the interaction of phenol with surfaces. These surfaces are amorphous and do not have well defined long range order. However, at the molecular scale, the long range order of the surface is not the main factor to impact the molecular interaction. The local chemistry of the functional group on the amorphous colloid might be expected to be similar to those of the crystalline forms. [28, 29]

The surface of goethite drawn lying parallel to the crystallographic c axis is shown is Figure 2.1. The goethite structure can be modeled as a combination of strips of condensed Fe (O, OH) octahedra. These strips as shown share O^{2-} ions and give an open structure in which the cap is linked by a hydrogen bond (dashed line). Three different types of hydroxyl groups (labeled A, B, C) are present on the surface of goethite. Of these surface hydroxyls only type A, which coordinates to only one Fe^{3+}, can form intermolecular hydrogen bonds 3 Å long along the surface.

In addition, type A surface hydroxyls can be protonated to form a Lewis acid site. Type B hydroxyl is coordinated with three Fe^{3+}. The type C hydroxyl is coordinated with two Fe^{3+} and cannot form intermolecular hydrogen bonds on the surface layer because all adjacent available hydroxyls are already saturated at co-coordination number of 2 or 3. In addition, only type C hydroxyl groups are found perpendicular to the crystallographic b axis. Framer *et al.* proved that these three surface hydroxyl groups have different infrared absorption spectra compared to the bulk structural hydroxyl groups.[28] They also observed coordination between one water molecule and Fe^{3+}, the water molecule acting as a lewis acid site.

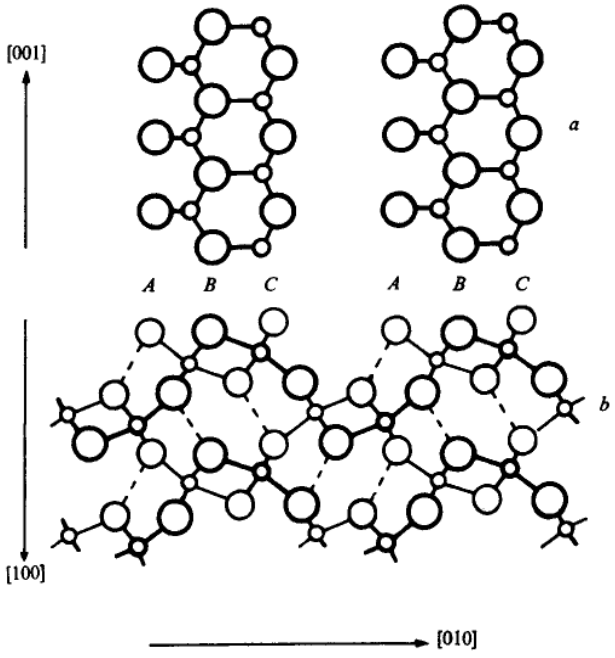

Figure 2.1 Plan (a) of (001) and section (b) of (100) face of goethite[28].

Gibbsite is an aluminum hydr(oxide) that takes in the form of thin hexagonal plates some 250 nm in diameter and 9 nm in thicknesses, and incorporates bulk OH groups that are involved in interlayer bonding. [30] At the surface, some of these OH groups are not involved in interlayer

bonding, and are therefore available to be deprotonated or protonated under varying pH conditions. Figure 2.2 shows how the hydroxyls coordinate to Al^{3+} cations on the surface, perpendicular to the gibbsite crystallographic c axis. The hydroxyls bound to Lewis acid sites are more reactive when they are on an edge plane and perpendicular to the basal plane.[31]

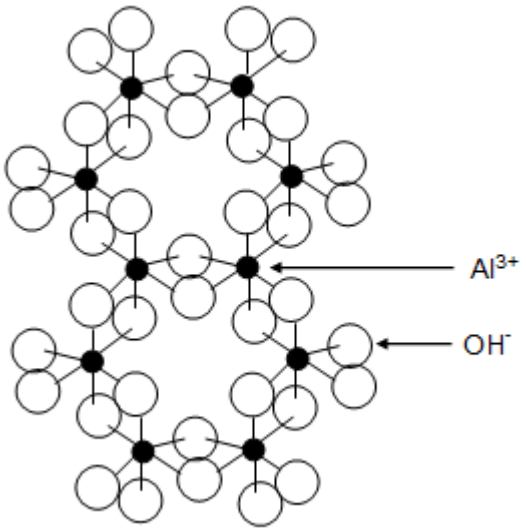

Figure 2.2 Hydroxyls groups on gibbsite (γ-$Al(OH)_3$) surface perpendicular to the gibbsite crystallographic c axis.

2.3 Metal cations in soil aquatic systems and its adsorption on iron/aluminum (hydr)oxides

Metal ions in aqueous water systems generally take the form of hydrated ions due to the large dipole and dielectric constant of the water molecule. When the water is sufficiently alkaline, further deprotonation steps may occur. For instance, the hydrated aluminum ion and the hydrated iron ion can lose several protons, eventually becoming neutral insoluble solid hydroxide.

In fact, in naturally occurring water environments, many substances such as phosphate and organic matter can substitute for water as more stable ligands and form new complexes with these ions. On the other hand, the solubility of Fe^{3+} and Al^{3+} salts in water is sufficiently low that

excessive Fe^{3+}, Al^{3+} and OH^- concentrations readily lead to the formation of colloidal particles. These oxides are often negatively charged in naturally occurring water environments due to the dissociation of a surface hydroxyl group ($\sim OH \rightarrow \sim O^- + H^+$). At low pH, many oxides are positively charged which is attributable to the process ($\sim OH_2^+ \leftarrow \sim OH + H^+$).

Metal cations can form both inner-sphere and outer-sphere surface complexes on the iron/aluminum (hydr)oxides. Or metal cations can just be attracted close to the surface by electrostatic force without any complexes or ligand binding formed, if the surface is of opposite charge. Meanwhile, if other ligands (such as hydroxide ion) have strong affinity with metal cations and the surface of (hydr)oxides, metal cations can also bind to the (hydr)oxides through these ligands.[32]

2.4 Phosphate in soil aquatic systems and its adsorption on iron/aluminum (hydr)oxides

Terrestrial phosphates are found in a number of specific minerals including apatite, $Ca_5(PO_4)_3(F,Cl,OH)$, and vivianite, $Fe_3(PO_4)_2 \cdot 8H_2O$ and are always present in soils where plants and animals grow and decay. In water, phosphorus exists as P(V) species, particularly in forms of ortho-phosphate, which are shown as follows in equations [2.4.1]~[2.4.3]

$$H_3PO_4\ (s) + H_2O(l) \rightleftharpoons H_3O^+(aq) + H_2PO_4^-(aq) \qquad Ka_1 = 7.5\times10^{-3} \qquad [2.4.1]$$

$$H_2PO_4^-(aq) + H_2O(l) \rightleftharpoons H_3O^+(aq) + HPO_4^{2-}(aq) \qquad Ka_2 = 6.2\times10^{-8} \qquad [2.4.2]$$

$$HPO_4^{2-}(aq) + H_2O(l) \rightleftharpoons H_3O^+(aq) + PO_4^{3-}(aq) \qquad Ka_3 = 2.14\times10^{-13} \qquad [2.4.3]$$

If no account was taken of the solution ionic strength and interactions with other species, the distribution of phosphate species can be illustrated in Figure 2.3 as the fraction (α) of four possible ionization states as a function of aqueous solution pH.[9]

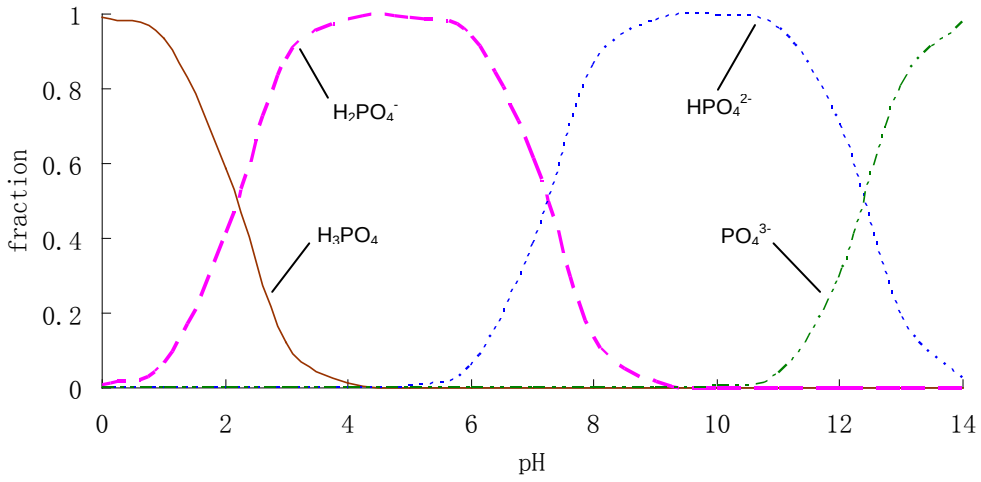

Figure 2.3 Distribution of the fraction of four possible phosphorus ionization states as a function of aqueous solution pH.

In this work, to synthesize the phosphate modified colloidal particles, the solution containing phosphate was adjusted to pH 6. According to the Figure above it is reasonable to presume the predominant species is $H_2PO_4^-$.

Phosphate is usually present in low concentration since its solubility is controlled by other cations such as aluminum, iron, or calcium, which form insoluble phosphates. Phosphate also has a strong affinity with the surface of the metal oxides, as discussed earlier. To increase the quantity of soluble phosphate, which is one essential nutrient for all plants, fertilizers are applied in agriculture. On the other hand, phosphate leached from agricultural soils is one of the main problems of phosphate in ecosystems. Ecosystems are particularly sensitive to the changes in the concentrations of the limiting phosphate since it is one essential nutrient. In aqueous systems, the high nutrient levels (eutrophication) can cause overproduction of algae and waterweeds, and then lead to the death of animals and other plants. Some authors suggest that phosphate anion forms a binuclear complex by replacing singly coordinated OH groups on the goethite surface. [33-35] In

contrast, the adsorption of ions such as NO_3^- or Cl^- does not involve ligand exchange.[36, 37] In addition, the adsorption process of phosphate anions is faster than the precipitation reaction with Al^{3+} and Fe^{3+}. After the adsorption process of phosphate anions on the metal (hydr)oxide surface, the diffusion of phosphate species into the bulk solid phase can occur and finally convert to a solid phosphate precipitate, for instance as in the following reaction:

$$Al(OH)_3 + H_2PO_4^- + H^+ \rightleftharpoons AlPO_4 \cdot 2H_2O(s) + H_2O \qquad [2.4.4]$$

2.5 Humic substances (HS) in soil aquatic systems and its adsorption on iron/aluminum (hydr)oxides

Humic substances (HS) are very complex mixtures of refractory, dark or brown colored, heterogeneous organic compounds and, as natural organic substances, are ubiquitous in water, soil, and sediments.[14] Since HS are of paramount important in the environment and among the most widely distributed organic materials in the soil, numerous studies have focused on how to explore the structures and basic chemical and reactive nature of HS. However, up to this time, this field is still controversial and incompletely understood.

Early research suggested that HS can be divided into a three part fractionation scheme based on solubility under acidic or alkaline conditions[38]: a) humin, the insoluble fraction of humic substances; b) humic acid (HA) (generally pH < 2), the fraction soluble under alkaline conditions; c) fulvic acid (FA), the fraction soluble under all pH conditions. The traditional view provided a “polymer model” to describe the structure of humic substances: that humic substances comprised randomly coiled macromolecules that had elongated shapes in basic or low-ionic strength solutions, but became coils in acidic or high-ionic strength solutions.[39] It was suggested that the molecules in humic substances had average molecular masses of 20,000-

50,000 Da, radii of gyration of 4-10 nm, and random coil conformations. Purely biological processes and biotic reactions were thought to be major sources of HS.[40-44]

More recent research [45] has challenged this early view of HS and suggested these traditional structures for HS do not exist in soils since artifact formation was common in these HS studies. They suggested that soil organic matter is composed of mixtures of plant, microbial constituents (carbohydrates, proteins, lipids, etc.) and the same constituents in various stages of degradation (partially degraded lignins and tannins, and microbial materials such as melanins and other polyketides [45, 46]. In this "supramolecular model", humic substances are present as dynamic supramolecular associations, in which many relatively small and chemically diverse organic molecules form associations stabilized by hydrogen bonds and hydrophobic interactions.[47, 48] This model emphasizes that all molecules are found to be intimately associated with a humic fraction, including biomolecules that cannot be separated without significant change of the chemical properties of the fraction.[38, 49, 50]

In addition, a derivative model from this supramolecular model is the micellar model of HS, in which intra- or intermolecular organization produces interior hydrophobic regions separated from the aqueous surroundings by an exterior hydrophilic layer.[51, 52]

The important surface functional groups of humic substance are carboxyl, carbonyl and phenylhydroxyl groups. The acidic character of humic substances is associated largely with the carboxylate and phenylhydroxyl groups. The former have pK_a values in the range between 2.5 and 5 depending on the proximity of electronegative atoms, and the latter have pK_a values around 9 or 10.[9] Both functional groups are capable of acting as the ligand in forming complexes with metal ions, especially the trivalent metal ions Al (III) and Fe (III), which have large stability constants to form complexes.

The interaction of humic-based organic compounds with mineral surfaces has crucial effects on natural aquatic environments, thus it has been extensively studied over the last several decades. The interactions of humic-based organic compounds with mineral surfaces is dominated by the deprotonable functional groups, such as carboxyls and phenolic hydroxyls, of the HS and the active binding sites of mineral surfaces, consisting mainly of Al-OH on aluminum (hydr)oxide at the edges of clay minerals, and Fe-OH on iron (hydr)oxide. Ligand exchange occurring between the carboxyl and hydroxyl groups and the metal (hydr)oxide surface is considered as the predominant mechanism for the adsorption of the humic substance on the metal (hydr)oxide by some studies.[53-55] In addition, hydrogen bonding and electrostatic interactions are also attributed to the adsorption of natural organic matter (NOM) on the surface of the metal (hydr)oxide.[56, 57] Followed by ligand exchange, hydrophobic effects should be important since some studies observed the hydrophobic constituents of NOM were preferentially absorbed, and the hydrophilic NOM was readily transported. [58, 59] In addition, some studies report that carboxylic groups govern NOM adsorption from low pH solution and phenolic groups determine NOM adsorption from high pH solution.[11, 57, 60] In particular, chelate formation involving two aromatic ortho-carboxylic groups, or one aromatic carboxylic group and ortho-phenolic group, or two aromatic phenolic groups is important for the adsorption of NOM on the surface of metal (hydr)oxides. Guan *et al*. suggested [11] that most of the aromatic carboxylates over the pH range of 5-9 directly interact with aluminum hydroxide, with intermediate water molecules present, which is known as an outer-sphere structure.

2.6 The competitive adsorption of phosphate and humic-based organic compound adsorption on colloids

Anions of phosphate can be strongly adsorbed on the surface of metal (hydr)oxide due to the formation of bidentate surface complexes with –OH surface binding sites.[5-8]As humic substances adsorb on the same type of site, phosphates strongly compete with humic substances in an aqueous environment for similar binding sites on the surface of metal (hydr)oxide when they are present in water together. Researches [1-4] focusing on competitive adsorption of phosphate with humic-based organic anions on the surface of iron or aluminum oxides have shown that phosphate adsorption is affected by organic anions and vice versa. In general, organic anions can affect phosphate adsorption in five respects: 1) competing for the same surface binding site; 2) dissolving the adsorbent; 3) changing the surface charge of the adsorbent; 4) creating binding sites for adsorption of metal ions such as Al^{3+} and Fe^{3+}; 5) retarding the crystal growth of poorly ordered aluminum and iron oxides.[5, 8, 61, 62] Some studies indicate that the organic matter on phosphate adsorption is transient, so the order of addition of phosphate and organic compounds and concentration are quite important for the adsorption behavior.

In this work, gallic acid and tannic acid (a commercial form of tannin), instead of the more complicated humic substances, have been chosen as relatively simple models to study the competitive adsorption with phosphate for binding sites on the surfaces of hydrous iron and aluminum oxides. Gallic acid (3,4,5-trihydroxybenzoic acid), Figure 2.4, is a subunit of complex humic acid with both phenolic and benzoic groups. The benzoic group has a pK_a of 4.26 and the phenolic groups have a first pK_a of 8.70 and a second pK_a of 11.45.[63] Tannic acids (the formula for commercial tannic acid is often given as $C_{76}H_{52}O_{46}$, but in fact it contains a mixture of related compounds) contain a glucose center attached to a variable number of gallic

acid and benzoic acid end-groups by ester linkages.[64] As shown in Figure 2.4, tannic acid is a polyphenol, which has been used in studies of water treatment[65] and in the field of soil science. [66] Its weak acidity (pK_a around 10) is due to the predominance of these phenol groups in the structure.

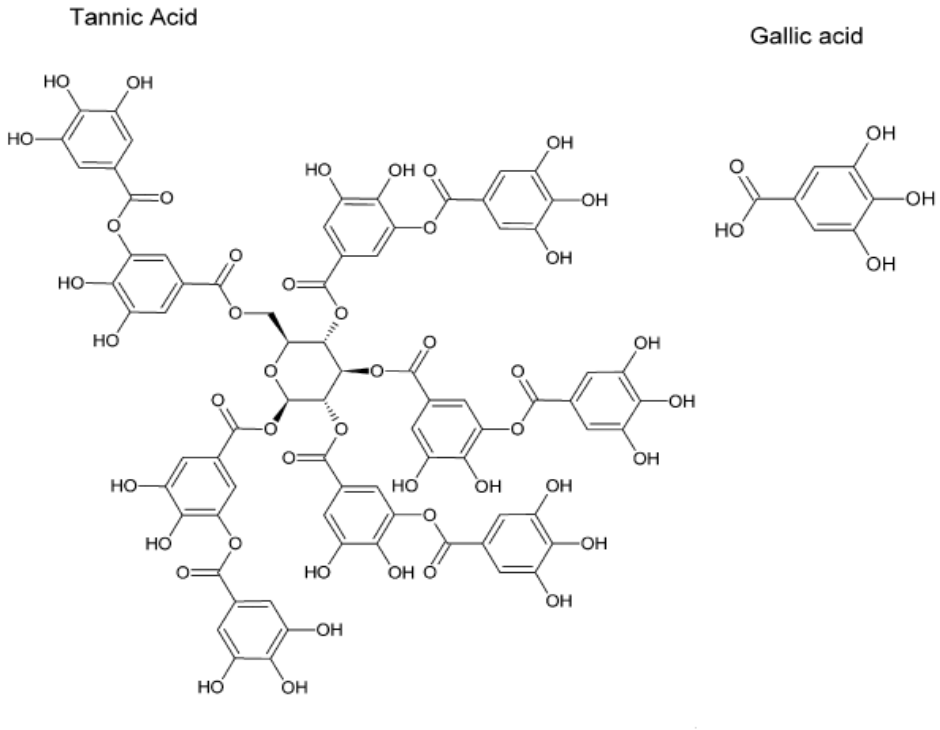

Figure 2.4 Chemical structures for tannic acid (TA), and gallic acid (GA). The structure shown for tannic acid is a representative molecule for tannic acid, an imprecisely defined mixture of hydrolysable tannins.

2.7 Al (III) and Fe (III) coagulants in the wastewater treatment process

To decrease the phosphate and humic substance content in waste water so that it can match regulations, chemical coagulants are frequently applied in order to maximize removal of potential pollutant chemical species such as phosphates, organic compounds and small solid particles of

various materials. Both Al^{3+} and Fe^{3+} are the most predominant cationic fraction used as coagulants and their behavior in wastewater treatment is somewhat similar.

Aluminum (III) sulfate and iron (III) chloride are common coagulants used in wastewater treatment. However, aluminum (III) sulfate is a more common coagulant than iron (III) chloride since the solution of iron (III) chloride is acidic and oxidizing, which can cause metallic parts of the system to corrode.[9] Both Al and Fe hydroxide precipitates in the flocculated form have a very large surface area. Depending on conditions, the hydrous aluminum and iron oxide precipitates have a point of zero charge (pH_0) value that is as high as pH 9.[9] Therefore, under pH 9 their positive surface charge can partially neutralize the negative charges of suspended matter such as clay, some organic matter, and bacteria, all of which have much lower pH_0 values. This adsorption process allows the colloidal particles to settle out together into larger aggregates.

In addition, Al^{3+} and Fe^{3+} are able to react with phosphate, and then precipitate together in the form of highly insoluble aluminum phosphate as the chemical equations expressed below:

$$Al^{3+}(aq) + PO_4^{3-}(aq) \rightarrow AlPO_4(s) \qquad [2.7.1]$$

$$Fe^{3+}(aq) + PO_4^{3-}(aq) \rightarrow FePO_4(s) \qquad [2.7.2]$$

However, the actual processes are more complex. When aluminum and iron cations are added directly to a low alkalinity waste stream containing phosphate, some direct reactions ([2.7.1] [2.7.2]) may occur. When they are added directly in large excess to a highly- alkaline waste stream, Fe^{3+} or Al^{3+} anions hydrolyze so quickly that they are already converted to an insoluble hydrous oxide form before they are able to react with phosphate. However the iron and aluminum (hydr)oxides are still able to remove phosphate by the specific adsorption with the binding sites on surface of the freshly precipitated floc as the chemical equations expressed below:

$$Al(OH)_3 + HPO_4^{2-}(aq) + H_2O \rightarrow AlOH(HPO_4)\cdot H_2O(s) + 2OH^-(aq) \qquad [2.7.3]$$

$$Fe(OH)_3 + HPO_4^{2-}(aq) + H_2O \rightarrow FeOH(HPO_4)\cdot H_2O(s) + 2OH^-(aq) \quad [2.7.4]$$

In addition, the adsorbed phosphate can slowly migrate to the interior of the colloid floc and leave fresh surface to continue the adsorption process. Finally the hydrous oxide gradually converts more and more into hydroxyphosphate or phosphate.

2.8 PDMS and its surface modification

Crosslinked PDMS is the most common elastomeric polymer used in microfluidic devices due to some advantages such as simple fabrication by soft lithographic techniques, biocompatibility, permeability to gases, nontoxicity, chemical inertia, and optical transparency down to 280 nm. Its low surface energy ($\approx$ 22-25mJ m^{-2}) is also suitable for micro printing. [67] However, native hydrophobic PDMS makes filling microchannels with aqueous solution difficult, adsorbs small organic molecules into its bulk, and causes proteins to bind strongly and non-specifically to the native PDMS surface.

The adsorption of protein or other species on the hydrophobic surface could cause surface fouling, increase the surface to volume ratio and lead to substantial sample loss. Thus, it is important to enhance PDMS surface protein resistance ability by surface modification. In addition, PDMS swells in most organic solvents, which makes PDMS-based microfluidic devices only compatible with aqueous solutions and certain organic solvents. [68]

Usually, surface modification of PDMS is required for specific applications. To change the native hydrophobic surface to a hydrophilic surface, commonly methods used include plasma oxidation, UV/ozone, and corona discharges. In this work, the plasma method was chosen. Plasma is an electrically conductive gas, which is composed of a certain portion of ionized particles. It is still not clear the mechanism by which silanol groups are formed on the surface after plasma oxidation. But there is an agreement that the surface consists of a stiff SiO_x skin

layer, which easily leads to cracks on the surface. In contrast to the behavior of most other oxidized polymers, the oxidized PDMS surface may seal irreversibly to itself without using adhesive. Oxidized PDMS can also seal irreversibly to other material surfaces, such as glass, Si, SiO_2, quartz, silicon nitride, polyethylene, polystyrene and glassy carbon.[69] However, the freshly oxidized PDMS surface rapidly regains its native hydrophobic properties after exposure in ambient conditions for several hours. The cracks on the oxidized PDMS were observed after oxidation, which are due to the different elasticity between the oxidized layer and bulk. Owen *et al.* estimated the depth of the cracks on the surface in the range of 0.3 to 0.5 μm, which is much larger than the 10 nm depth of the SiO_x skin layer. [70] The recovery of surface hydrophobicity is suspected to be a result of the migration of low molecular weight molecules (LWM) of PDMS to the surface through the deep cracks. Whitesides' group concluded the freshly oxidized PDMS channel can support reliable eletroosmosis flow used in quantitative analyses for only 3 hours after oxidation. [69] Vickers *et al.* have shown that the hydrophilic SiO_x is stable for at least 7 days if the LWM are extracted by a series of solvents. [71]

The surface modification methods can be divided into two categories: physical modification and chemical modification. Besides the surface oxidation method mentioned previously, which can create reactive silanol functional groups on the surface, physical adsorption is another important modification, which mostly utilizes hydrophobic forces or electrostatic forces and is experimentally quick and simple. However, due to the weak interaction between the molecules or ions and PDMS substrate, the physical adsorption on modified PDMS surface is not robust in thermal, mechanical and solvolytic aspects. [72]

Covalent modification can introduce a self-assembled monolayer (SAM) or polymer coating on the surface, which makes this method more robust than physical modification. The polymer coating method was chosen in my research work. [72] Trichlorosilanes, triethoxysilanes,

trimethoxysilanes and their derivatives may form polymer coatings and introduce different head groups on both oxidized PDMS surface and glass. [72] Following a combination of oxidation followed by covalent modification, the surface may be made much more stable and surface "healing" was slowed.

2.9 Microfluidic system

The first concept of "miniaturized total chemical analysis system" was introduced by Manz *et.al.* in 1990. [73] The development of microfluidic systems, such as micro total analysis systems (μTAS) or lab on a chip (LOC), have received more and more attention due to the reduction of sample and reagent consumption, analysis time and enhanced detection limitation and portability. Microfluidic systems are a combination of microchannels with cross sectional dimension under 100μm, pumps, mixers and valves. All of the components are combined to control and manipulate small amount of fluids (10^{-9} to 10^{-18} litres). [74] The fluid flow in microfluidics is usually controlled by mechanical or electrokinetic methods. To perform effective functions (such as mixing, detection) microfluidic systems are usually combined with other techniques, such as optics, magnetics, or electrics. Four kinds of electrokinetic phenomena are very important in the field of microfluidics: (a) Electrophoresis: the movement of charged particles in the stationary fluid induced by an applied electric field; (b) Electro-osmotic flow: the movement of liquid in the surface charged microchannel induced by an applied electric field; (c) Sedimentation potential: the electrical potential induced by the movement of the charge particle in the stationary liquid; and (d) Streaming potential: the electrical potential induced by the movement of liquid in the surface charged microchannel.

2.9.1 Basic physical principles of microfluidics

Reynolds number

As the system reduces to micro- or nano-size, the surface to volume ratio is significantly enhanced so that surface effects become much more important in microsystems compared to macrosystems. The Reynolds number (Re) is one of many dimensionless parameters in fluid study, which is a ratio of inertial forces (ρV^2L^2) to viscous forces (μVL).

$$R_e = \frac{\rho VL}{\mu} \qquad [2.9.1.1]$$

where ρ is the density of the fluid, V is the mean fluid velocity, L is a characteristic linear dimension, and μ is the dynamic viscosity of the fluid. In microscopic fluid, Re is usually much less than 100. Viscosity forces are dominant and flow is completely laminar and no turbulence occurs.

Electro-osmotic flow (EOF)

When the microchannel is full of ionic fluid and the wall of microchannel has surface charges, the excessive charges in the diffuse layer of the EDL will move towards the electrode of opposite polarity and drag the surrounding liquid molecules in the same direction due to the viscous effects under an applied electric field. This fluid flow moving as a plug is referred to as electro-osmotic flow (EOF). This fluid plug has the ability to minimize the broadening of flow. If electrodes are added at the both ends of the microfluidic channel, the velocity profile of the EOF is uniform across the entire width of the channel, as shown in Figure 2.5. EOF is the common pumping method used in the field of microfluidics. However, high voltages are required, which make it difficult to miniaturize microfluidic equipment and causes Joule heating effects.

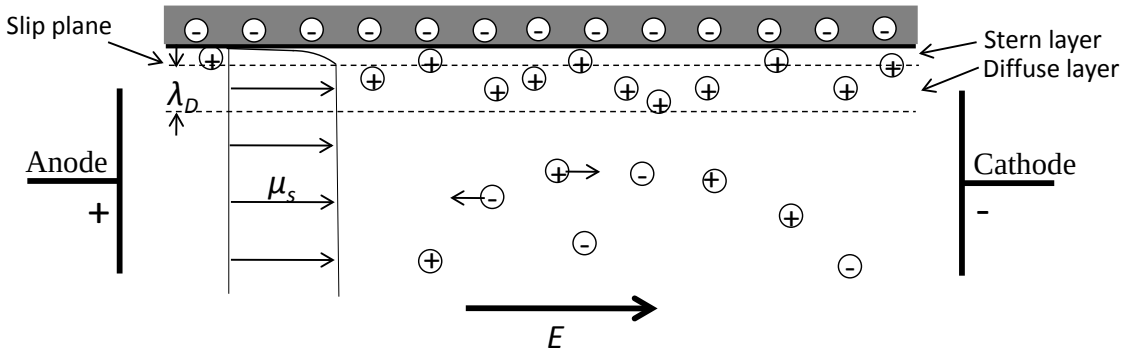

Figure 2.5 Schematic graph of electro-osmotic flow in the microfluidic channel.

In microfluidics, the thickness of the EOF is much smaller than the diameter of the microfluidic channel. Thus, the velocity of the EOF (μ_{eof})can be expressed by Helmholtz-Smoluchowski equation:

$$\mu_{eof} = \frac{\varepsilon E_Z \xi}{\mu} \qquad [2.9.1.2]$$

where E_z is the applied electric field strength, ζ is the zeta potential at the liquid-solid interface, μ is the solution viscosity, and $\varepsilon = \varepsilon_0 \varepsilon_r$: ε_0 is the dielectric constant of vacuum ($\varepsilon_0 = 8.854 \times 10^{-12}$ F/m), and ε_r is the relative permittivity.

Ajdari *et al*. investigated the consequence of charge nonuniformity on the generation of electro-osmotic flow and concluded that the heterogeneous surface of the microfluidic channel may cause non-uniform surface zeta potential or charge density, which results in regions of bulk flow circulation.[75] Whitesides' group studied two samples of surfaces with patterned surface charges and demonstrated the movement of recirculating EOF is generated perpendicular to the applied field, which might be a mixer in the microfluidics application.[76] However, surface heterogeneity may be caused by many mechanisms. For example, the adsorption of proteins,

peptides, or ions on the surface of the wall of the microfluidic channel, impurities in the material, and defects from surface modification.[77] Any change of the surface of the microfluidic channel will impact the velocity of EOF, making it difficult to manipulate the velocity of the EOF in some cases.

Pressure-Driven flow

When the flow in a microfluidic channel is driven by applied pressure, the movement of ions due to the mechanical pressure results in the electrical current in the pressure-driven flow direction (shown in Figure 2.6) , which is referred to as the streaming current. The streaming current induces the streaming potential. The counter ions in the electrical double layer move in the opposite direction to the streaming current under the streaming potential, which is referred to as the conduction current. The counter ions in the conduction current will drag the liquid molecules around them, thus forming a liquid flow in the opposite direction to the pressure driven flow, which decreases the velocity of the pressure driven flow and is referred to as the electro-viscous effect.

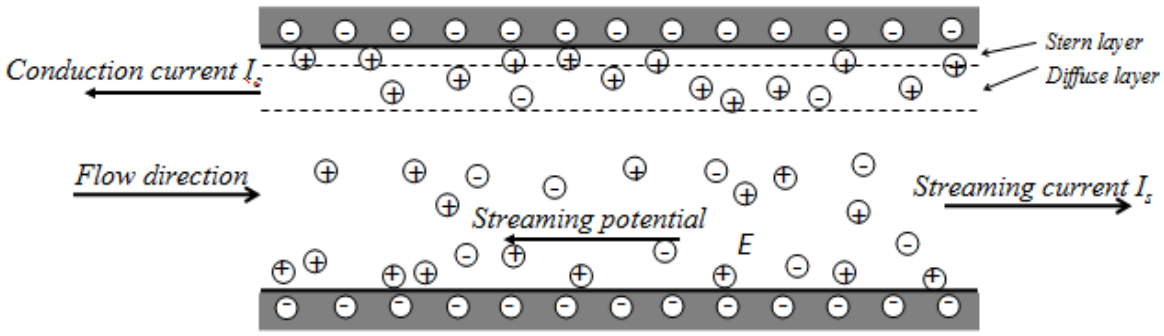

Figure 2.6 Schematic graph of the pressure-driven flow in the microfluidic channel. [77]

The streaming current is given by

$$I_s = \int_{A_c} V \rho dA_c \qquad [2.9.1.3]$$

where V is velocity of the pressure-driven flow, ρ is the net charge density, A_c is the cross-section area of the microfluidic channel.

The conduction current is given by

$$I_c = \frac{\lambda_b E_s A_c}{L} \qquad [2.9.1.4]$$

where λ_b is the electrical conductivity of the liquid, E_s/L is streaming potential gradient, A_c is the cross-section area of the microfluidic channel. [77]

2.9.2 Materials used in the fabrication of microfluidic systems

Silicon and glass are two materials first used in microfluidic devices due to well-developed photolithography technique in the silicon microelectronics industry. However, the fabrication of microchannels on silicon and glass must be carried out in a clean room, which makes cost expensive. Also, silicon is opaque, which is not suitable to combine any optical component. Glass is optically transparent, but it is difficult to etch channels on its surface. As this field developed, polymer materials such as poly(dimethylsiloxane) (PDMS), poly(methylmethacrylate) (PMMA), polycarbonate or polyolefin have received more attention due to faster design time and low cost.

Our studies focused on PDMS, which is an optically transparent, soft elastomer as it shows promise in the fabrication and application of water-based and biological microfluidic systems. Effenhauser *et. al* introduced the first miniaturized capillary electrophoresis (CE) systems in PDMS. [78] They observed that the unmodified PDMS microchannel supported a very weak EOF and negatively charged ions moved toward the anode. This is consistent with the assumption that

native PDMS surface will weakly support EOF as there are no charged groups on the surface. However, Ocvirk *et al.* observed that the PDMS microchannel supported a cathodic EOF from pH 3 to pH 10.5 and EOF is highly pH dependent.[79]. They summarized the possible reasons might include adsorption of charged particles onto the surface, charges from leftover polymerization catalyst or added fillers, and charges produced by surface acid-base chemistry such as silanol.

2.9.3 Fabrication of microchannel in PDMS

Whitesides' group demonstrated that soft lithography is one quick and efficient way to make a PDMS microchannel (20-100μm) without the conditions of a cleanroom. [80] Soft lithography mainly includes rapid prototyping and replica molding. Rapid prototyping includes several steps as shown in Fig 2.7. The microfluidics design graph was created by a computer-aided design (CAD) program then printed out to form photomask in which the design part is transparent. Then this photomask can be used in a photolithography process to "print" out the design on the photoresist covered silica wafer. After the dissolving the unpolymerized photoresist, the silica surface is a positive relief design which can serve as a master.

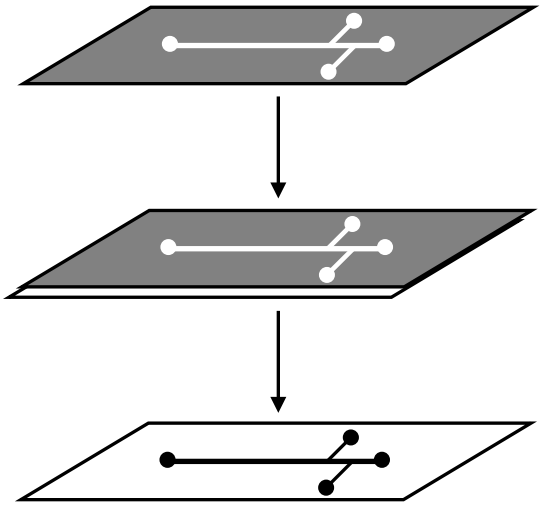

Figure 2.7 Scheme for rapid prototyping of PDMS microfluidic devices.

After rapid prototyping, PDMS microfluidic devices can be made faster by replica molding. The prepolymer of PDMS is cast on the master. Then, after one hour curing in oven at 60° C, the PDMS replica can simply be peeled from master to form PDMS microfluidic devices. The PDMS replica can form a reversibly seal with several of other flat surfaces due to the *Van der Waals* force. Oxidized PDMS can irreversible seal with oxidized PDMS, glass, SiO_2, quatz and hydrophilic surfaces due to the formation of Si-O-Si covalent bonding. [69]

2.10 The interaction of protein with surfaces

The binding of proteins to receptors of interest through their physical shape, topography, and chemical properties is referred to as specific binding. During the specific binding process, proteins may have other chances to physically adsorb onto a solid substrate without specific interactions, which is referring to as nonspecific binding. In particular applications, for example biosensors, nonspecific binding may cause high background noise or false positives. Enhancing the specific binding and reducing nonspecific binding are required for most materials used in biotechnology applications. Different functional SAMs have been utilized to modify different surfaces for the minimization of nonspecific adsorption because the self-assembled monolayer can completely change surface properties at the molecular scale. In addition, SAMs or other surface coatings can be used in fundamental research in the study of the interaction of proteins with surface as they provide a method to control the surface properties. In this section, the protein adsorption on SAM modified surfaces will be briefly discussed.

The adsorption and desorption of protein on the surface are complicated even between a simple well-defined protein and surface. Besides the obvious fact that an equilibrium exists between adsorption and desorption of the proteins (a in Figure 2.8), the protein adsorbed on the surface may laterally interact with neighboring proteins; change conformation but retain

biological activity; or completely denature. The basic adsorption and desorption processes are summarized in Figure 2.8.[81, 82]

To study the orientation, conformation or the degree of denaturation of proteins adsorbed on the surface, X-ray crystallography, multidimensional NMR spectroscopy or infrared spectroscopy can be utilized. To measure the content of protein adsorption on the surface, surface plasmon resonance spectroscopy, waveguide interferometry, and ellipsometry are available depending on the experimental requirement.

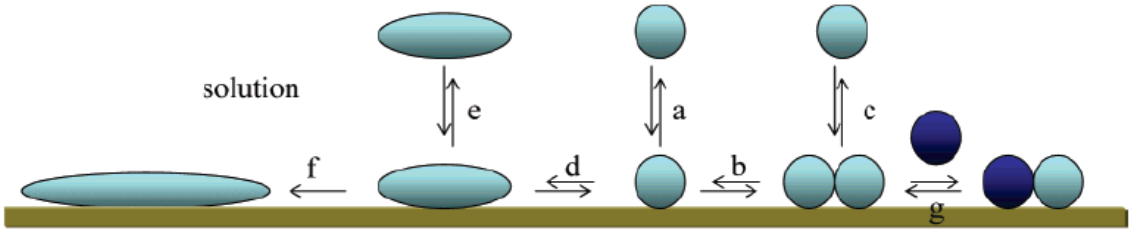

Figure 2.8 The equilibrium of protein on the surface. (a) protein adsorption-desorption to the surface, (b) lateral mobility of protein, (c) dissociation of a protein adjacent to another protein, (d) conformation change of adsorbed protein on the surface, (e) dissociation of a deformed protein to the surface, (f) denaturation of the protein, (g) exchange of adsorbed protein with exterior protein[81, 82]

The hydrophobic amino side groups of globular proteins aggregate through hydrophobic interaction to form the tertiary structure of proteins. These tertiary structures also enhance the formation of secondary structures such as α-helices and β-sheets, which exist in most globular proteins and are stabilized by hydrogen bonding and hydrophobic interactions. However, the tertiary structure of proteins is marginally stable as the formation of it costs the loss of entropy. When proteins come into contact witha solid surface, the interaction between the two may change the protein conformation, the extent of which depends on the properties of both of surface and

proteins. The forces involved in this process include van der Waals, hydrophobic and electrostatic interactions, and hydrogen bonding.

To understand the interaction between proteins and surface, the surface properties need to be well-defined in some cases. A self-assembled monolayer is an ideal tool to modify the surface and control the properties of the surface at molecular scale. Two commonly used self-assembled monolayers are alkanethiolates on Au and hydroxylated surfaces. Both will be discussed in detail in the following section (2.11).

The primary surfaces developed to resist the adsorption of several model proteins are SAMs of alkanethiols terminated in short oligomers of the ethylene glycol groups (OEG_n) [$HS(CH_2)_{11}(OCH_2CH_2)_nOH$: n=2-7].[83] OEG_n terminated alkylsilanes have the ability to resist smaller proteins but are less efficient to larger proteins. [84]

Our group has focused on the study of specific and nonspecific adsorption of proteins on the fluorinated PDMS surface. Bhushan *et al.* reported fluorinated PDMS surface had a higher water contact angles and exhibited lower surface energy, adhesion and friction than unmodified PDMS.[85] Kawaguchi *et al.* reported 1H, 1H, 2H, 2H-perfluorooctyltriethoxysilane self-assembled monolayers on PDMS blocked the nonspecific adsorption of bacteria (Escherichia coli). [86] The previous work from our group showed that the fluorinated PDMS substrate was able to selectively adsorb a fluorous-tagged peptide in aqueous solutions [22].

Here, we use surface plasmon resonance to monitor in situ protein adsorption. The perfluorinated self-assembled monolayer is used instead of fluorinated PDMS because the structures of polymer and glass are mostly undefined at the molecular level [23] while self-assembled monolayers provide well defined surface composition and properties, suitable for the study of protein adsorption.[81]

As the stability of protein is also a very important factor to impactingadsorption, we chose to two model groups: soft proteins (α-lactalbumin, myoglobin) and hard protein (lysozyme C, RNase A). According the definition gave by Arai and Norde[188] [192-193] soft protein will adsorb on hydrophilic surface accompanied by significant loss of structure, which makes the adsorption possible even under electrostatic repulsion, whereas hard proteins only adsorb to hydrophilic surface under electrostatic attraction. The surface hydrophobicity and protein flexibility are calculated hereand the possible mechanisms of protein adsorption are discussed.

2.11 Self-assembled monolayers

Self-assembled monolayers (SAMs) are highly ordered two-dimensional thin films (typically ca. 2 nm). The SAM has the ability to completely change the surface properties.[87] Two common SAMs that form spontaneously on certain surfaces are monolayers of alkanethiolates assembled on gold surface and organosilicon derivatives assembled on hydroxylated surfaces, such as the surfaces of glass or silica. [88, 89] In my research, the former method was used to modify a gold-coated AFM tip, while the latter was used to modify freshly oxidized PDMS. Thus, two kinds of monolayers are discussed in this section including the formation mechanism, the surface geometry after modification, and the stability of the SAM**Alkanethiolates self-assembled monolayers on Au**

The self-assembled alkanethiol monolayer on Au surface has been extensively studied. It is very stable and free of holes on the surface. [90-92] In this work, we use 4-(12-mercaptododecyl)- phenol, one type of long chain thiol compound with a terminal phenolic group, to modify the Au (111) surface. To form thiol monolayers on specific solid surfaces of substrates, the substrates are immersed in (usually alcohol) solutions of low thiol concentration, typically 1mM, for 1-10h. Bain *et al.* reported a two-step SAM formation, in the first, quick step the film

thickness and contact angle reaches ~ 90% of final values within the first minute of reaction, and in a second, slower step the SAM forms completely after several hours. [93] They also observed the SAMs with longer chain n-alkyl thiol (n>8) are better ordered than SAMs with a shorter chain. Alkanethiol molecules are densely packed and highly ordered since the thiol coordinates to the gold surface in the first step, and the polymethylene chains in an all-trans conformation tilted slightly from normal to the surface and the terminal group reorientation occurs in the second step. Poirier *et al*. reported the thiol SAM is arranged with an epitaxial overlayer $(\sqrt{3}\times\sqrt{3})R30°$ on an Au (111) surface. [94]

By using adsorbents having the structure $HS(CH_2)_nR$, self-assembled monolayers (SAMs) can present a more- or less- well-ordered array of the group R at the interface. R itself could be one of many functional groups of chemical and biological interest and the selection of R imparts a high degree of control over the structure of these films. For alkyl chains of form $HS(CH_2)_nR$ (where $n\geq10$), the surface properties depend primarily on the tail group R, are independent of the chain length, and are influenced only indirectly by the sulfur-gold coordination. Versatile functionalized films are a convenient method of controlling the chemical and physical properties of a surface. Some researchers[92] also verify that phase segregation on the Au (111) surface can be observed when mixed alkanethiols have a chain length difference of more than three carbon atoms. Other than thiols, disulfides (RSSR), sulfide (RSR), and phosphines (R_3P) can also form stable monolayers on gold.[95]

SAMs on the gold surface are quite stable. For instance, mononolayers of alkanethiols on gold are stable in air or in contact with water or ethanol at room temperature until heated to 70º C.[93] Bain and Troughton *et al*., reported monolayers of octadecanethiol on gold were unaffected by immersion in 1N HCl or 1N NaOH for one day, but after one month deterioration did take place.[93]

Alkylsiloxanes self-assembled monolayers on hydroxylated surface

Alkyltrichlorosilanes, alkyltriethoxysilane or alkyltrimethoxysilane are usually used to form SAMs on hydroxylated surface such as glass, silicon oxide and oxidized PDMS. Before the self-assembly reaction, the surfaces usually need to be activated using strong acid or a plasma to form the maximum number of hydroxyl groups. [96] The surface is enhanced in hydrophilicity and covered with a thin layer of water after activity, which is essential to the next step in the self-assembly reaction. [96]

The formation of the SAM can be carried out in solution or through vapor phase deposition techniques under anhydrous conditions. In solution, the reaction reagents undergo a fast hydrolysis reaction to form three silanols, then through a slow condensation process to form oligomers. The oligomer and surface hydroxyls bond via hydrogen bonds. The hydrogen bonds transform to covalent bonds during the curing or baking process. So far, the arrangement of the covalent bonds is still not fully defined. Usually the SAM will form with neighboring siloxanes to form a cross-linked network of Si-O-Si bonds. One of three silanol groups of the silane compound usually forms a covalent bond to a hydroxyl group and two other silanols may be free or in condensed form.[97]

By cross-linkage of the molecules and covalent anchoring to the substrate, the alkylsiloxanes SAM on hydroxylated surface is more stable thermally than a thiol SAM on Au surfaces. [81] [87] SAMs of OTS are stable up to 150˚C and cannot be damaged using organic solvents, hot water, or detergent solution [98-100] Perfluorinated SAMs are more resistant. For example, 1H,1H,2H,2H-perfluorodecyltrichlorosilane coatings are stable up to 400˚C.[101]

2.12 The electrical properties of the charged surfaces in aqueous solution

The electrical properties of the charged surface in aqueous solution are a crucial factor to understand the interaction between the colloidal particles and an AFM tip. They are also fundamental to the study of electrokinetics in microfluidics. In this section, the basic theories of surface electrical properties are introduced.

Surface charge and surface dipoles

The net charge on the surface in an electrolyte solution may be increased due to several reasons. First, surface functional group dissociation or ionization gives the surface a net charge, such as the silanol group on the surface of oxidized PDMS (-SiOH $\rightarrow$ -SiO^- + H^+). Depending on the pH of solution, the ionizable functional group gives a negative or positive surface charge. Secondly, the ion adsorption or ion exchange on the surface could also cause charge. Thirdly, the surfaces of certain crystal planes may contain surface charges.

The surface density of net total particle charge (σ_p) can be expressed as:

$$\sigma_p \equiv \sigma_{in} + \sigma_{IS} + \sigma_{OS} = \sigma_0 + \sigma_H + \sigma_{IS} + \sigma_{OS} \qquad [2.12.1]$$

in which σ_{in} is the intrinsic surface charge density, σ_0 is the permanent structure surface charge density, σ_{IS} is the surface density of inner-sphere complex charge, and σ_{OS} is the surface density of the outer-sphere complex charge.

The ions in solution, which did not form any complex with surface functional groups, will neutralize the net total particle charge in the solution, which can be expressed in the equation:

$$\sigma_p + \sigma_D = 0 \qquad [2.12.2]$$

where σ_D is the equivalent surface density of dissociated charge. The point of zero charge (PZC) is the pH condition at which total net particle charge is zero ($\sigma_p = \sigma_D = 0$).[32]

Due to electrostatic repulsion, the individual charged sites are isolated from one another, with the distance between sites usually in the range of 1~5 nm. Assuming that the individual charge *q* is located evenly at a distance *d* on the surface as shown in Figure 2.9, the field E_z at the z direction is given by [102]

$$E_z = \frac{\sigma}{2\varepsilon\varepsilon_0}\left[1 + 2(\cos\frac{2\pi x}{d} + \cos\frac{2\pi y}{d})e^{-2\pi z/d} + ...\right] \qquad [2.12.3]$$

If dipoles are perpendicular to the surface, the field E_z at the z direction can be given by

$$E_z \approx \pm(2q/\varepsilon\varepsilon_0 d^2)e^{-2\pi z/d} \qquad [2.12.4]$$

The electric field induced by surface charges will attract counter ions and repel the co-ions. Thus, there are excessive counter ions in a thin layer of liquid close to the charged surface, which balances the surface charges. The charged surface and the thin layer of liquid containing excessive counter ions is called the electrical double layer (EDL).[103] Stern provided the concept of the compact layer (Stern layer) and diffuse layer as shown in Figure 2.10 [104]

The compact layer is a layer of ions which are strongly adsorbed to the surface and are immobile. The thickness of this layer is usually about several Å, depending on the surface charge group and counterions. The diffuse layer consists of mobile ions, which are less influenced by electrostatic force as compared to the compact layer.

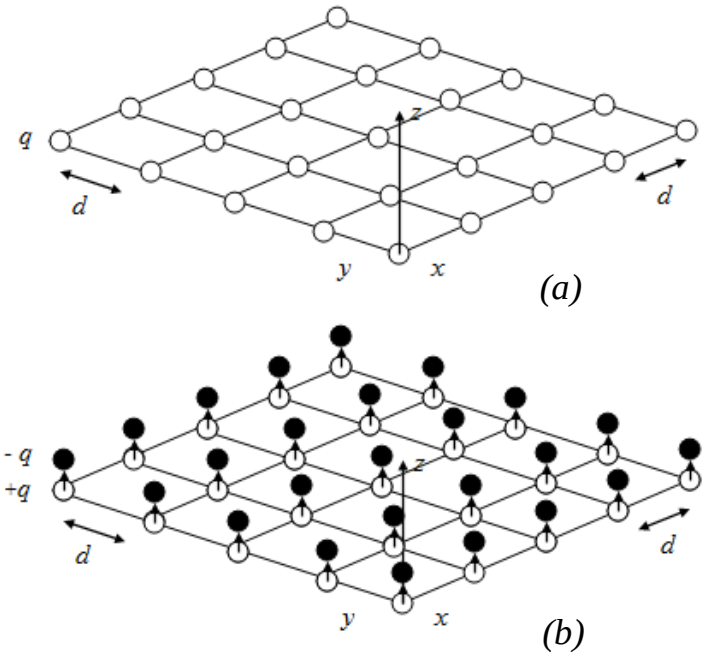

Figure 2.9 a) section of infinite lattices of charges b) section of infinite lattices of dipoles [102]

Electrical double layer

The excess concentration of the ions in this layer gradually decreases to zero as it closes to the neutral bulk liquid. The thickness of the diffuse layer is affected the ionic strength of the liquid and dielectric properties of the liquid. In pure water or organic liquid, the thickness of the diffuse layer can be up to one or two micrometers, which is much larger than the nanometer thickness of the diffuse layer in the high concentration solution.

The boundary between Stern layer and the mobile diffuse layer is called the shear plane. The potential at the shear plane is refer to as zeta potential (ξ). The thickness of the electrical double layer, κ^{-1}, is defined as the distance from the shear plane to the point at which the charge is reduced to 1/e times of the zeta potential. Figure 2.10 shows a representation of the surface of charge distribution of a colloid that is negatively charged, the zeta potential (ξ), and the Stern layer.

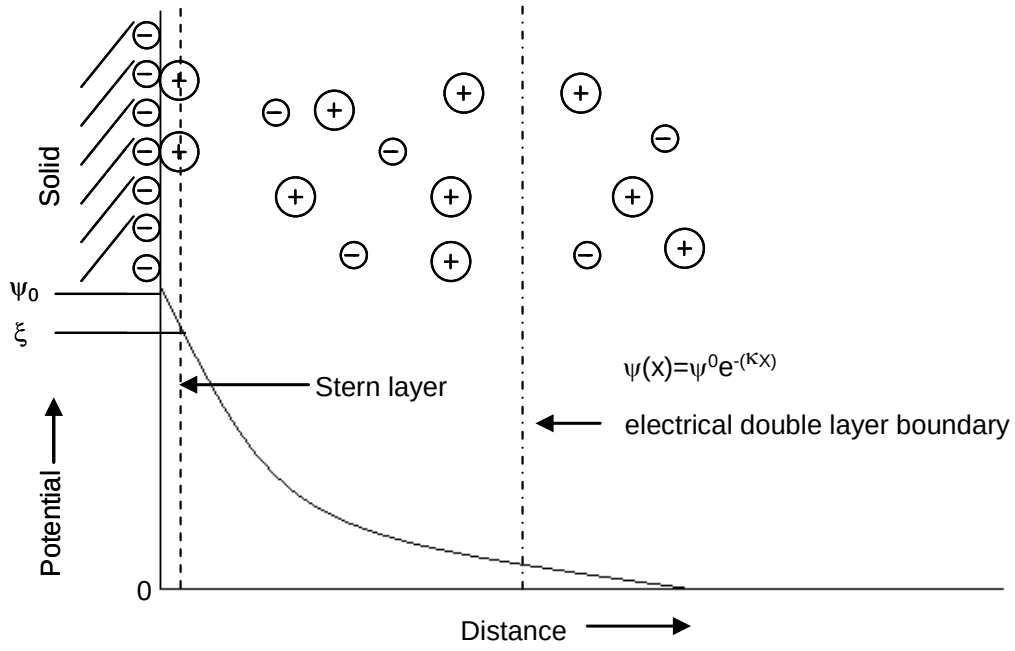

Figure 2.10 The surface of negatively charged particle, the zeta potential (ξ), the Stern layer and the electrical double layer.

In addition, the distribution of ions and potential in the diffuse layer obeys the Poisson-Boltzmann equation (PBE):[105]

$$\nabla^2\psi = \frac{-1}{\varepsilon_0\varepsilon}\sum_i n_i^0 z_i e \exp\left(\frac{-z_i e\psi}{kT}\right) \qquad [2.12.5]$$

in which ψ is the electrical potential, n_i^o is the number density of ions of valence z_i, k is the Boltzmann constant, T is the absolute temperature, ε_0 is the permittivity of vacuum, ε is the dielectric constant of component *i*, e is the elementary charge. The external electrical field is inconsequential compared to the EDL field unless it is extremely high. [77]

2.13 The non-contact force between two surfaces with small distance

The first part of my research work focuses on the study of the interaction force between phenol-terminated AFM tip and sample. In this section, the interaction forces between two surfaces with small distance are discussed, including the DLVO forces and non-DLVO forces. These non-contact forces play an essential role in the stabilization and aggregation of the colloidal particles.

2.13.1 The DLVO theory

About seventy years ago Derjaguin, Landau, Verwey, and Overbeek developed a theory (DLVO theory) to explain the phenomenon of the aggregation of aqueous colloidal particles.[106] In this theory, the assumption is that the interaction force between two surfaces is controlled by the van der Waals force and electrostatic double-layer force, which are both long range forces.

As shown in Figure 2.11, the total interaction energy is a sum of electrical double layer repulsive energy and van der Waals attractive energy. When the electrical double layers of two colloidal particles start to overlap, electrostatic double-layer forces will be raised as a repulsive force that opposes further approach. The electrostatic double-layer force is more sensitive to variations of the electrolyte concentration and pH compared to van der Waals attractive force. At the beginning of the overlaying of the electrical double layers, the van der Waals attractive force exceeds the electrical double layer repulsive force and leads to a significant secondary minimum (W_s), as the repulsive force arise more slowly than the van der Waals attractive force which takes the form of a power law interaction ($W \propto -1/D^n$). As the two charged layers approach further (1nm-4 nm), the energy barriers rises due to the increase of electrical double layer repulsive force.

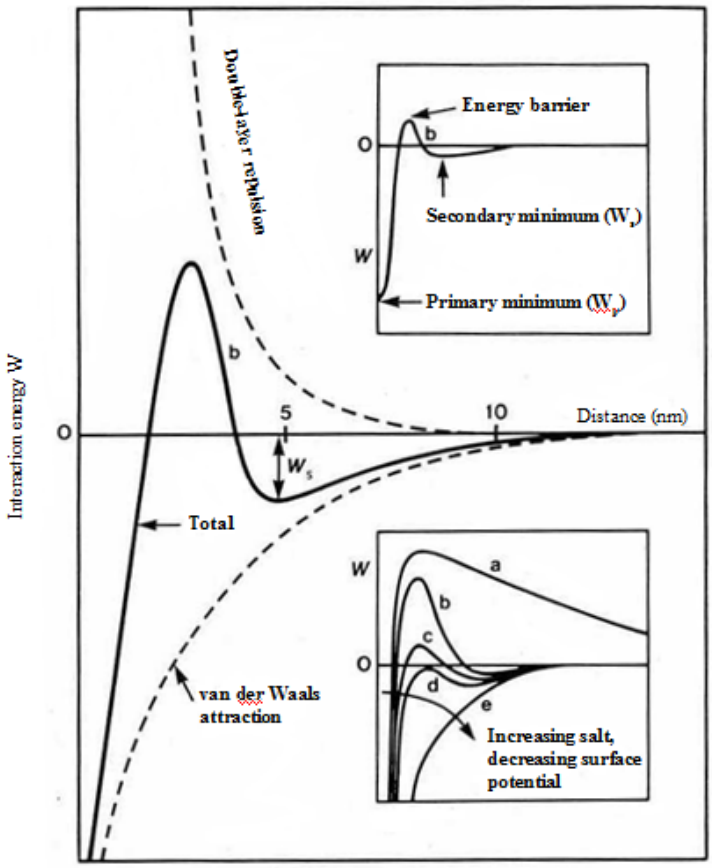

Figure 2.11 Schematic energy versus distance profiles of DLVO interaction. [107]

The coagulation process is strongly controlled by the surface properties of colloidal particles, particularly the surface charge. When the surface is surrounded with electrolyte or associated with other molecules or ions with covalent bonding, known as specific adsorption, the repulsive electrostatic double-layer force and the energy barrier is decreased, which can lead to the coagulation process.

2.13.2 DLVO forces

The Van der Waals force between two similar particles in a medium is an attractive force which readily aggregates the colloidal particles. For polar molecules, three different forces

contribute to van der Waals force: the induction force, the orientation force and the dispersion force. Meanwhile, the electrostatic double-layer plays the role of a repulsive force which stabilizes the colloidal particles from coagulating. The Van der Waals force between two particles can be calculated by microscopic methods and macroscopic methods, which are based on different assumptions. [108]

Hamaker and de Boer assumed pairwise additivity of interatomic dispersion energies between spherical bodies and the influence of neighbouring atoms on the interaction between any pair of atoms can be ignored. They demonstrated that the interaction range for colloidal bodies is on the order of their dimensions. [109] For two spheres of equal radius, a, the total interaction energy, V_A, is given by:

$$V_A(D) = -\frac{A}{6}\left[\frac{2a^2}{D^2+4aD} + \frac{2a^2}{(D+2a)^2} + \ln\left(1-\frac{4a^2}{(D+2a)^2}\right)\right] \qquad [2.13.2.1]$$

where D is the surface to surface separation distance apart along the centre-to-centre axis, and A is Hamaker constant, which is defined as

$$A = \pi^2 C \rho_1 \rho_2 \qquad [2.13.2.2]$$

where C is the coefficient in the atom-atom pair potential, ρ_1 and ρ_2 are the number of atoms per unit volume in the two bodies. [107]

The attractive force between two colloidal particles can then be calculated from the interaction energy using the following equation[107]

$$F_A = -\frac{dV_A}{dD} \qquad [2.13.2.3]$$

The Lifshitz theory [110] neglects additivity and treats large bodies as continuous media. The equations [2.13.2.1] and [2.13.2.2] are still suitable for the calculation of Lifshitz theory. The only difference is that the Hamaker constant is expressed as the bulk properties of different media

as following equation

$$A \approx \frac{3}{4} kT\left(\frac{\varepsilon_1 - \varepsilon_3}{\varepsilon_1 + \varepsilon_3}\right)\left(\frac{\varepsilon_2 - \varepsilon_3}{\varepsilon_2 + \varepsilon_3}\right) + \frac{3h}{4\pi}\int_{\nu_1}^{\infty}\left(\frac{\varepsilon_1(i\nu) - \varepsilon_3(i\nu)}{\varepsilon_1(i\nu) + \varepsilon_3(i\nu)}\right)\left(\frac{\varepsilon_2(i\nu) - \varepsilon_3(i\nu)}{\varepsilon_2(i\nu) + \varepsilon_3(i\nu)}\right)d\nu \qquad [2.13.2.4]$$

in which $\varepsilon_1, \varepsilon_2, \varepsilon_3$ are the static dielectric constants of two surface media and the medium between two surfaces, $\nu_n = (2\pi kT/h)n$. The first term in the equation [2.13.2.4] is contributed by zero-frequency energy of the van der Waals interactions including the Keesom and Debye contributions. The second term is contributed by the dispersion energy and includes the London energy contribution.[107]

Electrostatic double-layer force

For dilute systems, only considering two particle interactions, there are many expressions for the calculation of the repulsive interaction energy between two spherical colloidal particles based on various assumptions for sphere-sphere double layer interaction. The LSA method calculates interactions at large separations for all surface potentials and particle sizes [111]; Derjaguin's integration gives calculations based on large particles at short distances [112]; and the McCartney and Levine formulation is a good approximation based on small potentials at all separations.[108]

For concentrated colloidal dispersions, multiparticle interaction occurs so that the modification of the two body interaction model is necessary. The cell model is a solution of multiparticle interactions including numerical solutions of non-linear PBE in spherical co-ordinates. [113, 114]

2.13.3 Non-DLVO forces

DLVO theory considers two long range force theories, electrostatic double-layer repulsive force and van der Waals attractive force, which are both continuum theories and ignore the other factors that may impact the interactions such as the size, shape, and the surface functional group

on the individual surface. Thus, the DLVO theory cannot explain the force of two bodies below a few nanometers as non-DLVO interaction forces cannot be ignored at this distance. In addition, non-DLVO interaction forces can be stronger than either of the two DLVO forces and can be monotonically repulsive, monotonically attractive, or oscillatory. In this section, three main non-DLVO forces are introduced: solvation (or hydration forces in water), hydrophobic force, and steric force.

Solvation or hydration forces

To understand the interaction force between two surfaces of solid bodies in liquid, the liquid structure and density near the surface should be discussed as it is one important factor to impact the interaction. Unlike the even density in the bulk, over several molecular diameters at the interface the density profile of many liquids close to the solid surface oscillates around the bulk density with a periodicity on the order of a molecular diameter, as shown in Figure 2.12.

During the surface approach, the closing gap squeezes the liquid molecules between the surfaces and leads to the solvation force, which can be expressed by the equation:

$$P(D) = kT[\rho_s(D) - \rho_s(\infty)] \qquad [2.13.3.1]$$

where $P(D)$ is the solvation pressure between two surfaces separated by liquid, $\rho_s(\infty)$ is the density of liquid at interface, $\rho_s(D)$ is the density of liquid between two close walls, which is a function of the separation distance D between two walls. The above equation is applicable to none interaction between the walls and liquid molecules. Figure 2.13 shows the molecular ordering changes as the separation D changes.

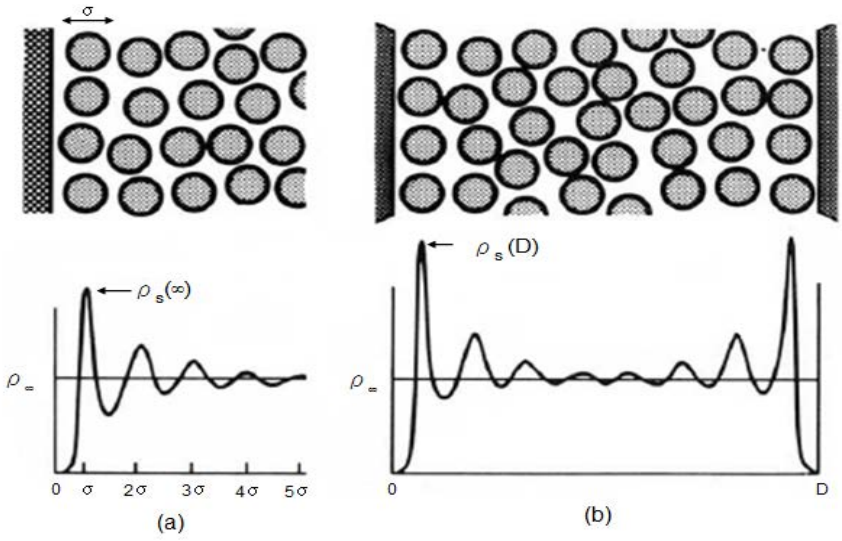

Figure 2.12 (a) Liquid density profile normal at an isolated solid/liquid interface. ρ_∞ is the density of bulk liquid and ρ_s (∞) is the density of liquid at the interface. (b) Liquid density profile normal between two walls with a distance D. ρ_s (D) is the density of liquid between two close walls. [107]

Van der Waals forces and oscillatory solvation forces are not additive. Israelachvili mentioned: "it is more correct to think of the solvation force as the van der Waals force at small separations with the molecular properties of the medium taken into account." [107] The solvation force is thought to arise from overlapping solvation zones of two surfaces. On the other hand, the interaction between liquid molecules can impact solvation force. For example, hydrogen bonding and long range dipole polarization between water molecules leads to a monotonically decaying repulsive hydration or attractive hydrophobic interaction in addition to the shorter range oscillatory interaction. [115, 116]

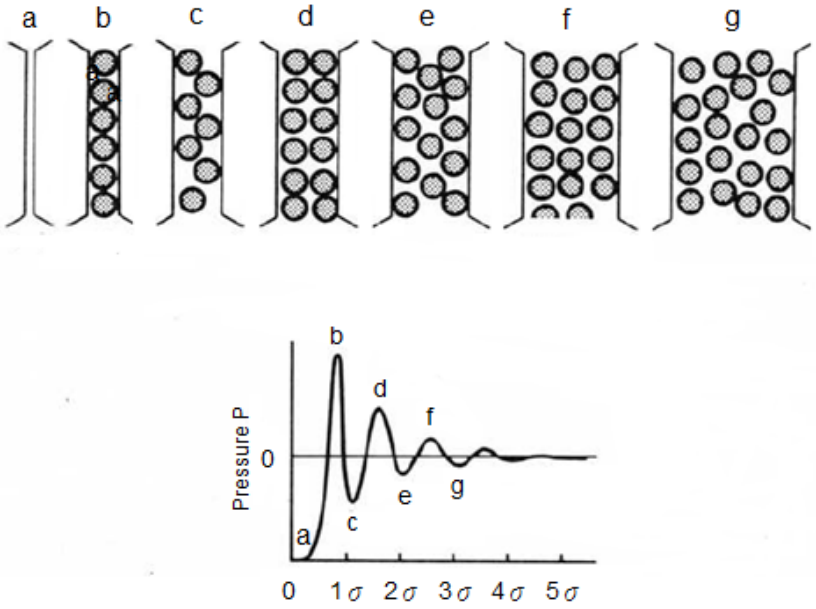

Figure 2.13 Variations liquid pressure and the molecular ordering changes as a function of the separation, D, between two adjacent surfaces[107]

In aqueous solution, the solvation force refers to hydration, structural or hydrophilic forces, which is a short range exponentially repulsive force. The physical mechanism of solvation force is still not clear. One possible reason is at the water molecules interact with surface hydrophilic groups, and to break the ordered water molecules extra energy needs to be added.

Hydrophobic forces

Usually, there are no polar or ionic groups or hydrogen bonding sites on the hydrophobic surface so that there is almost no interaction between the water molecules and surface. The presence of a water layer between the hydrophobic surfaces is entropically unfavorable; therefore two hydrophobic surfaces tend to attract each other together. Hydrophobic forces can be much stronger than van der Waals forces and act as long range forces. [107, 108]

Qi Lin *et.al* measured hydrophobic forces in water between double-chained surfactant monolayers on mica using normal and high-speed video cameras to track the dynamics and rate-

dependence of force-distance profiles from 1000 Å to adhesive contact. They reported that the hydrophobic interaction follows a double-exponential function down to separations of 50 Å, after which the attractive force appears to become considerably stronger. [117]

Steric forces

Polymers are macromolecules composed of monomer units or segments, which are soluble in good solvents, and hold a coil shape in poor solvents. In addition, they are easily adsorbed on most surfaces and reach their saturation point in low concentration solution. When two polymer-covered surfaces approach, the outer polymer layers begin to overlie. The approach process usually results in a repulsive entropic force due to unfavorable free energy during the chains overlaying and compressing, which is known as the steric force. Apparently, surface coverage is one of several important factors that impact steric force. At high coverage, the steric force arises from the osmotic and volume restricting effects of compressed polymer coil. At low coverage, polymer bridges contribute to the attractive forces between two surfaces.

2.14 The contact force (adhesion force) between two surfaces

2.14.1 Theoretical models of adhesion force

When an AFM tip contacts with the sample, the actual molecular species on the tip involved in the interfacial interaction are on the order of tens to hundreds. Two theoretical models have tried to estimate the adhesion force between numbers of molecular species based on continuum contact mechanics theories and the contact area is considerate as a flat circle of radius a. In the Derjaguin-Muller-Toporov (DMT) model [118], the adhesion force is given by:

$$F_a = 2\pi R W_{132}, \qquad [2.14.1.1]$$

where W_{132} is the thermodynamic work of adhesion and equates $W_{132} = \gamma_{13} + \gamma_{23} - \gamma_{12}$.

It predicts that the contact radius at the zero load is:

$$a_{0(DMT)} = (\frac{2\pi W_{132} R^2}{K})^{1/3} \quad [2.14.1.2]$$

K is the effective elastic constant of the system, given by:

$$K = \frac{4}{3}(\frac{1-\nu_1^2}{E_1} + \frac{1-\nu_2^2}{E_2})^{-1} \quad [2.14.1.3]$$

where ν is the Poisson ratio and E is the Young' modulus. R is the effective radius.
In addition, the contact radius at the zero load at the separation point is

$$a_{s(DMT)} = 0. \quad [2.14.1.4]$$

In Johnson-Kendall-Roberts (JKR) mode [119], the adhesion force is given by:

$$F_a = \frac{3}{2}\pi R W_{132}. \quad [2.14.1.5]$$

In addition, it predicts that the contact radius at the zero load is

$$a_{0(JKR)} = (\frac{6\pi W_{132} R^2}{K})^{1/3} \quad [2.14.1.6]$$

and at the separation point is

$$a_{s(JKR)} = \frac{a_{0(JKR)}}{4^{1/3}} \approx 0.63 a_{0(JKR)} \quad [2.14.1.7]$$

Apparently, the difference of two models is based on differing predictions of the separation contact area. To determine which model is suitable for specific calculation, the Tabor elasticity parameter [120] can be utilized:

$$\mu = (\frac{16}{9}\frac{R W_{132}^{\ 2}}{K^2 z_0^3})^{1/3} \quad [2.14.1.8]$$

where z_0 is the equilibrium distance in the Lennard-Jones potential. The DMT model is suitable for $\mu < 0.1$ and the JKR model is more appropriate for $\mu > 5$.

When a bond can be formed between the tip and sample, observation of equilibrium unbinding is difficult. Usually, the tip needs to be driven slowly by a stiff cantilever. In addition,

the equilibrium is independent of the loading rate. For the non-equilibrium (dynamic) system, the unbinding process happens at a narrow range of the applied force which increases linearly with time and the unbinding force exponentially increases with the increase of loading rate [121]. Evan and Williams[122] studied the *N* number of parallel bonds and gave the equation of the unbinding force as:

$$f_{pull-off} = \frac{k_B T}{x_\beta} \ln\left(\frac{r_f}{r_0} N \exp\left(\frac{(N-1)E_0}{k_B T}\right)\right) \quad [2.14.1.9]$$

r_0 is expressed as: $r_0 = \frac{k_\beta T}{x_\beta} \cdot \frac{1}{\tau_D \exp\left(\frac{E_0}{k_B T}\right)}$ [2.14.1.10]

In above two equations, x_β is the distance to the transition state, E_0 is the depth of energy well, r_f is the constant loading rate of the tip, τ_D is the inverse of the diffusion-limited attempt frequency.

2.14.2 Hydrogen bonds and ionic hydrogen bonds

In this research, the interaction force between the AFM tip and substrate is often dominated by hydrogen bonding and ionic hydrogen bonding.

Chemical bond strengths are in the range from several nN to several pN, which corresponds to a strong covalent bond and a weak van der Waals “bond”. The strength of a hydrogen bond is in the range of 10 ~ 40 kJ mol^{-1}, which is much weaker than covalent bonds (~500 kJ mol^{-1}). [107] Hydrogen bonds are important in many fields such as acid-base chemistry, ionic crystals, surfaces, protein folding, formation of membranes and proton transport, amongst others.

The ionic hydrogen bond is formed between ions and molecules with bond strengths of 21~146 kJ mol^{-1}, which is much stronger than the normal hydrogen bond. [123]

If the total adhesion force is raised from N bonds including both hydrogen bonds and ionic hydrogen bonds, the total adhesion force (F_a) could be expressed as

$$F_a = Nf_{hb}[2(1-\beta)\beta m + (1-\beta)^2 m] \qquad [2.14.1.11]$$

where β is a fraction of dissociated groups, m is a weighting factor and f_{hb} is the single hydrogen bond strength. [124, 125]

The ionic hydrogen bond reaction can occur between a protonated base and the hydrogen receptor (reaction 1) or between a deprotonated Bronsted acid and a hydrogen donor (reaction 2).

$BH^+ + B' \rightarrow BH^+ \cdot B'$

$A^- + A'H \rightarrow A^- \cdot HA'$

The strengths of ionic hydrogen bond $BH^+ \cdot B'$ or $A^- \cdot HA'$ formed between the hydrogen donor and acceptor correlate with the efficiency of proton transfer. After bonding, the atomic charge , bond length and angle change are redistributed. For the homodimer, the strength of a ionic hydrogen bond is almost unaffected by the absolute proton affinities of the monomer. For the heterodimer, the strength of ionic hydrogen bond decreases when the difference of absolute proton affinities of the monomer is higher. In addition, the monomer can add stepwise to form a cluster $BH^+ \cdot nL$.

In my research work, the ionic hydrogen bonds are $OH_2^+ \cdot O$ and $O^- \cdot HO$, which have similar bond energies of 30 kcal/mol. [19, 20]

Chapter 3
Experimental Instruments

The surface properties of colloidal particles and modified PDMS have been characterized by several surface techniques in this thesis. To probe surface topography, atomic force microscopy (AFM) imaging is used, which is of resolution up to the nanometer scale. AFM also has the ability of sensing forces between AFM tip and sample on the order from nN to pN, which was used to study the interaction between phenol functionalized tip and sample. X-ray photoelectron spectroscopy (XPS) was used to determine chemical composition of surfaces. In addition, Auger electron spectroscopy (AES) provided extra information of the surface elemental composition as a complement to XPS data in this work. Attenuated total reflection- Fourier transform infrared spectroscopy (ATR-FTIRS) was used to explore the surface chemical composition and the orientation of self-assembled monolayer on gold surface. The surface zeta potentials of colloidal particles and PDMS were respectively measured by microelectrophoresis and electro-osmotic methods. Surface plasmon resonance was used to test protein adsorption on the modified surfaces.

3.1 Atomic Force Microscopy

Atomic force microscopy (AFM) is a derivative of scanning tunneling microscopy (STM), which was invented by Bining and Rohrer for atomic scale surface analysis.[126] Unlike STM, which can only image conducting or semiconducting materials, AFM can image almost every kind of solid surfaces at a nano-level resolution (topography measurements) and measure the interactive forces between a nanometer sized AFM tip and sample substrate (force spectrometric measurements). Other techniques use a scanning probe close to the surface (the same method as AFM) but measure different parameters such as magnetic force microscopy (MFM), lateral force

microscopy (LFM), scanning nearfield optical microscopy (SNOM), etc. Collectively, these techniques, including AFM are referred to as scanning probe microscopy (SPM).

Topography measurements

A standard AFM machine is composed of several principal components as shown in Figure 3.1. The main components include a very small radius (<100nm) tip on a Si cantilever, a laser reflection part to measure cantilever deflections produced by interactive forces between the tip and the sample surface, a set of piezoscanners that allows the tip to move across the surface in three dimensions, an electronic feedback system to control the Z height of the tip while obtaining topographic or other type of information, and software to collect and interpret data. The set point is one very important parameter set up by AFM users. Basically it is a measure of the force applied to the sample by the tip. In contact mode, it is a certain deflection of the cantilever, which keeps the constant force between the tip and sample. In tapping mode, it is certain amplitude of oscillation of the cantilever, which controls the force as the tip taps on the sample.

Changes in tip deflection are measured by laser reflection off the back of the cantilever into a four–quadrant photodetector. The difference voltage between sectors (1+2) and (3+4) (Figure 3.1) is a signal proportional to the vertical motion of the cantilever, and the difference voltage between sectors (1+3) and (2+4) is a signal proportional to the torsion of the cantilever. The latter is used in frictional force measurements and was not implemented in the work described in this thesis.

Usually a feedback loop is used to regulate the tip–sample distance in most AFM machines. As shown in Figure 3.1, the difference signtal, which is produced by comparison of the signal arising from the signal processing circuit to the error signal arising from the set point, corresponds to the cantilever deflection in contact mode or the amplitude of the cantilever oscillation in tapping mode. Thus, it is used to control the tip–sample separation through a high-

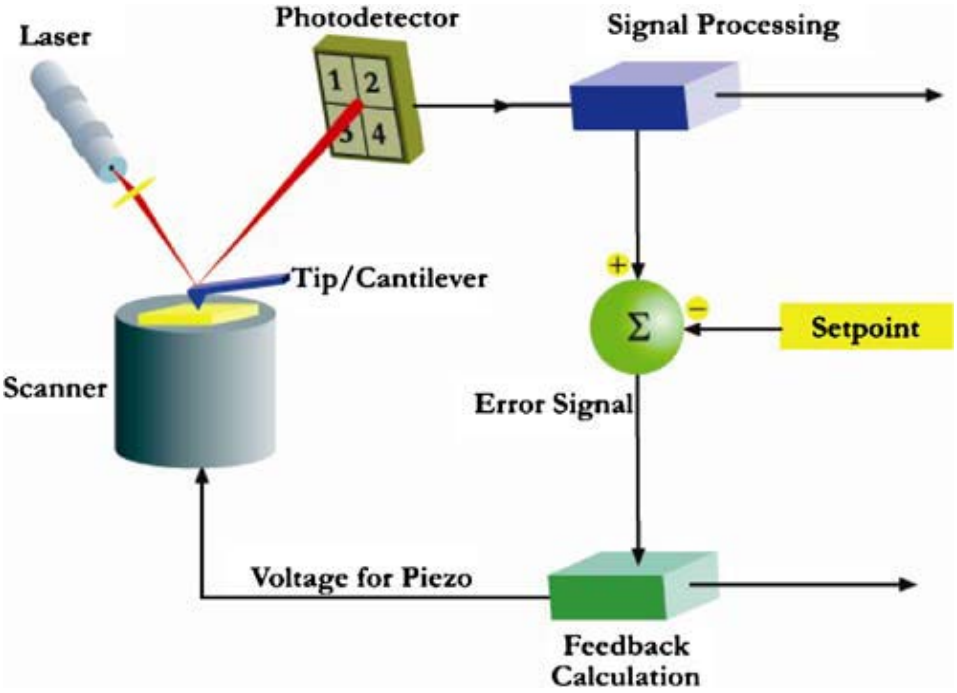

Figure 3.1 Schematic illustration of a typical AFM setup. [127]

voltage amplifier and fed to a piezoscanner that changes the tip–sample separation. The function of the feedback calculation is to keep the error signal equal to zero. Finally, the output of the feedback calculation is a representation of the sample topography or height. Usually, the best images are obtained with the minimised deflection or amplitude signals because the deflection or amplitude images are the error signals in AFM.

Three common operation modes of AFM are contact mode AFM (C-AFM), intermittent-contact mode (also known as tapping mode AFM) (IC-AFM), and noncontact mode AFM (NC-AFM). To obtain topographic images the tip is rastered in the x and y dimension across the surface by the piezoscanner.

In contact mode, scanning is usually performed by maintaining a constant deflection of the cantilever by the feedback loop. However, the contact mode should be in a very small scan area

or on a compliant surface, otherwise the tip or sample will be damaged with large changes in height of the sample surface.

In tapping mode, the interaction between the tip and surface is in the contact and non-contact region intermittently, so it is also called intermittent contact mode. Compared to contact mode, the tip and sample are not easily damaged in tapping mode. The tip is oscillated at its resonant frequency using an external driver. The tip displacement (d) can be described as a function of time, t, as $d = A_o \cdot \sin(\omega t)$, in which ω is its resonant frequency and A_o is the amplitude of the oscillation of the tip when it is far from the surface. When the tip approaches the surface, the amplitude of tip oscillations changes and a phase shift occurs due to the interaction between the tip and surface. The feedback loop is used to maintain a constant ratio (r_{sp}) between the free amplitude and the set point amplitude, which can be expressed as $r_{sp} = A / A_o$. Because the phase difference between the driving oscillation and the detected cantilever can be measured, a phase difference image can also be obtained. In addition to topographic images, heterogeneous surfaces (relative softness / hardness or chemical composition) easily give a contrast in phase images.

In the non-contact mode, the cantilever stays close to the sample with much smaller oscillation amplitude compared to tapping mode so that non-contact mode is more sensitive and can obtain images with atomic resolution.

Chemical force spectrometry

While AFM is routinely used to image materials, the work described in this thesis is mainly focused on non-topographic methods. The nanometer size of the AFM tip has the ability to measure adhesion forces in the range of 50pN to 100nN, which are mediated by specific forces and non-specific forces. Chemical force spectrometry (CFS) is the force measurement after the AFM tip is modified with self-assembled monolayers (SAMs) terminated with specific organic

functional groups. It is a tool to investigate specific chemical interactions between the tip and sample.

Reproducible chemical force measurements require homogeneous, well-defined monolayers on the tip surface to ensure fixed contact points between multiple functional groups on tip and sample.[127] In this work, the covalent modification with alkanethiol self-assembled monolayers on gold-coated AFM tips was used to create stable, robust, crystalline monolayers on the AFM tip.[127, 128] This method also allows various controlled functionalization of the AFM tip by change of the specific alkanethiol head group. Attachment of silica or polystyrene beads to AFM tips has also been performed for chemical force measurements and allows for tip modification with peptides, proteins, and other biomolecules.

Due to adsorption of condensed water molecules between tip and sample, force measurement in atmospheric environments results in capillary forces that can be ten times greater than the tip-sample force of adhesion.[129] Thus, all useful measurement must take place in a liquid environment or vacuum. In aqueous solvents, force measurements are dominated by van der Waals hydrogen bonding, hydrophobic and electrostatic forces. The adhesive force of solvated functional groups is dependent on the solution pH, ionic strength, and composition of the surface.

In AFM, the deflection of the cantilever is proportional to the interactive force F, between the tip and sample substrate. If the force is measured as a function of the distance between the tip and surface, it is called a force spectrometry. A schematic illustration of a force–distance curve of the interactive force between the AFM tip and sample surface is shown in Figure 3.2.

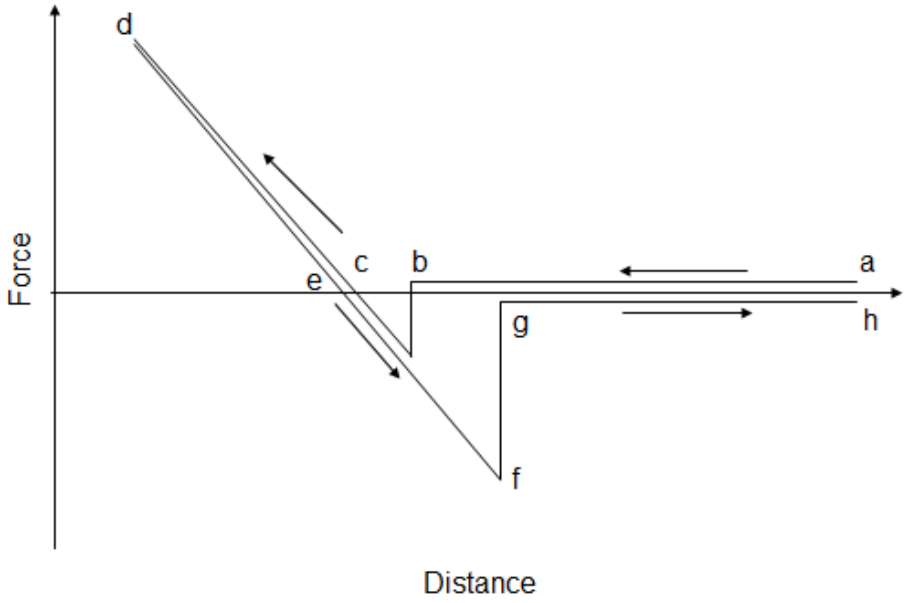

Figure 3.2 Schematic illustration of force–distance curves of the interactive force between the AFM tip and sample surface. a→b→c→d approach curve; d→e→f→g →h retract curve [130]

As shown in Figure 3.2, during the approach curve, from a to b, the cantilever is not deflected since the attractive force is quite small; from b to c, the tip on the cantilever suddenly jumps to the surface since the total force gradient on the cantilever is greater than the spring constant of the cantilever. This phenomenon is called the snap-to-contact; from c to d, the force between the tip and sample surface is repulsive as the tip is driven deeper into the sample. Due to the snap-to-contact effect, the shape of the approach curve does not directly follow that of an idealized Van der Waals potential well and information about the approach cycle well depth is lost. The line d→e→f→g is the retract curve. At point d, the tip and sample begin to separate. If the slope of c to d and d to e are different, then some degree of deformation occurred; from e to f, the deflection of the tip is proportional to the attractive forces including capillarity forces or other adhesion forces; from f to g, the total force gradient is greater than the spring constant as the tip is released from the surface; from g to h, the cantilever is not deflected. The adhesive force is thus a

function of the well depth of retract curve and the force constant of the cantilever (k_f), which can be determined using Hooke's law:

$$F_x = k_{f,} \Delta x \qquad [3.1.1]$$

where Δx is the displacement of the cantilever and k_f is the spring constant of the cantilever.

The real distance (D) between the tip and substrate is given by:

$$D = z - \Delta z \qquad [3.1.2]$$

Where z is the distance between the substrate and the rest position of the cantilever, Δz is the sum of the displacement of the cantilever (Δx) and the deformation of the sample (Δy) at the direction of tip approach. [131]

Usually, hundreds or thousands of individual pull-off measurements are measured for one statistical determination of interaction force. Furthermore, the width of the distribution of pull-off measurements is significantly impacted by the width of local curvature distribution.

Even though the force constants are provided by manufacturers when the AFM tips are purchased, the force constant may deviate from this value. To measure the actual value of the force constant of the cantilever used in individual experiment, some researchers developed experimental and mathematical methods. Cleveland *et al.* reported a method that was used to calculate the force constant of the cantilever, in which the resonant frequency of cantilever was measured before and after adding a small amount of mass (ng) on the tip. [132] Sader *et al.* reported a nondestructive method for evaluation of the spring constant based on the determination of the unloaded resonant frequency of the cantilever: knowledge of the density or mass and dimension of cantilever. [133] Hutter and Bechhoefer introduced a method to calculate the spring constant of cantilever based on the thermal fluctuation of the oscillation cantilever when it is not

in contact with a sample surface. [134] The resulting power spectral density of fluctuations is used to calculate the force constant by the method

$$k_f = k_B T / P \qquad [3.1.3]$$

where T is a given temperature, k_B is Boltzmann constant and P is the area of the peak in the power spectrum measuring thermal fluctuations.

Chemical force titration

When the chemical force measurements are performed in-situ over a range of pH they are termed chemical force titrations (CFT). The measurements of tip-sample adhesive forces using certain ionic strength solutions of varying pH results in one titration curve providing information on surface ionizable groups. These are important in studies of acid/base chemistry, biomolecules adsorption, colloids, micelles, and other reactions in aqueous media.[135]

At low ionic strength (IS) $<10^{-4}$ M conditions, the CFT shows the high adhesion between neutral groups and low adhesion between charged groups due to the double-layer repulsion. Compared to the hydrogen bonding, the relatively strong ionic hydrogen bonding can be observed between neutral and charged groups. The ionic hydrogen bonding usually is stronger than neutral hydrogen bonding. [125]

At the fraction of dissociated groups β = ½, the F_a is the maximum as the maximum number of strong ionic hydrogen bonds are formed. Thus, a chemical force titration curve can provide the dissociation constant ($pK_{1/2}$) of ionizable surface groups by a distinct change at pH = $pK_{1/2}$ in adhesion force, at which half the functional groups are ionized. This parameter ($pK_{1/2}$) may be slightly shifted for surface bound functional groups compared to the free functional groups in solution. [127] This is caused by decreased degrees of freedom of the bound groups to the surface, and is affected by the low dielectric permittivity of the neighboring hydrocarbon region in the monolayer, as well as affected by the excess electrostatic energy of the substrate and change in

solution dielectric constant near a charged surface.[127] It is quite important to note that the adhesion titration probes the interactions between the AFM modified tips and substrates as a function of the pH of the bulk solution rather than the pH at the surface of the molecular monolayer. The pH at the surface (pH_{surf}) is related to the pH of the bulk solution (pH_{∞}) by the following equation:[136]

$$pH_{surf} = pH_{\infty} + \frac{\psi}{2.303RT/F} \qquad [3.1.4]$$

where ψ is the surface potential, R is the ideal gas constant, T is the absolute temperature and F is the Faraday constant. The pK_a of the surface groups (pK_{asurf}) is related to the fraction of surface sites which are ionized (β)

$$\log\frac{\beta}{1-\beta} = pH_{surf} - pK_{asurf} \qquad [3.1.5]$$

Therefore, pK_{asurf} is related to the bulk pH, $pH_{\infty,}$ by the following equation

$$\log\frac{\beta}{1-\beta} = pH_{\infty} + \frac{\psi}{2.303RT/F} - pK_{asurf} \qquad [3.1.6]$$

In practice, it is hard to measure ψ and hence pH_{surf}. The ψ correction term is also usually small (usually < 1 pH unit). Therefore, we usually quote values of $pK_{1/2,}$ defined as the bulk pH at which half the surface sites are ionized.

In this work, the focus is on the chemical force titrations analysis of 4-(12-mercaptododecyl) phenol SAM modified both Au (111) surfaces and AFM tips (Figure 3.3). The ionizable surfaces have increased interaction with the modified tip due to neutral and ionic hydrogen bonding as well as repulsive electrostatic forces at varying pH. The $pK_{1/2}$ is determined from the point of maximum tip-sample adhesive force, which arises from ionic hydrogen bonding. Chemical force titrations are also used to study the interactions between 4-(12-mercaptododecyl)

phenol SAM modified AFM gold-coated tip and the surface of various unmodified or modified aluminum hydroxide and various unmodified or modified iron hydroxide.

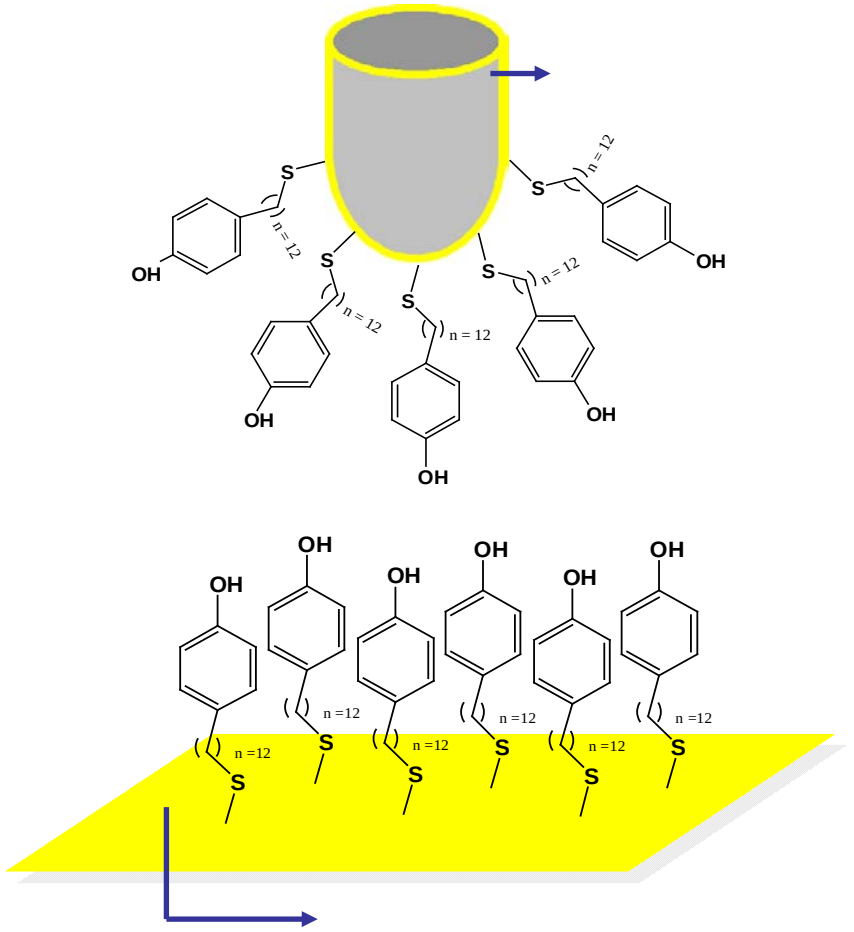

Figure 3.3 Schematic illustration of the self-assembled monolayer of 4-(12-mercaptododecyl) phenol modified AFM gold coated tip and gold coated mica substrate during chemical force titration to measure the dissociation constant ($pK_{1/2}$) of the head phenol group.

3.2 X-ray photoelectron spectroscopy (XPS)

X-ray photoelectron spectroscopy (XPS), also known as electron spectroscopy for chemical analysis (ESCA) is a widely used powerful surface analysis technique since it can determine the composition and the chemical states of surface constituents. This method was developed by Kai

Siegbahn in the mid 1960's. XPS spectra are obtained by irradiating a material with a beam of X-rays, simultaneously measuring the kinetic energy of the ejected electrons and plotting a spectrum of intensity of emitted electrons (counts) as a function of their kinetic or binding energy. In this section, I will discuss the basic physical principles, instrument setup, and data processing of XPS.

3.2.1 Physical principles of XPS

The incoming X-ray with an energy hν may provoke the emission of a photoelectron. The most prominent features in XPS spectra are the peaks arising from direct excitation of core-level electrons. Due to conservation of energy, the kinetic energy (E_k) of the outgoing electron is directly related to the binding energy (E_B) of the electrons in the solid, the energy of the X-ray photon (hν), and a term known as the work function (ϕ), which is the energy required for an electron at the Fermi energy to escape to the vacuum, usually on the order of 1 – 4 eV (Eq. 3.2.1.).

$$E_k = E_B - h\nu - \phi \qquad [3.2.1.1]$$

In one XPS spectrum, the area of the peak is proportional to three factors: the density of states, the transition probability, and the electron mean free path (escape depth) of the electrons in the solid. Thus, the electron mean free path (λ) is an important parameter, which is the depth at which *1/e* of the electrons make it to the surface. As electrons move through the solid, they collide with other electrons or the ion cores, are scattered, and hence lose energy. Thus, only electrons that can reach the surface without interacting will be detected. The intensity of signal from the XPS line of a particular element is given by

$$I = I_o e^{-d/\lambda} \qquad [3.2.1.2]$$

where I_o is the original signal that is acquired from the surface layer, d is the depth in the solid at which the photoelectron is being ejected, and λ is the electron mean free path, as shown in Figure 3.4. The low kinetic energy of the photoelectrons emitted, typically in the range of 20 – 2000 eV

gives XPS and XAES an extreme surface sensitivity, since the corresponding electronic inelastic mean free path in solids is on the order of several atomic distances.[137]

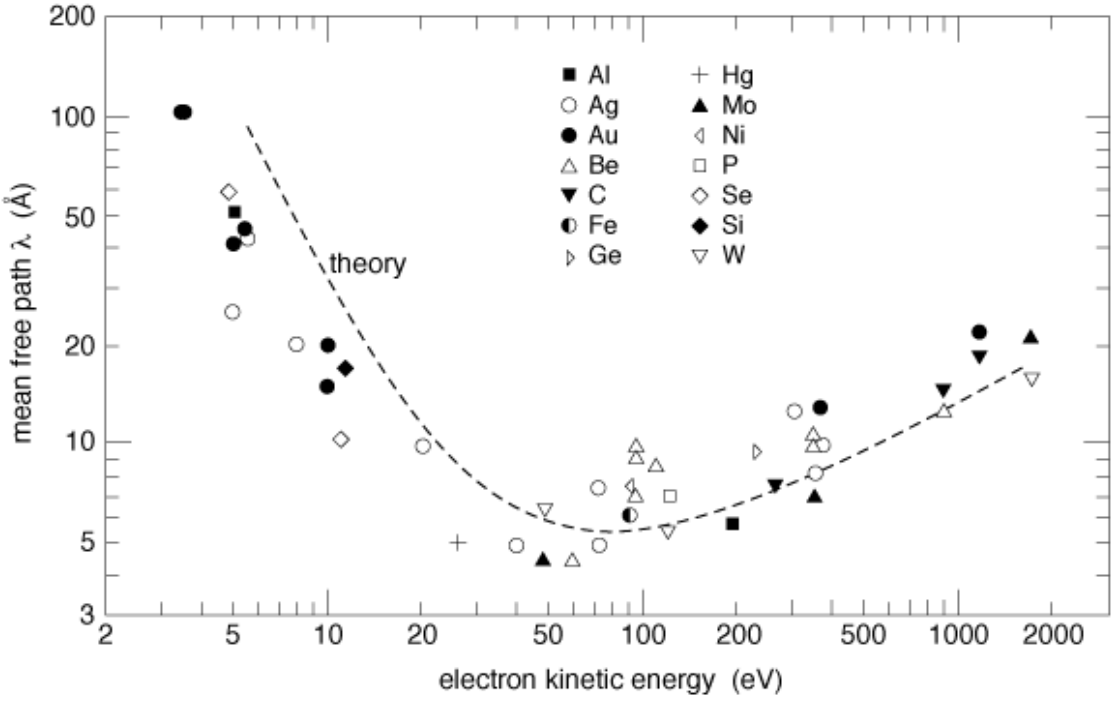

Figure 3.4 The mean free path vs. electron kinetic energy for various materials. The dots are measurements, the dashed curve is a calculation.[138]

The kinetic energy of the electrons depends on the binding energy of the electrons in the participating core shells of the excited atom and hence carries chemical information. In many cases the information about the oxidation state and chemical state of the elements are also available since the chemical environment does perturb the energy of a core electron. By comparing experimental and theoretical line shapes and positions, electronic structure and bonding information can be obtained.

The binding energy of one core level electron of an atom is attributable to three factors: the binding energy in the standard state of the element (E_o), the difference in energy required to remove an electron from an ionized centre versus the standard state (ΔE^+), and the extra-atomic

relaxation term (R_{EA}).[139] The sign and magnitude of ΔE^+ generally depends on the oxidation state of the relative element. For instance, positive oxidation numbers usually lead to an increase in ΔE^+, and then the increased binding energy makes the electron more difficult to remove from a positively charged species. The extra-atomic relaxation term (R_{EA}) arises due to electron density donation from neighbouring atoms to the ionized atom. Generally the value of R_{EA} is negative, and is roughly tied to how polarizable the surrounding atoms are in the solid (eq. 3.2.3).

$$E_B = E_o + \Delta E^+ - R_{EA} \qquad [3.2.1.3]$$

The binding energy shift (also called chemical shift, ΔE_B) observed for the core level of an atom arises because of the chemical environment around the atom from which an electron has been ejected. It can be described as follows:

$$\Delta E_B = \Delta E^+ - R_{EA} \qquad [3.2.1.4]$$

Wagner[140] defined the Auger Parameter (α) as follows:

$$\alpha = E_{k(Auger)} - E_{k(XPS)} + h\nu \qquad [3.2.1.5]$$

where $E_{k(Auger)}$ is the kinetic energy of the Auger peak, and $E_{k(XPS)}$ is the kinetic energy of the XPS peak.

The Auger Parameter (α) is very useful since it is independent of any surface charging and work function of analyzer and it is more sensitive to precise chemical state of an element than the energies of either photoelectron or Auger peaks. Thus, the Auger parameter is a means to compare data from different labs under difficult calibration conditions.

After a series of calculations and assumptions[139, 141], an Auger parameter shift for an element in two different environments can be deduced to be

$$\Delta\alpha = 2R_{EA} \qquad [3.2.1.6]$$

This above equation [3.2.1.6] is true only if the Auger transition does not involve any valence levels. In addition, the equation [3.2.1.4] can be expressed as followed equation [3.2.1.7] based on equation [3.2.1.6].

$$\Delta E^{+} = \Delta E_B + \Delta\alpha/2 \qquad [3.2.1.7]$$

As such, the Auger parameter can be used to determine the magnitude of the ΔE^{+} term. It is also a means of deconvoluting the polarization and charge contributions to the binding energy.

For quantification, the measured XPS intensity, I_A is relative to the atomic concentration c_A at depth z as the following equation: [142]

$$I_A = kI_S S_A \int_0^{\Lambda} c_A(z) \exp(-\frac{z}{\lambda \cos\theta}) dz \qquad [3.2.1.8]$$

in which k is an instrument variable, I_s is the primary electron beam current, S_A is the elemental sensitivity, θ is the take-off angle of the emitted electron, λ is the inelastic mean free path of the photoelectron trajectory multiplied by $cos\theta$, and Λ is the escape depth, $\Lambda = 3\lambda \cos\theta$.

3.2.2 Instrumentation of XPS

A schematic diagram of a typical configuration in one X-ray photoelectron spectrometer is shown in Figure 3.5. The general experimental setup for XPS consists of X-ray source, sample stage, a concentric hemispheric analyzer (CHA), and electron multiplier detector, and control and analysis system. X-rays bombard the sample surface to eject photoelectrons, Auger electrons and secondary electrons from a sample, all of which have specific kinetic energy. The electrons with different kinetic energy separated by analyzer, then intensity signal are detected by a detector. Finally the computer analysis system will give the spectrum with the intensity signal (counts/second) as a function of binding or kinetic energy (eV). The bombardment, analysis, and detection process all take place in an ultra-high vacuum (UHV) chamber with an ultimate vacuum

in the 10^{-10} torr range. The UHV prevents surface contamination of samples from adsorbed gas molecules in the atmosphere.

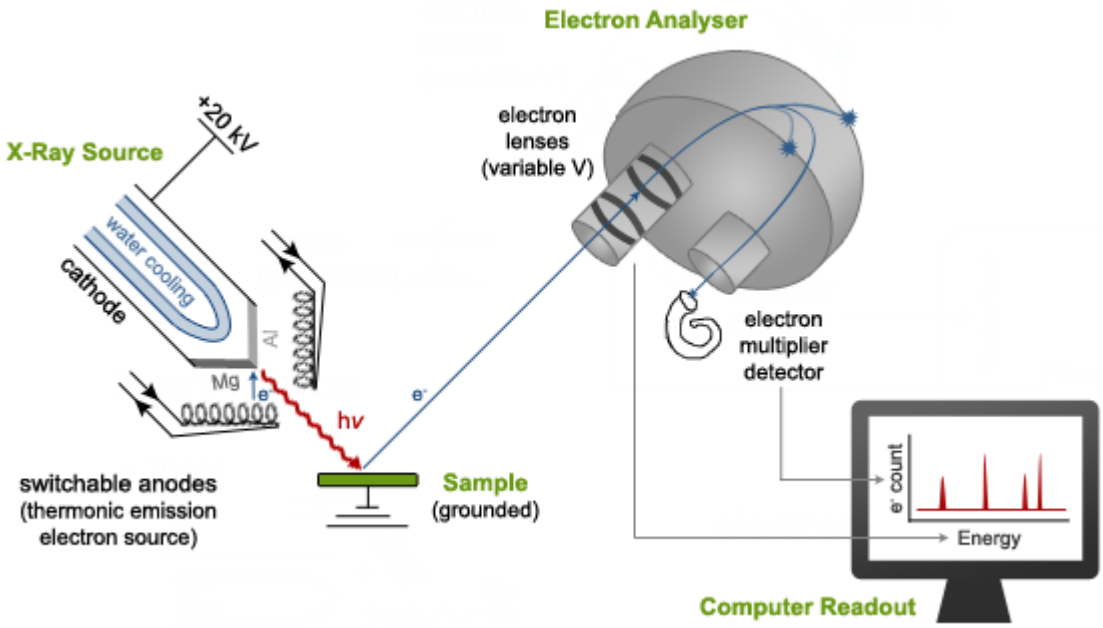

Figure 3.5 A schematic graph of an X-ray photoelectron spectrometer. (Courtesy of Dr. J.H. Horton, Queen's University, Department of Chemistry)

X-ray source

In XPS, X-ray emissions from either Mg Kα or Al Kα are generally used due to their ease of fabrication, high thermal conductivity, and narrow X-ray line width. The X-ray source is usually of a switchable type, the two cathodes being made of different materials that generate X-rays via X-ray fluorescent mechanism when bombarded by electrons. An advantage of using dual anode sources is its ability to recognize XPS and XAES peaks in a spectrum. It does this by switching between the two sources since the peak of XAES is independent of energy of the X-ray source.

However, even though Mg (Kα line at 1253.6 eV)and Al (Kα line at 1486.6 eV) X-rays have some of the narrowest Kα X-ray lines (0.7 eV for Mg and 0.85 eV for Al), these sources can

also make contributions to photoelectron line widths which are comparable to or greater than the lifetime broadening of many core levels.[143]

Concentric hemispherical analyzer

The concentric hemispherical analyzer (CHA) is commonly used for X-ray photoelectron spectroscopy, ultra-violet photoelectron spectroscopy, and Auger electron spectroscopy. As shown in Figure 3.6, the irradiated photoelectrons with a take-off angle θ pass though the first group of lens (lens 1) which determines the accepted analysis area in conjunction with the diaphragm. Then the photoelectrons pass a series of retarding lenses (lens 2) to slow down (or accelerate) the kinetic energy of these photoelectrons from the pass energy (E_{pass}) of interest to the pass voltage (generally 20 to 100 eV). Ultimately, the photoelectrons will be filtered by the two concentric plates (radius r_2 and r_1) of the analyzer, which have fixed voltages (V_2 at the outer plate and V_1 at the inner plate) so that only electrons of the pass voltage will go through (all others hit the inside or outside wall of the hemisphere). The electrons of interest then pass through to the detector (typically some sort of electron multiplier).

The absolute resolution (ΔE) is defined as the full width at half-maximum (FWHM) of a chosen peak. The relative resolution ($R = \Delta E / E$) is defined as the ratio of the absolute resolution of a chosen peak and the kinetic energy of same chosen peak. If the electron with an energy $E = eV_0$ passes though the entrance slit along the equipotential surface and reaches the exit slit of CHA, the relationship between V_2 ,V_1 and V_0 will be

$$V_2 - V_1 = V_0(r_2 / r_1 - r_1 / r_2) \qquad [3.2.1.9]$$

If the electron passes though the CHA with an angular spread $\Delta\alpha$, the relative resolution is given by:

$$\Delta E / E = (w_{en} + w_{ex}) / 4r_0 + (\Delta\alpha)^2 \qquad [3.2.1.10]$$

where w_{en} and w_{ex} are respectively the widths of the entrance and exist slits.[144]

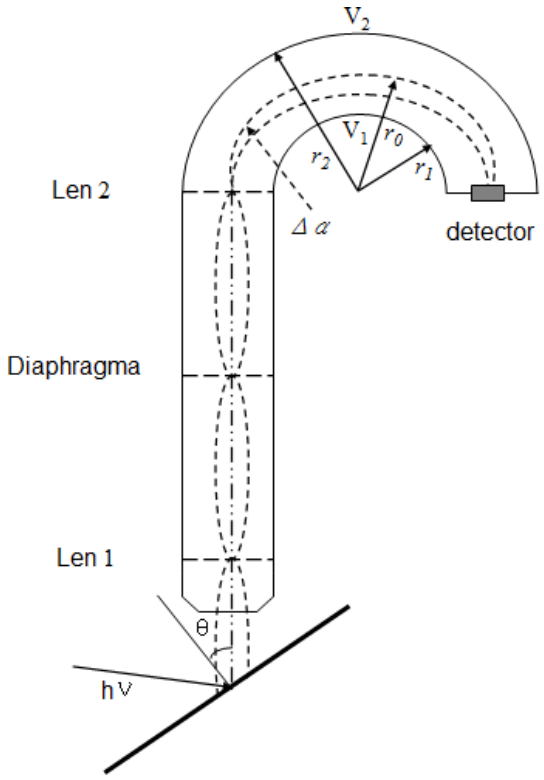

Figure 3.6 A schematic graph of concentric hemispherical analyzer. [144]

3.2.3 Data processing of XPS

The background correction and peak fitting are two important parts of data processing of XPS for high quality analysis. The main reason for background arising in the XPS spectrum is the presence of secondary electron. The peaking broadening is taken into consideration during the peak fitting method.

Background correction

The linear Shirley and Tougaard methods are three of the most common background subtraction methods. The Shirley and linear background correction algorithms are based on pure mathematic algorithms. The Tougaard method takes energy loss processes which are caused by

inelastic scattering of electrons into consideration. [145-147]

The linear background is determined by drawing a line based on the two points close to each side of the XPS peak base and subtracting the area below this line from the total peak area. This method effectively subtracts the background when the sample materials are not significantly affected by energy loss processes, such as in polymers. However, this method is not suitable for strongly sloping background from metal or heterogeneous samples. In addition, results are more dependent on the starting and ending points chosen by the user as compared to other methods.

The Shirley background correction is used when the sample materials are dramatically affected by energy loss processes, such as metallic samples or, in the case of non-metallic samples, around photoelectron peaks corresponding to metallic elements.[148] The Shirley background correction is based on the assumption that the background is caused by inelastically scattered electrons which are assumed to arise from the scattering electrons at higher kinetic energies. [149]

The Shirley background algorithm correction is an iterative method which was introduced by Proctor and Sherwood. [149] The Shirley background subtracting line B(x) (shown in Figure 3.7) is calculated by the following equation:

$$B(x) = \frac{(a-b)\cdot Q}{(P+Q)} + b \qquad [3.2.1.11]$$

where a is the average start point, b is the average end point, (P + Q) is the total peak after background subtraction, Q is the peak area from point x to point k after subtraction, and P is the peak area from point 1 to point x after subtraction. The peak areas (Q and P) are calculated by the trapezoidal rule as the following equation:

$$A = h[(\sum_{i=x}^{k} y_i) - 0.5(y_x + y_k)] \qquad [3.2.1.12]$$

where h is the separation distance between n equally spaced points from point x to point k. The initial calculation of peak area is performed by choosing a constant magnitude b as shown in Figure 3.7 (line B1). The calculation results of peak areas are substituted in the equation [3.2.1.11] to form curve B2. Then the results of line B2 are substituted in the same equation to acquire curve B3. This iteration calculation continues until the P+Q area remains essentially the same. To reduce the calculation time, the start point is usually chosen close to the bottom of peak.

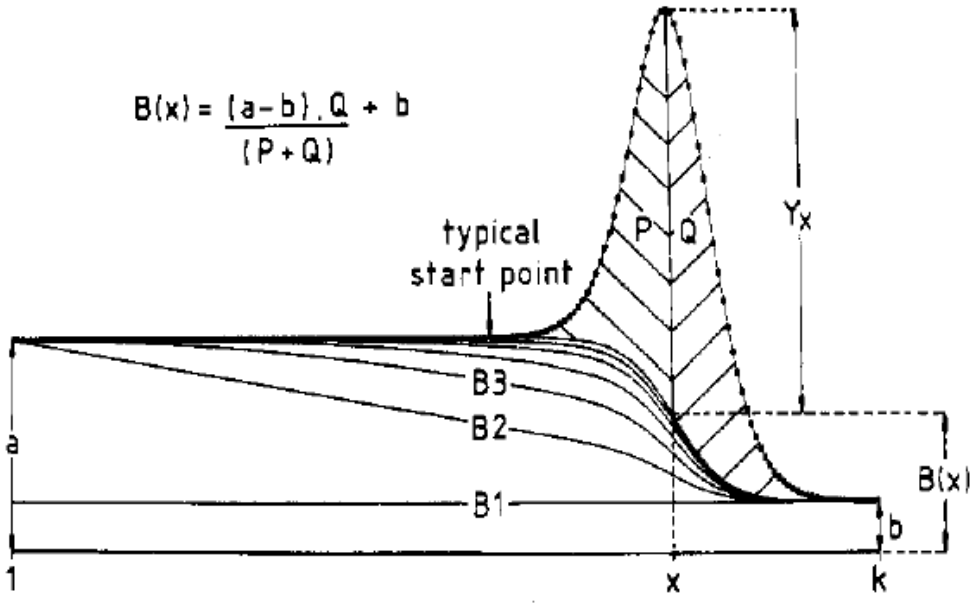

Figure 3.7 Shirley background subtraction. B(x) is the background at point x in the spectrum which contains k equally spaced points.[149]

The Shirley method is more accurate than the linear method. However, the Shirley method is relative to the one selected point at the low kinetic energy side of peak, so it accurately performs background subtraction when the peak region is narrow, on the order of 5 -10 eV.

The Tougaard method permits the user to choose parameters to estimate a universal cross-section, which is the general probability of losing energy during an inelastic collision involving an electron of certain kinetic energy as it moves through the solid sample.

However, the Tougaard method requires a peak width on the order of 30 -50 eV, which is not suitable for most of my XPS spectra. Thus, the Shirley background subtraction was chosen and performed in this work and the maximum number of iterations and the limit of convergence can be chosen.

3.3 Auger Electron Spectroscopy (AES)

Auger electron spectroscopy (AES) is a surface analytical tool related to XPS, which can provide the elemental composition and quantitative information about the elemental composition of the first layers of a solid.[141] This method is based on the Auger process as shown in Figure 3.8, which was discovered by Pierre Auger in 1925 while working with X-rays.

The inner hole can be created by various methods such as X-rays, plasma, ions and electrons, though most studies use electrons or photons. The emission of Auger electrons with low kinetic energy (some 10eV~ 3keV) can occur from atoms with a hole in their inner shell during the decay process. The low kinetic energy of such Auger electrons emitted gives AES an extreme sensitivity to the surface, since the corresponding electronic inelastic mean free path in solids is in the order of 1 nm. The kinetic energy of Auger electrons originating from a generic WXY transition can be estimated form the empirical relation:

$$E_{WXY} = E_W(Z) - E_X(Z) - E_Y(Z+\Delta) - \Phi_A \qquad [3.3.1]$$

The work function of the analyzer material is represented by Φ_A and the atomic number of the atom involved is represented by Z. The binding energy values are present as $E_{W,}$ $E_{X,}$ E_Y , all of which may be obtained from the X-ray emission energy tables.[137] The term Δ is introduced because the energy of the final doubly ionized state is somewhat larger than the sum of energies for individual ionization of the same levels. Experimental values for Δ lie between 0.25 and 0.75

eV. As this equation demonstrates, the Auger electron energies are characteristic of the target material and independent of the incident excitation energy.[150]

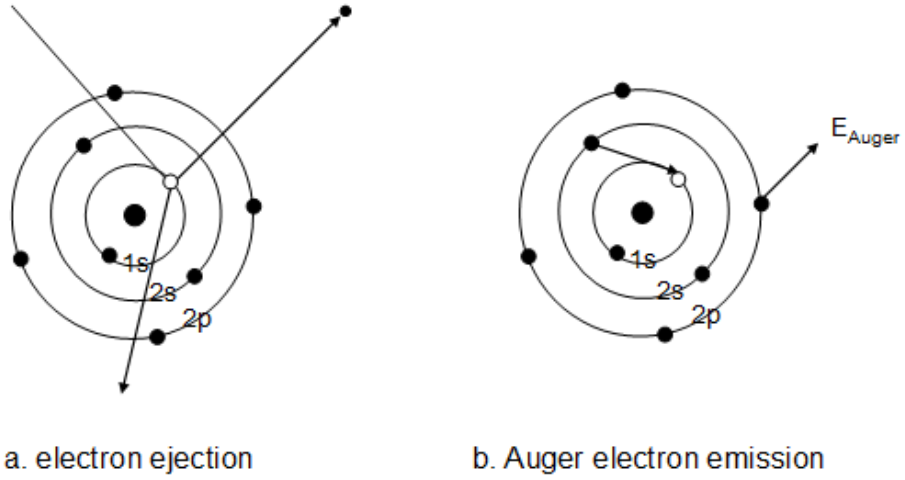

Figure 3.8 (a) An incident electron or photon creates a core hole in the 1s level. (b) Another 2s level electron fills in this hole and releases the transition energy. Simultaneously the transition energy is coupled to a 2p electron which is emitted as Auger electron.

From the intensity of the Auger electron signal, a quantification of the elemental concentrations in the surface layer is possible, but this quantification requires precise knowledge of the experimental parameters or comparison with reference samples.[141] It is obvious that at least two energy states and three electrons take part in an Auger process. Hence, H and He atoms cannot give rise to Auger electrons.

Since the Auger effect is not the only mechanism available for atomic relaxation, there is a competition between radioactive and non-radioactive decay processes as the primary de-excitation pathway. AES is sensitive to the lighter elements, for instance, for K-level based transitions, Auger effects are dominant for $Z<15$ while for L- and M-level transitions, AES data can be measured for $Z\leq50$. Conversely, for heavier elements, the X-ray yield becomes greater

than Auger yield, indicating an increased difficulty in measuring the Auger peaks for large Z-values. [151]

Scanning Auger microscopes (SAM) can produce high resolution, spatially resolved chemical images, which are obtained by stepping a focused electron beam across a sample surface and measuring the intensity of the Auger peak above the background of scattered electrons. The intensity maps are usually correlated to a gray scale on a monitor with white areas corresponding to higher element concentration. In addition, sputtering is sometimes used with Auger spectroscopy to perform depth profiling experiments. Sputtering removes thin outer layers of a surface so that AES can be used to determine the underlying composition. Depth profiles can be shown as either Auger peak height vs. sputter time or atomic concentration vs. depth.

3.4 Attenuated total reflection Fourier transform infrared spectroscopy

Infrared spectroscopy is a technique generally used for organic structure identification. It uses infrared radiation to stimulate vibrational, rotational, and bending modes in a molecule without exciting it from the electronic ground state. The attenuated total reflection (ATR) mode of infrared spectroscopy can perform specific surface analysis since it amplifies the intensity of the signal produced by the absorption of radiation by surface functional groups. Peaks in attenuated total reflection Fourier transform infrared (ATR-FTIR) spectroscopy are usually shifted to higher wave numbers due to the decreased degrees of freedom of the groups on the surface. In this work, ATR characterization was used to analyze self-assembled monolayers on Au-coated mica.

In the ATR mode of analysis, the sample (about 1–100 mg) is pressed into place in intimate physical contact with a special ATR crystal. Then, the sample and crystal are placed in the IR beam in such a position that the IR beam enters the crystal at an angle and is multiply reflected

along the length of the crystal. IR energy exiting at the opposite end of the crystal is measured vs. the respective wavelength. This technique is ideal for rapid quantitative and qualitative analysis. In particular, single and multiple internal reflection ATR accessories are well suited for highly infrared absorbent materials such as rubbers and polymers. In addition, ATR is suitable for providing information about the surface makeup or surface conditions of a material. Most importantly, it allows information about the orientation of various parts of the molecule under study to be evaluated in an oriented system.

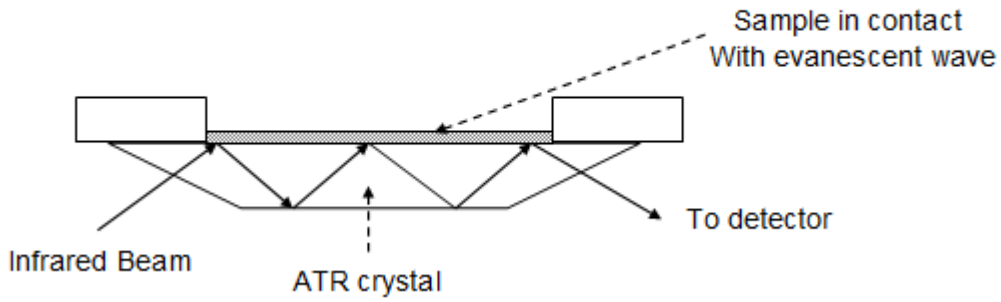

Figure 3.9 A schematic of multiple reflection ATR system. ATR spectroscopy functions to measure the changes that occur when a totally, internally reflected, infrared beam comes into contact with the sample.

3.5 Contact angle measurement

Surface tension $\gamma \equiv (\frac{\partial G}{\partial A})_{p,T}$ is defined as the Gibbs free energy per area for certain temperature and pressure. The contact angle θ_c is the angle at which a liquid/vapor interface meets a solid surface as shown in Figure 3.10.

The relationship between surface tension γ and contact angle θ_c is given by Young's equation,

$$\cos\theta = \frac{\gamma_{sg} - \gamma_{sl}}{\gamma_{\mathrm{lg}}} \qquad [3.5.1]$$

The limitation of Young's equation is that the solid surface need be smoothly flat, homogenous, inert, insoluble, and of non-deformable quality.

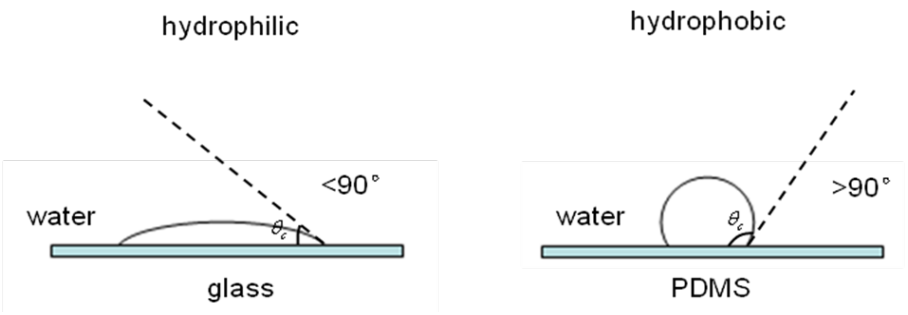

Figure 3.10 The water droplet on glass and PDMS. The contact angle $\theta_c > 90°$ θ_c (hydrophobic), $\theta_c < 90°$ (hydrophilic)

For a flat surface, the contact angle can be measured directly from the drop profile. The image of the resting drop at equilibrium is taken by computer and the contact angle is measured by software.

3.6 Zeta potential measurement

The zeta potential values of surfaces of colloidal particles and PDMS were respectively measured by microelectrophoresis and electroosmosis flow methods. In this section, these two methods will be discussed in detail.

3.6.1 The zeta potential of colloidal particles measured using microelectrophoresis method

The zeta potential values of colloidal particles are measured based on the determination of the rate and direction at which colloidal particles move in an applied electric field under observation with a microscope, which is referred to as microelectrophoresis phenomenon.

As shown in Figure 3.11, the particle with surface charge in electrolyte solution is surrounded by an electrical double layer. For a particle much larger than the Deby length, the speed of the particles motion can be given by:

$$u_{ep} = \frac{\varepsilon\zeta}{\eta} E \qquad [3.6.1.1]$$

Where ζ is the zeta potential of the charged particle, $\varepsilon = \varepsilon_r \varepsilon_0$ is the dielectric constant, η is the viscosity constant of the fluid.

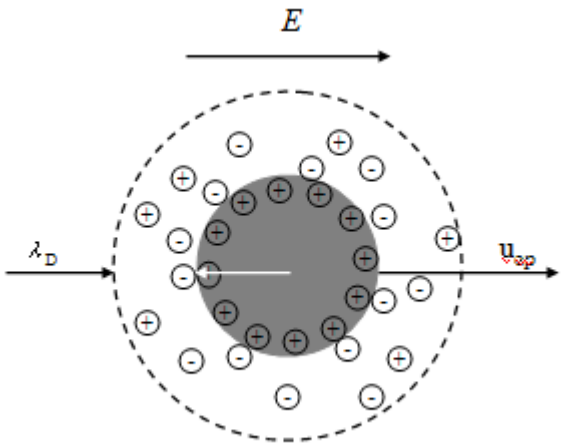

Figure 3.11 Motion of a charged particle in an applied electrical field (E). λ_D is the Deby length. u_{ep} is the electrophoretic velocity of the particle motion.

Thus, the magnitude and sign of the zeta potential of the colloid particles can be determined by observing the speed and direction of the particle movement under the applied field according to equation [3.6.1]. Due to the formation of the electroosmosis flow near the surface of two chamber walls and a return flow in the opposite direction in the center of the viewing chamber, the velocity of the particles must be measured at stationary layers of the chamber, otherwise, the measured velocity of the particles includes the movement of fluid. The position of the stationary

layer may be found before measurement based on the cell geometry calculation, in our case, by the equation: $X = 0.194 \times C \times M$ [3.6.1.2]

In above equation, X is the distance (mm) from the bottom inside of the chamber to the bottom stationary layer or from the top inside to the top stationary layer, C is the apparent depth (mm) of the cell and M is a dimensionless microscope constant. Both C and M are defined by the manufacturer.

As shown in Figure 3.12, after the microscope and laser are focused at the stationary layer, a zeta potential measurement can be performed by determining the magnitude and direction of the particle movement in the presence of the applied field. The relatively simple measurement is made by a prism located inside the microscope interposed between the objective lens and the eyepiece. The prism is mounted on a galvanometer which causes the prism to repeatedly rotate a few degrees and then flip back to start another cycle. The effect of this motion is to cause the image viewed through the microscope to repeatedly scan in one direction and then reset. A zeta potential measurement is made by adjusting the prism control until the motion of the colloidal particles appears stationary at a certain prism rotation rate because the electrophoretic velocity of the particles is equal to the translation of the view-screen image due to the prism rotation.

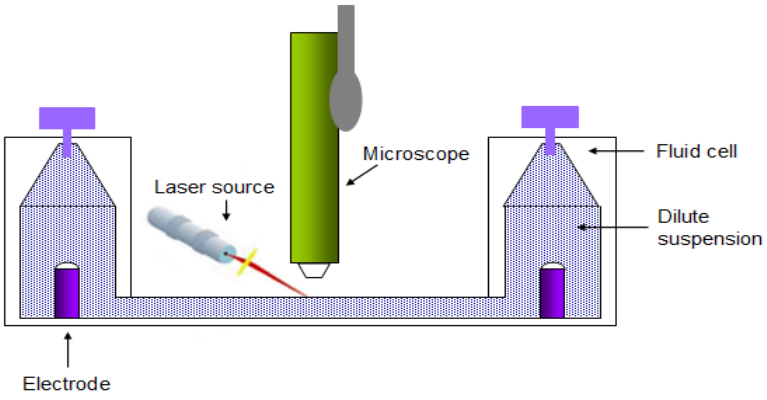

Figure 3.12 Diagram of light paths in the rotating prism method of micro-electrophoresis measurements.

3.6.2 The zeta potential measurement of PDMS surface by microfluidic kit

The measurement of the ζ-potential of the micro channels was performed using current-time monitoring with a microfluidic tool kit. The microchannel was first filled with a high-ionic-strength phosphate buffer solution. Then the inlet buffer in one reservoir was emptied and filled with a lower ionic-strength phosphate buffer solution. Platinum electrodes were immediately placed in the inlet and outlet buffer reservoirs. Finally an electric field was applied and current was monitored as a function of time.

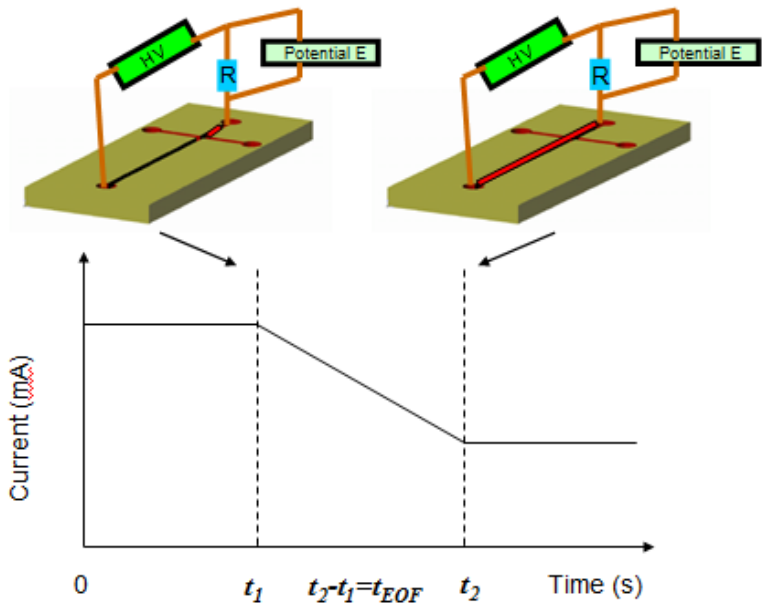

Figure 3.13 The time $t_{EOF} = t_1 - t_2$ of electroosmotic flow used to refill the microchannel

The electroosmotic flow velocity μ_{eo} could be measured based on equation [3.6.2.1], in which L is the length of microfluidic channel, t is the time needed for low concentration solution filling in whole channel

$$\mu_{eo} = \frac{L}{t} \qquad [3.6.2.1]$$

In addition, the Smoluchowski equation that the average electroosmotic flow velocity is given by

$$\mu_{eo} = \frac{\varepsilon_0 \varepsilon_\gamma \zeta}{\eta} E_Z \qquad [3.6.2.2]$$

where E_z is the applied electric field strength, ζ is the zeta potential at the interface, η is the solution viscosity, and $\varepsilon = \varepsilon_0 \varepsilon_r$, ε_0 is the dielectric constant of vacuum ($\varepsilon_0 = 8.854 \times 10^{-12}$ F/m), and ε_r is the relative permittivity. Hence, the ζ-potential at the interface could be calculated based on measured electro-osmotic flow velocity.

3.7 Surface plasmon resonance

As proteins may be separated and identified in PDMS microfluidic channel, understanding the adsorption characteristics of proteins on the PDMS surface becomes crucial. Our research group is pursuing two avenues to examine the adsorption of protein on surfaces. One method is to use MALDI – TOF mass spectrometry to measure the quantities of adsorbed proteins on chemically modified PDMS.[22, 152] The second that is used in my work is to explore the use of surface plasmon resonance (SPR) methods in measuring protein/peptide adsorption on the surface.

The spectroscopic shift of an Au surface plasmon resonance peak is highly sensitive to surface concentration of adsorbate, which has the ability to sense trace quantities (ng) of peptide adsorbed on the Au surface. The drawback is that the surface is Au, not our desired polymer. To overcome this problem, we simulated the functional group present on the polymer surface through adsorption of simple alkanethiol species directly to Au.

3.7.1 Physical principle of surface plasmon resonance

Excitation of surface plasmons

As one beam of light passes though material with a high refractive index (n_2) into material with a low refractive index (n_1) some light is reflected from the interface. As the angle of incidence (θ) is greater than the critical angle, the light becomes totally internally reflected (TIR). The critical angle is given by

$$\sin\theta_c = \frac{n_2}{n_1} \quad (n_1 > n_2). \qquad [3.7.1.1]$$

When TIR occurs, at the interface there is an evanescent wave. This is a harmonic wave which exponentially decays perpendicular to the interface as shown in Figure 3.14 (a). If the surface of the glass is coated with a thin film of metal (of thickness comparable to the wavelength of incident wave) the reflection is not total as a light wave propagating in the prism incident on the metal film will be reflected back into the prism. Part of this light wave propagates in the metal in the form of an inhomogeneous electromagnetic wave (Figure 3.14 b).

A second angle (surface plasmon resonance angle θ_{spr}) exists greater than the critical angle at which this loss is greatest and the intensity of reflected light reaches a minimum. This phenomenon occurs due to the oscillation of mobile electrons (plasma) at the interface of the metal thin film. These oscillating plasma waves are called surface plasmons. Only p-polarized (TM) incident light can induce the SPR as its electric field component perpendicular to the metal surface, which can generate a surface charge density at the interface that can be coupled to the photon field forming the SPR. When the amplitude of the wave vector in the plane of the metallic film matches the wavelength of the surface plasmons, the surface plasmon resonance phenomenon happens. If the metal film is thinner than 100 nm for light in visible and near infrared part of spectrum, the evanescent wave can penetrate through the metal film and couple with a surface plasmon at the outer boundary of the metal film (Figure 3.14 a)

As the propagation constant of a surface plasmon wave (SPW) is always higher than that of optical wave propagation in the dielectric, the SPW cannot be excited directly by an incident optical wave at a planar metal–dielectric interface. Therefore the momentum of the incident optical wave has to be enhanced to match that of the SPW. This can be achieved using attenuated total reflection (ATR) in prism couplers and optical waveguides, and diffraction at the surface of diffraction gratings. [153]

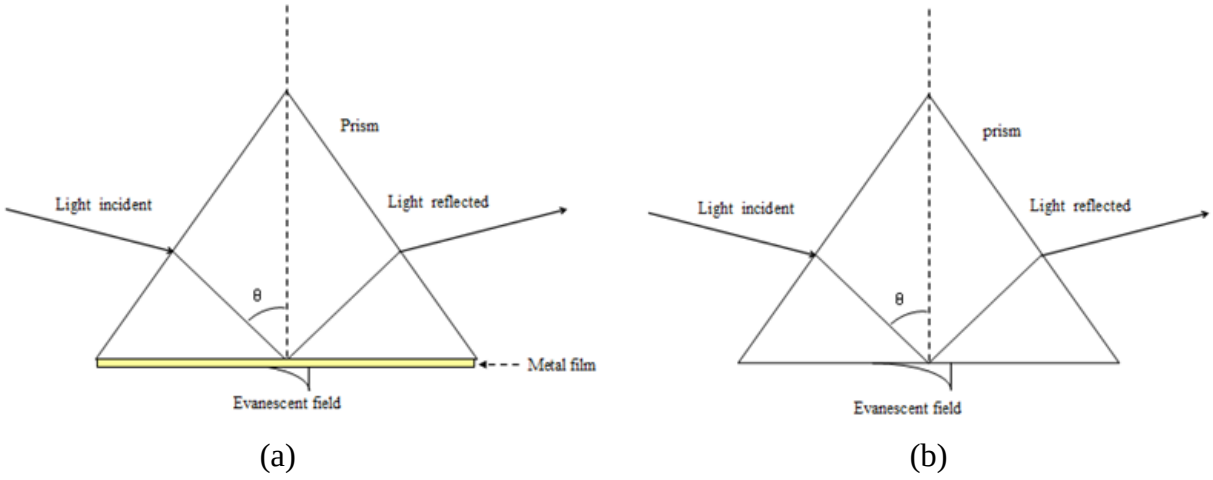

Figure 3.14 (a) Evanescent field occurs after a thin metal film coated between two media. (b) Evanescent field occurs at the total internal reflected interface. [153]

Properties of surface plasmon resonance wave:

This surface plasma resonance wave is a TM-polarized wave. The propagation constant of the surface plasma wave propagating at the interface between a semi-infinite dielectric and metal is given by the following expression:

$$\beta = k\sqrt{\frac{\varepsilon_m n_s^2}{\varepsilon_m + n_s^2}} \qquad [3.7.1.2]$$

where k denotes the free space wave number, ε_m is the dielectric constant of metal and n_s is the refractive index of the dielectric. In conclusion, surface plasma resonance wave may be supported by the structure providing that $\varepsilon_m < -n_s^2$. Au and Ag are the most commonly used to satisfy this condition. [153]

Due to high loss in the metal, the surface plasmon wave (SPW) propagates with high attenuation in the visible and near-infrared spectral regions. The electromagnetic field is distributed in an asymmetric fashion and the majority of it is concentrated in the dielectric medium. SPW, as one inhomogeneous wave, decays exponentially in the direction perpendicular to dielectric medium -metal interface and is therefore referred as to an evanescent wave. [153]

3.7.2 Instrumentation of surface plasmon resonance

The schematic drawing of the SPR affinity biosensor (shown in Figure 3.15) was used in my experimental configuration. The bare surface of the gold film was modified with a 1-octanethiol, 8-mercapto-1-octanol (MOT) or fluorinated octanethiol $CF_3(CF_2)_5(CH_2)_2SH$. Then, a phosphate buffer solution containing the globular protein passed through the flow cell interacts with the modified surface. As the protein binds to the surface, the refractive index shifts and the SPR-dip moves to larger angles. The movement of the SPR dip is monitored as a function of time. When a solution containing analyte molecules comes into contact with the SPR sensor, analyte molecules in solution bind to the molecular recognition elements, making an increase in the refractive index at the sensor surface.

The changes in the refractive index lead to a change in the propagation constant of the surface plasmon as described above, thus the coupling condition between an incident light wave and the surface plasmon is altered. Based on which characteristic of the output light wave is measured, SPR sensors can be classified as SPR sensors with angular, wavelength, intensity, phase, or polarization modulation.

In angular modulation, a monochromatic light wave is used to excite a surface plasmon at multiple angles. The incident angle of light wave with the strongest coupling with surface plasmon will change due to the change of the refractive index of surface of dielectric medium, thus it is used as another sensor output (Figure 3.16 a). In wavelength modulation, the incident angle of light wave is fixed and incident light comprises multiple wavelengths. The wavelength which has the strongest coupling with surface plasmon will change due to the change of the refractive index of the surface of the dielectric medium. Thus the wavelength with the strongest coupling is used as a sensor output (Figure 3.16 b).

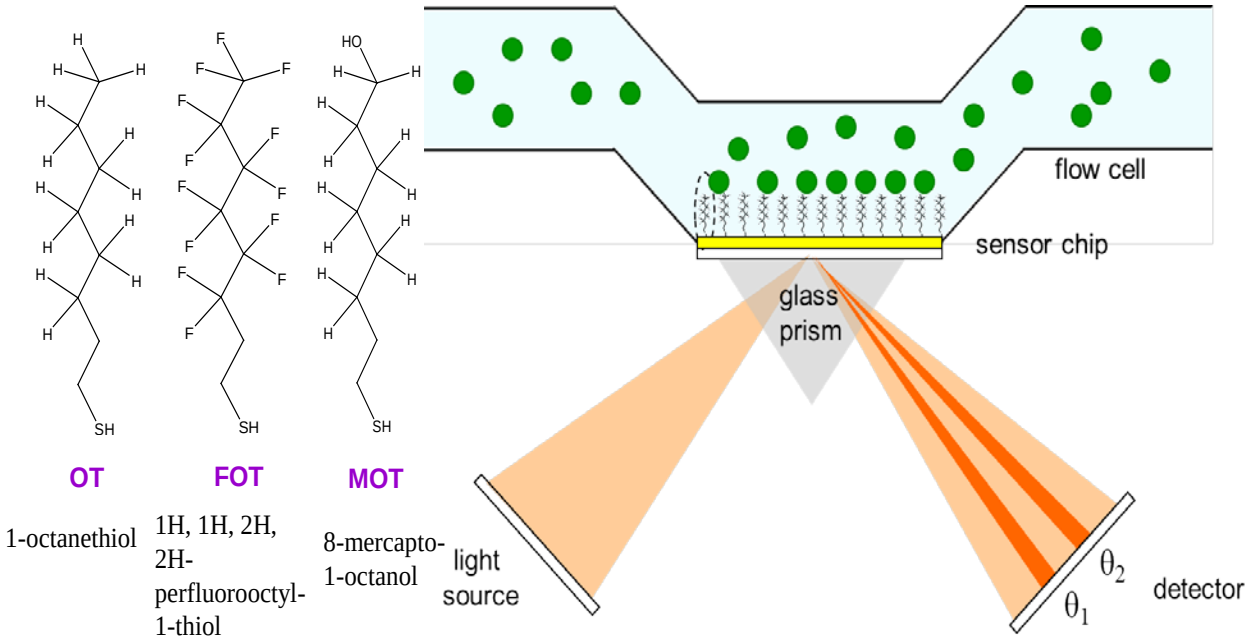

Figure 3.15 Schematic illustration of surface plasmon resonance affinity biosensor. The analyte passes through the flow cell and interacts with a 1-octanethiol (OT), modified 8-mercapto-1-octanol (MOT) modified or fluorinated 1-octanethiol (FOT) modified on Au surface. Due to the change of the thickness on the sensor, the resonance angle will respectively change from θ_1 to θ_2. (www.biacore.com)

The amount of the refractive index change Δn depends on the volume refractive index increment $(dn/dc)_{vol}$ and can be expressed as:

$$\Delta n = (\frac{dn}{dc})_{vol} \frac{\Delta \Gamma}{h} \qquad [3.7.2.1]$$

where $\Delta \Gamma$ is the change of surface concentration in mass/area, h is the thickness of a thin layer at the sensor surface.

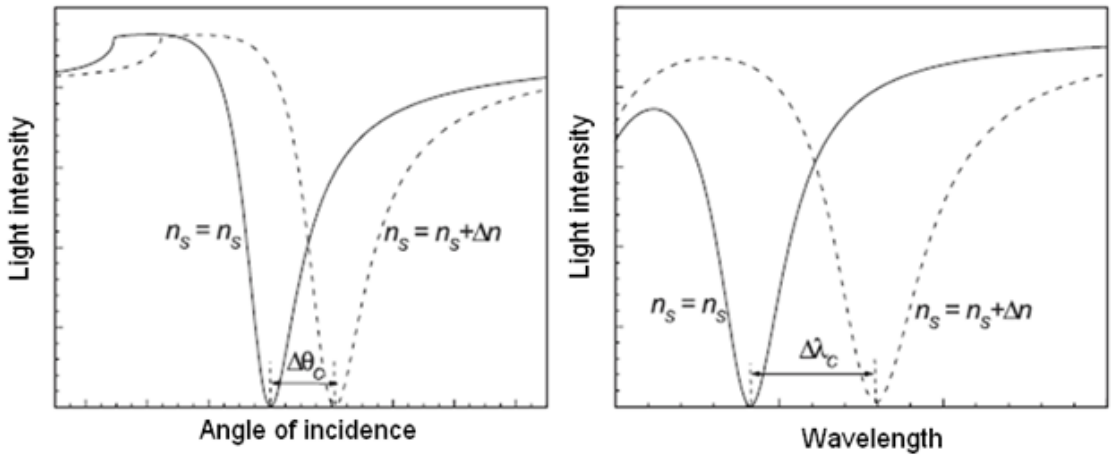

Figure 3.16 (a) The output signal of light intensity as a function of angle of incidence (b)The output signal of light intensity as a function of wavelength before and after the change (Δn)of refractive index (n_s) of surface of dielectric medium. [153], [154]

Biacore is a common commercial SPR system, which was used in my research. In the Biacore system, the metal side of a sensor chip makes contact with a microfluidics system. The running buffer goes through the microfluidics systems with certain running speed before and after sample injection. The computer system monitors the angular change of the reflected light as a function of time (called a sensorgram) shown in Figure 3.17, in which the unit of Y axis is the arbitrary resonance unit (RU) defined as 1/3000 of a degree in Biacore. [153]

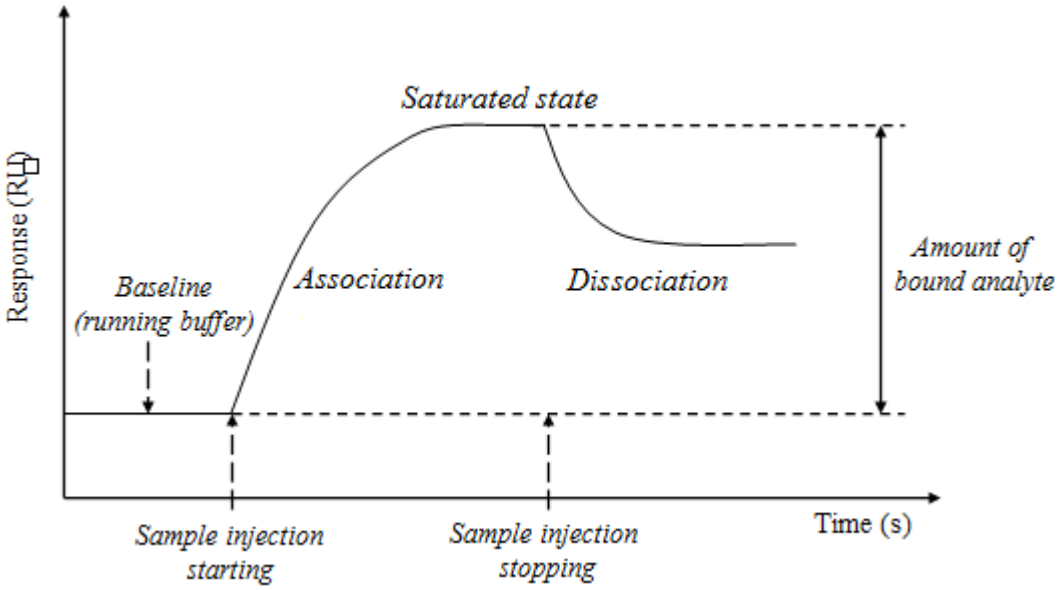

Figure 3.17 A typical Biacore sensorgram for one sample injection. (www.biacore.com)

The SPR sensorgram can also be used in kinetic and thermodynamic analysis. According to the sensorgram, the association rate (k_a), dissociation rate(k_d), and dissociation constant (K) can be calculated. Furthermore, if the association rate (k_a) and dissociation rate(k_d) are acquired at different temperature, the change in enthalpy, entropy, and free energy of the interaction can be determined by following equations. [153], [154]

$$k_a = A\exp(-\frac{E_a}{RT}) \qquad [3.7.2.2]$$

$$\Delta H^\circ = E_a(association) - E_a(dissociation) \qquad [3.7.2.3]$$

$$\Delta G^\circ = -RT\ln K_a = \Delta H^\circ - T\Delta S^\circ \qquad [3.7.2.4]$$

Chapter 4

Phenol Interactions with Hydrous Iron and Aluminum Oxide Colloids

Experimental Procedure

4.1 Synthesis of 4-(12-mercaptododecyl) phenol (3)

The lithiation of 4-bromoanisole followed by coupling with 1,12-dibromododecane to establish the $–CH_2-$ linkage in 1-(12-Bromododecyl)-4-methoxy-benzene [142] as shown in Figure 4.1. This is followed by removal of the methyl protection group to form the phenol [142] and finally substituting the mercapto group for the bromide group.[155, 156] 1H NMR spectra were recorded on a Bruker-400 spectrometer for the identification of the product after each synthetic step.

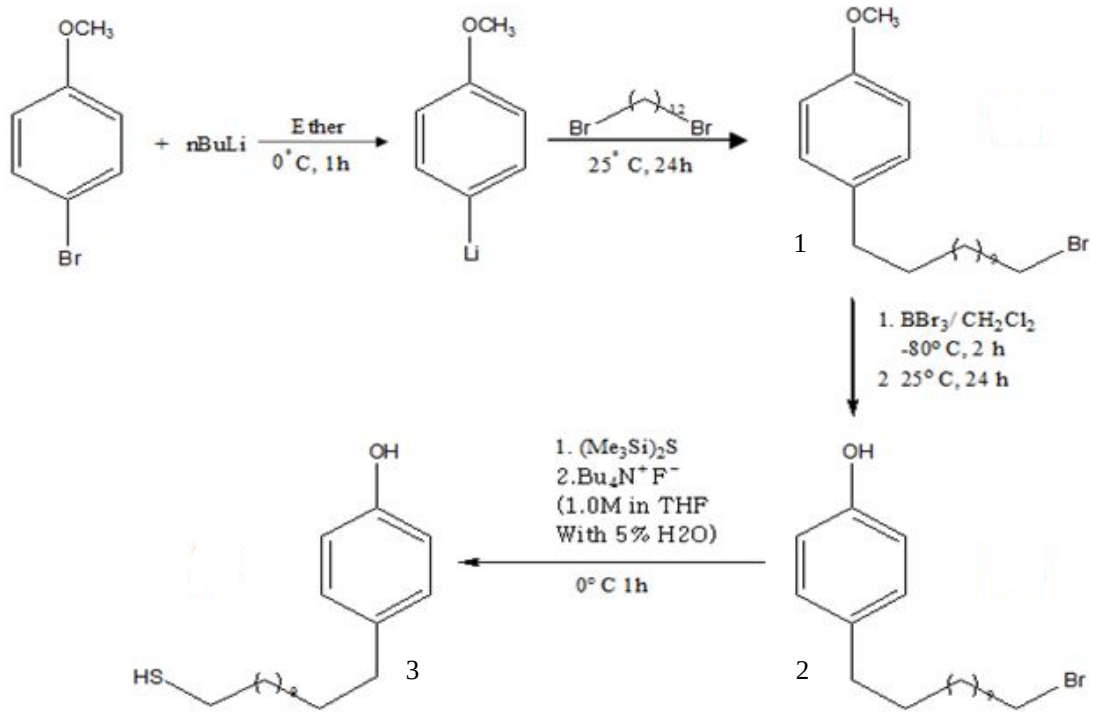

Figure 4.1 The synthesis route of 4-(12-mercaptododecyl) phenol. (3)

Synthesis of 1-(12-Bromododecyl)-4-methoxy-benzene (1)

To a stirred solution of 4-bromoanisole (1.87 g, 10 mmol) in anhydrous diethyl ether (20 mL) in a flame-dried flask under a nitrogen atmosphere, n-butyl-lithium (1.5 eq., 1.6 M in hexane) was added at 0°C dropwise. The yellow mixture was warmed to room temperature and stirred for one hour. A solution of 1,12-dibromododecane (3.0 eq.) in anhydrous diethyl ether (20 mL) was quickly added at 0°C by cannula under a nitrogen atmosphere. The reaction mixture was warmed to room temperature and refluxed for 24 hours then quenched with saturated NH_4Cl solution (20mL). The reaction mixture was partitioned between diethyl ether (40mL) and water (30mL). The aqueous phase was extracted with diethyl ether (3×30mL). The combined organic phase was dried over $MgSO_4$ and filtered. The solvent was evaporated in *vacuo* and purified by flash chromatography on silica gel (230 – 400 mesh) using ethyl acetate/hexane (3:50, v/v) as a mobile phase. The product 1-(12-Bromododecyl)-4-methoxy-benzene was obtained as a yellow solid (2.24 g, 63% yield).

1H NMR ($CDCl_3$, 400 MHz): δ 7.12 (d, 2H, Ph), 6.84 (d, 2H, Ph), 3.80 (s, 3H, CH_3-O-Ph) ,3.40 (t,2H, CH_2Br), 2.56 (t, 2H, CH_2-Ph), 1.88 (p, 2H, CH_2-CH_2Br), 1.60 (p, 2H, CH_2-CH_2-Ph), 1.30 (m, 16H, -$(CH_2)_8$-).

Synthesis of 4-(12-bromo-dodecyl)-phenol (2)

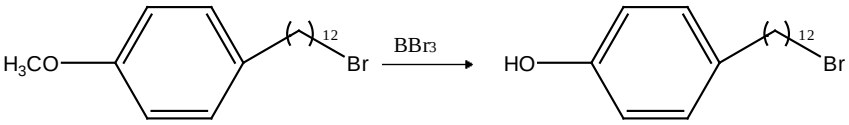

1-(12-Bromododecyl)-4-methoxy-benzene (2.24g, 6.3mmol) was dissolved in dry methylene chloride (20 mL) in a flame-dried flask under a nitrogen atmosphere, then cooled to -75°C. A solution of BBr_3 (2.0 eq.) in 10 mL of dry methylene chloride was added dropwise with stirring. Upon completing the addition, the reaction mixture was allowed to warm to room temperature and stirred for 24 hours. The reaction mixture was diluted with CH_2Cl_2 (20mL). The

brown mixture was washed with $NaHSO_3$ (0.01M 50mL) and $NaHCO_3$ (0.01M 50mL), and then washed with water until the washings were pH neutral. The organic phase was dried over $MgSO_4$, filtered and concentrated. The product 4-(12-bromo-dodecyl)-phenol was obtained as a brown solid (2.02 g, 94% yield), which was used in the next step without further purification.

1H NMR ($CDCl_3$, 400 MHz): δ 7.08 (d, 2H, Ph), 6.76 (d, 2H, Ph), 4.55 (s, 1H, H-O-Ph), 3.40 (t,2H, CH_2Br), 2.56 (t, 2H, CH_2-Ph), 1.88 (p, 2H, CH_2-CH_2Br), 1.60 (p, 2H, CH_2-CH_2-Ph), 1.30 (m, 16H, -$(CH_2)_8$-).

Synthesis of 4-(12-mercaptodecyl) phenol (3)

$$(Me_3Si)_2S \xrightarrow[-Me_3SiF]{TBAF} Me_3SiS^-Bu_4N^+ \xrightarrow[-Br^-Bu_4N^+]{RBr} RSSiMe_3 \xrightarrow[-(Me_3Si)_2O]{H_2O} RSH$$

A stirred solution of 4-(12-bromo-dodecyl)-phenol (1mmol, 0.341g approximately 0.5 M in freshly distilled THF) was cooled to -10 °C, and hexamethyldisilathiane (1.2 equiv, Aldrich) and tetrabutylammonium fluoride (TBAF) (1.1 equiv, 1.0M solution in THF with 5% water, Aldrich) were added. The resulting reaction mixture was allowed to warm to room temperature while being stirred. The reaction was shielded from room light with aluminum foil in order to avoid photo induced side reactions. After the disappearance of the bromide (about half hour at ambient temperature, as observed by TLC monitoring), the reaction mixture was diluted with diethyl ether and washed with saturated aqueous ammonium chloride. The aqueous phase was extracted with diethyl ether (3×30mL). The combined organic phase was dried over $MgSO_4$, and filtered. The solvent was evaporated and purified by flash chromatography on silica gel (230 – 400 mesh) using ethyl acetate/hexane (6:50, v/v) as a mobile phase. The product was obtained as a white solid (0.153g, 52% yield).

MS (EI) m/z (%) 294 (M^+, 100), 586 (M_2^+, 43). HRMS Calcd for $C_{18}H_{30}OS$ (M^+) 294.2016, Found 294.2017; for $C_{36}H_{58}O_2S_2$ (M_2^+) 586.3851, Found 586.3878

1H NMR ($CDCl_3$, 400 MHz): δ 7.08 (d, 2H, Ph), 6.76 (d, 2H, Ph), 4.61 (s, 1H, H-O-Ph), 2.68 (t, 1.4H CH_2S-SCH_2), 2.56 (t, 2.6H, CH_2-Ph, -CH_2SH), 1.60 (m, 4.2H, -CH_2-CH_2-Ph, -CH_2CH_2SH, -CH_2CH_2S-SH), 1.30 (m, 16H, -$(CH_2)_8$-).

MS and NMR show that the final product is a mixture of 4-(12-mercaptodecyl) phenol and its dimer as 4-(12-mercaptodecyl) phenol is unstable toward disulfide formation. But it is still acceptable for forming the SAM, as the S-S covalent bond will break up when S atom forms new covalent bond with Au atom.

4.2 Preparation of 4-(12-mercaptododecyl) phenol modified AFM tips and samples

The AFM tips that were modified with 4-(12-mercaptododecyl) phenol for measuring the adhesion force were Au-Cr coated silicon tips. (CSC38/Cr-Au, MikroMasch, USA). The substrates were gold coated mica substrates (Georg Albert PVD, Germany).

To form alkyl SAMs on the gold coated mica surface and a gold coated AMF tip, the tips and substrates were immersed in 1.0×10^{-3} M 4-(12-mercaptododecyl) phenol in isopropanol for 18 hours. Then the substrates were dried in a stream of nitrogen.

4.3 Preparation of various of colloidal samples used in AFM work

The colloidal particles were prepared using different procedures. Deposition of the colloidal particles on the mica substrate was, however, the same for all.

The preparation of unmodified FeO(OH) colloids

Ferric chloride solution (50 μL, 41%, Fanchem Ltd. Oakville, Ontario, donated by Ravensview Pollution Control Plant Kingston, Ontario) was added by micropipette into distilled water (1L) to form a solution of Fe^{3+} (7.0 ppm, pH 2~3). The pH was monitored and adjusted to pH 6.0 using $NaHCO_3$ (0.5M) with 300 rpm stirring. After the reddish-brown FeO(OH) colloids

precipitated from solution, the solution was continuously stirred for 20 minutes to age, and then settled for 10 minutes, and then collected by filtration.

The preparation of unmodified AlO(OH) colloids

Aluminum chloride solution (1.260×10^{-1} M, 1mL, Aldrich) was added by micropipette into distilled water (1L) to form a solution of Al^{3+} (7.0 ppm, pH 3~4). The solution pH was adjusted to pH 6.0 using $NaHCO_3$ (0.5M) with 300 rpm stirring. After the white AlO(OH) colloids precipitated from solution, the solution was continuously stirred for 20 minutes to age, settled for 10 minutes, and then collected by filtration.

The preparation of co-precipitated colloids with phosphate

NaH_2PO_4 (8.842×10^{-1} M, 1mL, Aldrich) was added by micropipette into distilled water (1L), and then ferric chloride solution (50 μL, 41% w/v) or aluminum chloride solution (1.260×10^{-1} M, 1mL) was added into NaH_2PO_4 solution (pH 3~4). The ratio of P:Fe or P:Al was set to 7:1. The pH of the solution was adjusted to pH 6.0 using $NaHCO_3$ (0.5M) with 300 rpm stirring. After the reddish-brown FeO(OH) colloids or the yellow-white AlO(OH) colloids precipitated, the solution was continuously stirred for 20 minutes to age, settled for 10 minutes, and then collected by filtration.

The preparation of co-precipitated colloids with GA or TA

Gallic acid (2.205×10^{-2} M, 1mL) or Tannic acid (2.205×10^{-2} M, 1mL) was added by micropipette into distilled water (1L), and then ferric chloride solution (50 μL, 41% w/v) or aluminum chloride solution (1.260×10^{-1} M, 1mL) was added into GA or TA solution (pH 2~4) to form a dark purple-blue colored solution. The molar ratio of (GA or TA): (Fe or Al) was set to 0.175:1. The pH of the solution was adjusted to pH 6.0 using $NaHCO_3$ (0.5M) with 300 rpm stirring. After the dark purple-blue FeO(OH) colloids or the dark purple-blue AlO(OH) colloids

precipitated, the solution was continuously stirred for 20 minutes to age, settled for 10 minutes, and then collected by filtration.

The preparation of post-precipitated colloids with phosphate

To make post-precipitated colloids with phosphate, NaH_2PO_4 (8.842×10^{-1} M, 1mL) was added into the prepared colloidal particles in 1L solution using the procedure described in the preparation of unmodified FeO(OH) and AlO(OH) colloids. Then the solution with a molar ratio of P: Fe= 7:1 or P: Al =7:1 was continuously stirred for 15 minutes to age, settled for 10 minutes, and collected by filtration.

The preparation of post-precipitated colloids with GA or TA

To make post-precipitated colloids with GA or TA, GA (2.205×10^{-2} M, 1mL) or TA (2.205×10^{-2} M, 1mL) was added to the colloidal particles in 1L solution, which was prepared previously using the procedure described in Section in the preparation of unmodified FeO(OH) and AlO(OH) colloids. The color of colloids changed to dark purple-blue after adding in GA or TA. Then the solution with a molar ratio of (GA or TA): (Fe or Al) = 0.175:1 was continuously stirred for 15 minutes to age, settled for 10 minutes, and collected by filtration.

The deposition of colloidal particles on mica substrate

To prepare the sample of colloidal particles used in the CFM work, the particles were evenly deposited on a flat substrate. In this work, double–sided tape adhered to a mica slide was used due to the low adhesion between colloidal particles and the mica slide. First, the double–sided tape adhered on the mica was placed on a filter paper (Whatman 50, fisher, Particle retention: > 2.7um) in the filter. Then, a concentrated slurry of colloidal particles, which was prepared by carefully decanting about ¾ of the solution layer above the precipitation layer, was transferred into the filter. After the aqueous phase was completely removed, the colloidal particles were collected on the double- sided tape on the mica slide. The sample was left in the air to dry for 24

hours. If the colloidal particles did not completely cover the substrate after drying, that sample would be replaced on the filter funnel and the same slurry of colloidal particles would be re-deposited on that sample to collect more particles. Usually, this procedure would be repeated for 5 or 6 times to acquire a sample on which the colloidal particles were usually seen to be evenly deposited.

4.4 Surface topography by atomic force microscopy (AFM)

AFM images were acquired using a PicoSPM operated in contact mode using a Nanoscope IIE controller (Digital Instruments, Santa Barbara, CA) under ambient conditions. The Si cantilevers are of a resonance frequency of 100 kHz, which were terminated with standard Si_3N_4 tips. Height and phase shift data were simultaneously recorded, as a function of both cantilever oscillation amplitude (A_o) and set point ratio $r_{sp}=A_{sp}/A_o$.

4.5 Force-distance curve measurement by CFS

The CFM tips for measuring the adhesion force were Au-Cr coated silicon tips. (CSC38/Cr-Au, MikroMasch, USA). The tip and both sides of cantilever are consecutively coated by continuous films of Cr (first layer) and Au (second layer) by the manufacturer. Both the Cr and Au layers are 20 nm thick. The radius of curvature is less than 10 nm, the tip height is between 20 to 25 μm, and full tip cone angle is less than 30°. The SEM images from the manufacturer are shown as below.

Due to some limitation of our AFM instrument, the tip on cantilever A (Schematic drawing is shown as Figure 4.3) was the easiest one to reflect the laser off during these CFM experiments. To keep consistency of all CFM experiments, cantilever A was always used in this work. The typical spring constant of cantilever A is 0.08N/m; the typical resonant frequency is 20 kHz.

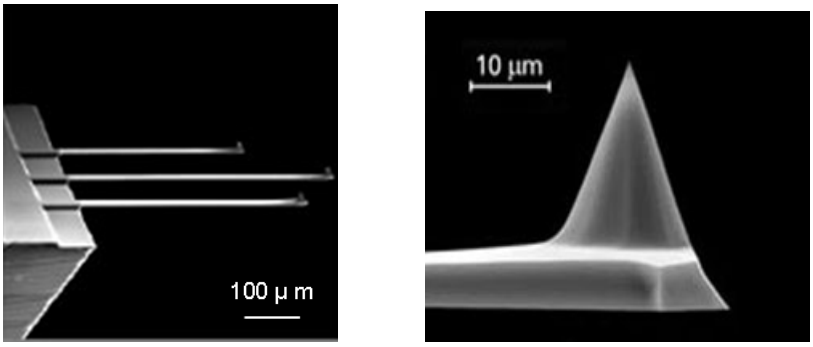

Figure 4.2 SEM images of the Au-Cr coated silicon cantilever as acquired from manufacturer.

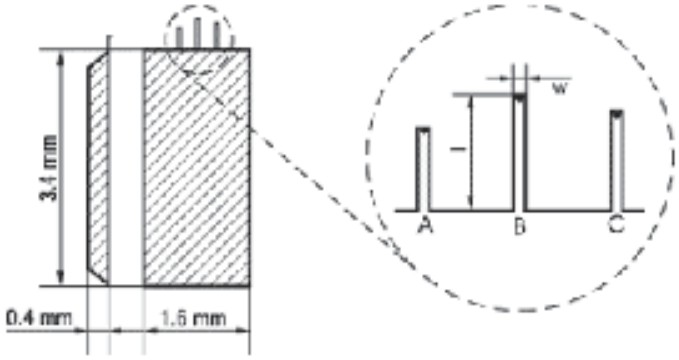

Au Series, Cantilevers	**Resonant Frequency, kHz**			**Spring Constant, N/m**			Length l ± 5, µm	Width w ± 3, µm	Thickness t ± 0.3, µm
	min	**typ**	max	min	**typ**	max			
A	14	**20**	28	0.02	**0.08**	0.2	250	35	1.0

Figure 4.3 Schematic drawing and characteristic parameters of the probe chip as acquired from the manufacturer.

Chemical force titration was used to determine the adhesive forces between the 4-(12-mercaptododecyl) phenol modified AFM tips and similarly modified gold-coated mica substrate and the adhesive forces between the 4-(12-mercaptododecyl) phenol modified AFM tips and various unmodified or modified iron/aluminum oxide colloids coated mica substrates.

The data were obtained using a PicoSPM in MAC mode (Molecular Imaging, Tempe, AZ) and a Nanoscope IIE controller (Digital instruments, Santa Barbara, CA).

The force curves were acquired under freshly prepared unbuffered NaOH or HCl solutions of pH ranging from 3 to 12. The unbuffered pH solutions are low ionic strength solutions (10^{-3} M) except pH 2 and pH 12 are of higher ionic strengths (10^{-2} M). The unbuffered pH solutions were used in order to prevent any unwanted interactions between the surfaces and ions originating from buffer solution.

The adhesive force between the tip and sample was measured from the average of the adhesive well depth of at least 150 force-distance curves at each pH value. The reported values of the adhesive interaction are an average of all of the adhesive forces, and the reported errors reflect the standard deviation of the data. For assuring the reproducibility of data, the adhesive force was re-measured several times between the same tip and different surface sites.

4.6 Infrared Spectroscopy

IR data were acquired for 4-(12-mercaptododecyl) phenol in a KBr disk in transmission mode with a Bomem MB-120 spectrometer which was combined with a 486 computer processor running BGRAMS 32 version 4.

ATR- FTIR data were acquired for 4-(12-mercaptododecyl) phenol modified gold coated mica using a Nicolet Avatar 360 E.S.P. FT-IR Spectrometer (Madison, Wisconsin, USA) with a single reflection diamond ATR accessory operating in ATR mode using a ZnSe crystal. One gold-coated mica slide was used as the blank sample as the spectral background for SAM modified gold-coated mica slide.

4.7 X-ray Photoelectron Spectroscopy

The XPS experiments were conducted using a Thermo Instruments Microlab 310F surface

analysis system (Hastings, UK). The analysis occurred in ultra-high vacuum conditions (10^{-9}–10^{-10} Torr) using a Mg Kα X-ray source (1253.6 eV).

X-ray photoelectron spectroscopy (XPS) was used to analyze 4-(12-mercaptododecyl) phenol modified gold-coated mica and various samples of unmodified or modified iron/aluminum oxide colloids, GA (analytically pure, Aldrich) and TA (analytically pure, Aldrich). Samples were affixed to aluminum sample mounts using double-sided Cu tape (SPI Supplies Toronto, Ontario), and then loaded it into the entry lock of XPS to degas overnight. Finally the samples were transferred to the analysis stage into the UHV analysis chamber via a precision manipulator.

The surface/detector take-off angle was set up to 75°. The number of scans was in the range of 2 –10, depending on the signal-to-noise level. The X-ray source is controlled on a z-drive so it can be maneuvered to the back of the vacuum chamber when not in use. The Mg anode X-ray source was used at a setting of 20 mA current and 15 kV voltage (300 W) since the Mg source has a narrower beam width than the Al beam. Both Auger and XPS peaks were observed in the spectrum and could be differentiated between by a simple change from Mg to Al radiation which causes a shift in the measured binding energies of the XPS peaks.

The Au 4f, S 2p, C 1s, N1s, O 1s, Si 2p, Na 2p, P 2p, Fe 2p3/2, Al 2s, P XAES, and valence band spectra were selectively collected for different samples as required. They were recorded with a step size of 0.1 eV, using a PHI 5400 ESCA instrument (base pressure $<1\times10^{-8}$ Pa) set at a constant analyzer pass energy of 20 eV.

The Advantage software program was used to process the resultant data. All the peak positions were deducted by the shift of charging effects based on bulk C1s line at 285.0 eV. The XPS spectrometer included the Advantage software program, which was used to process the resultant data. The Shirley algorithm was used as the background subtraction method. The

Powell peak-fitting algorithm was used for all peaks.

4.8 Zeta potentiometry

Zeta potentiometry measurements were performed on the various colloidal samples at room temperature using a Penkem Model 501 Lazer Zee Meter. Small portions of the prepared colloidal solution were diluted in the distilled water to make approximately 100mL of colloidal solution, which contained colloidal particles in a convenient range for the observation by the scattering of laser light. HCl (0.05 M) and NaOH (0.05 M) were used to adjust the pH of the colloidal solutions.

The zeta potential cell was rinsed twice before measurement with the solution sample. After the sample solution was injected into the cell using a syringe, the exterior of the cell was dried, especially the electrical contacts and the cell windows. Measurements were taken at the "stationary layer" of the cell, in which motion of the particles in not affected by solvent flowing in either direction. In this work, the stationary layer was calculated to be at a distance of 211 μm from the bottom inner cell surface, as discussed in section 3.6.2. After the colloidal particles in stationary layer were brought into focus, the electrical potential was added across the cell. The apparent motion of the colloidal particles can be observed, the rate and direction of motion depending on the sign and magnitude of their potential at the plane of shear. Then, the motion rate of the colloidal particles was adjusted to be relative stationary to the certain prism rotation rate. The average zeta potential of the colloidal particles was read directly from the display of the instrument. Each potential data point was the average of three measurements.

Results and Discussion

4.9 The characterization of self-assembled monolayer (SAM) of 4-(12-mercapto-dodecyl) formed on Au coated mica using ATR-FTIR

A standard IR transmission spectrum of 4-(12-mercaptododecyl) phenol and an ATR-FTIR spectrum of 4-(12-mercaptododecyl) phenol adsorbed on gold-coated mica are shown in Figure 4.4. These were acquired to confirm the surface composition and molecular orientation of the SAM.

All peaks in these two spectra are assigned in Table 4.1. From the spectra, we can clearly see the aromatic and aliphatic C-H stretches at 3020 cm^{-1} and 2900-3000 cm^{-1} respectively (peaks A and B in Figure 4.4). The CH_2 scissoring mode at 1445 cm^{-1} (peak E) is somewhat obscured by water vapor interference. That an aromatic ring is clearly present is indicated by the 1610 cm^{-1} and 1597 cm^{-1} doublet (peak C). The band at 1517 cm^{-1} (D) is the semicircle-stretching mode of the ring and its strength is an indicator of the presence of the OH group. [157] In IR transmission mode, there is no evidence for any residual S-H stretching in the range of 2600 to 2500 cm^{-1} that is associated with the stretching vibration of the S-H group, but this is a weak transition[158] and should be definitely absent in the SAM. In ATR-FTIR, the phenol end group is obscured by a very large OH absorbance of the blank sample so there is a strong negative peak in the spectrum beyond 3100cm^{-1} (not shown) because the gold surface is easily hydrated when the SAM is not present.

To compare the two IR spectra, the intense peak (phenol C-O stretching at 1257 cm^{-1}) was used as the internal reference peak as the two IR spectra were not directly comparable in two different instrumental methods. Qualitatively, these two spectra are similar, but several bands are considerably weaker in ATR-FTIR mode than in IR transmission mode. The similarity

demonstrates that 4-(12-mercaptododecyl) phenol was successfully deposited on the Au coated mica surface. The difference in peak intensities between the two spectra allows us to infer information on the molecular orientation of the SAM. The technique of ATR-FTIR is related to the technique of Reflective Adsorptive Infrared Spectrum (RAIRS), in which selection rules state that the vibration of a dipole cannot be detected if it lies parallel to the surface. The peak intensity of the aliphatic C-H stretch (2850 cm^{-1}, peak B), CH_2 scissors vibration (1445 cm^{-1}, peak E), out of plane aromatic C-H deformations (825 cm^{-1}, peak H), in plane alkyl CH_2 rocking (748 cm^{-1}, peak J) are all notably weaker in ATR mode than in transmission mode. These are shown in the Table 4.1, and if the molecule lies upright on the surface all will be directed parallel to the surface plane. By contrast, the C-O stretching mode at 1257 cm^{-1} (peak G) is not significantly reduced in intensity. This vibration has its dipole oriented perpendicular to the surface should the molecule be oriented upright. This suggests that the alkyl chains and the benzene rings of this molecule lie mainly perpendicular to the surface as shown in Figure 4.5. The 4-(12-mercaptododecyl) phenol SAM therefore should be lying upright on the Au surface.

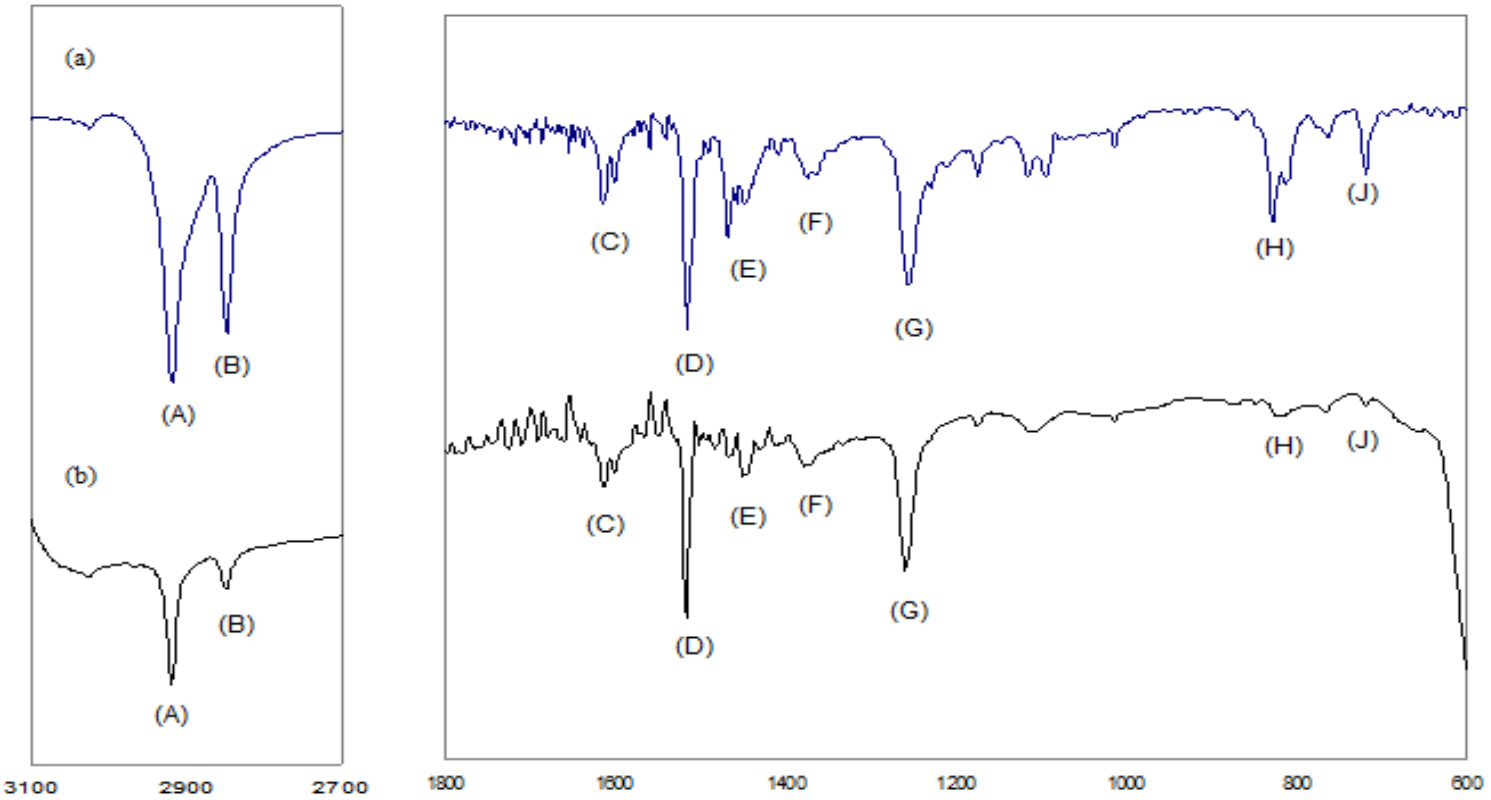

Figure 4.4 (a) a standard IR transmission spectrum of 4-(12-mercaptododecyl) phenol, (b) an ATR-FTIR spectrum of 4-(12-mercaptododecyl) phenol adsorbed on Au coated mica. To compare two IR spectra, the peak G (phenol C-O stretch at 1257 cm^{-1}) was used as the internal reference peak since two IR spectra are not directly comparable in two different instrumental methods.

Table 4.1 The associated table of Figure 4.4 about peak assignments and attenuation ratios of peak areas (ATR-FTIR/FTIR)

Peak	Range (cm^{-1})	Group	Assignment	Peak area ratio (ATR-FTIR/FTIR)
A	3020	aromatic	C-H stretching	0.44
B	2850	alkyl	C-H stretching	0.25
C	1610 1597	benzene ring	ring stretching	1
D	1517	aromatic	semicircle stretching	1
E	1445	alkyl	CH_2 scissors vibration	0.5
F	1380	phenol	O-H deformation	0.86
G	1257	phenol	C-O stretching	1
H	825	aromatic	out of plane C-H wagging	0.07
J	748	alkyl	in plane CH_2 rocking	0.13

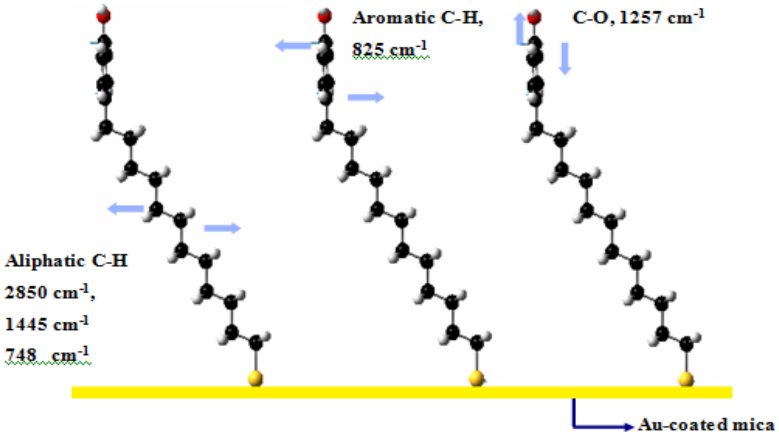

Figure 4.5 A model of the orientation of the molecules of 4-(12-mercaptododecyl) phenol on gold coated mica deduced by comparing ATR-FTIR with IR transmission.

4.10 Determination of the surface pK_a of phenol groups of SAM by chemical force titrations

Since the phenol terminated-AFM tip has an ionizable functional group, the surface pK_a is important in determining the surface charge status. The CFT method was used in this work to determine surface pK_a. In general, CFT profiles of two identical species on tip and sample show a maximum at a pH equal to the surface $pK_{1/2}$ - defined as the *bulk* pH at which exactly half the surface sites are deprotonated. When the pH of solution equals the solution pK_a, according to Henderson-Hasselbalch equation [4.10.1],

$$pH = pKa + \log\frac{[A^-]}{[HA]} \qquad [4.10.1]$$

half the acid groups will be deprotonated. In this condition, statistically the largest number of ionic H-bonds may be formed. Previous workers have shown that ionic H bonds are stronger than regular H bonds by up to a factor of 10~30 times.[18] Thus, the pH at which the strongest adhesion force occurred should correspond to the surface $pK_{1/2}$ of 4-(12-mercaptododecyl) phenol.

It is also important to note that the surface $pK_{1/2}$ is similar, but not equal to, the surface pK_a, which would be the surface pH value at which half the surface sites are deprotonated. The surface pH may vary slightly from that in the bulk solution due to changes in solution dielectric constant near the charged interface. Here, a maximum interaction force of 17 nN (Figure 4.6) is observed at a pH of 8.5, similar to the solution phase pK_a (9.99) of phenol. Other than the differences due to bulk and surface pH values, this shift may be caused by in-plane H-bonding between molecules on the surface, and the limited ability of the solvent to shield charged species at the interface as compared to solution. [127] In addition, the adding sequence of the pH solutions does not affect the measurement of the adhesion forces between the modified tip and substrate.

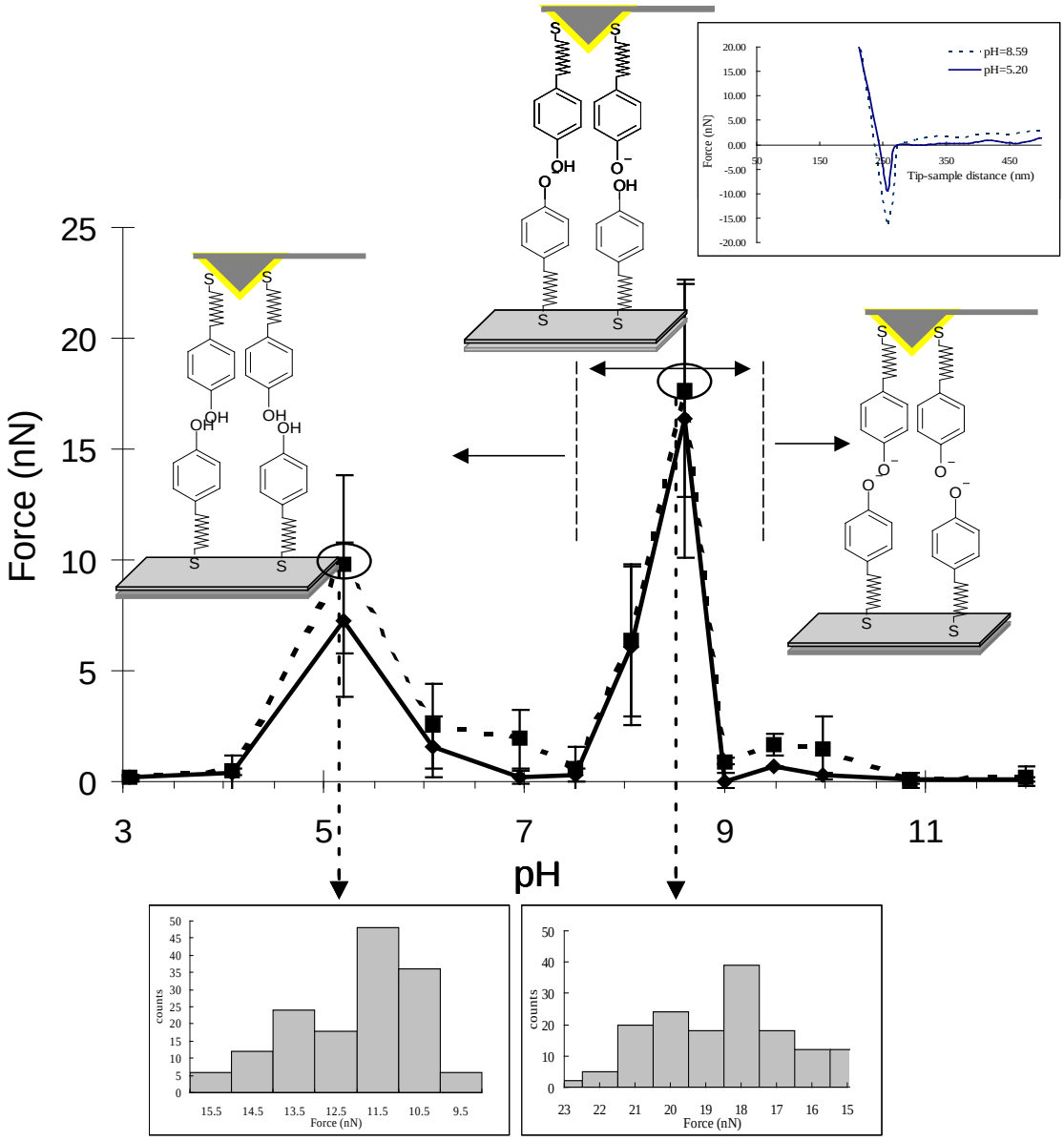

Figure 4.6 Chemical force titration curves showing two trials of the adhesion force between phenol-terminated AFM tip and phenol-terminated Au-coated mica substrates as a function of pH. The error bars represent the standard deviation in the adhesion force as measured from the average of 150-200 force-distance curves. Solid line: the first trial measured from low pH to high pH. Dashed line: the second trial measured from high pH to low pH. The insets show two force curves and two typical histograms of the adhesion forces observed at pH 5.2 and 8.6.

The second maximum peak in the CFT profile, observed at pH 5.2, is more unexpected as it lies in the weaker neutral H-bond regime. Peaks in this range have been observed in CFT curves of carboxylate or benzoic acid species on the surface.[159-161] The possibility is the partial oxidation of the phenol to a dienone, since the phenol is prone to oxidation. As we suspected that phenol had been partially oxidized during the CFT experiments, we used XPS to search for evidence of carbonyl peaks arising from the above species, which will be discussed in section 4.11.

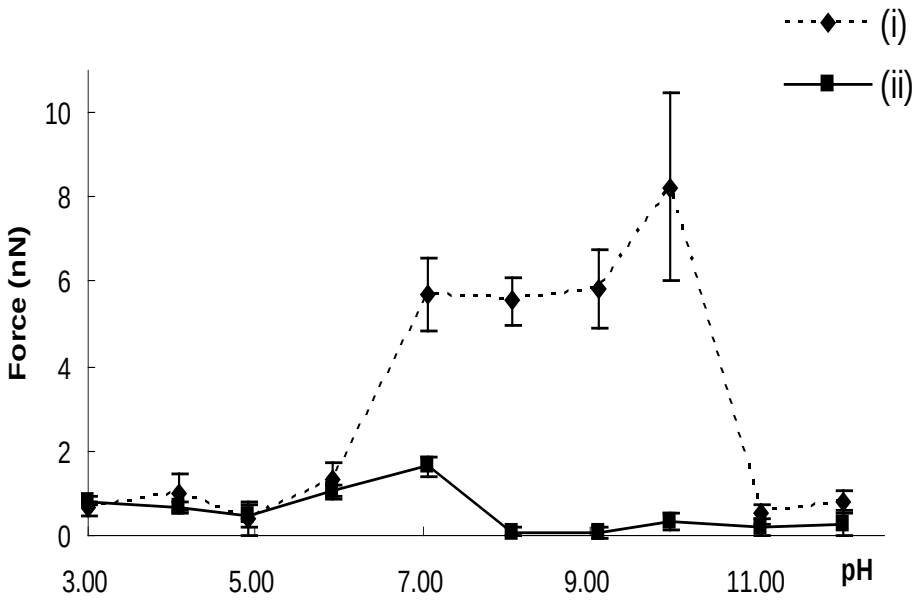

Figure 4.7 Chemical force titration curves showing two trials of the adhesion force between (i) methyl-terminated AFM tip, (ii) bare Au-coated AFM tip mica substrates against phenol-terminated Au-coated mica surface as a function of pH. The error bars represent the standard deviation in the adhesion force as measured from the average of 150-200 force-distance curves.

Considering the possibility of the deformation or mechanical instability of SAM in the contact area which may cause methylene (-CH_2-) groups or bare gold to be exposed in the outer

shell, the CFT profiles curve measured between a methyl-terminal AFM tip (12-mercaptododecane modified) and a bare gold tip, used as controls, against a phenol-terminated substrate (Figure 4.7). CFT of the methyl-terminated tip against phenol substrate shows the relative strong interaction occurred between pH 7 and pH 10 and the bare gold tip with phenol substrate shows no strong interactions over the whole pH range. These two CFT curves have no similarities with the CFT curve of phenol tip against phenol substrate, which demonstrates the interactions between phenol tip against phenol substrate truly arise from surface phenol interactions.

4.11 X-ray Photoelectron Spectroscopy

XP spectra of 4-(12-mercaptododecyl) phenol adsorbed on gold-coated mica were acquired from binding energy regions containing peaks arising from all elements that should be present on the sample: C 1s, O 1s, S 2p, and Au 4f as shown in Figure 4.8. In addition, a low-resolution survey scan indicated that there were no other elements present on the sample surface except for small quantities of Si, presumably arising from the mica support.

The ratio of C: S is 19.3:1 by comparison of the areas of the C1s and S2p peaks. This is greater than the expected ratio of C: S (18:1) from the stoichiometry. This may be expected as S lies at the base of the SAM and the S 2p signal will be slightly attenuated by the overlying SAM.

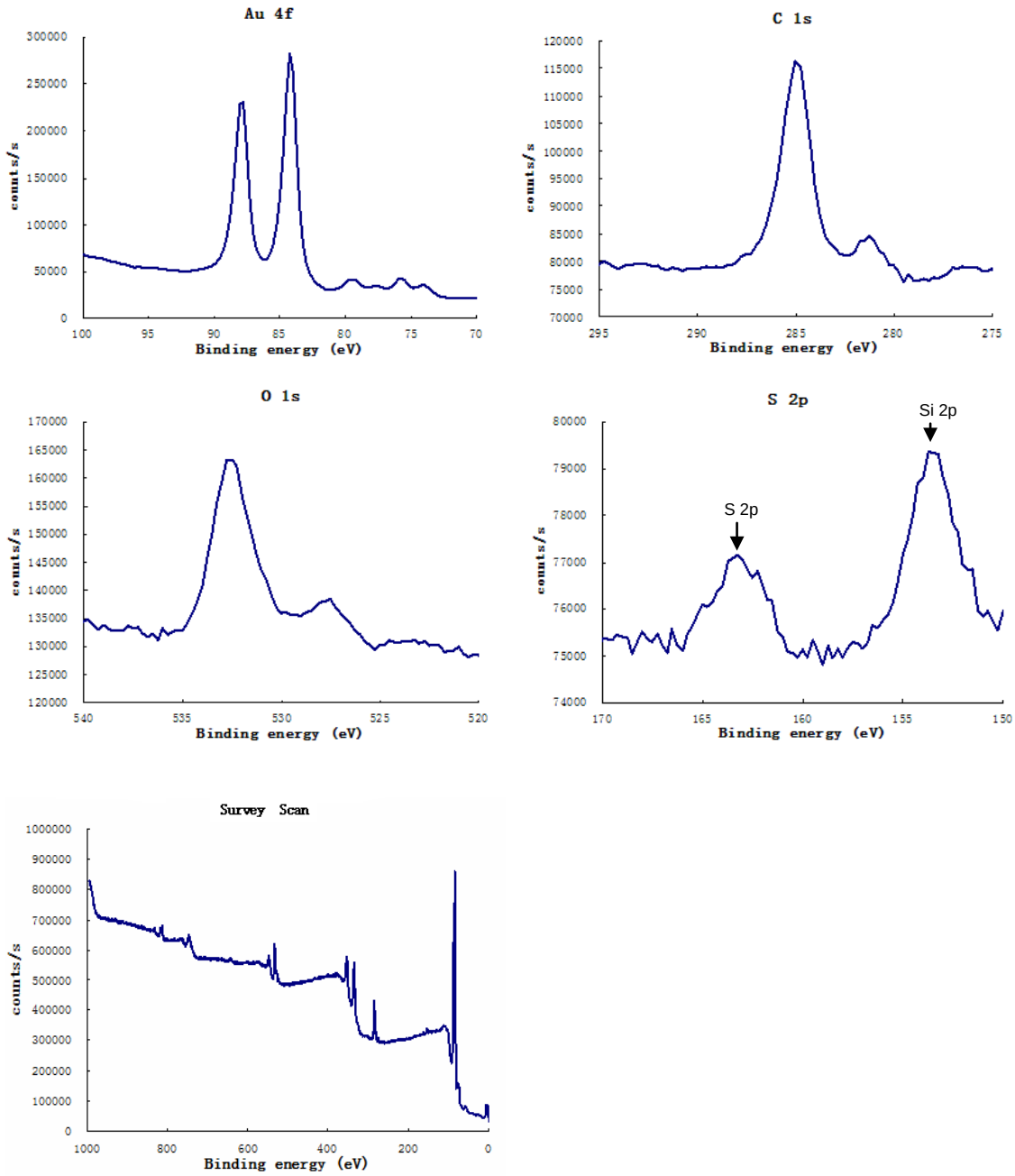

Figure 4.8 XP spectra of Au 4f, C 1s, O 1s, S 2p, and a survey scan (0 eV~ 1000eV) of 4-(12-Mercaptododecyl phenol modified gold-coated mica.

As we suspected that phenol had been partially oxidized during the CFT experiments, we examined a series of samples of 4-(12-Mercaptododecyl) phenol coated on gold-mica substrates using XPS, which had been respectively exposed to different pH solutions (pH 3~12) for five minutes (similar to the time taken to carry out a CFT experiment). Figure 4.9 shows that no peak was observed at 288eV, which is where C in a carbonyl environment is expected. Nor did the spectra appear to change significantly under different pH conditions.

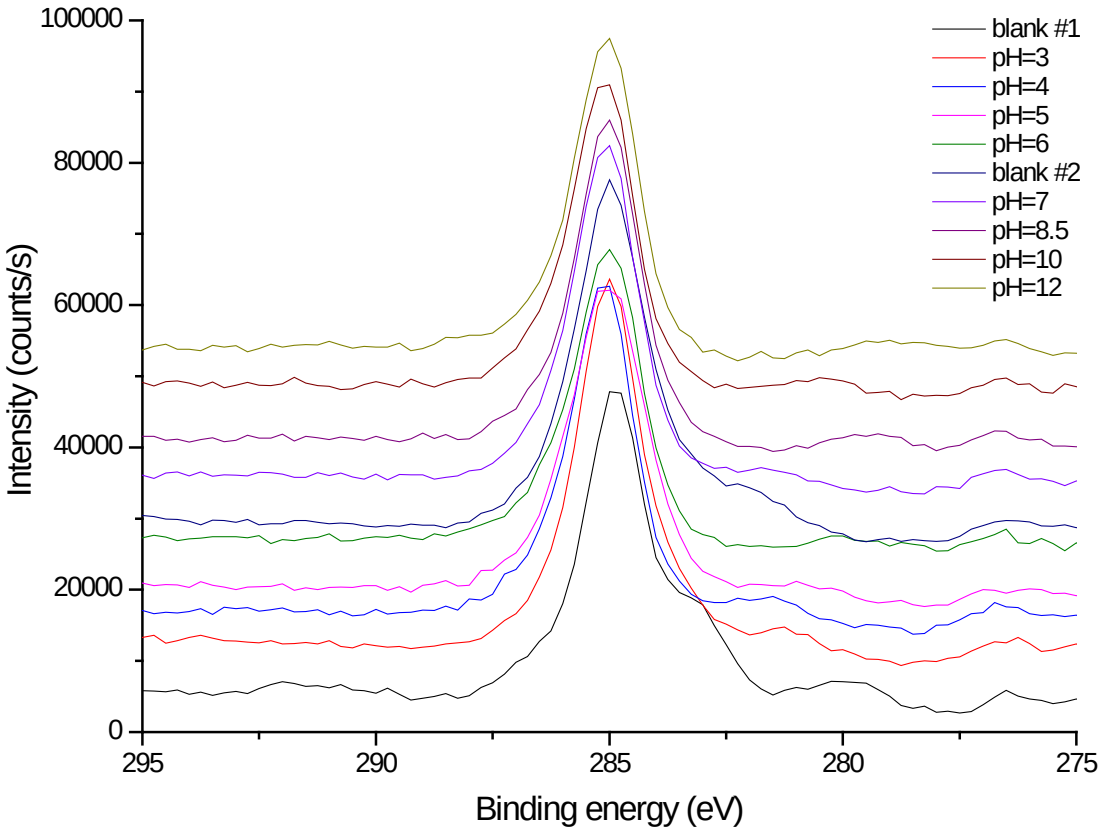

Figure 4.9 XP spectra of C1s peaks of a series of samples of 4-(12-mercaptododecyl) phenol coated on gold-mica substrates, which had been respectively exposed to different pH solutions (pH 3~12) for five minutes.

In the second trial, two substrates both modified with 4-(12-Mercaptododecyl) phenol were sequentially immersed in a series of ten solutions ranging from pH 3 to pH 12, for 5 minutes each. Then XPS C 1s of sample one was acquired immediately following exposure, while that of the second sample was acquired after 24 hours exposure to air following exposure to the pH solutions. Still no evidence was observed for C in a carbonyl environment using XPS. This suggests that the phenol SAM is stable under the conditions used in the CFT experiments. The peak in Figure 4.6 at lower is caused due to a regular H bonding interaction between the tip and substrate.

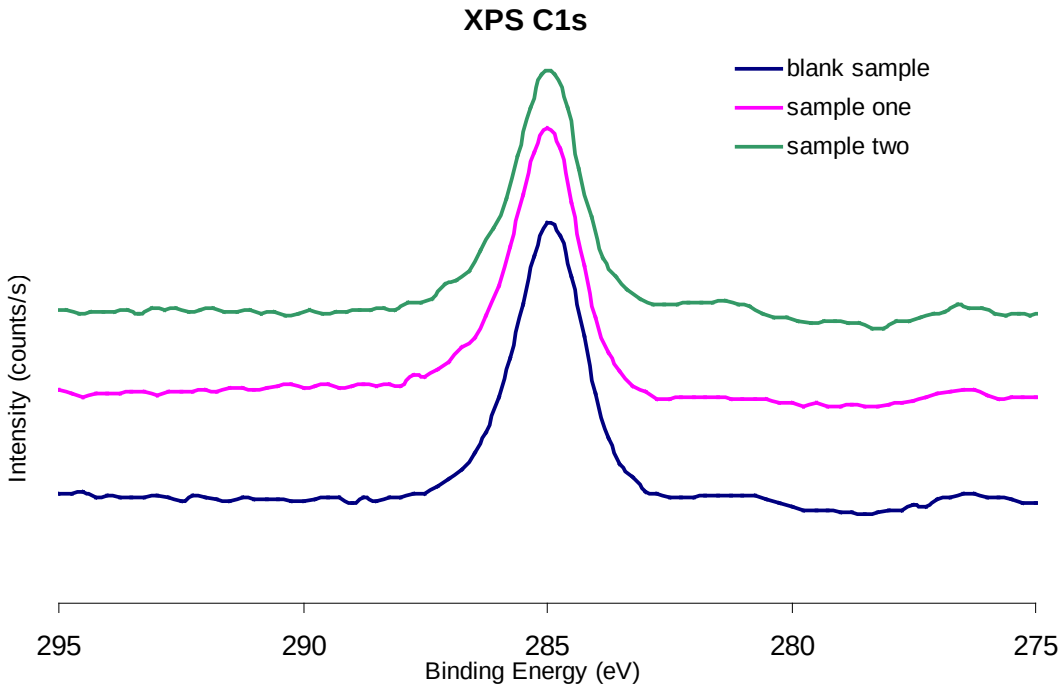

Figure 4.10 C1s XP spectra of two samples, which were sequentially immersed in a series of pH solutions from pH 3 to 12, each pH solution for 5 minutes. The spectrum of sample one was acquired immediately following removal from solution. That of the second sample was examined after 24 hours exposure to air following exposure to the pH solutions.

4.12 Determination of the surface loading of the modifying molecules on the surface of various modified colloids using XPS

To explore the surface loading of modifying molecules on various colloidal particles, XPS was used to analyze various colloidal particles modified with NaH_2PO_4, gallic acid (GA), or tannic acid (TA) using both the co-precipitation or post-precipitation method. Unmodified iron and aluminum oxide colloid samples were analyzed as blank samples.

XPS spectra of dehydrated iron/aluminum (hydr)oxide colloidal particles were acquired from binding energy regions containing peaks arising from all elements that should be expected on the samples: O 1s, Fe 2p, Al 2s, Na 2p, C1s, and (for phosphate-modified colloids) P 2p. Two typical sets of spectra for the dehydrated iron/aluminum (hydr)oxide colloidal particles are respectively shown in Figure 4.11 and 4.12. The C 1s spectra of two types of colloidal particles indicate there are two different carbon species on the surface. For iron/aluminum (hydr)oxide colloidal particles, the oxygen to metal ratio was close to 3:1, roughly consistent with the stoichiometry of the crystalline solid oxides. The peak at binding energy 290 eV is consistent with a CO_3^{-2} anion introduced by $NaHCO_3$, which was used to adjust the pH value. In the samples involving GA or TA, however, the C=O group in GA or TA will also contribute to this signal. The second carbon species at 285.0 eV is residual carbonaceous matter introduced by surface contamination. The Fe $2p_{3/2}$ spectra are at a binding energy of 711.6 eV and Al 2s spectra are at a binding energy 119.7 eV, consistent with Fe and Al in the +3 oxidation state. [162] A survey scan indicated that there were not any other elements beyond those listed above present on the sample surface.

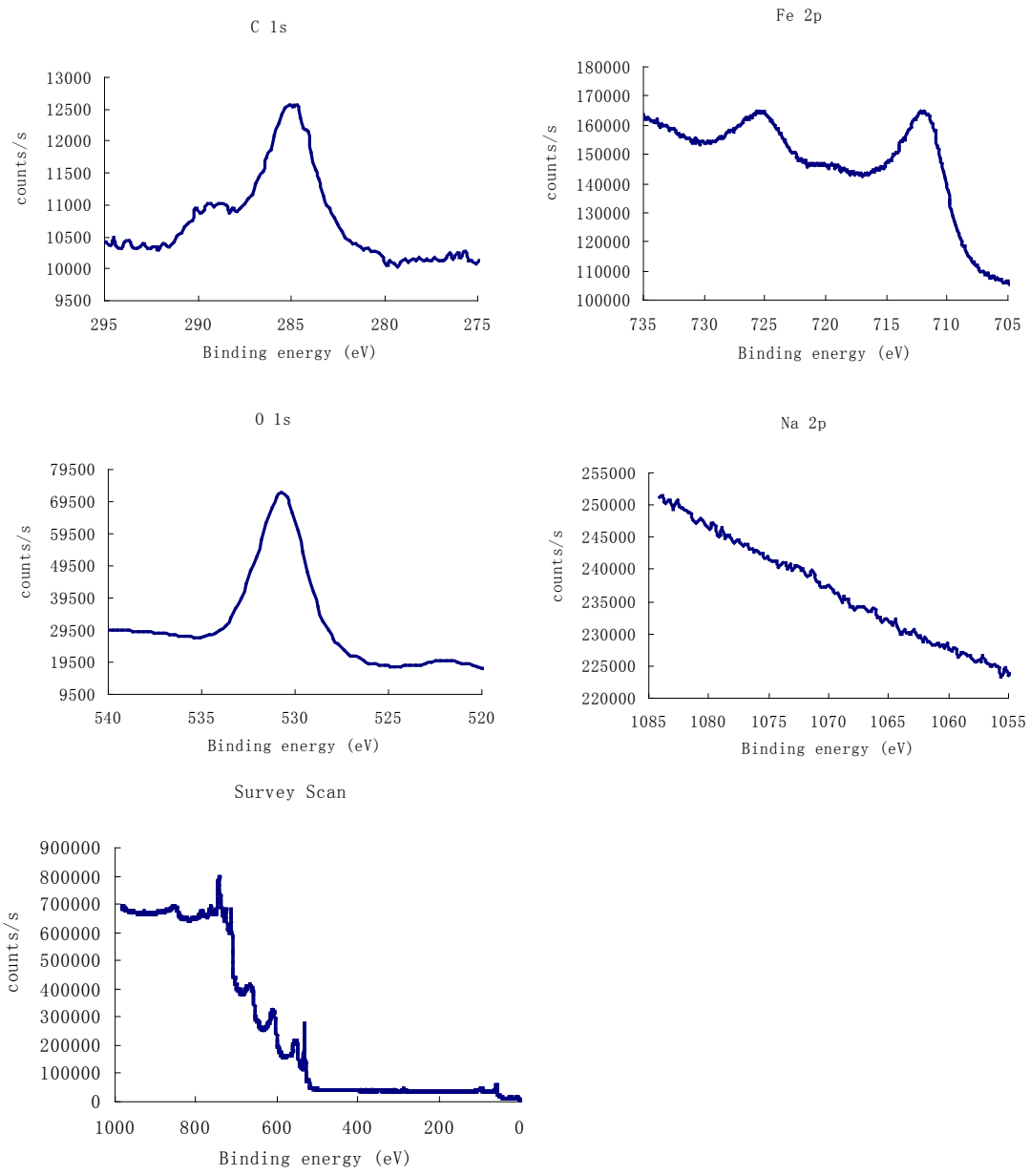

Figure 4.11 C 1s, O 1s, Fe 2p, Na 2p XP spectra and a survey scan (0 eV~ 1000eV) of bare iron oxide.

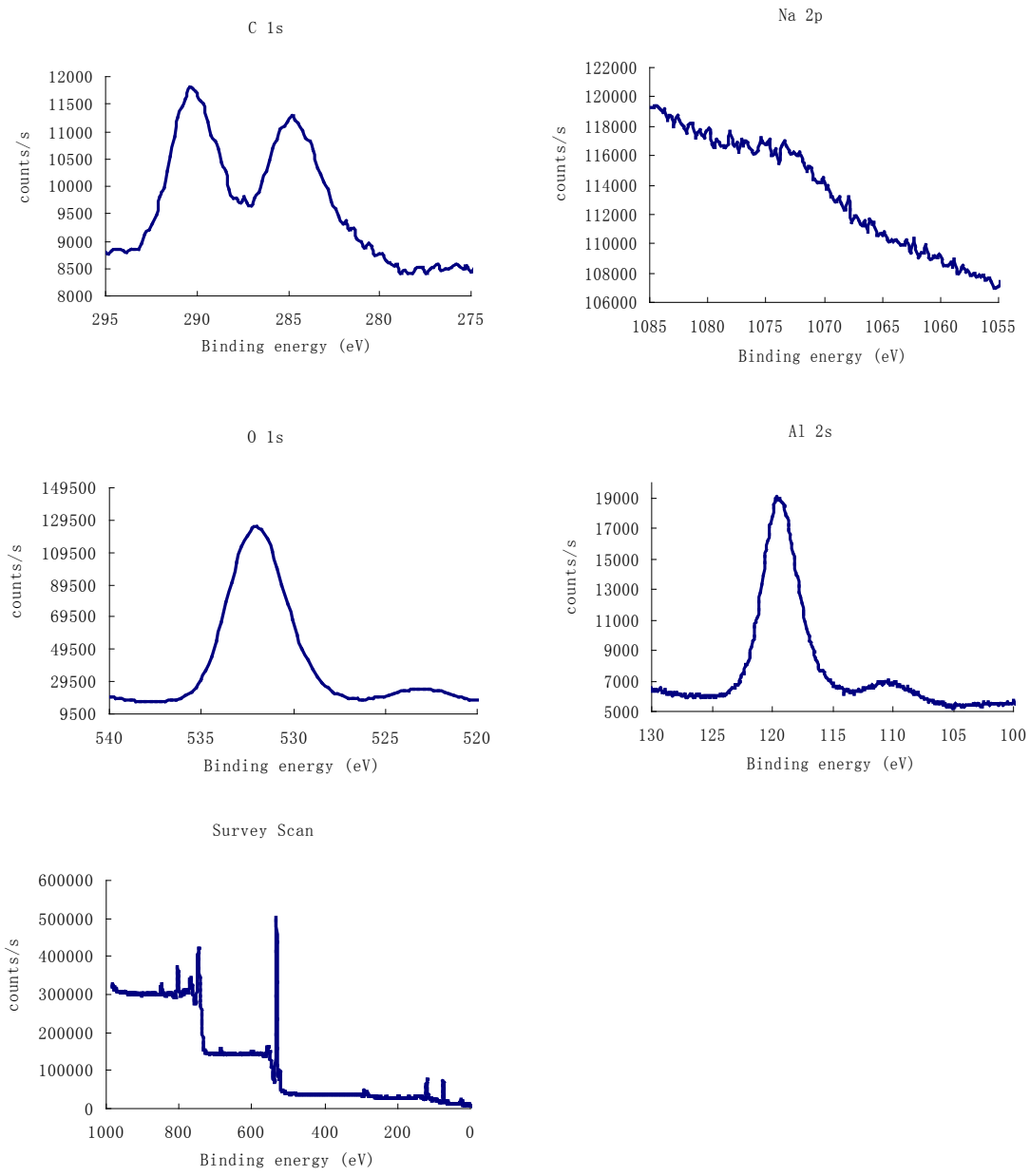

Figure 4.12 C 1s, O 1s, Al 2s, Na 2p XP spectra and a survey scan (0 eV~ 1000eV) of bare aluminum oxide.

The XPS spectra from the modified ion/aluminum oxide colloids are respectively summarized in Table 4.2 and Table 4.3, which give peak areas as determined by the Shirley fitting method. As XPS is a semi-quantitative analysis method, here only the peak area ratios were taken into consideration for comparison of surface loading. The elemental ratios P/Fe, P/Al, C_{total}/Fe, C_{total}/Al, O/Fe, O/Al were calculated from the peak areas corrected for sensitivity factors and are shown in Table 4.4.

To explore the surface composition of the iron (hydr)oxide modified with GA or TA, pure GA and TA were tested by XPS as reference, with the results shown in Table 4.5. The experimental ratios of both C=O/C_{total} (0.10) and O/C_{total} (0.67) of pure GA are close to the theoretical ratios (0.14 and 0.71 respectively) from stoichiometry. The lower values of both experimental ratios are presumably caused by trace residual carbonaceous matter introduced by surface contamination. The experimental ratio C=O/ C_{total} (0.10) of GA is lower than observed for the colloids, suggesting that there is still significant CO_3^{2-} incorporation to the GA modified iron (hydr)oxide colloids. The experimental ratio of C=O/C_{total} of pure TA is 0.37, and the experimental ratio of O/C total of pure TA is 0.24. As TA contains a mixture of related compounds, which contain a glucose center attached to a variable number of gallic acid and benzoic acid end-groups by ester linkages (the chemical formula for commercial tannic acid given as $C_{76}H_{52}O_{46}$), it is impossible to exactly predict the ratios of C=O/C_{total} and O/C_{total} from stoichiometry. But we can make an approximation based on a representative molecular structure mode for tannic acid as shown in Figure 2.4; the ratio of C=O/C_{total} is 0.13 and the ratio of O/C is 0.61. However, the experimental ratio of C=O/C_{total} is greater and O/C_{total} less by comparison of the respective ratios based on the stoichiometry (Table 4.5). They were presumably caused by sample variation depending on source.

In the samples involving GA or TA, the carbonyl, C=O, group will also contribute to the signal at 289.9 eV. XPS spectra of pure GA gave a C=O to total carbon ratio of 0.10 (Table 4.5). Measured ratios for the GA colloids were higher than this value, demonstrating that some residual CO_3^{2-} is likely incorporated into the colloid. For TA, the experimental ratio of C=O to total carbon was 0.37, somewhat higher than that observed in the TA modified colloids. The XPS spectra clearly indicated that a thick overlayer of TA has been formed on the surface, as indicated by the considerable attenuation of Fe or Al peaks in comparison to C and O. Total C to metal and O to metal ratios in all the GA or TA modified colloids were much higher than in the unmodified colloids, consistent with the incorporation of large amounts of organic material into the colloids. However, these ratios are larger in the in co-precipitated colloids, consistent with more additive being present and presumably distributed throughout the colloid as opposed to being isolated on the surface.

Evidently, for the iron/aluminum oxide colloids modified with NaH_2PO_4, the co-precipitated particles have higher overall phosphate loading than the post-precipitated particles. Similarly, the C_{total}/Fe or C_{total}/Al ratio of the colloids modified with GA or TA using the co-precipitation method is always higher than that of the post-precipitated colloids. While residual carbonaceous matter introduced by surface contamination was inevitable, the results are still consistent with a higher overall PO_4^{3-}, GA or TA loading in co-precipitated colloids, consistent with the additive being distributed throughout the colloid as opposed to being isolated on the surface.

Table 4.2 The XPS peak areas of C1s, O 1s, Fe 2p, P 2p, and Na 2p of various iron oxide colloids.

XPS peak areas of elements on the surface of various iron oxide colloids

Modifying reagent (X)	modification method	mole ratio (X:Fe)	specific peak areas ($\times 10^4$ counts/s times eV) and binding energy (eV)					
			P 2p 133.8 eV	Fe $2p_{3/2}$ 711.80 eV	C 1s 285.0 eV	C 1s (CO_3 + C=O) 288.0 eV	Na 2p 1072.5 eV	O 1s 531.7 eV
unmodified	Not applicable	**0:1**		**1.31**	**1.06**	**0.37**		**16.16**
NaH2PO4	Co-precipitated	**7:1**	**3.21**	**6.95**	**2.48**	**0.27**	**1.24**	**26.88**
	Post-precipitated	**7:1**	**1.05**	**10.32**	**0.97**	**0.04**	**0.41**	**19.81**
GA	Co-precipitated	**0.175:1**		**9.92**	**2.67**	**1.09**		**16.14**
	Post-precipitated	**0.175:1**		**11.65**	**1.64**	**0.76**	**1.34**	**14.74**
TA	Co-precipitated	**0.175:1**		**2.21**	**6.18**	**1.79**	**2.31**	**13.37**
	Post-precipitated	**0.175:1**		**2.68**	**6.45**	**1.43**	**2.19**	**14.04**

Table 4.3 The XPS peak areas of C1s, O 1s, Al 2s, P 2p, Na 2p on the surface of various aluminum (hydr)oxide colloids.

XPS peak areas of elements on the surface of various aluminum oxide colloids

Modifying reagent (X)	modification method	mole ratio (X: Al)	specific peak areas ($\times 10^4$ counts/s times eV) and binding energy (eV)					
			P 2p 133.9 eV	Al 2s 119.7 eV	C 1s 285.0 eV	C 1s (CO_3+ C=O) 288.0 eV	Na 2p 1072.5 eV	O 1s 531.7 eV
unmodified	Not applicable	**0:1**		**4.71**	**1.32**	**0.87**		**4.71**
NaH_2PO_4	Co-precipitated	**7:1**	**4.90**	**2.17**	**4.32**	**0.70**	**2.66**	**41.20**
	Post-precipitated	**7:1**	**3.57**	**2.62**	**1.18**	**0.47**	**3.11**	**41.71**
GA	Co-precipitated	**0.175:1**		**3.09**	**4.76**	**1.02**		**32.72**
	Post-precipitated	**0.175:1**		**3.14**	**0.81**	**3.40**	**0.95**	**32.54**
TA	Co-precipitated	**0.175:1**		**0.56**	**7.70**	**1.48**	**2.20**	**18.59**
	Post-precipitated	**0.175:1**		**0.66**	**6.68**	**0.53**	**0.96**	**14.96**

Table 4.4 Experimental XPS peak area ratios, corrected for relative sensitivity[27], for various elements in Fe and Al oxide colloids.

modifying reagents (X)	modification method	mole ratio (X: Fe)	GA or TA	iron oxide colloids				aluminum oxide colloids			
			C=O/ C_{total}	P/Fe	C_{total} /Fe	O/Fe	C=O/ C_{total}	P/Al	C_{total}/Al	O/Al	C=O/ C_{total}
unmodified	Not applicable				**0.87**	**3.73**	**0.26**		**3.71**	**3.03**	**0.40**
NaH_2PO_4	Co-precipitated	**7: 1**		**2.37**	**3.16**	**11.72**	**0.10**	**1.33**	**18.51**	**57.52**	**0.14**
	Post-precipitated	**7: 1**		**0.52**	**0.79**	**5.82**	**0.04**	**0.80**	**5.04**	**48.18**	**0.28**
GA	Gallic acid alone		**0.10**								
	Co-precipitated	**0.175:1**			**3.03**	**4.93**	**0.29**		**14.97**	**32.09**	**0.18**
	Post-precipitated	**0.175:1**			**1.64**	**3.83**	**0.32**		**10.72**	**31.43**	**0.18**
TA	Tannic acid alone		**0.37**								
	Co-precipitated	**0.175:1**			**28.83**	**18.34**	**0.22**		**130.21**	**99.85**	**0.16**
	Post-precipitated	**0.175:1**			**23.55**	**15.89**	**0.18**		**87.35**	**68.62**	**0.07**

Table 4.5 The XPS peak areas of C1s, O 1s, Fe 2p, P 2p, Na 2p of various iron oxide colloids substrates and the experimental ratios of CO_3/C_{total} and O/C_{total} by comparison of relative elemental XPS peak area of GA as well the theoretical ratios of CO_3/C_{total} and O/C_{total} from stoichiometry of GA. The elements sensitivity factors used here for the calculation of mole ratios based on the peak areas were C 1s (0.25), O 1s (0.66). [163]

	peak areas ($\times 10^5$ counts/s·eV)			**peak ratios**			
	C 1s 285 eV	**C 1s (C=O) 288 eV**	**O 1s 533 eV**	**Exp. C=O /Ctotal**	**Theo. C=O /Ctotal**	**Exp. O/Ctotal**	**Theo. O/Ctotal**
GA ($C_7H_6O_5$)	**1.05**	**0.12**	**2.04**	**0.10**	**0.14**	**0.67**	**0.71**
TA ($C_{76}H_{52}O_{46}$)	**1.56**	**0.93**	**1.56**	**0.37**	**≈0.13**	**0.24**	**≈0.61**

Auger parameters [164] of P in the iron/aluminum colloids were also acquired as shown in Table 4.6. For iron oxide, both P Auger parameter values are similar to each other but somewhat higher than those published for Na_2HPO_4 (1983.90 eV) and $FePO_4$ (1984.30 eV)[165]. The shift of the P Auger parameter to a higher value suggests that P in the phosphate modified iron oxide is in a more polarizable environment [164] than in either Na_2HPO_4 or $FePO_4$. This may be due to the relatively low density of P within the colloid compared to the pure ionic compounds, allowing it to have more Fe^{3+} neighbours. For aluminum oxide, both Auger parameters of P are similar to each other and consistent with the Auger parameter of P in a range of phosphate salts: $BaPO_4$ (1984.10 eV), $Ni_3(PO4)_2$ (1984.20), $FePO_4$ (1984.30 eV)[165], but lower than the Auger parameter of P in phosphate modified iron oxide (1984.2 eV vs. 1985.3 eV). It demonstrates that upon adsorption of phosphate, the iron oxide has the higher extra atomic relaxation energy than the aluminum oxide.

Table 4.6 The auger parameters of P on the surface of iron (hydr)oxide modified with NaH_2PO_4

Modifying reagent (X)	**modification method**	**P 2p BE eV**	**P AG KE eV**	**P Auger parameter eV**
NaH_2PO_4 (FeO(OH))	Co-precipitated	134.0	1851.2	1985.2
	Post-precipitated	133.8	1851.6	1985.4
NaH_2PO_4 (AlO(OH))	Co-precipitated	134.8	1849.5	1984.3
	Post-precipitated	134.5	1849.6	1984.1

The thickness of the modifying overlayer on iron /aluminum (hydr)oxide was estimated based on equation [4.12.1] . The results are shown in Table 4.7.

$$I = I_o e^{-d/\lambda} \qquad [4.12.1]$$

Here, I_o is the Fe 2p or Al 2s peak area of the unmodified iron (hydr)oxide, I is the peak area of Fe 2p or Al 2s of modified iron (hydr)oxide respectively with phosphate, GA, or TA, d is the thickness of modification overlayer. 'λ' is respectively escape depth value of 1.12 nm and 2.12 nm[166] for Fe 2p and Al 2s photoelectrons at a kinetic energy of 1200 eV.

The calculation results are consistent with the co-precipitation method forming higher surface loading than post-precipitation method. In addition, tannic acid modified colloids have much thicker surface layers than the GA or phosphate modified colloids, presumably caused by its relatively large molecular weight. It should be noted that equation [4.12.1] explicitly assumes that there are no Fe atoms contained within the overlayer region. If there are, the Fe signal will not be as strongly attenuated. Therefore, the values in Table 4.7 represent a minimum possible overlayer thickness.

Table 4.7 The calculation of thickness of modification overlayer on iron/aluminum oxide.

Modifying reagent (X)	Modification method	Thickness of Phosphate layer (nm)	Thickness of GA layer (nm)	Thickness of TA layer (nm)
NaH_2PO_4 (FeO(OH))	Co-precipitated	0.71	0.31	2.00
	Post-precipitated	0.27	0.13	1.78
NaH_2PO_4 (AlO(OH))	Co-precipitated	1.64	0.89	4.50
	Post-precipitated	1.24	0.86	4.17

4.13 CFT of phenol tip against unmodified iron/aluminum (hydro)xide colloidal particles

Topographical images of the bare iron and aluminum oxide substrates used in performing the adhesion force measurements are shown in Figure 4.13, which shows that the iron/aluminum hydroxide colloidal particles were deposited on the mica substrate as a continuous amorphous layer. Our previous work [160,161] using X-ray diffraction analysis has demonstrated that the iron oxide colloidal particles are entirely amorphous. However, the functional groups present on the colloid might be expected to be similar to those of the crystalline forms, which have been well-studied and are known to have three distinct hydroxyl sites. [28,29] The A site (oxo site), in which a hydroxyl group is bound to a single iron atom Fe-OH; B site (μ_3-oxo site), in which oxygen is bond to three irons, Fe_3O; and C site (μ-oxo site), in which oxygen bridges to two irons, Fe_2O. The A site is amphoteric with a first pK_a ($FeOH_2^+$/FeOH) lying in the range of 4.2 to 7.09, and the second pK_a lying in the range of 8 to 10. B and C sites have a pK_a in the range of 8.05 to 9.79, depending on the exact iron oxide species and crystal face.

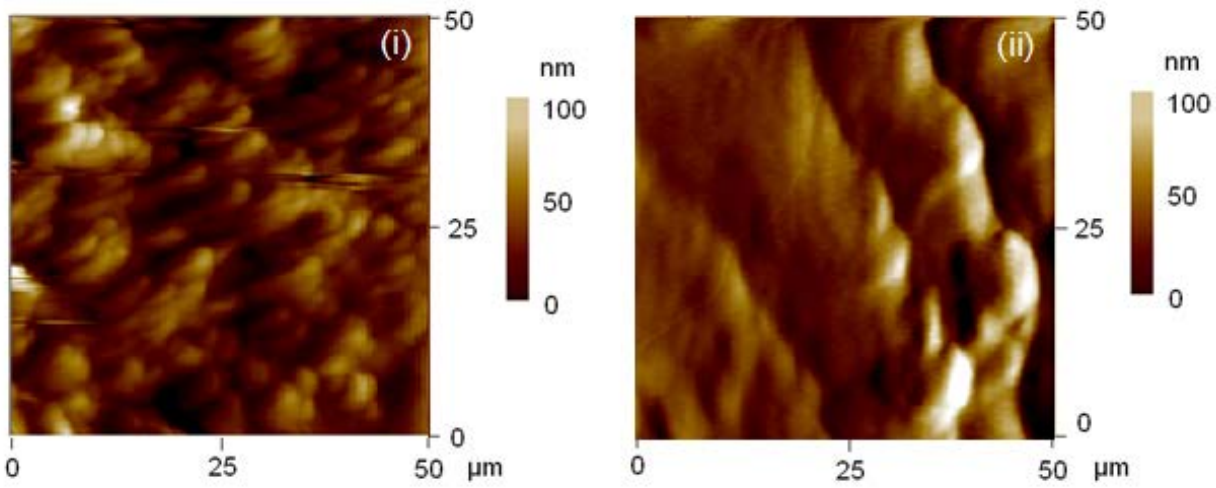

Figure 4.13 AFM images (50µm×50µm) of the colloid particles deposited on the mica substrate. (i) iron hydroxide particles and (ii) aluminum hydroxide particles.

The CFT profile of the phenol tip against unmodified iron hydroxide colloidal particles (Figure 4.14) shows that the maximum adhesion force observed was approximately 22 nN centered at pH of 7.5; a second maximum adhesion force of 9 nN is centered at pH of 4.8; At pH values above 9, a much weaker band of adhesion interactions was observed. Titrations from high to low or low to high pH are reproducible. The zeta potential of the iron hydroxide colloids as a function of pH shown as an inset reproduced from reference [159], which indicates its isoelectric point is around pH 5.

The interaction observed for the phenol tip on the unmodified iron (hydr)oxide may be considered as the interplay of H-bonding interactions of phenol groups with oxo Fe-OH surface sites and electrostatic forces. For pH values above 9, the main interaction is electrostatic repulsion as both surfaces were mostly negatively charged. As the pH falls below 8.5, the tip falls below its surface pK_a as discussed earlier while the zeta potential on the colloid remains strongly negative; this leads to the formation of strong ionic H-bonding interactions. When the pH became lower, A and C sites on the colloid protonate, and it gradually reaches its point of zero

charge (pzc) as seen in the zeta potential profile (Fig. 4.14). The phenol tip is also neutral, so ionic hydrogen bonding is turned off and the total interactions drops due to a regime of neutral hydrogen bonding. In the pH range of 4 to 6, a strong interaction is observed again as the amphoteric B sites on the colloid are protonated and the ionic H bonding forms again.

The CFT profile of a phenol tip against unmodified aluminum (hydro)xide colloids (Fig 4.15) shows the maximum adhesion force observed was approximately 15 nN centered at a pH of 10, and a much weaker band of adhesion forces was observed in the pH range of 3 to 7. The zeta potential curve as an inset in Fig. 4.15 shows that these particles are amphoteric and its pzc around pH 9. Previous work on alumina thin films using XPS has shown the presence of amphoteric Al-OH sites on the aluminum oxide surface, in addition to more basic Lewis acid O^- anionic sites. When formed under more strongly alkaline conditions, the Al-OH sites tended to dominate. [33]

Similar to the approach used to explain the CFT profile of phenol against bare iron oxide colloids, the ionic hydrogen model bonding may also reasonably explain the force titration profiles of phenol against aluminum oxide, as seen schematically in Figure 4.15. For pH above 11, the adhesion force between the tip and sample is quite small due to the electrostatic repulsion of two negatively charged surfaces. For pH values in the range of 9 to 11, the tip begins to protonate and the surface of aluminum oxide is negatively charged so ionic hydrogen bonds can be formed. For pH in the range of 7 to 9, the surface of the colloids are near at the point of zero charge, thus ionic H-bonding is turned off and adhesion force is reduced. As we move to even

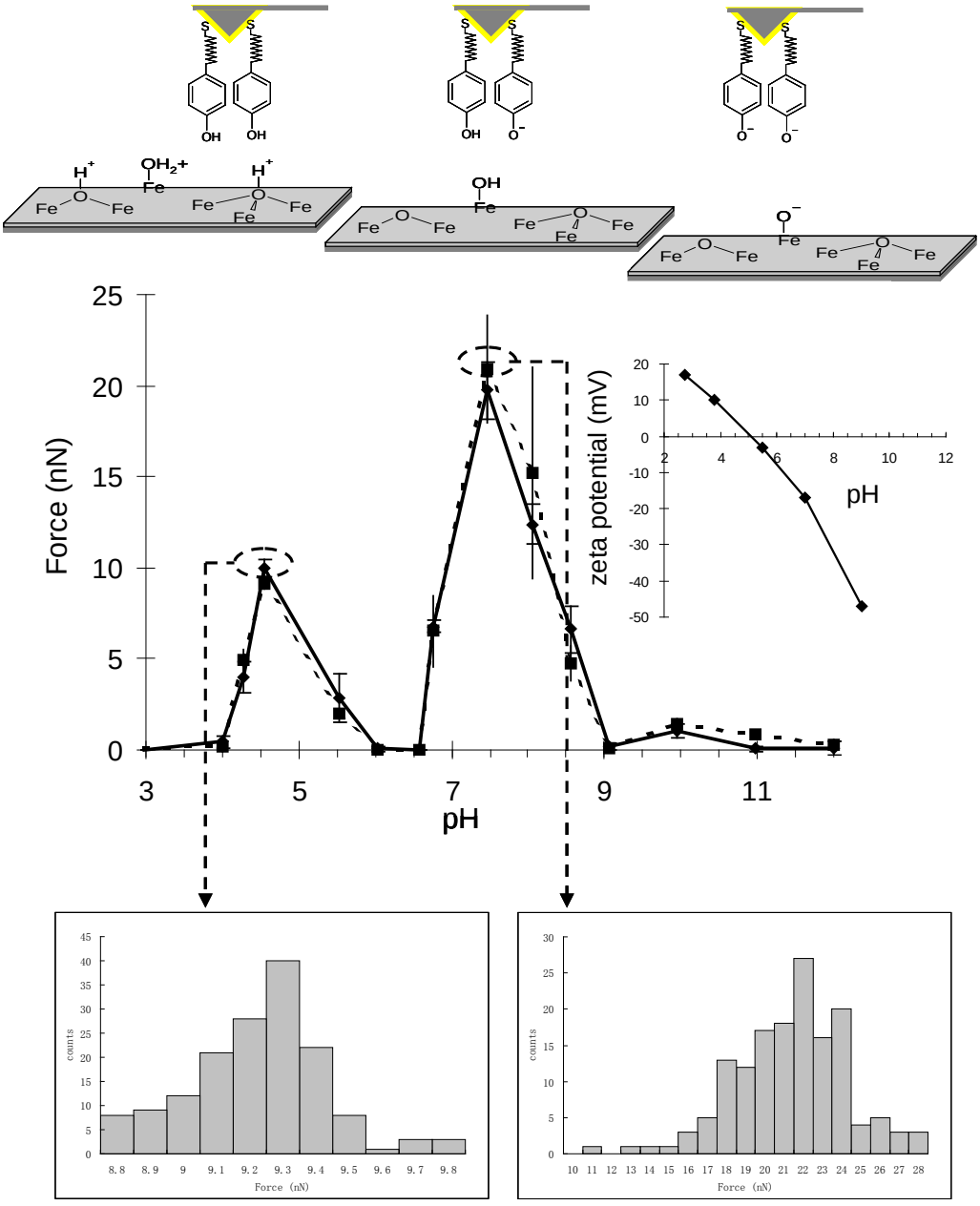

Figure 4.14 Chemical force titration curves showing two trials of the adhesion force between a phenol-terminated AFM tip and unmodified iron (hydr)oxide substrates as a function of pH. The error bars represent the standard deviation in the adhesion force as measured from the average of 150-200 force-distance curves. The upper inset shows the zeta potential of the bare iron hydroxide colloidal particles as a function of pH, which is from reference.[159] The lower shows two typical histograms of the adhesion forces observed at pH 4.5 and 7.5.

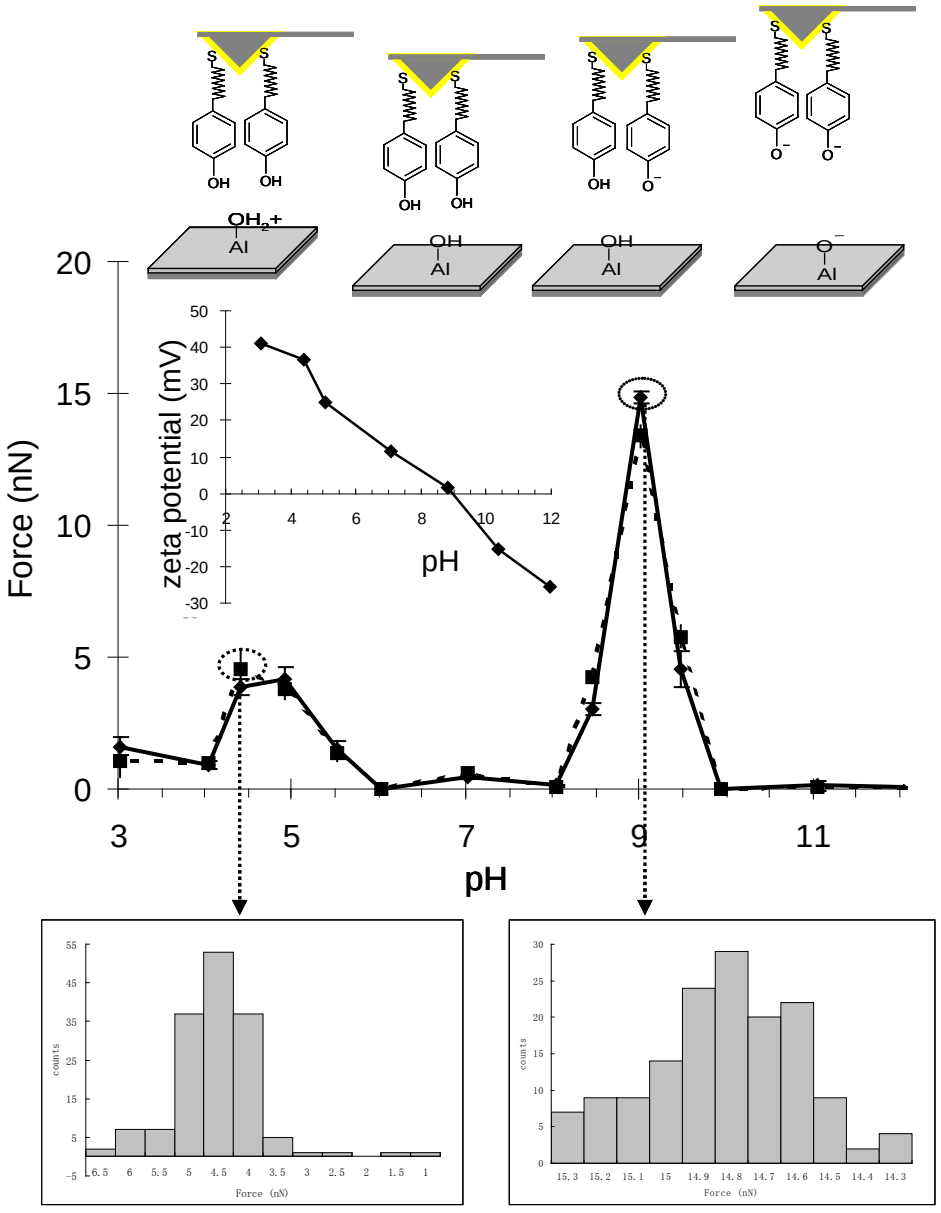

Figure 4.15 Chemical force titration curves showing two trials of the adhesion force between a phenol-terminated AFM tip and unmodified aluminum hydroxide substrates as a function of pH. The error bars represent the standard deviation in the adhesion force as measured from the average of 150-200 force-distance curves. The upper inset shows the zeta potential of the bare aluminum hydroxide colloidal particles as a function of pH. The lower shows two typical histograms of the adhesion forces observed at pH 4.4 and 9.0.

lower pH values, the aluminum oxide particles became protonated and positively charged at the amphoteric Al-OH sites and the ionic H bonding once again forms between neutral phenolic groups and Al-OH_2^+ sites.

Figure 4.16 shows that the force-distance profile of phenol tip on iron (hydr)oxide (pH 4.5 and 7.4) and phenol tip on aluminum (hydr)oxide (pH 4.4 and 9.0). The slopes of force curves of phenol tip on iron (hydr)oxide are greater than its of phenol tip on aluminum (hydr)oxide, which indicates that iron (hydr)oxide colloids are more stiff than iron (hydr)oxide colloids.

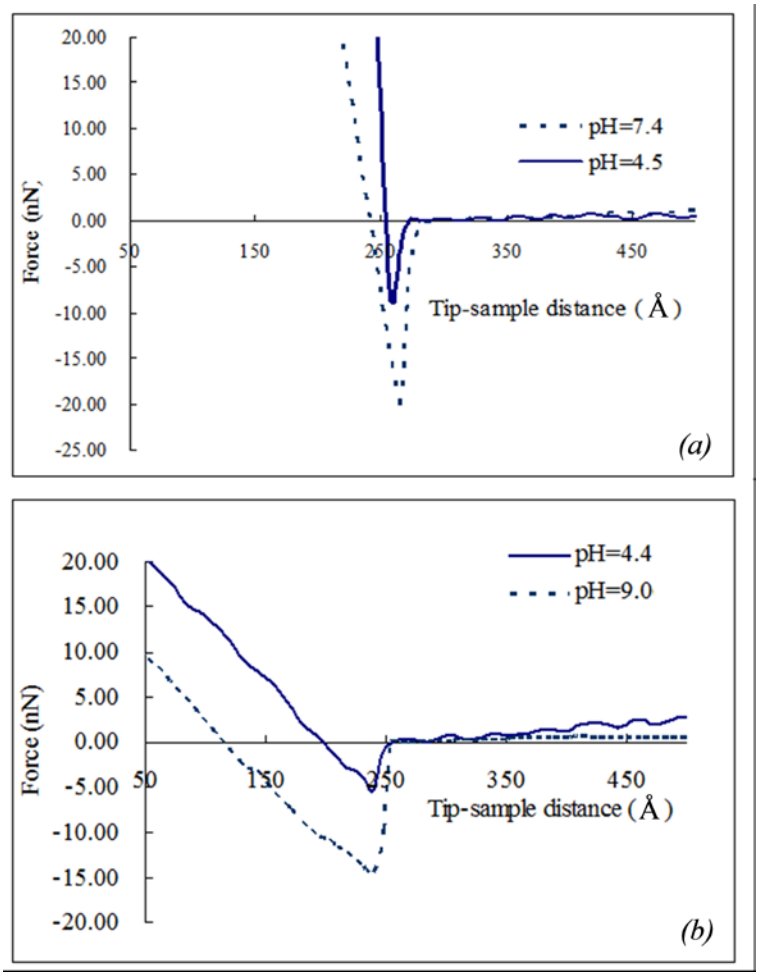

Figure 4.16 Force-distance profile (a) phenol tip on iron (hydr)oxide at pH 4.5 and 7.4 (b) phenol tip on aluminum (hydr)oxide at pH 4.4 and 9.0.

4.14 CFT of phenol tip against iron/aluminum (hydro)xide colloidal particles modified with phosphate

The chemical force titration profiles of phenol tip against FeO(OH) colloids and AlO(OH) colloids, which were co-precipitated or post-precipitated with phosphate, are respectively shown as Figure 4.17 and Figure 4.18. As seen in the figures, the adhesion forces between phenol groups and two colloids modified with phosphate are quite small compared with the unmodified colloid. Recall that the co-precipitated (hydr)oxide particles have a higher surface phosphate loading than the post-precipitated species. (co-precipitated P/Fe=2.37; post-precipitated P/Fe=0.52; co-precipitated P/Al= 1.33; post-precipitated P/Fe=0.80 by XPS discussed in section 4.12)

The ξ potential measurements in Figure 4.19 demonstrate that both iron hydr(oxide) co-precipitated/post-precipitated with NaH_2PO_4 are amphoteric. The point of zero charge (PZC) of the former has been determined to be approximately 3.5 and of the latter is approximately 4.0. The point of zero charge (PZC) of the co-precipitated aluminum (hydr)oxide has been determined to be approximately 3.5. For post-precipitated aluminum (hydr)oxide in the pH range of 3 to 12, it is always negatively charged as shown in Figure 4.19. Compared to unmodified colloidal particles, ξ potential values of colloids modified with phosphate are shifted to much lower pH values.

If H bonding and surface charge were the sole interaction forces operating, we would expect force titration profiles similar to that the bare colloid, but with a shift to lower pH. However, as shown in Figure 4.17 and 4.18, the adhesion forces between phenol groups and phosphate modified colloids are small and relatively pH independent. This will occur if the phosphate anions can block the phenol from interacting with surface binding sites.

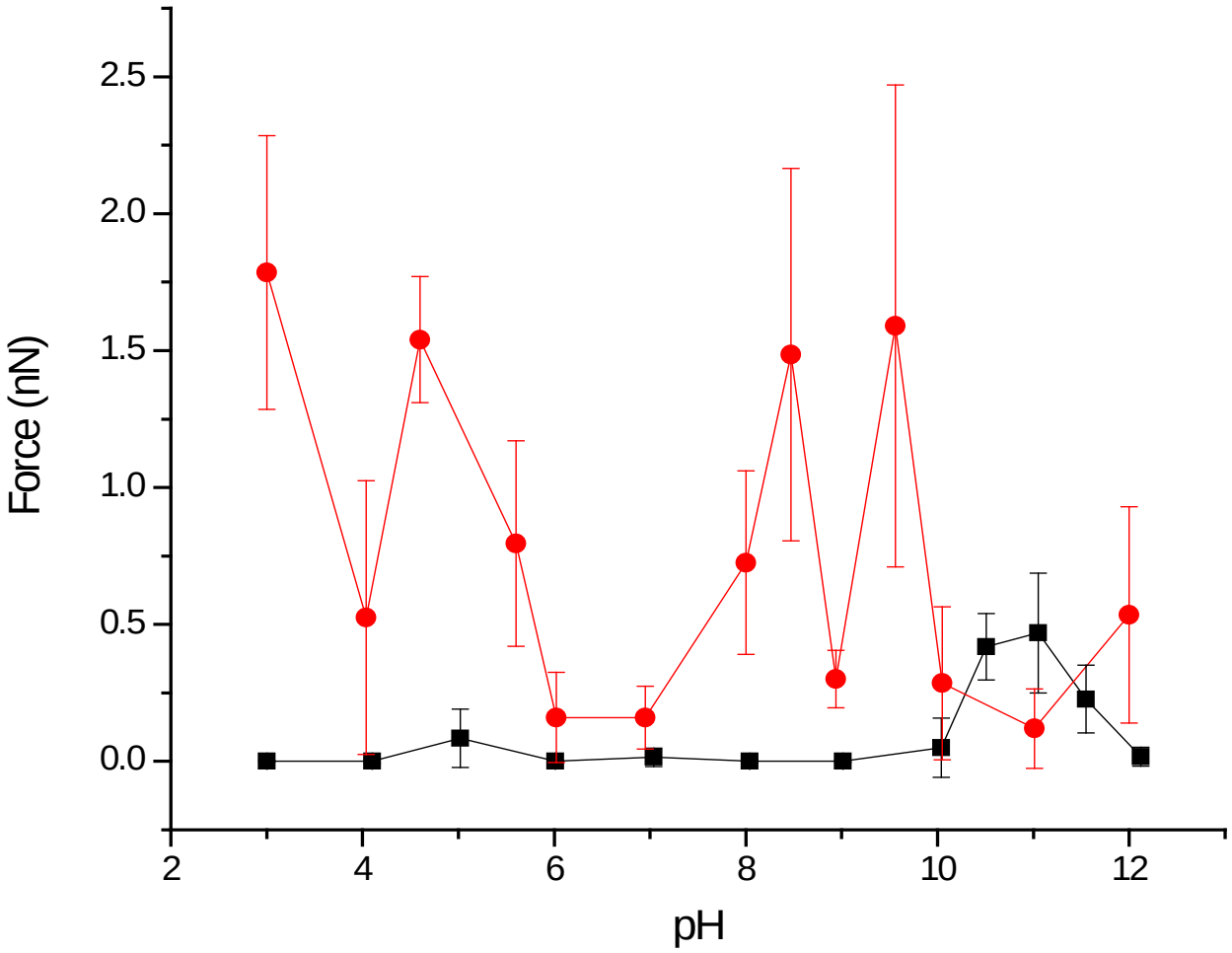

Figure 4.17 Chemical force titration curves showing the adhesion force as a function of pH between a 4-(12-mercaptododecyl) phenol-terminated AFM tip and iron (hydro)xide substrates that were (●) post-precipitated and (■) co-precipitated with phosphate. The error bars represent the standard deviation in the adhesion force as measured from the average of 150-200 force distance curves.

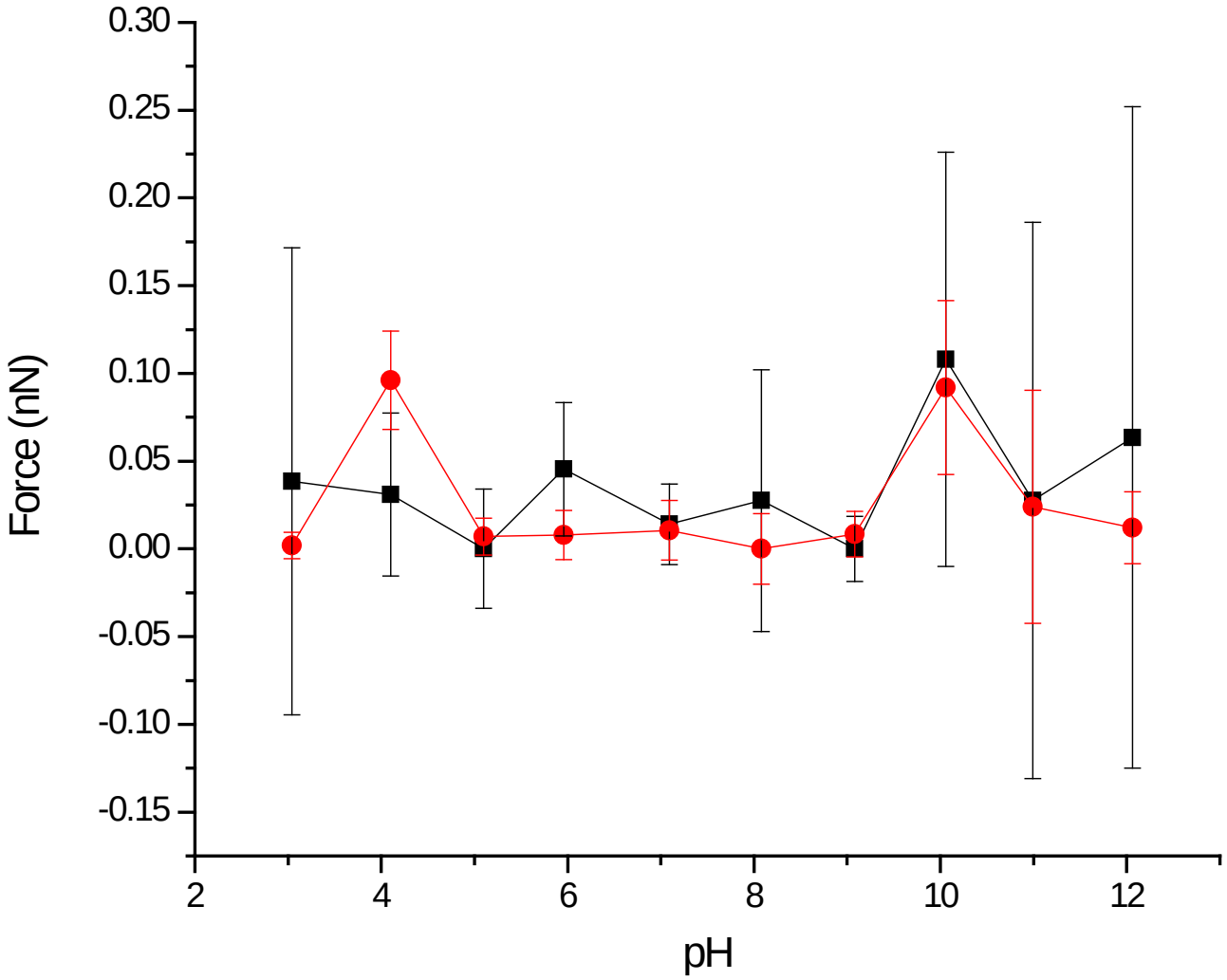

Figure 4.18 Chemical force titration curves showing the adhesion force as a function of pH between a 4-(12-mercaptododecyl) phenol-terminated AFM tip and aluminum (hydro)xide substrates that were (●) post-precipitated and (■) co-precipitated with phosphate. . The error bars represent the standard deviation in the adhesion force as measured from the average of 150-200 force distance curves.

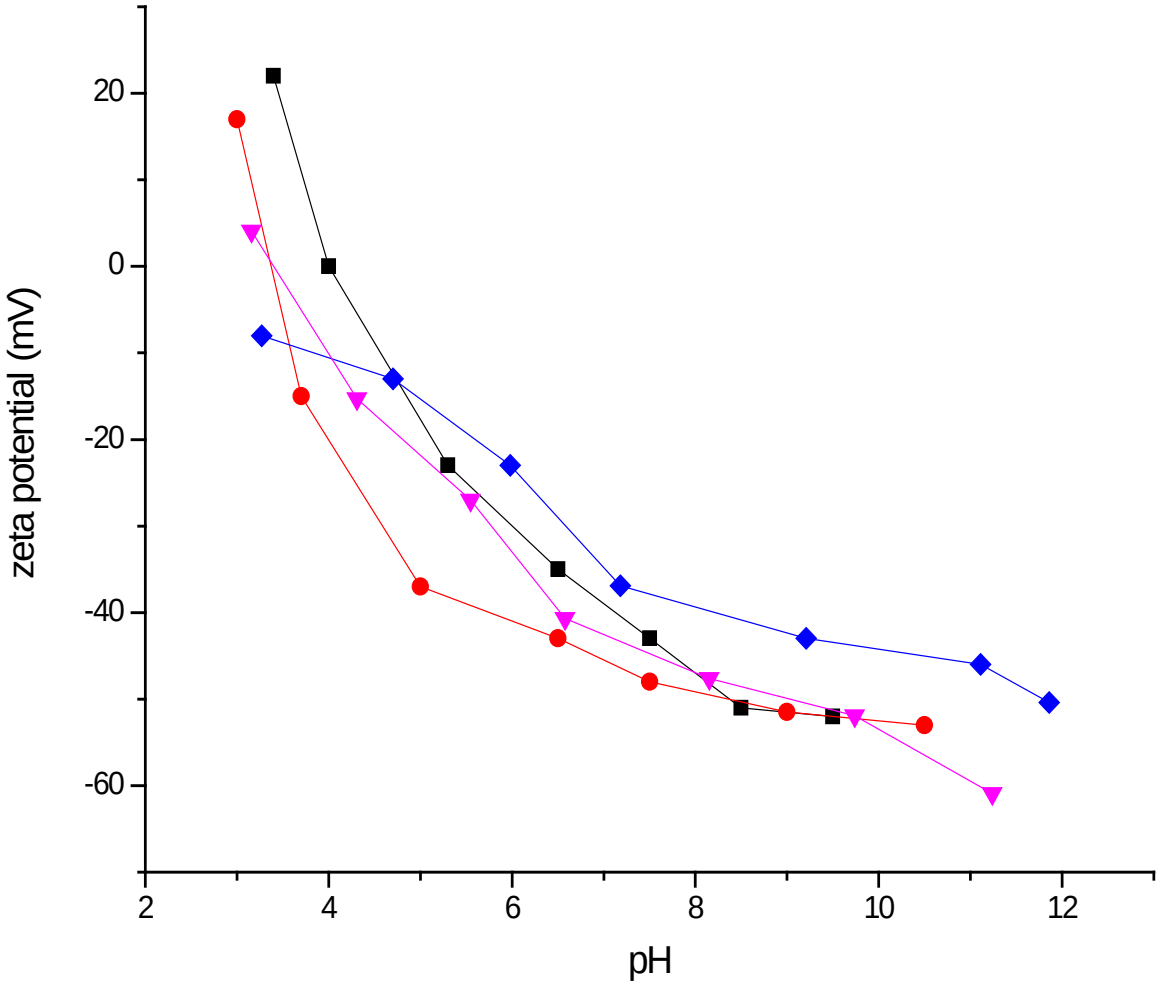

Figure 4.19 Zeta potential of the iron/aluminum hydroxide co-precipitated colloids or post-precipitated with phosphate as a function of pH. (■) post-precipitated iron hydroxide colloid with phosphate (ref[159]), (●) co-precipitated iron hydroxide colloid with phosphate (ref[159]), (◆) post-precipitated aluminum hydroxide colloid with phosphate, (▼) co-precipitated aluminum hydroxide colloid with phosphate.

4.15 CFT of phenol tip against iron/aluminum (hydro)xide colloidal particles modified with GA

The CFT of phenol tip against GA modified iron hydroxide colloids (Fig. 4.20) and aluminum hydroxide colloids (Fig. 4.21) provide much more instructive data than those of the phosphate colloids.

Figure 4.20 shows that the chemical force titration curves of phenol tip against iron (hydro)xide colloids modified with GA. For co-precipitated iron (hydr)oxide with GA, the maximum adhesion force was approximately 18 nN centered at pH ≈ 5.2. Above pH 7, the adhesion force fell to zero. For the post-precipitated iron (hydr)oxide with GA, a maximum adhesion force of approximately 10 nN is centered at pH ≈ 9, adhesion force gradually reduced in the pH range of 8 to 10. Outside this pH range , the adhesion force was close to zero.

The zeta potential of post-precipitated iron (hydro)xide colloids with GA as a function of pH are also shown in Figure 4.20 as an inset, reproduced from reference[159]. The PZC has been determined to be approximately 2.5. Only when the pH is lower than 2.5, is the surface of the GA modified FeO(OH) colloids positively charged. Thus, in the pH range of force titrations (3 to12), the surface of post-precipitated iron (hydro)xide colloids with GA became increasingly negatively charged with increasing pH. For co-precipitated iron (hydr)oxide in the pH range of 3 to 12, it is always negatively charged.

The maximum of the chemical force titration curve of the phenol tip against GA co-precipitated iron (hydr)oxide suggests that the surface binding groups are benzoate groups. The benzoic group has a pK_a of 4.26.[63] Thus the ionic hydrogen bonding between benzoate and phenolic groups can be formed in the pH 4 to 7 range, consistent with the maximum adhesion force centered at pH ≈ 5.2.

By contrast, the chemical force titration curve of the phenol tip against GA post-precipitated iron (hydr)oxide suggests that the surface binding groups are phenolic groups. The phenolic groups of gallic acid have a first pK_a of 8.70 and a second pK_a of 11.45.[63] The maximum number of ionic H bonding between phenolic groups occurring in the pH 8 to 10 range is consistent with the first pK_a of phenolic groups of GA. It is presumably caused as the first associated hydroxyl groups of GA dominate the adhesion interaction between the phenol tip and GA modified iron (hydr)oxide colloids. In addition, there was no adhesion force found in the pH range of 6.5 to 8 for post-precipitated colloids. This demonstrates that the surface of substrate was fully covered by the molecules of GA, so the binding site of iron (hydr)oxide could not form any ionic hydrogen bonding with the phenol tip.

The chemical force titration experiment demonstrates that the molecule of GA switched adsorption functional group between the two modification methods. In the high surface loading method (co-precipitated method), the surface binding groups of GA are the phenolic group; in the low surface loading method (post-precipitated method), the surface binding groups of GA are benzoate groups.

Figure 4.21 shows that chemical force titration profile of phenol tip against aluminum (hydro)xide colloids modified with GA. For aluminum (hydr)oxide co-precipitated with GA, the maximum adhesion force was approximately 23 nN centered at pH ≈ 9. The adhesion force is gradually increases and decreases in the broad pH range of 4 to 11, and outside this pH range, the adhesion force is close to zero. For the aluminum (hydr)oxide post-precipitated with GA, the maximum adhesion force approximately 10 nN centered at pH ≈ 9, with the adhesion force gradually increases and decreases in the pH range of 8 to 10. Outside this pH range, the adhesion force was close to zero.

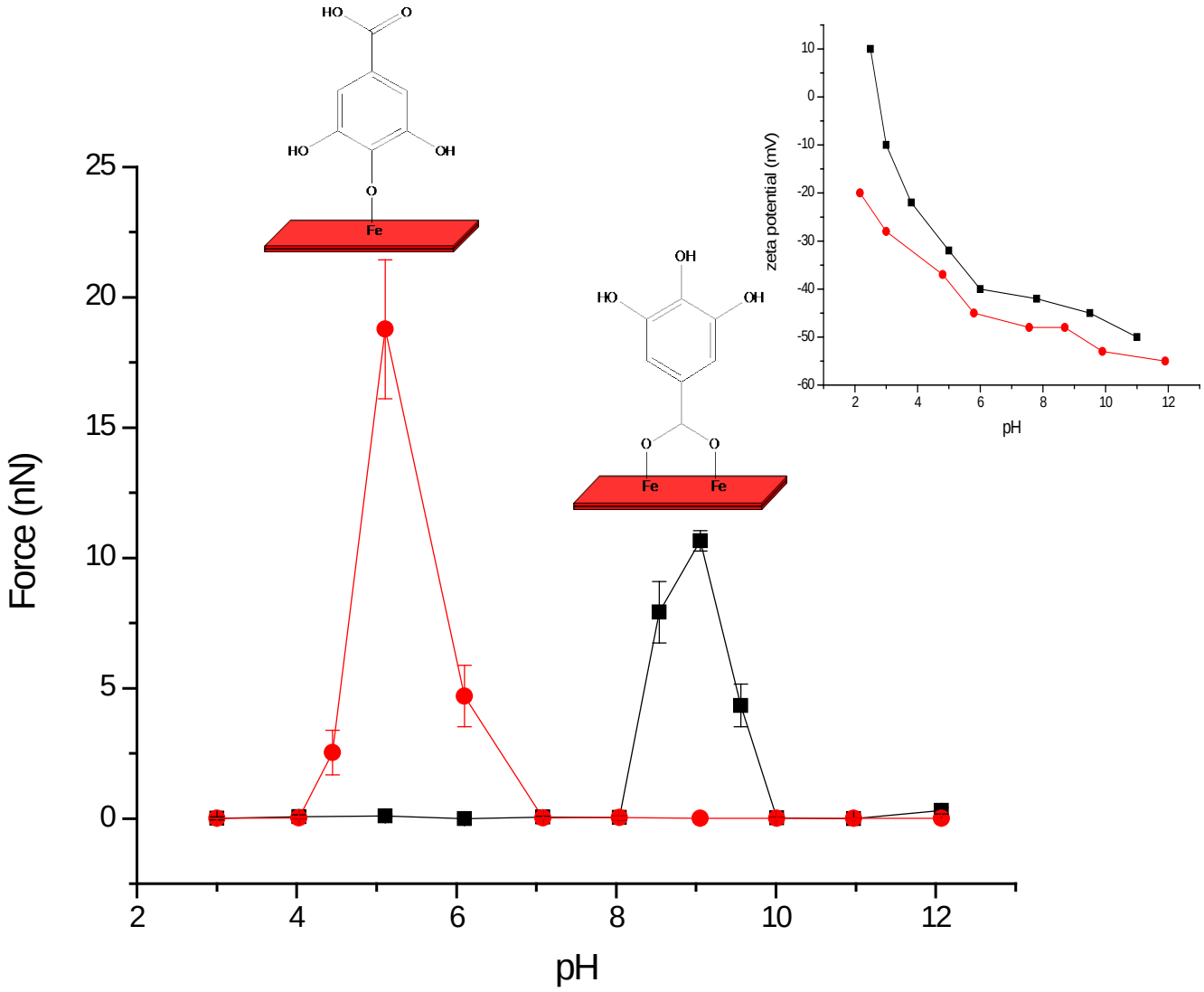

Figure 4.20 Chemical force titration curves showing the adhesion force as a function of pH between a phenol-terminated AFM tip and iron hydroxide substrates that were (■) post-precipitated, (●) co-precipitated with GA. The error bars represent the standard deviation in the adhesion force as measured from the average of 150-200 force-distance curves. The inset shows the zeta potential of the GA modified colloids as a function of pH, (■) post-precipitated (ref[159]), and (●) co-precipitated with GA.

The zeta potential of GA modified aluminum (hydr)oxide colloids as a function of pH is also shown in Figure 4.21 as an inset. It demonstrates that both co-precipitated and post-precipitated GA modified aluminum (hydr)oxide colloids are amphoteric. The PZC of co-precipitated and post-precipitated GA modified aluminum (hydr)oxide colloids has been respectively determined to be approximately 6 and 4. These are both shifted to lower pH values than unmodified colloid. In addition, the zeta potential data (the inset to Fig. 21 and 22) indicate that co-precipitated colloids have a lower point of zero charge, consistent with the surface being dominated by more strongly acidic functional groups, which is consistent with the CFT results.

The chemical force titration curve of phenol tip against co-precipitated aluminum (hydr)oxide with GA shows the adhesion forces are significant over a broad pH range (4 to 11). It suggests that the surface binding groups are a combination of phenol groups and benzoate groups. The former has a pK_a of 4.26 and the latter a first pK_a of 8.70 and a second pK_a of 11.45.[63] The combination of these two functional groups are consistent with the adhesion force, being significant over a broad pH range of 4 to 11, at which the maximum number of ionic H bonding occurs. The force in the pH range of 8 to 9 (15 nN to 23 nN) are greater than the force in the pH range of 5 to 6 (6nN to 3nN). It suggests that the number of the surface phenol binding groups is larger than the number of the surface benzoate binding groups. In other words, in the co-precipitated colloid, the molecules of GA are more prone to interact with the surface binding sites (Al-OH) though benzoate groups, even though the interaction with the surface binding sites (Al-OH) though phenol groups is also significant. Thus, binding of GA to the surface of co-precipitated aluminum (hydr)oxide colloids will be through the benzoate and phenolic group of GA molecule. This is in contrast to that the iron (hydr)oxide colloids which has evidence for adsorption only though the phenol group.

The maximum of the chemical force titration curve of the phenol tip against post-

precipitated GA modified aluminum (hydr)oxide colloids suggests that the surface binding groups are phenolic groups. The maximum number of ionic H bonding between phenolic groups occurring in the pH 8 to10 range is consistent the first pK_a of phenolic groups of GA. Similar to GA modified iron (hydr)oxide colloids, it is presumably caused as the first associated hydroxyl groups of GA dominates the adhesion interaction between the phenol tip and GA modified aluminum (hydr)oxide colloids. Thus, binding of GA to the surface of post-precipitated aluminum (hydr)oxide colloids will be through the benzoate functional group of GA molecule. By contrast, the maximum adhesion force of phenol tip against co-precipitated GA modified aluminum (hydr)oxide colloids is over twice as high as the maximum adhesion force of phenol tip against post-precipitated GA modified aluminum (hydr)oxide colloids (23nN vs. 11nN). These observations are consistent with the co-precipitated aluminum (hydr)oxide particles having a higher surface GA loading than the post-precipitated species.

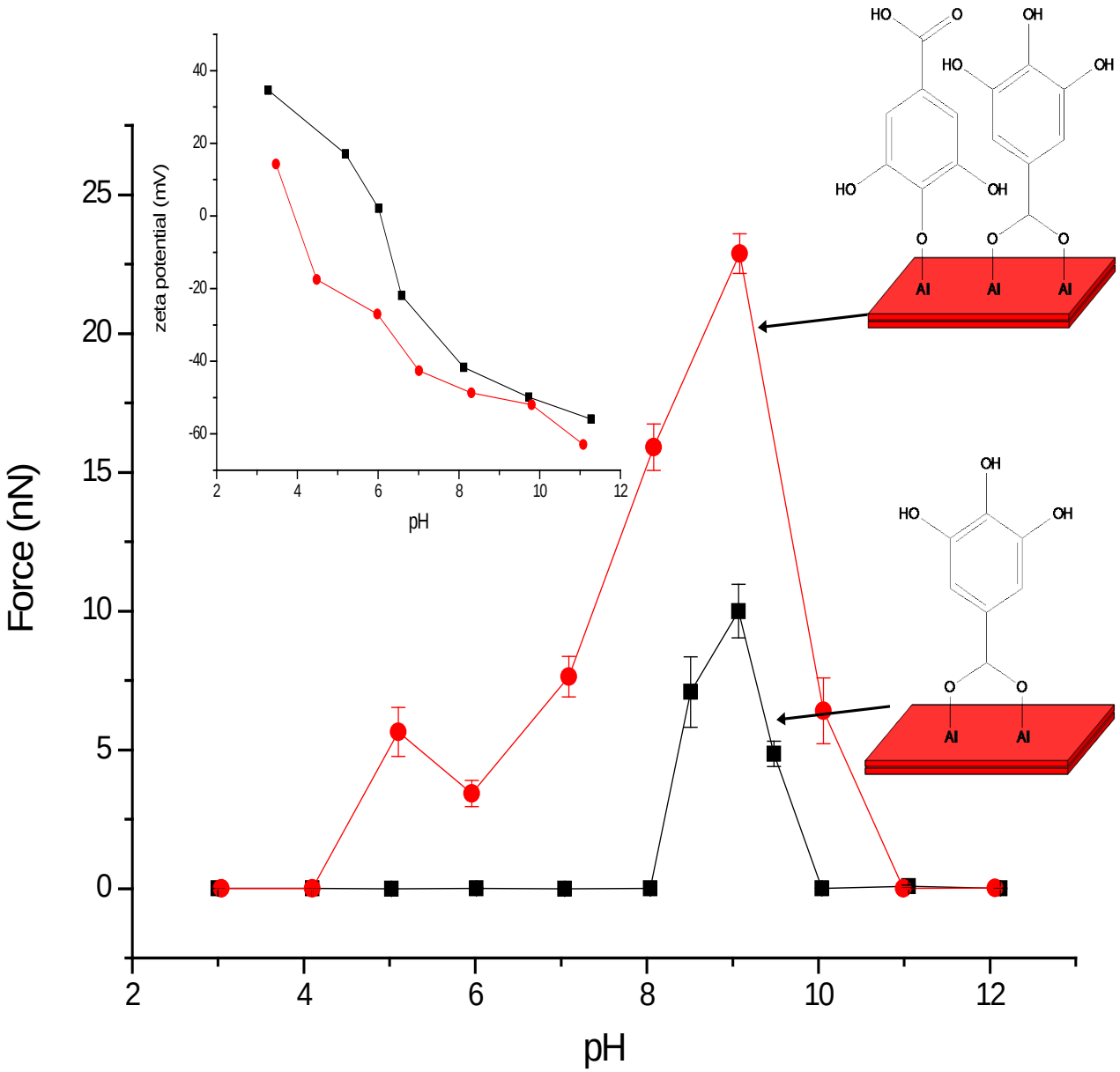

Figure 4.21 Chemical force titration curves showing the adhesion force as a function of pH between a phenol-terminated AFM tip and aluminum hydroxide substrates that were (■) post-precipitated and (●) co-precipitated with GA. The error bars represent the standard deviation in the adhesion force as measured from the average of 150-200 force- distance curves. The inset shows the zeta potential of the GA modified colloids as a function of pH, (■) post-precipitated and (●) co-precipitated with GA.

4.16 CFT of phenol tip against iron/aluminum (hydro)xide colloidal particles modified with TA

TA contains a mixture of related compounds, containing saccharide and aromatic as well as $-COO^-$ and phenolic -OH groups. It represents a more complicated model to study the interactions between the NOM and iron (hydr)oxide than GA. It has been used as a model compound for soluble organic matter in studies on water treatment[16, 17] as well as in studies on soil science since it is similar in some ways to soluble fulvic acid.

The chemical force titration curves of phenol tip against FeO(OH) and AlO(OH) colloids which were co-precipitated or post-precipitated with TA are respectively shown in Figure 4.22 and 4.23. As seen in the curves, the chemical force titration of phenol tip against co-precipitated and post-precipitated iron or aluminum (hydr)oxide with TA shows adhesion forces are weak as compared to the unmodified or GA modified iron (hydr)oxide colloids.

In addition, the ξ potential measurements demonstrate that TA post-precipitated modified iron hydr(oxide) are amphoteric. The point of zero charge (PZC) of it has been determined to be approximately 4.0 (Figure 4.24), somewhat higher than post-precipitated GA modified iron hydr(oxide). For co-precipitated aluminum (hydr)oxide in the pH range of 3 to 12, it is always negatively charged as shown in Figure 4.24. The zeta potential measurements demonstrate that TA modified aluminum (hydr)oxide colloids are negatively charged throughout this pH range.

The chemical force titration experiments can demonstrate that TA coating also blocks surface binding sites on the surface of iron/aliminum oxide to phenolic groups. This result is somehow difficult to understand as the TA is a strongly hydrophilic organic acid. However, TA is a more complicated model to study the interactions between the NOM and iron (hydr)oxide than GA. The small interactions are presumably caused as we focused on the system containing

one phenol site, which has not very strong interactions with the substrate, or the SAM on the AFM tip was somehow disordered as it is close to the surface of substrate.

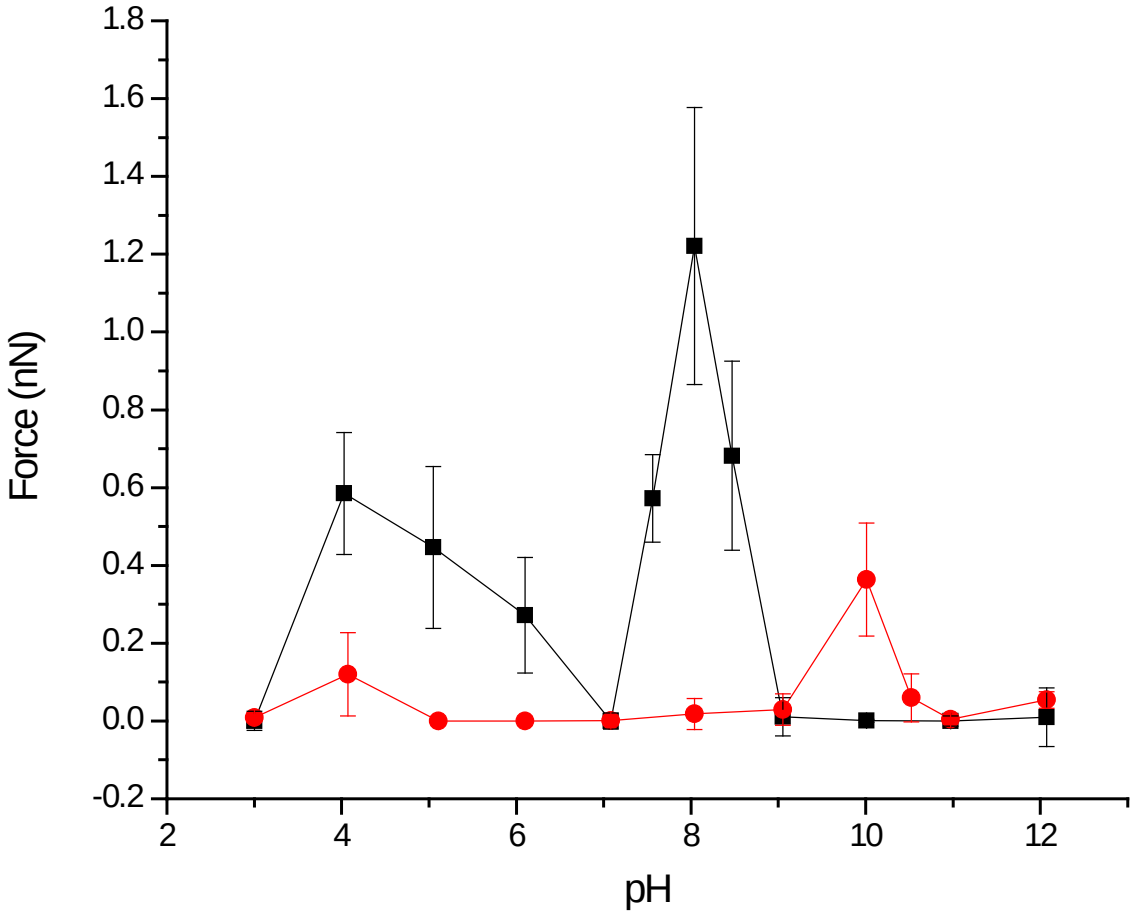

Figure 4.22 Chemical force titration curves showing the adhesion force as a function of pH between a 4-(12-mercaptododecyl) phenol-terminated AFM tip and iron (hydro)xide substrates that were (●) post-precipitated and (■) co-precipitated with TA. The error bars represent the standard deviation in the adhesion force as measured from the average of 150-200 force distance curves. Co-precipitated and post-precipitated aluminum (hydro)xide colloids with TA.

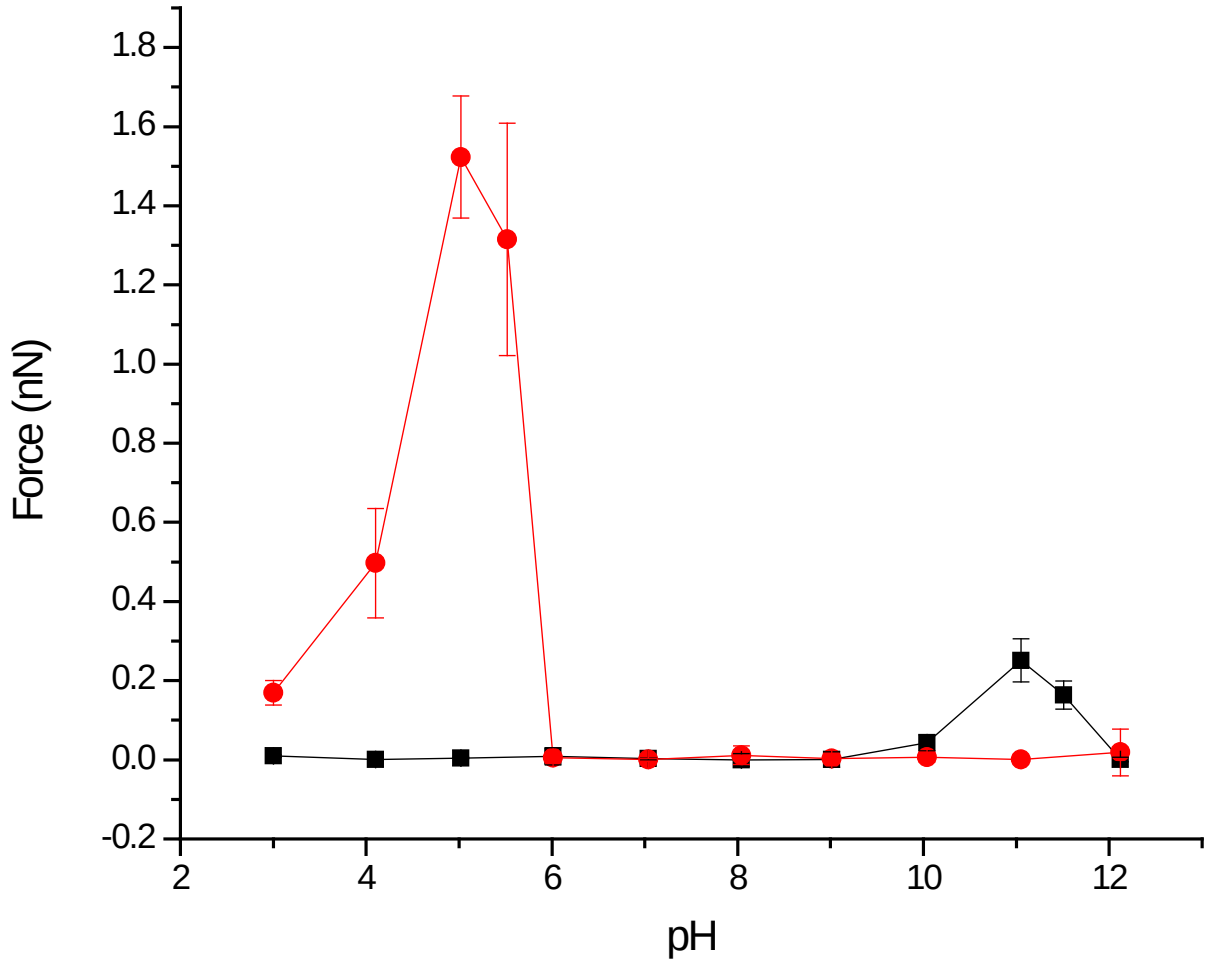

Figure 4.23 Chemical force titration curves showing the adhesion force as a function of pH between a 4-(12-mercaptododecyl) phenol-terminated AFM tip and aluminum (hydro)xide substrates that were (●) post-precipitated and (■) co-precipitated with phosphate with TA. The error bars represent the standard deviation in the adhesion force as measured from the average of 150-200 force distance curves. The inset shows the ξ potential of the post-precipitated colloids as a function of pH.

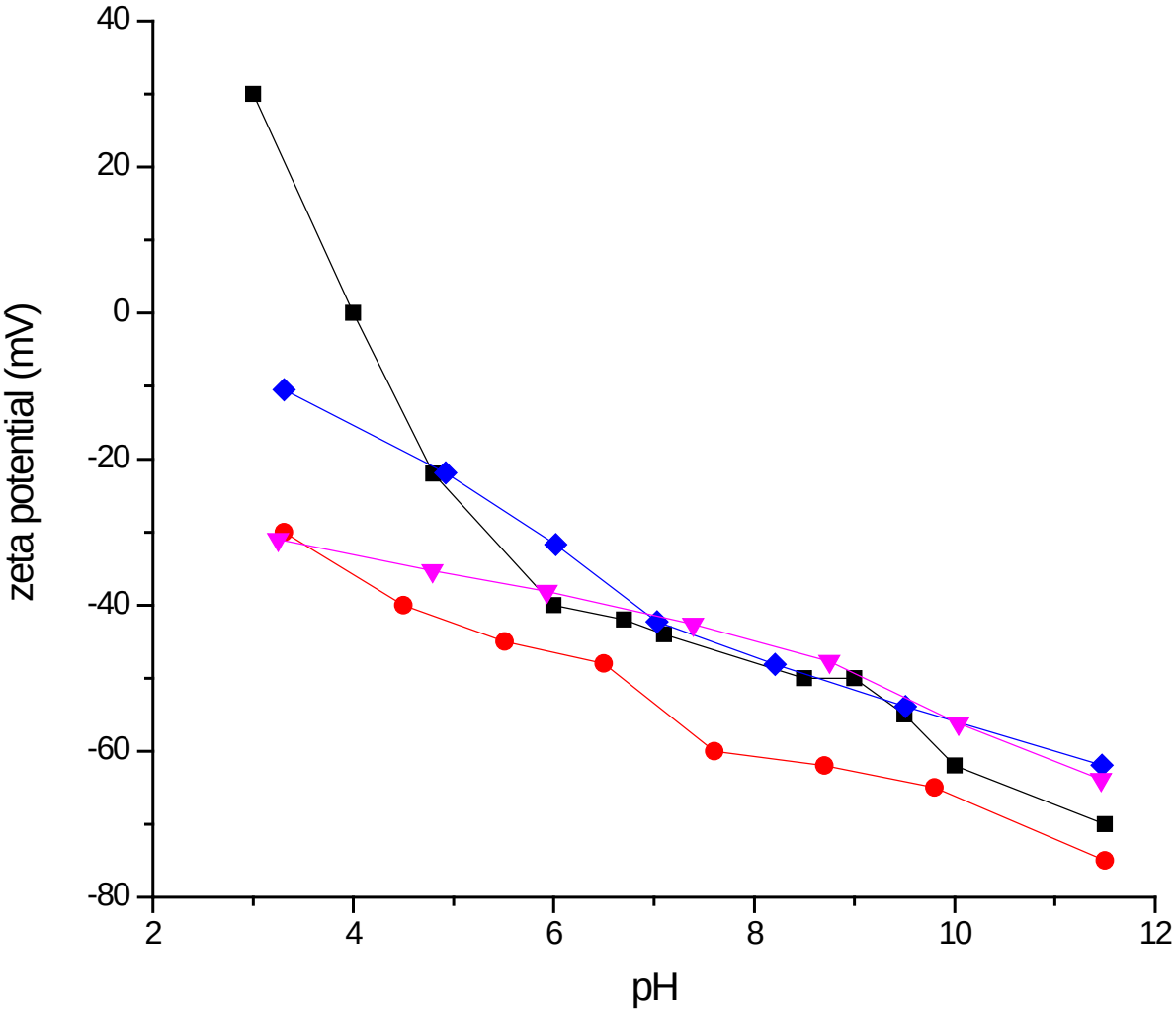

Figure 4.24 Zeta potential of the iron/aluminum hydroxide co-precipitated colloids or post-precipitated with TA as a function of pH. (■) post-precipitated iron hydroxide colloid with TA (ref[159]), (●) co-precipitated iron hydroxide colloid with TA, (◆) post-precipitated aluminum hydroxide colloid with TA, (▼) co-precipitated aluminum hydroxide colloid with TA.

Conclusions

The phenol self-assembled monolayer was characterized by several techniques. ATR-FTIR demonstrated that the molecules of 4-(12-mercaptododecyl) phenol were deposited with the OH

group exposed to the solution phase. CFT was used to determine a surface $pK_{1/2}$ (pH 8.5) for the self-assembled monolayer of 4-(12-mercaptododecyl) phenol. XPS confirmed that the surface was covered with SAM without any other contamination.

CFT was used to study the adhesion force between phenol-terminated AFM tip and various iron/aluminum hydr(oxide) colloidal particles which were modified by phosphate, GA or TA. The results of CFT experiments support the following conclusions:

1. The formation of strong ionic hydrogen bonding, between phenol and all oxo Fe-OH surface sites at higher pH and between phenol and protonated Fe-OH sites at lower pH dominate the adhesion force interactions of the phenol-terminated tip against the iron hydroxide colloid surface.

2. Similarly, strong ionic hydrogen bonding between phenol and Al-OH surface sites in the pH range of 9 to 11 and 3 to 7 dominate the adhesion force interaction of the phenol-terminated tip against the surface of aluminum hydroxide colloid.

3. Adsorption of phosphate anions or TA blocks surface binding sites on both colloids to phenol groups.

4. GA switches the adsorption functional geometry depending on precipitation method. In the high surface loading (co-precipitation method), the phenol groups of GA bind to the surface of iron oxide; in the low surface loading method (post-precipitation method), the benzoate groups of GA bind. The CFT of the phenol tip against the GA modified aluminum oxide colloids gave similar results, though on the co-precipitated colloids evidence was seen for GA binding through both phenolic and benzoic groups.

Chapter 5

Fluorinated PDMS in the Application of Microfluidic Devices

Experimental Procedure

5.1 Fabrication and surface modification of the PDMS microchannel chip

Sylgard 184 PDMS prepolymer and its cross-linking agent (Dow Corning, Midland, MI, USA) were mixed at 10:1 (w/w) and degassed by a vacuum desiccator. Then, the mixture (20g) was poured onto a petri dish with capillary columns (164 μm o.d.) on the bottom that had been fixed in advance. After curing in a 65 ˚C oven for 4 h, the PDMS layer was peeled off from the petri dish. Then, this patterned PDMS microfluidic substrate was cut into channel plates 9 cm in length by 2 cm in width to form the microfluidic channel plate. PDMS cover plates were prepared in the same manner as the channel plates, except there were no capillary columns fixed at the bottoms of the petri dish. Then, using a borer, two holes (4mm diameter) were drilled in each cover, separated by 8 cm, which became the inlet and outlet of the microfluidic channel.

The PDMS microfluidic channels and unpatterned covers were treated using an air plasma generator (Harrick Scientific Corporation, Ossining, NY) for varying times according to the requirements of the experimental run (10.2 W, 10 MHz rf level at 400 millitorr). Then, the freshly-oxidized PDMS substrate and cover were immediately immersed in a 4mmol solution of nonafluorohexyltriethoxysilane (PF6) (Gelest, Inc.) 1H,1H,2H,2H-perfluorooctyltriethoxysilane (PF8), 1H,1H,2H,2H-perfluorodecyltriethoxysilane (PF10), or 1H,1H,2H,2H-perfluorododecyltriethoxysilane (PF12) in perfluorodecalin solvent (SynQuest Laboratories, Inc.) for 10 hrs, then washed with ethanol and dried in a stream of nitrogen (ultra high purity). A schematic of this process is shown in Figure 5. 1. The cover and microchannel could be sealed without any adhesive if the modification process occurred in PFD solvent. The self-sealing was

unsuccessful when PDMS substrates were modified in toluene.

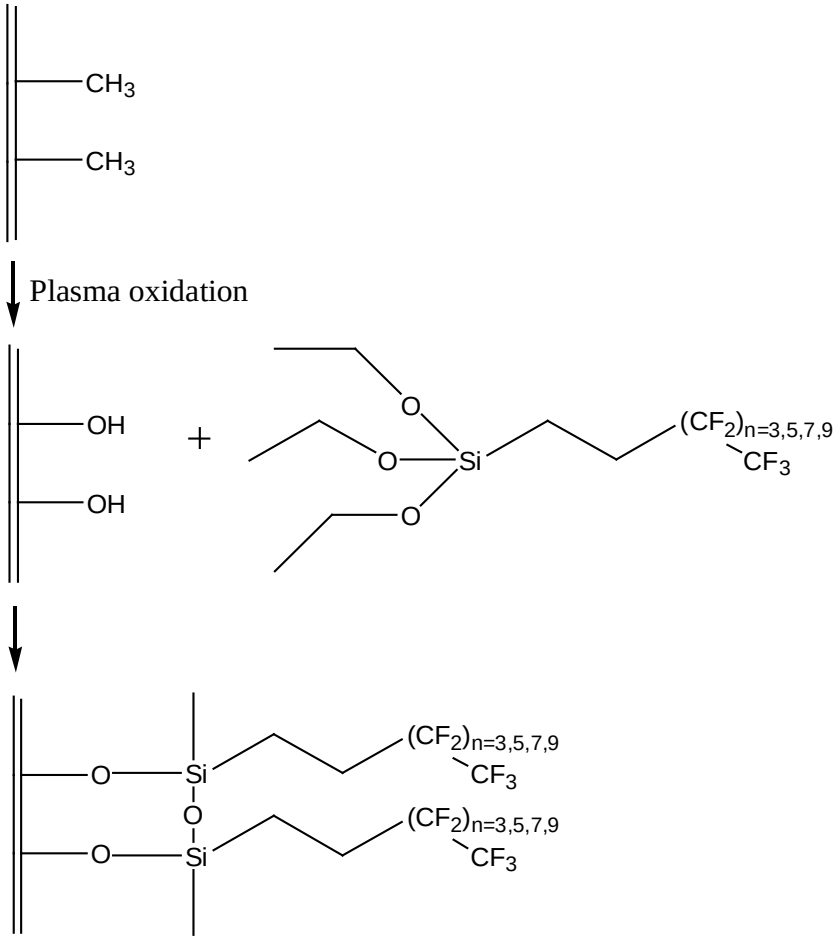

Figure 5.1 Schematic of grafting perfluoroalkyl triethoxysilanes onto the PDMS surface.

5.2 ζ-potential measurement

Zeta-potential measurements were performed via the measurement of the velocity of electro-osmotic flow (EOF) by monitoring the EOF current vs. time. When an electrolyte flows under an applied electric field through a microchannel, whose wall has a surface charge, the excess charge in the diffuse region of the electrical double layer (EDL) will move towards the electrode of opposite polarity, dragging the surrounding liquid molecules in the same direction due to viscous

effects. This is referred to as electro-osmotic flow. In microfluidics, the velocity of the EOF (μ_{eof}) can be expressed by the Helmholtz-Smoluchowski equation [142]:

$$\mu_{eof} = \frac{\varepsilon E_Z \zeta}{\mu}$$

where E_z is the applied electric field strength, ζ is the zeta potential at the interface, μ is the solution viscosity, and $\varepsilon = \varepsilon_0 \varepsilon_r$ is the product of the dielectric constant of a vacuum ($\varepsilon_0 = 8.854 \times 10^{-12}$ F/m), and ε_r , the relative permittivity.

The measurement of the ζ-potential of the micro channels was performed using current-time monitoring with a microfluidic tool kit (Micralyne, Edmonton, Alberta). The microchannels were first filled with a phosphate buffer solution (30 mmol/L). Phosphate buffer was prepared from stock solutions (30 mmol/L) of monobasic, dibasic potassium phosphate, phosphate acid and potassium phosphate. The inlet buffer (see schematic, Figure 5.2) was emptied and filled with a lower ionic-strength phosphate buffer solution (28.5 mmol/L). Platinum electrodes were immediately placed in the inlet and outlet. Finally an electric field (strength E = 0.5 kV-1 kV) was applied and current was monitored as a function of time. As the concentration of solution at inlet was 95% of that at the outlet, the observed current would gradually decrease until the solution with lower concentration filled in the whole channel (Figure 5.2). A small concentration difference (5%) was used in this work so that the changes in the electrical double layer (EDL) would be negligible, which could lead to electrokinetically generated pressure gradients.[167, 168] As the electroosmotic flow velocity is a function of concentration, the experimental electroosmotic flow velocity is approximately equal to electroosmotic flow velocity that takes place at the average of solution concentrations of inlet and outlet.

The electroosmotic flow velocity μ_{eo} could be measured simply by measuring the time, t,

taken to flow down the known length, L, of the channel (Figure 5.2).

$$\mu_{eof} = \frac{L}{t}$$

In this work, the measured value of the ζ potential was determined at least three times for each data point. It was repeatable within ± 5%.

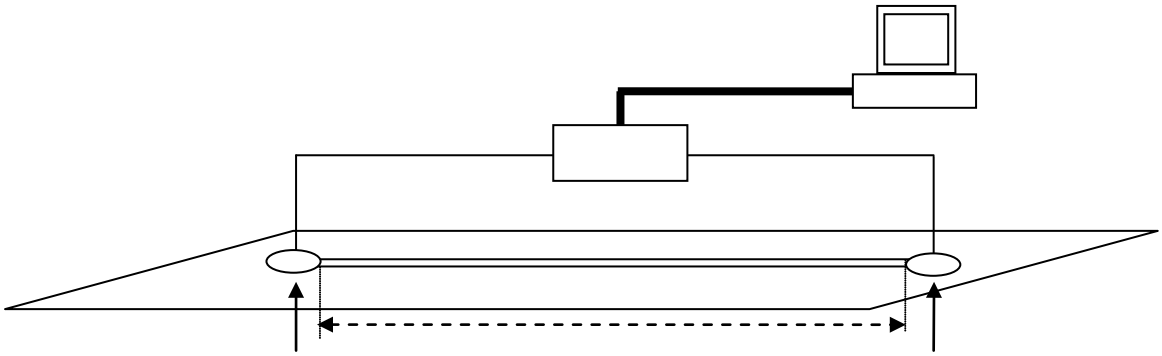

Figure 5.2 Schematic of the experimental setup used to measure the current variation as a function of time to complete displacement for a two-concentration system during electroosmosis.

5.3 Contact angle measurements

Contact angles were measured using a VCA optima (AST Products, Inc.) system. A 1μL drop of deionized water was placed on the substrate, and static contact angles were measured on both sides of the drop. The contact angles were measured at least three distinct spots on every sample, and the reported values represent the average and standard deviation of the measurements.

5.4 X-ray photoelectron spectroscopy

X-ray photoelectron spectroscopy (XPS) was used to analyze the surface composition of unmodified, oxidized and fluorinated PDMS. The equipment setup and data process were described in above section 4.7. Rather than using a Mg Kα X-ray source (1253.6 eV) described in section 4.7, here we used Al Kα x-rays (1486.6 eV). XPS spectra were acquired from binding energy regions containing peaks arising from all elements expected on the samples: C 1s, O 1s, F 1s, and Si 2p. A survey scan indicated that there were no other elements present on the sample surface beyond those listed. The PDMS samples used in XPS analyses were prepared using the same prepolymer, curing agent and modification process as noted above.

5.5 AFM images

The AFM topographic images were acquired in the tapping mode of the Veeco multimode microscope equipped with a Nanoscope Ⅲa controller. The tips used were standard Si_3N_4 tips (a radius of curvature typically less than 5 nm) with a resonance frequency of 100 kHz. Height images were recorded at scan rates of 1–2 Hz.

Results and Discussion

5.6 Optimization of oxidation time and solvent concentration for the modification using PF8 in perfluorodecalin

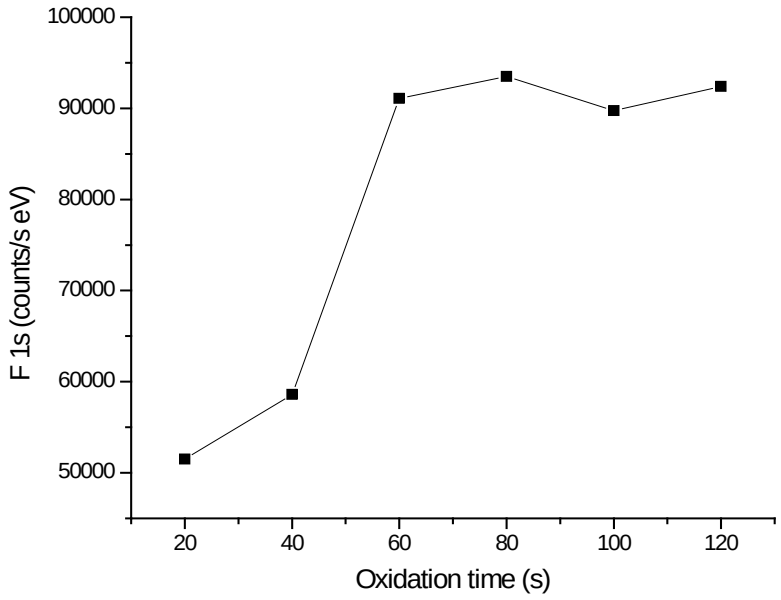

Figure 5.3 Plot of peak area of XPS F1s (at 689 eV) of PF-8 modified PDMS as a function of oxidation time (s) of PDMS at plasma energy of 10.2 W and 40 millitorr of Air.

To confirm that the surface of PDMS was efficiently oxidized for the next step in the grafting process, different oxidation exposure times were carried out prior to grafting of the PF-n species. Figure 5.3 shows the F 1s peak area for oxidized surfaces exposed to a 2 mmol solution of PF-8 in perfluorodecalin. The F 1s signal shows no significant increase for oxidation times greater than 60 s. Thus 60s was used as an oxidation time.

Due to the fact that oxidized PDMS quickly recovers its hydrophobic properties, the concentration of PF-n in solution might also determine the overlayer coverage on the surface because the dynamic process of overlayer formation competes with the diffusion of hydrophobic

oligomers to the surface of the oxidized PDMS. Thus, different concentrations of PF-8 in perfluodecalin were used to form an overlayer on freshly oxidized PDMS substrates (oxidization time 60s). The peak area of F 1s (at 689 eV) of each modified sample was plotted as a function of the concentration of PF-8 (Figure 5.4). Figure 5.4 indicates that a 4mmol concentration of PF-8 in perfluorodecalin is effective for the overlayer formation process and any concentration higher than this value has no significant effect on the increase of F surface concentration.

The XPS C 1s of PF8 modified PDMS in perfluorodecalin signal can be fitted as four peaks for both samples, which correspond to C in different chemical environments (Figure 5.5): The terminal CF_3 group (294.8 eV); CF_2 (292.0 eV); and the methylene spacer group -$(CH_2)_2$- (286.9 eV). In addition, the C 1s signal at 285.0 eV represents the methyl groups of PDMS.

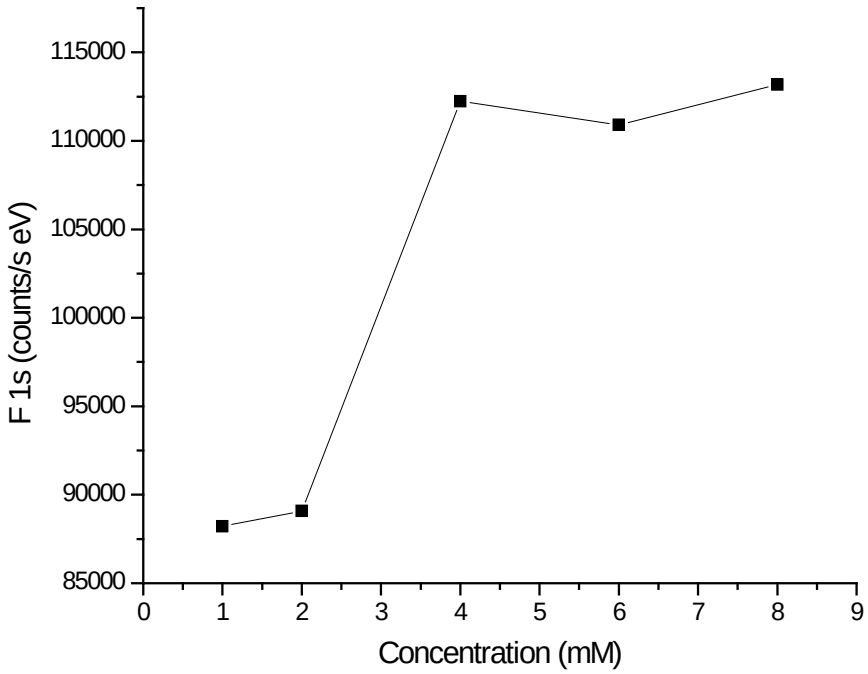

Figure 5.4 A plot of peak area of the F1s signal at 689 eV for PF-8 modified PFMS (oxidation 60s) as a function of concentration of PF-8 in perfluorodecalin.

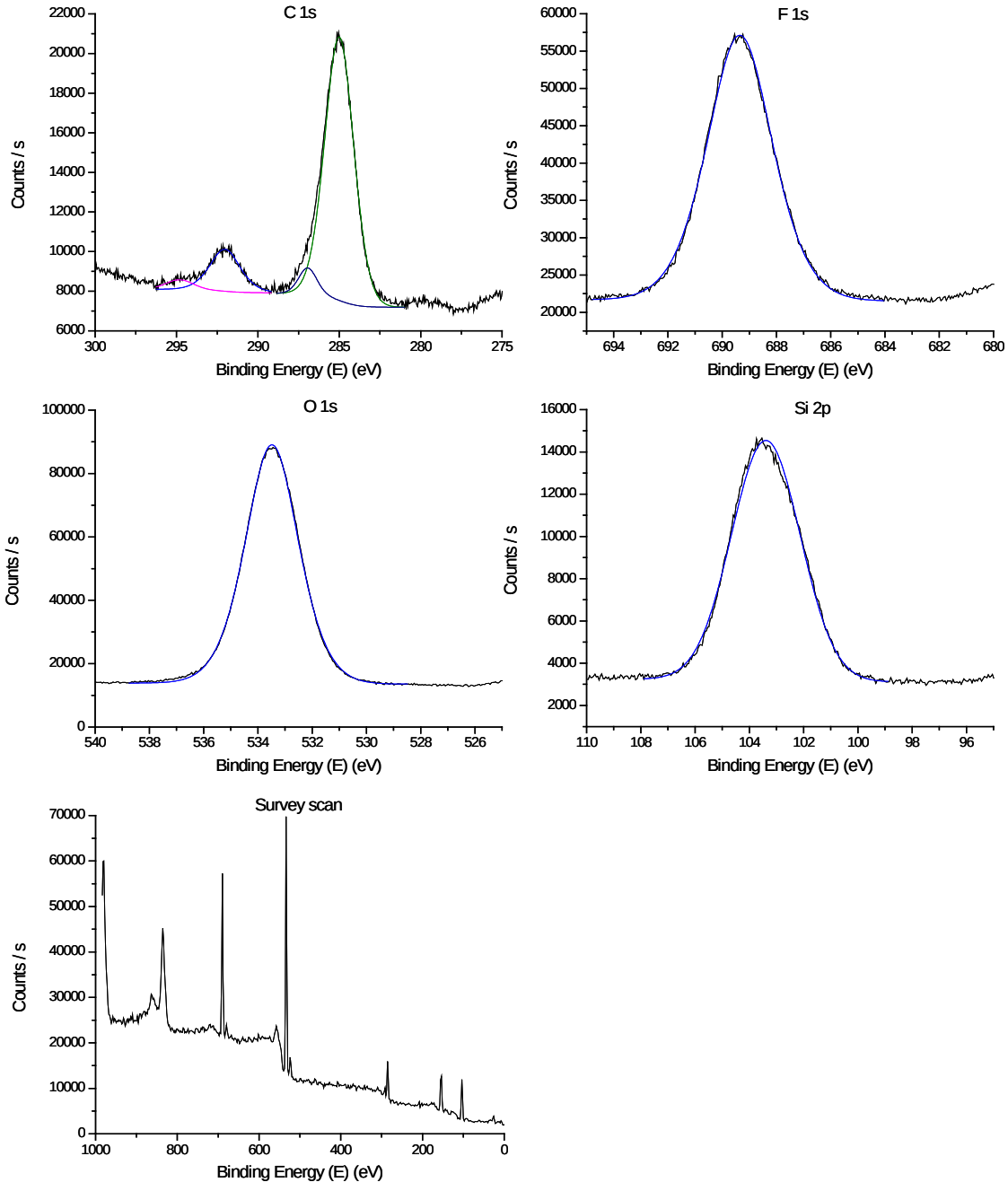

Figure 5.5 XP spectra of C 1s, F 1s,O 1s, Si 2p, and a survey scan (0 eV~ 1000eV) of PF8 modified PDMS in perfluorodecalin with oxidation time 60s PDMS at plasma energy of 10.2 W and 40 millitorr of Air.

The theoretical ratio of methylene peak (286.8 eV) to CF_3 (294.6 eV) is 2:1 from stoichiometry. The experimental ratio of these two carbon species is 1.80 for PF-8 modified PDMS in perfluorodecalin, slightly lower than the expected ratio and presumably caused due to electron attenuation as the methylene species lies at the base of the overlayer.

5.7 PDMS oxidation

The contact angle (Fig. 5.6) of freshly oxidized PDMS ($39.6 \pm 0.8^{\circ}$) is much less than that of unmodified PDMS ($109.5 \pm 0.3^{\circ}$), again consistent with the formation of surface hydroxyl groups.

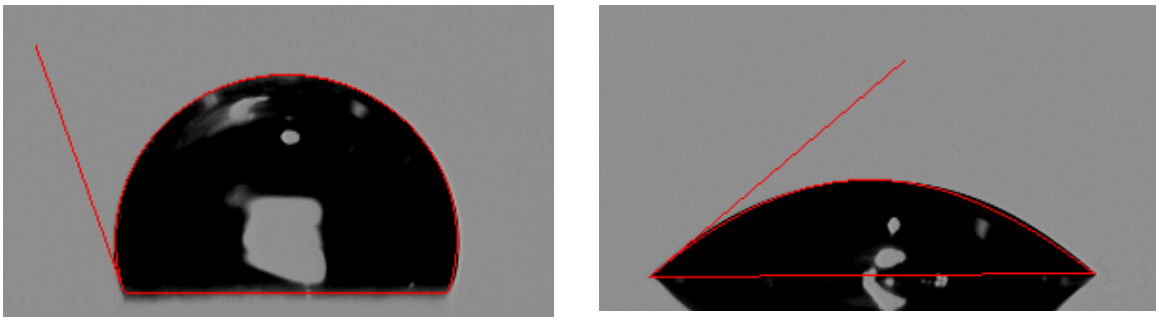

Figure 5.6 The contact angle measurements of (a) native PDMS ($109.5 \pm 0.3^{\circ}$) and (b) freshly oxidized PDMS ($39.6 \pm 0.8^{\circ}$).

AFM topographic images of native PDMS, freshly-oxidized PDMS and PF-8 modified PDMS in both toluene and perfluorodecalin are shown in Figure 5.7. The freshly plasma-oxidized PDMS demonstrates a pattern with higher surface roughness (R_{RMS}=2.90 nm) compared to bare PDMS (R_{RMS}=1.12 nm). There is general agreement that on the oxidized PDMS, surface silanol groups are formed due to the formation of a stiff SiO_x skin layer.[69] This is consistent with the XPS data: after plasma oxidation, the XPS surface percentage of O 1s and Si 2p signals increased, while the XPS surface percentage of C 1s area decreased. The rougher surface of oxidized PDMS is evidence of the high energetic bombardment of plasma particles during the oxidation process.

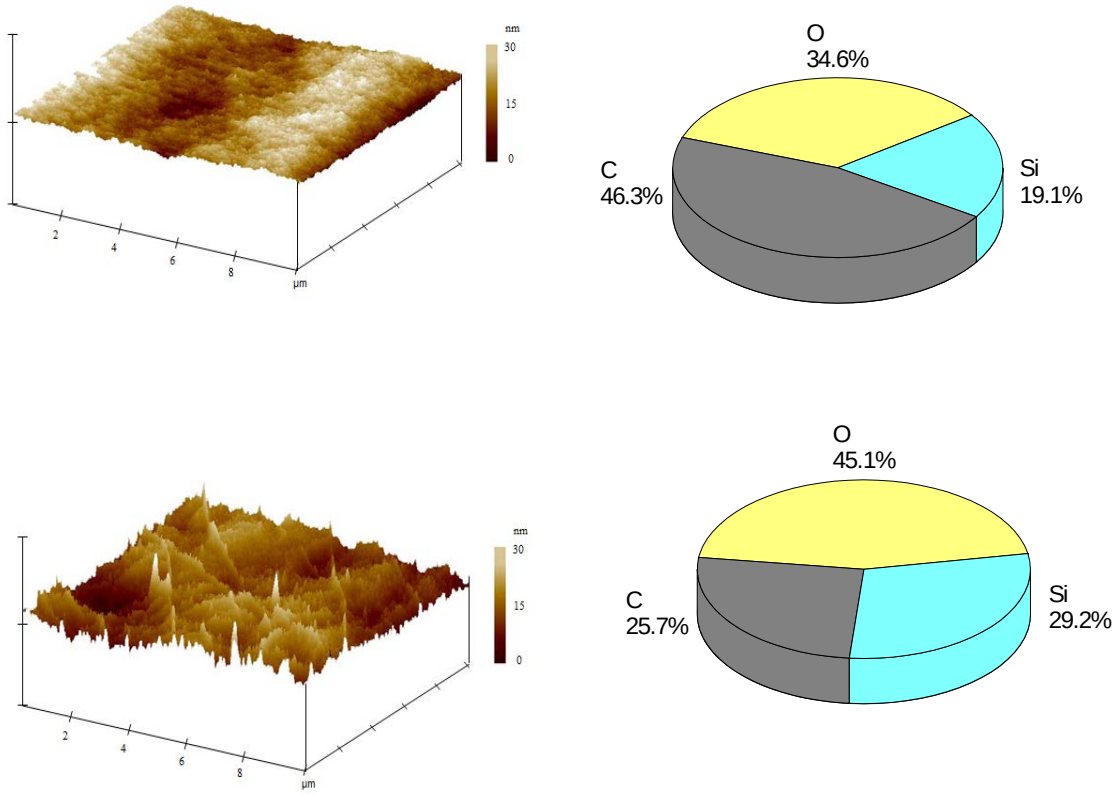

Figure 5.7 Topographic AFM images (10 µ m • 10 µ m) and surface percentage of O, C, Si elements from XPS of (a) bare PDMS (surface roughness parameter RRMS=1.12 nm) (b) freshly-oxidized PDMS (RRMS=2.90 nm)

5.8 Solvent effect

PDMS swells in most organic solvents due to high solubility. Following modification, PDMS can shrink to its original size during the drying process. This cycle of swelling and shrinking can be another factor to impact the surface properties after modification. Here, toluene was chosen to compare with perfluorodecalin to study the solvent effects. Toluene is a highly swelling solvent for PDMS, with a swelling ratio (S) of 1.31 ($S=D/D_0$, where D is the length of

material saturated with solvent and D_0 is the length of the dry material), and perfluorodecalin is a non-swelling solvent.[169]

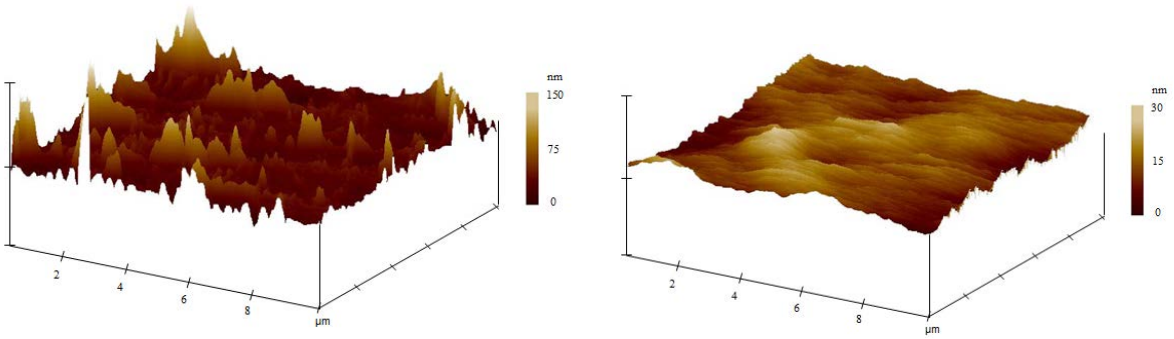

Figure 5.8 (a) PF8-PDMS modified in toluene (R_{RMS}=14.19 nm) and (b) PF8-PDMS modified in perfluorodecalin (R_{RMS}=2.69 nm).

The AFM topographic image of PF-8 modified PDMS in toluene clearly shows that it has much higher surface roughness (R_{RMS}=14.19 nm) compared to oxidized PDMS (R_{RMS}=2.90 nm). For PF-8 modified PDMS in perfluorodecalin, the surface roughness (R_{RMS}=2.69 nm) is comparable to that of oxidized PDMS. Taking the swelling ratio into consideration, the high surface roughness of PF-8 modified PDMS in toluene must be caused due to the swelling and shrinking cycle during modification.

XPS data shows that PF-8 modified PDMS in perfluorodecalin exhibits much stronger F 1s, O 1s or C 1s signals (1.3, 1.5, and 1.9 times respectively) than those observed when toluene is the solvent. Oxidized PDMS exposed to perfluorodecalin without PF-8 present was tested as a control. No relative changes in O 1s or C 1s signal were observed and only a trace of F 1s signal is observed.

The C 1s signal can be fitted as four peaks corresponding to C in different chemical environments: the terminal CF_3 group (294.6 eV); CF_2 (292.1 eV); and the methylene spacer group $-(CH_2)_2-$ (286.8 eV), and the C 1s signal at 285.0 eV represents the methyl groups of PDMS.

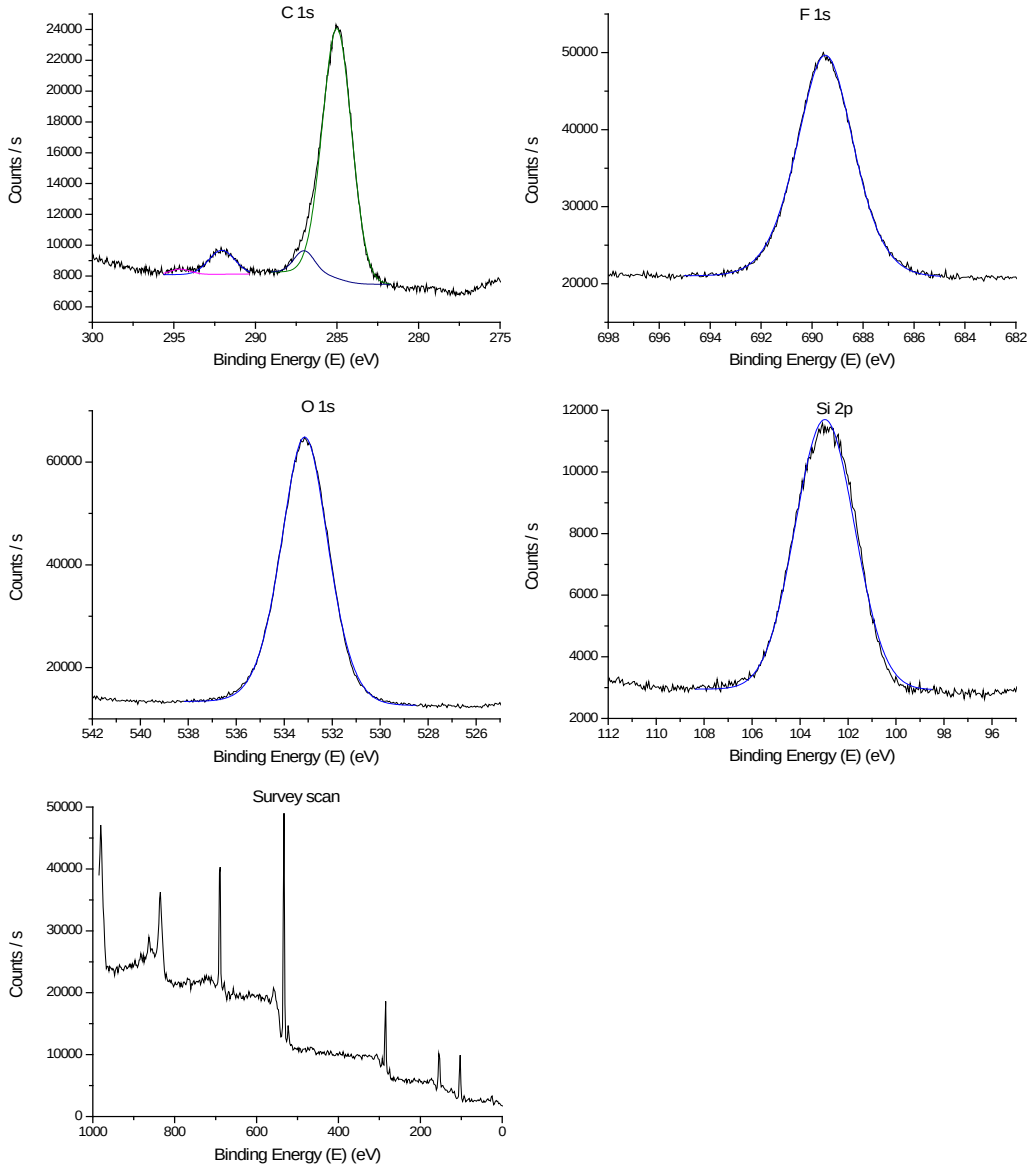

Figure 5.9 XP spectra of C 1s, F 1s,O 1s, Si 2p, and a survey scan (0 eV~ 1000eV) of PF8 modified PDMS in toluene with oxidation time 60s PDMS at plasma energy of 10.2 W and 40 millitorr of air.

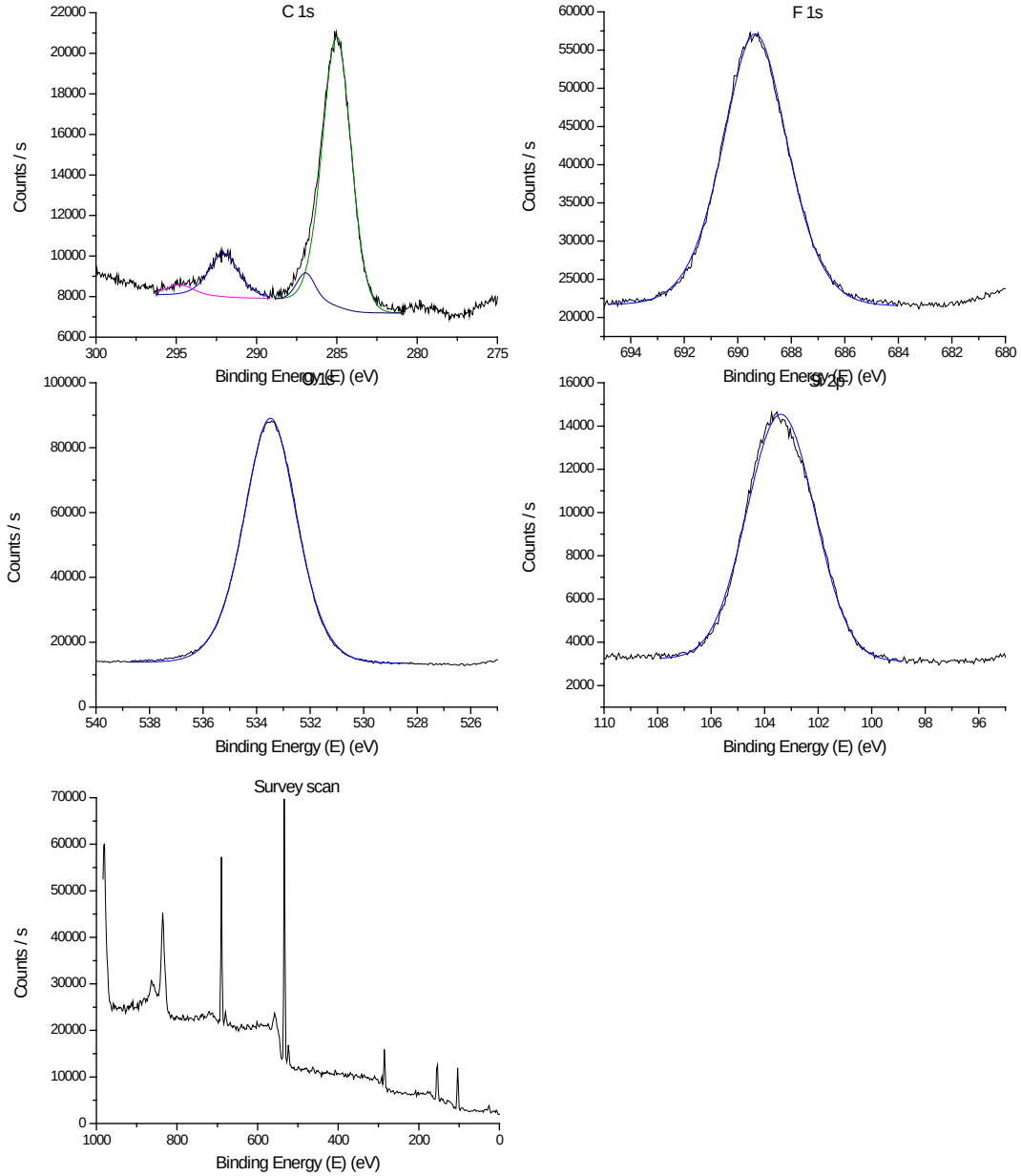

Figure 5.10 XP spectra of C 1s, F 1s,O 1s, Si 2p, and a survey scan (0 eV~ 1000eV) of PF8 modified PDMS in perfluorodecalin with oxidation time 60s PDMS at plasma energy of 10.2 W and 40 millitorr of air.

The C 1s ratio of methylene peak (286.8 eV) to CF_3 (294.6 eV) is 4, which is greater than the expected theoretical ratio (2) calculated from stoichiometry. This suggests that the overlayer of PF-8, when deposited in toluene, is sufficiently disordered such that the CF_3 head lies buried below the surface layer and its XPS signal is consequently attenuated relative to that of the methylene linker.

5.9 Surface characterization of fluorinated PDMS surfaces

Topographic images of PF-6, PF-10 and PF-12 modified PDMS in perfluodecalin are shown in Figure 5.11. These are similar to those of the PF-8 modified PDMS and also have decreased surface roughness compared to freshly oxidized PDMS. In addition, PF-6 modified PDMS has the lowest surface roughness compared to other modified surfaces.

The C 1s signals of the PF-6, PF-10 and PF-12 modified PDMS also can be fitted by four peaks, which is similar to that of the PF-8 modified surface. In addtion, the C 1s peak area ratio between the CF_3 signal at 294.6eV and methylene signal at 286.8 eV for each sample is close to the theoretical ratio (Table 5.1), consistent with the formation of a well-ordered layer on the PDMS surface.

Table 5.1 C 1s peak area ratio between C1s at 294.6eV ($-CF_3$) and C1s at 286.8 eV ($-CH_2-$) for PF-6, PF-8, PF-10 and PF-12 modified PDMS in perfluodecalin.

C 1s peak ratio (C1s at 294.6eV/C1s at 286.8eV)

Theoretical Ratio	Experimental Ratio			
2.00	PF6-PDMS	PF8-PDMS	PF10-PDMS	PF12-PDMS
	2.18	1.80	1.80	1.85

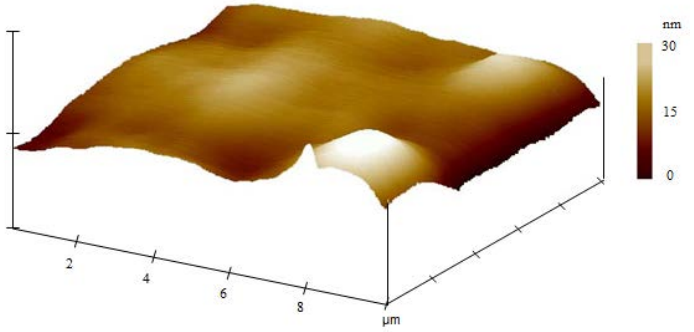

(a)

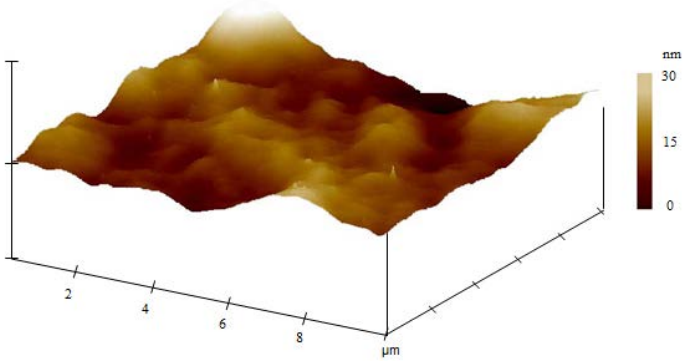

(b)

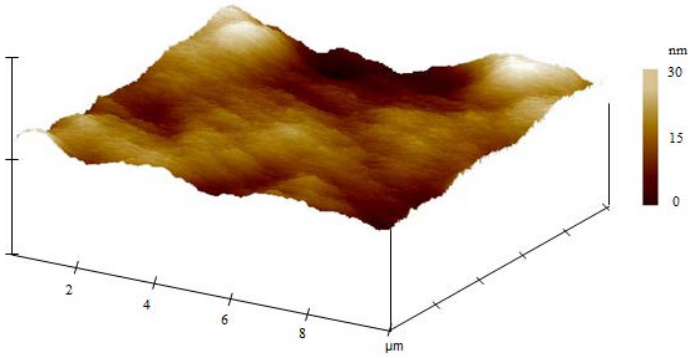

(c)

Figure 5.11 Topographic AFM images (10µm×10µm) of (a) PF-6 modified PDMS (surface roughness parameter (R_{RMS}=1.31 nm) (b) PF-10 modified PDMS (surface roughness parameter (R_{RMS}=2.69 nm) (c) PF-12 modified PDMS (R_{RMS}=2.27 nm) in perfluorodecalin.

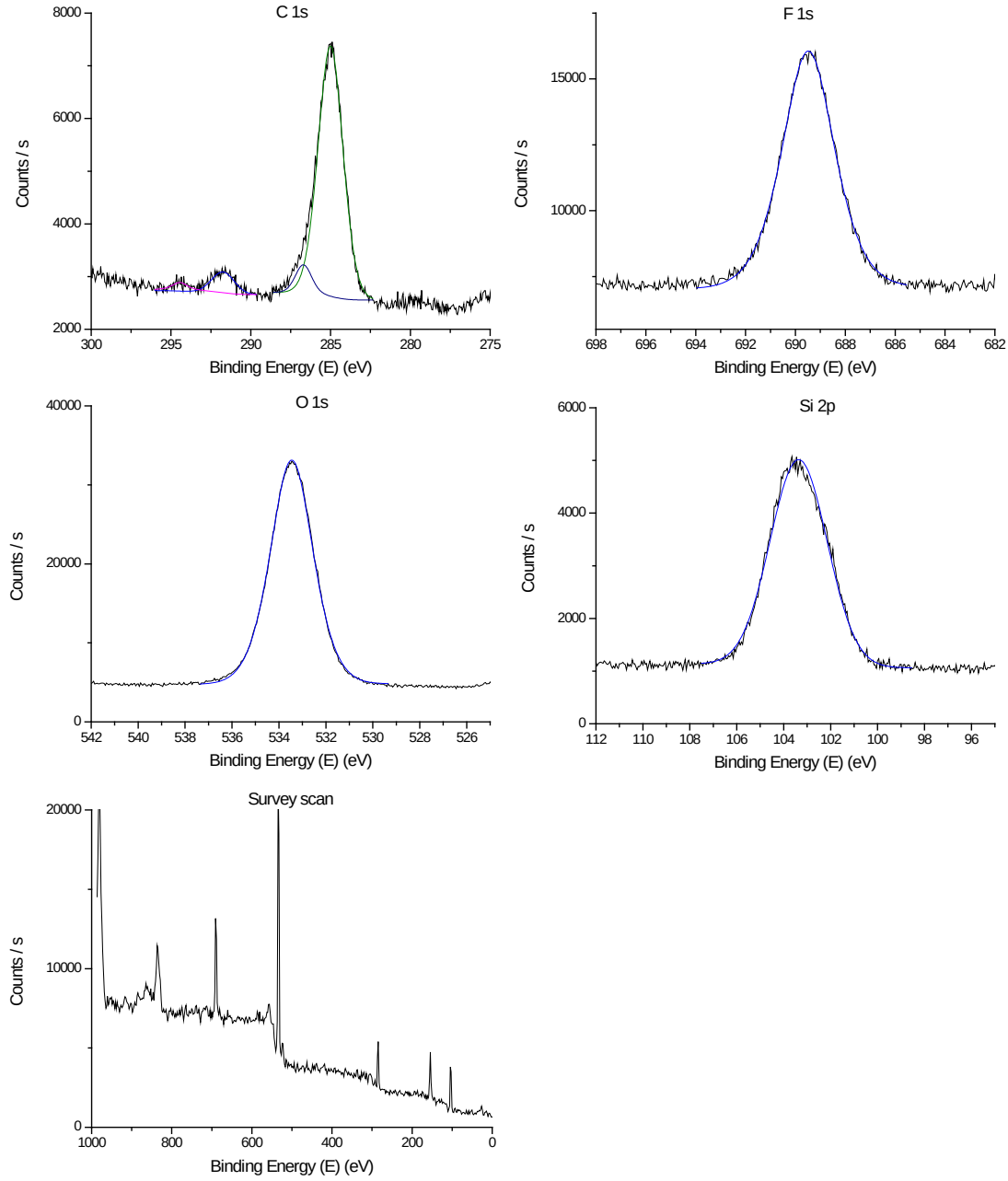

Figure 5.12 XP spectra of C 1s, F 1s,O 1s, Si 2p, and a survey scan (0 eV~ 1000eV) of PF6 modified PDMS in perfluorodecalin with oxidation time 60s PDMS at plasma energy of 10.2 W and 40 millitorr of air.

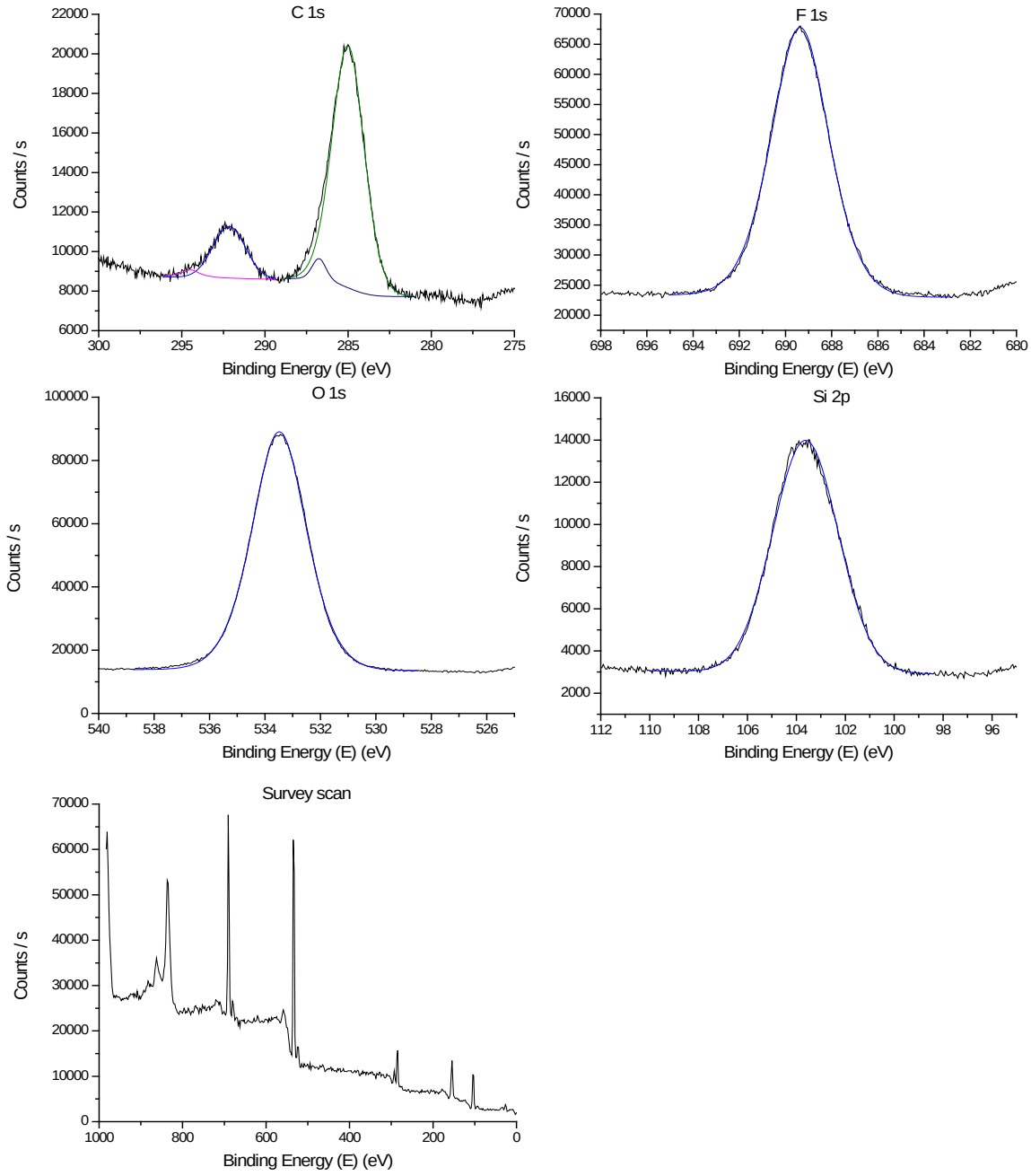

Figure 5.13 XP spectra of C 1s, F 1s,O 1s, Si 2p, and a survey scan (0 eV~ 1000eV) of PF10 modified PDMS in perfluorodecalin with oxidation time 60s PDMS at plasma energy of 10.2 W and 40 millitorr of air.

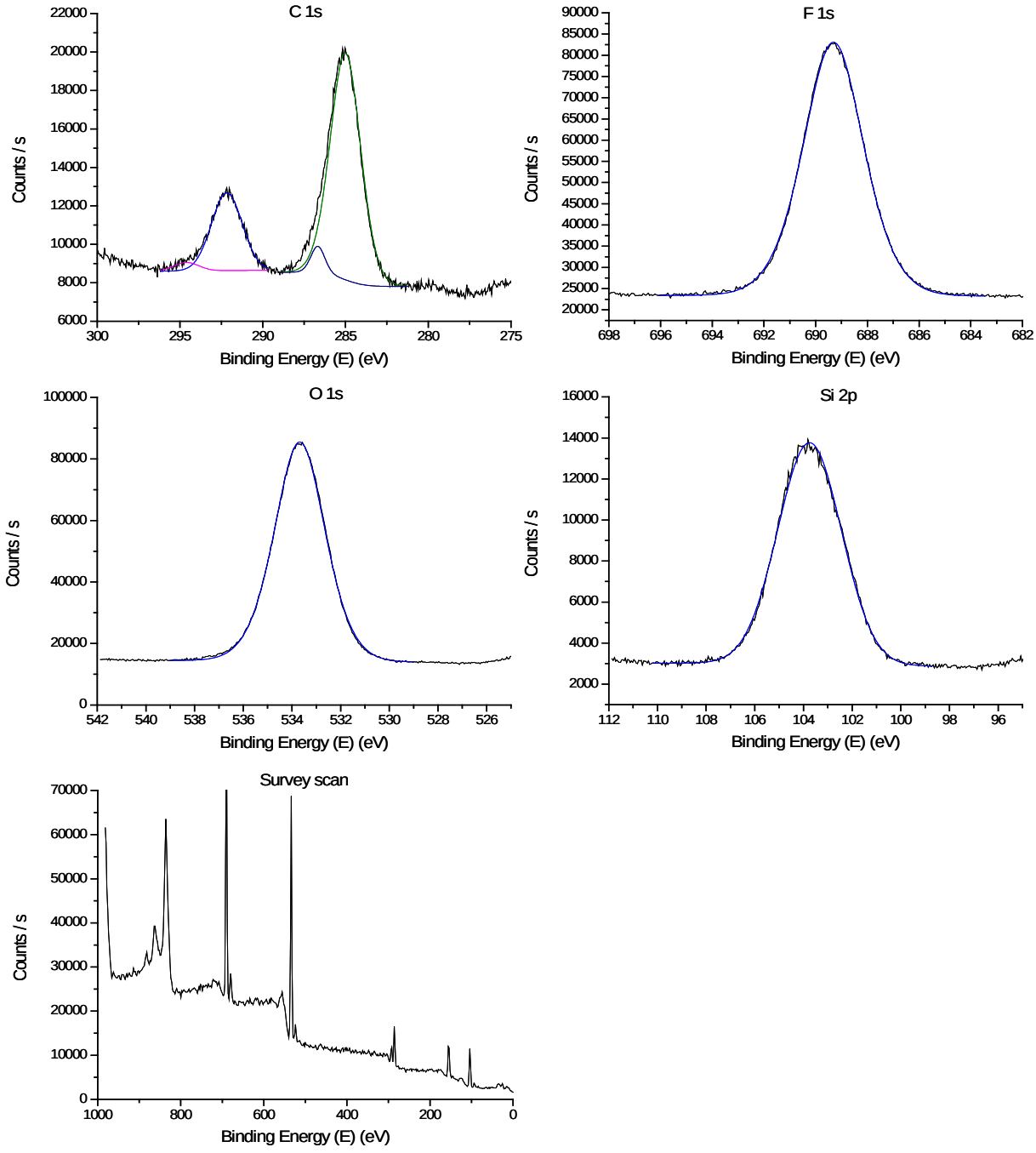

Figure 5.14 XP spectra of C 1s, F 1s,O 1s, Si 2p, and a survey scan (0 eV~ 1000eV) of PF12 modified PDMS in perfluorodecalin with oxidation time 60s PDMS at plasma energy of 10.2 W and 40 millitorr of air.

The F 1s peak area of each sample with different perfluoroalkyl chains shows that the amount of F increased concomitant with the number of C in the alkyl chain. The XPS experimental ratio of F content (PF6-PDMS: PF8-PDMS: PF10-PDMS: PF12-PDMS) is 0.22:1:1.30:1.64 compared to the stoichiometric ratio of F 0.69:1:1.31:1.62. So the surface molar densities of fluoroalkylriethoxysilanesilane molecules on PF8-PDMS, PF10-PDMS and PF12-PDMS are similar, however PF6-PDMS only has 1/3 surface molar density compared to the others. This result indicates that short-chain fluoroalkylriethoxysilanesilane does not form a continuous surface overlayer, and when the chain is longer than or equal to 8, the density of the surface modification layer does not increase with the growth of chain length.

The contact angles of all four perfluorinated PDMS surface types were the same within experimental error (111.0 ± 0.7°). This is slightly higher than that of unmodified PDMS (109.5 ± 0.3°) but much higher than that of oxidized PDMS (39.6 ± 0.8°).

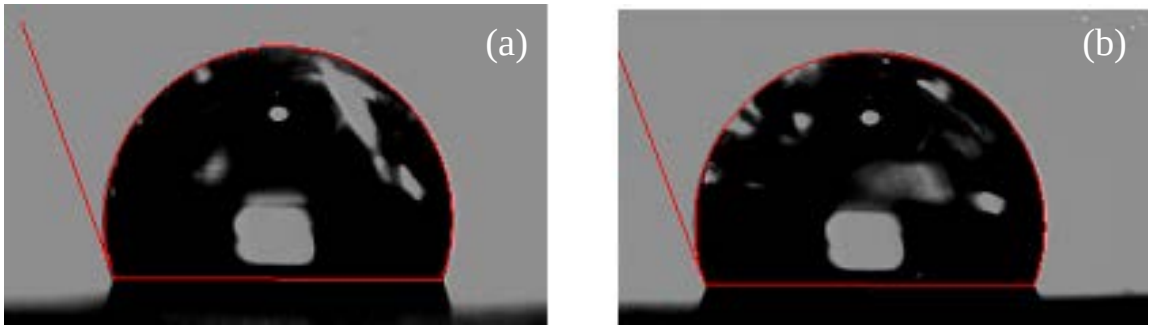

Figure 5.15 The contact angle measurements of (a) native PDMS (109.5 ± 0.3°) and (b) fluorinated PDMS (111.0 ± 0.7°).

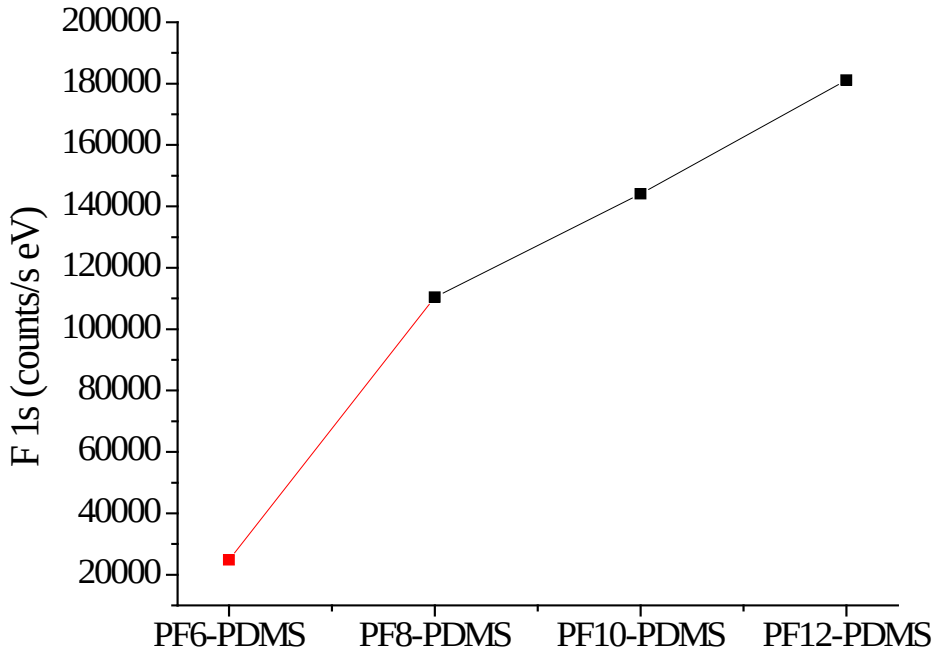

Figure 5.16 The XPS F 1s peak areas as a function of the length of fluorinated alkyl chain.

5.10 ζ-potential Measurement

Zeta-potential values at the interface between various PDMS surfaces and phosphate buffer solution (30 mmol) were measured as a function of pH. These were tested based on a measurement of the electro-osmotic flow velocity using the current monitoring method.

The ζ-potential values of bare PDMS are essentially independent of pH in the range of 3 – 11, with values in the range of -117±3 mV (Figure 5.18). The ζ potential values of freshly-oxidized PDMS are strongly pH-dependent, decreasing from low pH to high pH. This is consistent with the presence of ionizable surface silanol groups, which can be deprotonated in aqueous solution leaving a negative surface charge. The ζ-potential measurements were also performed on an oxidized PDMS sample after immersion in perfluorodecalin for 15 hours in the

absence of any PF-n species. The ζ-potential of this sample was identical to unmodified PDMS demonstrating that the surface relaxation effect had resulted in complete hydrophobic recovery within this time period.

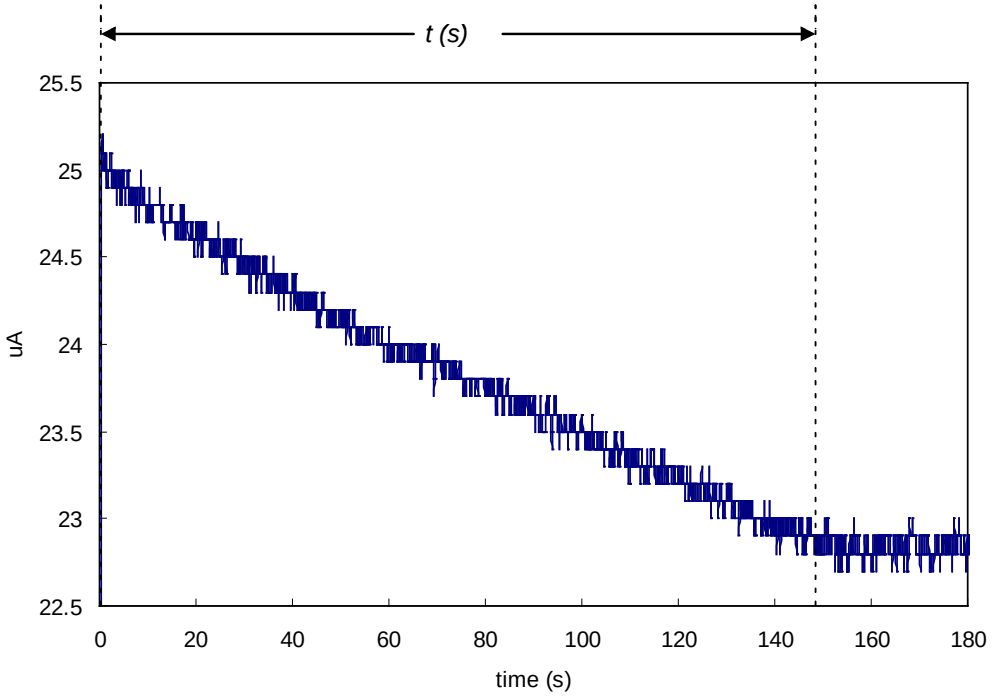

Figure 5.17 A plot of current vs. time for a zeta potential measurement of PF-8 modified PDMS at pH 7.80. The time (*t*) is that taken for the low concentration phosphate buffer (28.5 mmol) to replace the high concentration phosphate buffer in the entire microfluidic channel.

Figure 5.19 shows that the perfluorinated PDMS samples exhibit more negative ζ potential values compared with bare PDMS, but are also essentially independent of pH. Those of PF-6 modified PDMS lie in the range -137±3 eV, those of PF-8 modified PDMS lie in the range -146±2 eV while those of PF-10 and PF-12 modified PDMS lie in the range -155±4 eV and -155±2 eV respectively.

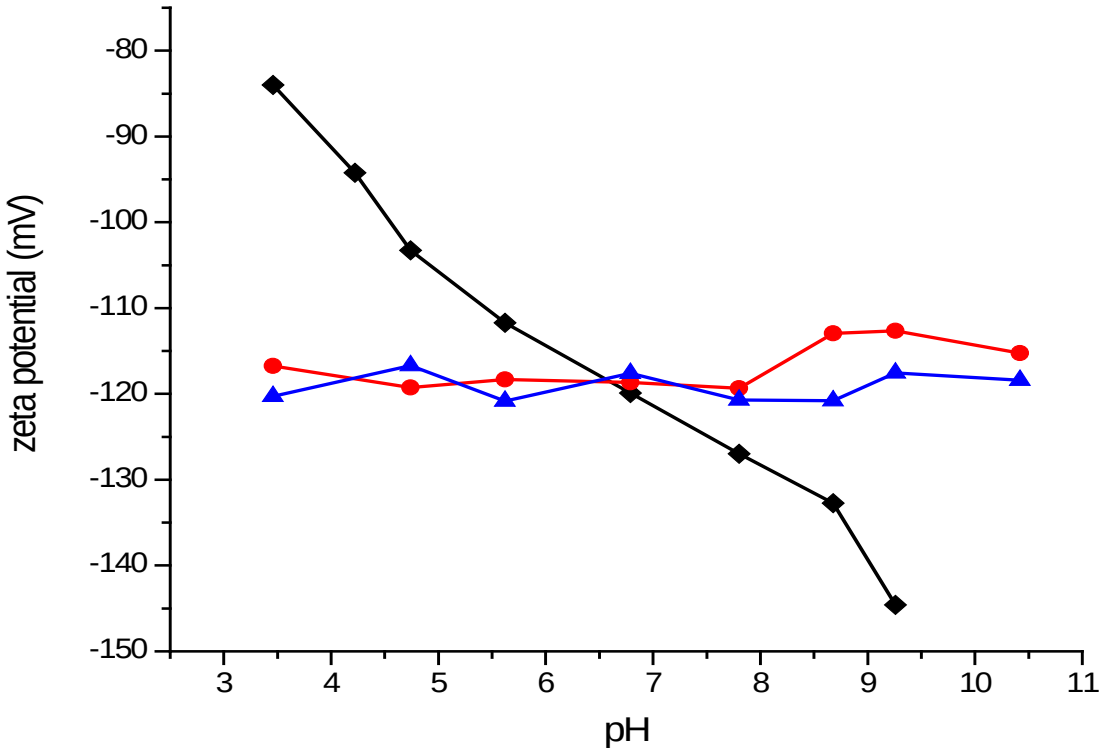

Figure 5.18 Zeta-potential values as a function of pH for native PDMS (●), freshly oxidized PDMS (♦), and oxidized PDMS exposed to perfluorodecalin for 15 hrs (▲)

PDMS and perfluorinated PDMS are both hydrophobic, and the absence of a strong pH effect on ζ-potential demonstrate that they lack surface ionizable groups. Nonetheless, the large ζ-potential shows that they must exhibit significant surface charge. The origin of charges at water/ hydrophobic interfaces are still not well understood due to the complexities of slip phenomena and uncertainties in interfacial structures.[170, 171] Ocvirk *et al.* concluded that impurities in PDMS introduced by manufacturer are the origin of charge, but this is not well supported experimentally. [79, 172, 173] The specific adsorption of ions onto the surface has

also been used to explain the origin of charge on the hydrophobic surface.[174]

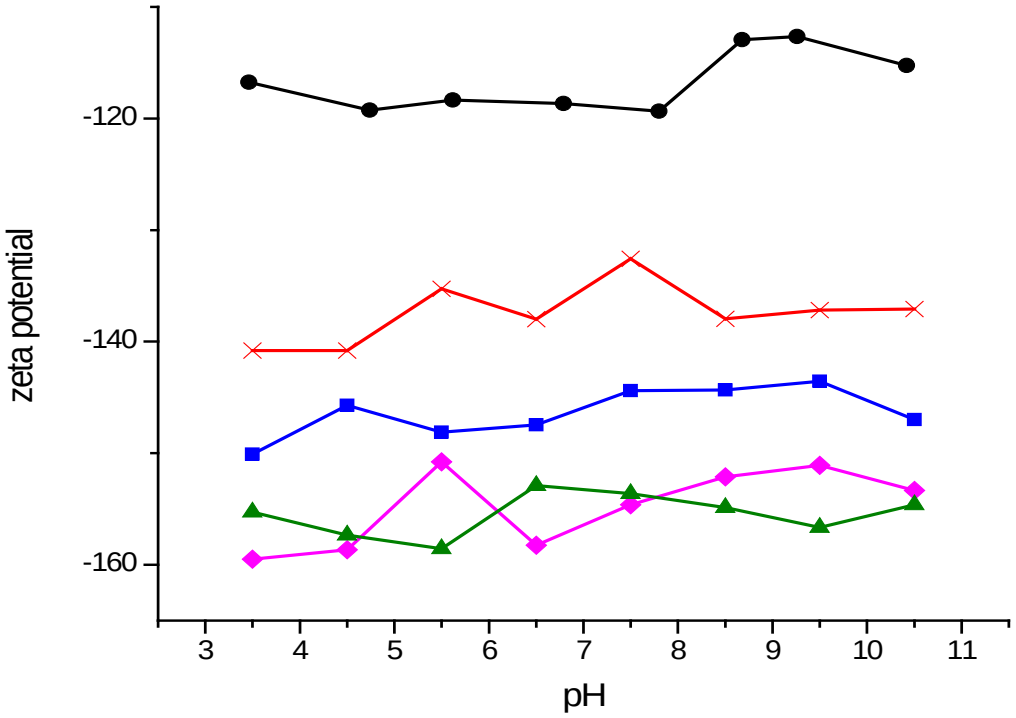

Figure 5.19 The ζ-potential values of PDMS (●), PF6-PDMS (×), PF8-PDMS (■), PF10-PDMS freshly oxidized PDMS (♦), and PF12-PDMS (▲) under 29.25mmol phosphate buffer as a function of pH.

The results reported here show that the trend of magnitude in the ζ-potential is PF-12 ≈ PF-10 > PF-8 > PF-6 > PDMS. PF-6 is of lowest magnitude in the ζ-potential compared to other fluorinated surfaces. Presumably this is the case as it exhibits the lowest surface density of modifying species. By contrast the results here show that PF-12, PF-10, PF-8 perfluorinated surfaces have similar surface roughness, chemical composition, and surface modifying molecular density, yet exhibit different zeta potentials. One explanation for the increase in zeta potential might be the surface molecular dipole [$CF_3(CF_2)_{3,5,7,9}\rightarrow(CH_2)_2$] introduced by fluoroalkylsilane

on the PDMS surface. The dipole moments as calculated using the AM1 method are respectively 2.87, 2.97, 3.02, and 3.09 Debye for PF6, PF8, PF10, and PF12. However, the distance from center of dipole moment to the surface is larger as the fluoroalkyl chain grows longer. Thus, the zeta potential values of perfluorinated PDMS by the overlayer of fluoroalkylsilane are impacted by both of surface dipole and fluoroalkyl chain lengths.

Conclusions

We studied the surface modification of PDMS using overlayers of fluoroalkylsilane molecules (PF6, PF8, PF10, PF12), which have similar structure but different fluoroalkyl chain length.

The experimental results showed the solvent compatibility has an important impact on the deposition process. A solvent such as toluene with relative large swelling ratio for PDMS, formed a lower density and more disordered overlayer with higher surface roughness compared to the solvent with minimal swelling effect such as perfluorodecalin.

PDMS covered with a flourous-terminated overlayer exhibits lower surface roughness compared to freshly-oxidized PDMS and, other than the short chain PF-6 species, have a similar fluoroalkylsilane molar density on the surface, regardless of chain length. The ζ potential values of unmodified PDMS and various perfluorinated PDMS were quite independent of pH with the order of magnitude of ζ potential PF-12 $\approx$ PF-10 > PF-8 > PF-6 > PDMS. This may be explained by a combination of changes in surface modifying molecule density, relative surface dipole moments and fluoroalkyl chain lengths.

Chapter 6
Nonspecific Protein Adsorption on Self-assembled Monolayers

Experimental Procedure

6.1 Materials

1H, 1H, 2H, 2H-perfluorooctyl-1-thiol (FOT) was obtained from SynQuest and used as received. 1-octanethiol (OT), 8-mercapto-1-octanol (MOT), cytochrome c (from horse heart, C2506), ubiquitin (from bovine red blood cells erythrocytes, U6253), lysozyme (from chicken egg white, 62970), ribonuclease A (from bovine pancreas, R6513), α-lactalbumin (from bovine milk, L6010), and myoglobin (from equine skeletal muscle M5696) were obtained from Sigma Aldrich and used as received. Phosphate buffers (30 mmol) at different pH values (pH 4.5, 5.5, 6.5, 7.5 and 8.5) were prepared by adding stock solutions of H_3PO_4, NaH_2PO_4, $Na_2HPO_4 \cdot 12H_2O$, and Na_3PO_4 (30mmol). The pH of each buffer was verified using a Fisher Scientific Accumet Basic pH meter.). Phosphate buffers at pH 7.4 (12.5 mmol and 5 mmol) were diluted from stock solution phosphate buffer 1M, pH 7.4 (Sigma Aldrich).

6.2 Self-assembled monolayer on Au

Gold coated mica substrates (Georg Albert PVD, Germany) and Biacore SPR sensor chips Au (GE healthcare, US) were respectively immersed in 1.0×10^{-3} M FOT, MOT, or OT in anhydrous ethanol for 15 hours to prepare the self-assembled monolayer on the surfaces. Then the surfaces were washed with anhydrous ethanol and dried in a stream of nitrogen.

6.3 Attenuated total reflectance-infrared spectroscopy (ATR-IR)

ATR-IR was conducted with a Nicolet 6700 FTIR spectrometer (Thermo scientific) using a liquid nitrogen cooled mercury cadmium telluride (MCT) detector and the smart Orbit accessory

as the ATR accessory. The ATR spectrum of the monolayer was collected at 2 cm^{-1} resolution and 64 scans.

6.4 Contact angle measurement

Contact angles of OT, FOT and MOT coated gold-mica were measured using same equipment and method described in section 5.3.

6.5 X-ray photoelectron spectroscopy (XPS)

X-ray photoelectron spectroscopy (XPS) was used to analyze the surface composition of OT, FOT, MOT modified gold coated mica. The equipment setup and data process were described in section 4.7. XPS spectra were acquired from binding energy regions containing peaks arising from all elements expected on the samples: C1s, S2p, O1s, F1s, and Au4f. A survey scan indicated that there were no other elements present on the sample surface beyond those listed above.

6.6 Surface plasmon resonance spectroscopy (SPR)

Biacore 3000 (Biacore AB, Uppsala, Sweden) was used for in-situ all protein adsorption studies. Biacore SPR sensor chips (Au) were modified with self-assembled monolayers before analysis, as discussed before. All the buffer, regeneration reagent, and protein solutions were degassed before experiment. Each protein sample was ultracentrifuged for 5 mins at 10,000 rpm before injection.

For the adsorption of lactalbumin, RNase A, lysozyme, and myoglobin, phosphate buffer (5 mmol, pH 7.4) was used as running buffer at a flow rate 10μl /min. Each protein was prepared with six concentrations at 90μmol, 60μmol, 30μmol, 10μmol, 5μmol and 1μmol. The KINJECT command (30μl, 180s) was used for protein adsorption measurements and the dissociation time

was set up to 180 s. Regeneration was performed using one or two quick injection of 5μl SDS (10mg/mL) + NaCl (30mM) in phosphate buffer (5 mmol, pH 7.4). The injection for one protein at a given concentration was repeated twice.

For the adsorption of cytochrome c and ubiquitin (10μmol), phosphate buffer (30 mmol, pH 5.5) was used as running buffer at a flow rate 10μl /min. The KINJECT command (30μl, 180s-300s) was used for protein adsorption measurements and the dissociation time was set to 180 s. Regeneration was performed with one or two quick injections of 10μl SDS (10mg/mL) in SDS buffer. Each adsorption measurement of one protein at a given pH was repeated twice. Each pH phosphate buffer was tested using the same KINJECT method and dissociation time, and then was subtracted from protein adsorption SPR sensorgram which used same pH buffer to deduct the pH effect.

The resonance angle was monitored by response units (RUs). 10000 RUs equate to a shift of 1 degree in resonance angle. One RU represents the adsorption binding of approximately 1pg protein/mm^2. [175, 176] The data were analyzed by standard procedure using BIAevaluation software (version 4.1).

6.7 Circular Dichroism (CD)

Circular Dichroism (CD) Spectroscopy (Secondary Structure)—CD Spectra were measured on a Chirascan Circular Dichroism Spectrometer (Applied Photophysics Ltd, UK) using a cylindrical cuvette of 0.1 mm pathlength (Hellma). The 50 mM ubiquitin and cytochrome c in 30 mM sodium phosphate buffers at different pH (pH 4.5, 5.5, 6.5, 7.5, 8.5) were scanned by sampling data at 1nm intervals between 260 and 185 nm. The 30mM sodium phosphate buffer at each pH value was scanned repeatedly to establish an average baseline circular dichroism, which was subtracted from subsequent scans of the protein solutions. Wave scans were automatically selected by Proviewer software.

6.8 Differential scanning calorimety (DSC)

Lactalbumin , RNase A, lysozyme, and myoglobin (0.2 mg/mL) samples in phosphate buffer (12.5 mM, pH 7.4) were scanned in a VP-DSC Calorimeter (Microcal Inc, Northampton, MA) over a temperature range of 20°C to 100°C, at a scan rate of 60°C per hour. All buffers scanned in DSC experiments were from the same stock used to wash protein samples prior to experiment, so as to be identically matched. All samples were thoroughly degassed in ThermolVac (Microcal Inc, Northampton, MA). Prior to loading into the calorimeter, and initial equilibration was accomplished around 20°C for 30 minutes prior to the start of each scan.

Results and Discussion

6.9 The self-assembled monolayers on Au were characterized using XPS, contact angle measurement and ATR-IR.

From Figure 6.1, the survey scan of XPS spectra, the F1s (689.7 eV) peak of the FOT monolayer and the O1s (531.8 eV) peak of the MOT monolayer were clearly evident. The S 2p peaks (163.3 eV) of three monolayers cannot be readily observed on the survey scan due to low concentration and sensitivity factor of sulfur, but it could be clearly observed in a scan with higher resolution (Figure 6.2, 6.3 and 6.4)

XPS can be used to measure the thicknesses (t) of thin (<10 nm) overlayer films. [177] Here the elastic electron scattering is neglected, thus the overlayer film thickness t can be obtained from the expression

$$t = -(\cos\theta)\lambda_i \ln\frac{I_S}{I_0} \qquad [6.9.1]$$

where θ is the takeoff angle (here, it is 15°), I_s is the substrate signal intensity after deposition of the film, I_0 is the substrate signal intensity from the uncovered substrate and λ_i is the inelastic mean free path.[177] In here, λ_i = 1.45 nm, which is the inelastic mean free paths of a Au4f

photoelectron of binding energy 84 eV.[178] The thickness of overlayers shown in Table 6.1 is consistent with the formation of a monolayer, compared to the theoretical thickness calculated using Gaussian AM1 semiempirical method.[179] .

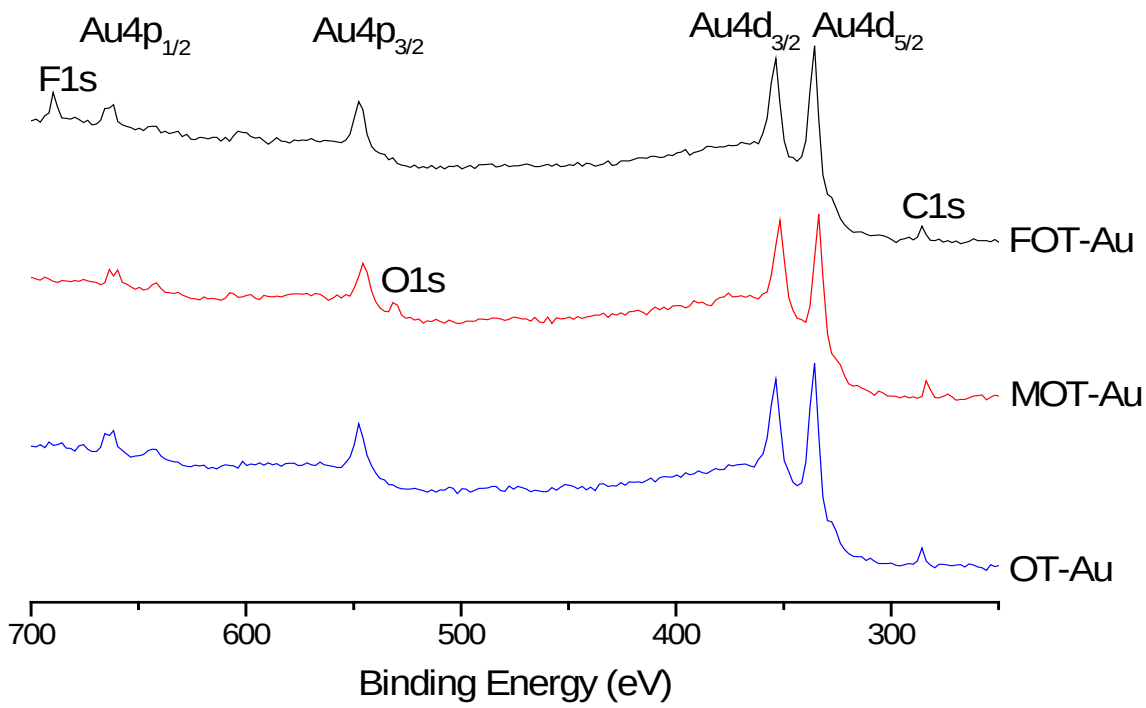

Figure 6.1 XPS survey scans for the surfaces of FOT-Au, MOT-Au, OT-Au.

Table 6.1 The thicknesses of FOT, MOT, OT monolayer on gold coated mica, calculated by XPS and Gaussian AM1 method respectively.

Surfaces	Thickness of monolayer (nm)	
	calculated by XPS	calculated by Gaussian
FOT-Au	1.82	1.26
MOT-Au	1.84	1.33
OT-Au	1.80	1.20

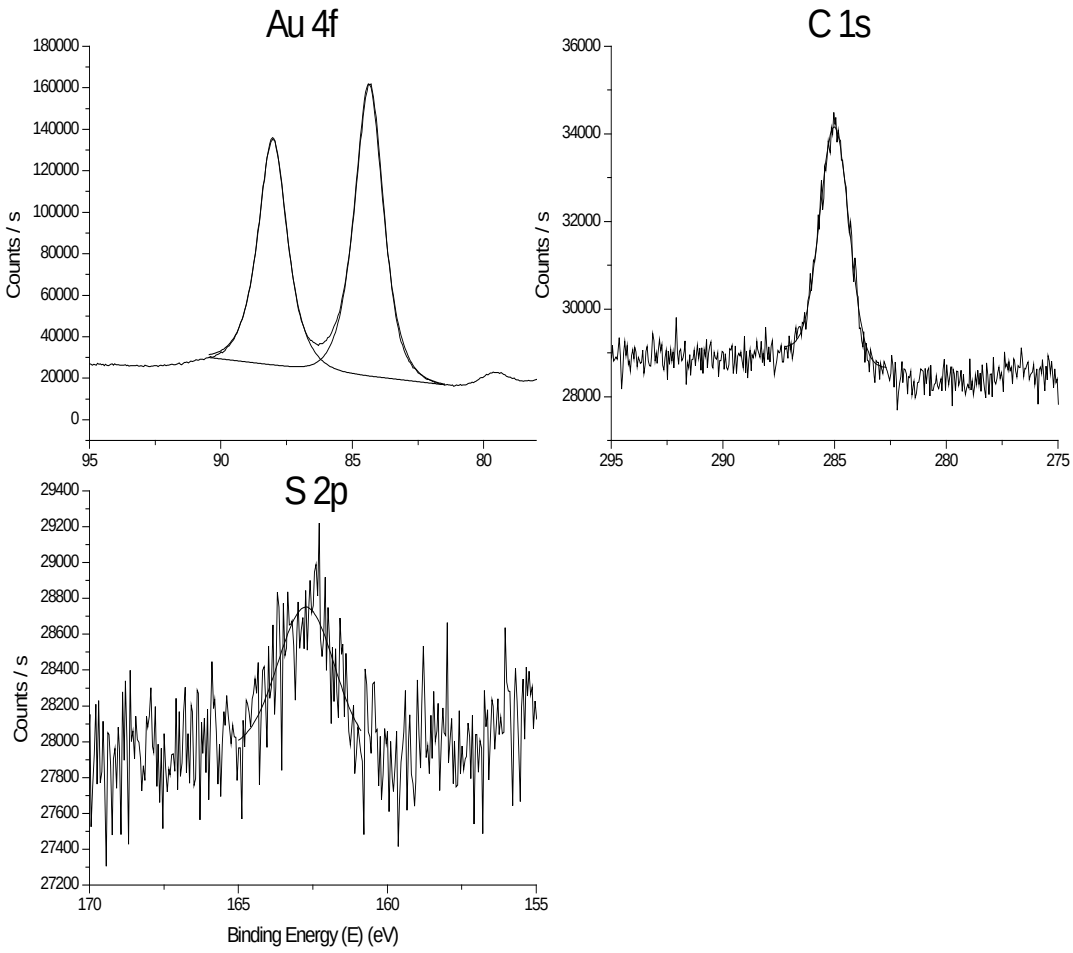

Figure 6.2 XPS spectra of Au 4f, C 1s and S 2p of OT SAM on Au

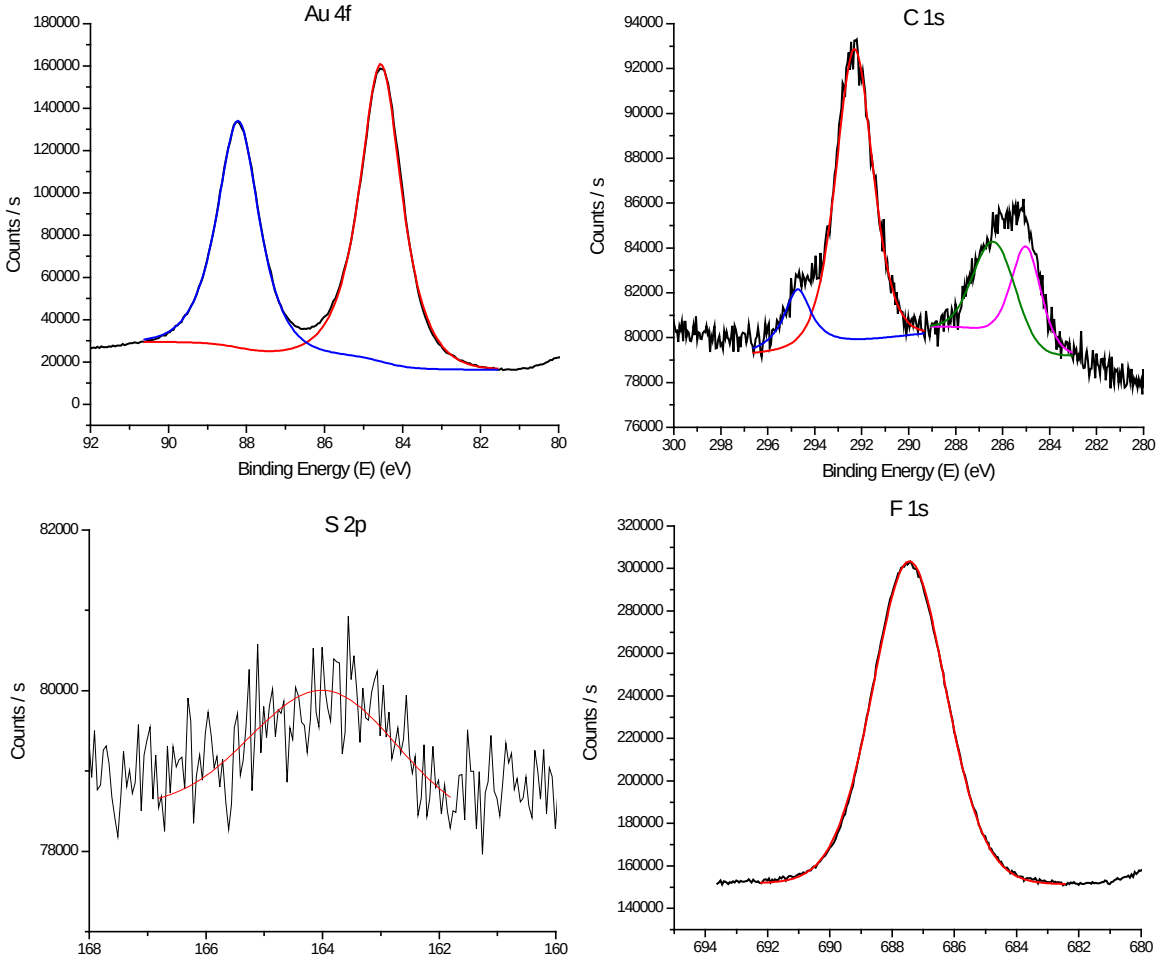

Figure 6.3 XPS spectra of Au 4f, C 1s, F 1s and S 2p of FOT SAM on Au

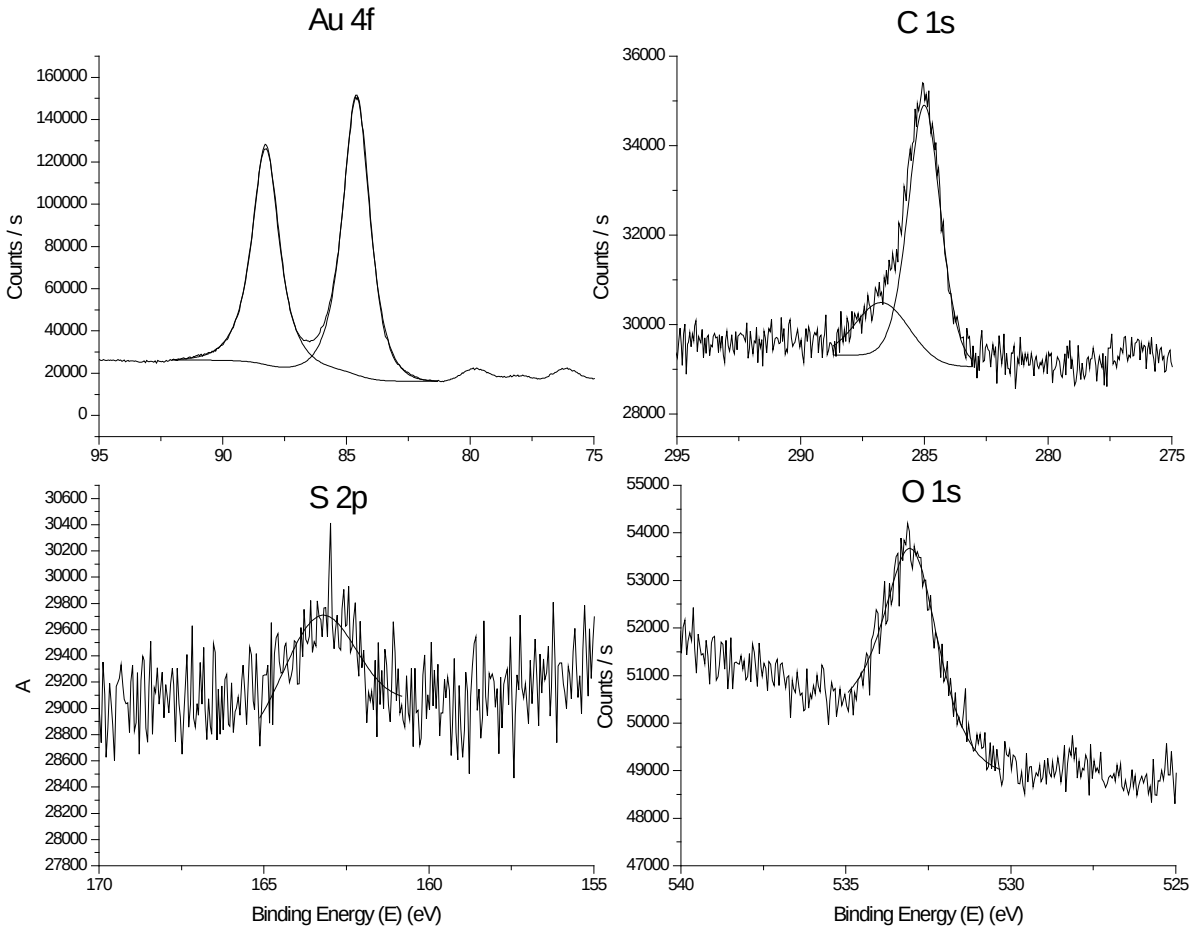

Figure 6.4 XPS spectra of Au 4f, C 1s, O 1s and S 2p of MOT SAM on Au.

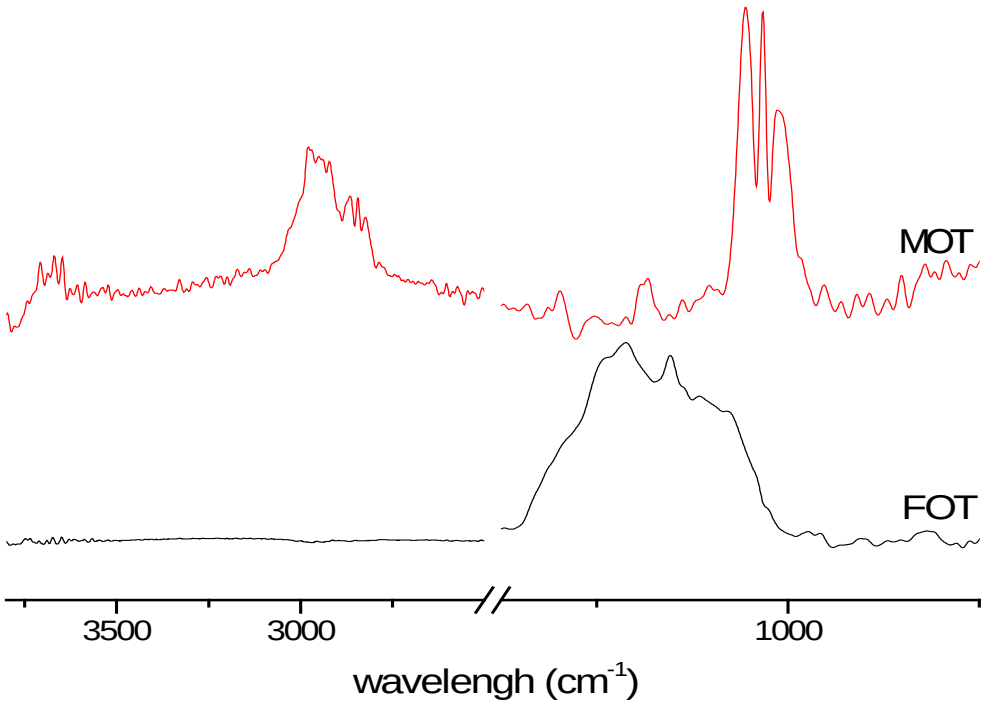

Figure 6.5 ATR-FTIR spectra of MOT and FOT absorbed on Au coated mica.

ATR-IR spectra of FOT and MOT surface are shown in Figure 6.5. On the FOT-Au sample, the C-F stretching mode shows a strongly absorption over a wide range of 1400-1000 cm^{-1}. On the MOT-Au sample, the alkyl C-H stretching vibrations is in the range of around 2800-3100 cm^{-1}, the O-H stretching is at 3650 cm^{-1} and C-O stretching is in the range of 1100-970 cm^{-1}.

The FOT-Au surface is extremely hydrophobic (contact angle 115±1°), OT-Au is less hydrophobic than the FOT surface (contact angle 87± 1°), and the MOT surface is hydrophilic (contact angle 50±1°). The MOT may participate in hydrogen bonding with liquid water. Even though the C-F bond is strongly polar, it cannot take part in the hydrogen bonding with liquid

water due to its low polarizability. [180]

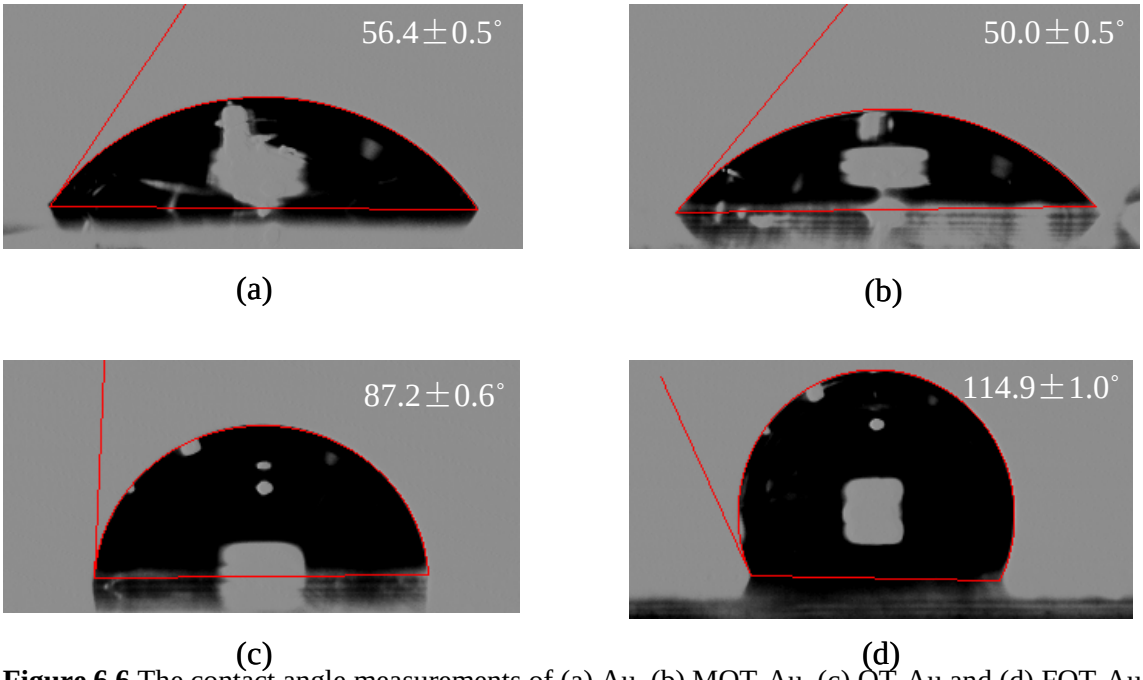

Figure 6.6 The contact angle measurements of (a) Au, (b) MOT-Au, (c) OT-Au and (d) FOT-Au

6.10 The calculation of hydrophobicity of RNase A, lysozyme c, α-Lactalbumin and myoglobin, ubiquitin and cytochrome c

We used four proteins of similar size: RNase A, Lysozyme c, α-Lactalbumin and Myoglobin to study the relationship of protein stability and adsorption kinetics on the hydrophobic OT and FOT surfaces. We used the two proteins ubiquitin and cytochrome c to study the pH effect on protein adsorption on the OT, FOT and MOT surfaces. Since protein surface hydrophobicity is one of most important physical properties of proteins and it may have important effect on adsorption kinetics and thermodynamics, in this section we calculated the average superficial hydrophobicity (ASH) for all proteins used here.

The ASH may be predicted to an acceptable level for many practical applications such as hydrophobic interaction chromatography and partitioning using only the amino acid composition. [181]. The protein ASH was computed assuming that each amino acid in the protein surface

contributes, proportionally to its abundance, and hydrophobic strength (hydrophobic scales as detailed below) using the following expression [182]:

$$\left\langle \phi_{surface} \right\rangle = \sum_{i \in A} \hat{r}_i \phi_i \qquad [6.10.1]$$

where $\left\langle \phi_{surface} \right\rangle$ is the average superficial hydrophobicity for a given protein, A is the collection of all amino acids in the given protein and ϕ_i is the hydrophobicity scale of the amino acid of type *i*. $\hat{r}_i$ is the fraction of superficial area occupied by the amino acid *i*, which is defined by

$$\hat{r}_i = \frac{S_i}{\sum_{j \in A} S_j} \qquad [6.10.2]$$

where S_i is the total accessible suface area for the amino acids of type *i*, $\sum_{j \in A} S_j$ is the total accessible superficial area (ASA) for a given protein, which is the sum of the accessible superficial area for each type of amino acid *j*. The program STRIDE [183] was used to calculate the solvent accessible surface areas (SAA) of the 20 amino acid residues and the total solvent accessible surface area (TSAA).

Here we used two normalized hydrophobicity scales: the Cowan-Whittaker scale[184] and Berggren scale[182] (Table 6.2). The Cowan-Whittaker scale was developed based on the retention times of 20 amino acids and their methyl, ethyl and benzyl esters, which were determined under standard conditions on reversed-phase high-performance liquid chromatography at pH 3.0 and pH 7.5. [184] Here we chose Cowan-Whittaker scale at pH 7.5 as our adsorption test under the condition of phosphate buffer (5mmol, pH 7.4). The Berggren scale is based on partition behavior of 20 amino acids in aqueous two phase systems. [182]

The solvent accessible area of each amino acid of RNase A, Lysozyme C, Lactalbumin and Myoglobin as calculated by the program STRIDE are listed in Table 6.3. The ASH results of each protein are summarized in Table 6.4.

Table 6.2 The hydrophobicity scales of amino acids used in this work.

Amino acid	Hydrophobicity scales*	
	Cowan–Whittaker[184]	Berggren[182]
ALA	0.628	0.169
ARG	0.163	0.000
ASN	0.291	0.257
ASP	0.000	0.099
CYS	0.731	0.169
GLN	0.307	0.257
GLU	0.050	0.099
GLY	0.540	0.109
HIS	0.377	0.035
ILE	1.000	0.264
IEU	0.992	0.264
LYS	0.153	0.000
MET	0.817	0.169
PHE	0.965	0.796
PRO	0.751	0.169
SER	0.382	0.169
THR	0.472	0.169
TRP	0.879	1.000
TYR	0.638	0.870
VAL	0.872	0.870

*The scales are normalized in the interval [0; 1].

Table 6.3 The solvent accessible area of each amino acid of RNase A, lysozyme C, lactalbumin, myoglobin, ubiquitin and cytochrome c calculated by the program STRIDE[183].

	solvent accessible area (Å)					
amino acid	RNase A	Lysozyme C	Lactalbumin	Myoglobin	Ubiquitin	Cytochrome C
ALA	426.2	253.6	218.2	572.2	--	203.8
ARG	409.2	1505.9	337.1	166.5	114.5	80.8
ASN	819.4	1052.8	206.5	216.8	544.4	328
ASP	282.1	505.4	1220.2	741.2	176.4	192.8
CYS	49.6	87.2	76	--	427.0	60.6
GLN	446.5	235.1	679.2	384.3	435.5	406.4
GLU	382.4	127.4	551.8	1159.7	704.4	1011.5
GLY	203.3	543.6	83.9	516	464.0	470.5
HIS	149.4	29.5	450.4	670.2	82.2	124.6
ILE	18.6	81.6	341.5	196.2	67.1	215.1
IEU	62.3	204.8	180.1	312.3	343.7	69.1
LYS	1163.7	500.4	1050.2	1814.6	624.1	2153.9
MET	50.4	0.8	72.8	11.8	52.8	63.1
PHE	23.6	91	101.6	206.6	90.0	144.9
PRO	235.4	191.3	114.4	292.2	135.9	215.3
SER	1027.7	348.9	403.1	183.2	173.0	--
THR	464.5	363.3	456.6	379.2	405.1	436.3
TRP	--	237	68.6	19.4	--	14.3
TYR	405	144.7	215.2	47.4	41.4	102.1
VAL	148.5	193	113.7	141.5	39.9	141.1

Table 6.4 The calculation results of average superficial hydrophobicity of RNase A, Lysozyme C, Lactalbumin and Myoglobin

Protein	average superficial hydrophobicity	
	Cowan–Whittaker[184]	Berggren[182]
ribonuclease A	0.359	0.195
lysozyme C	0.377	0.201
α-lactalbumin	0.339	0.177
myoglobin	0.347	0.143
ubiquitin	0.349	0.147
cytochrome c	0.331	0.147

6.11 The calculation of average protein flexibility of ubiquitin and cytochrome c

The average protein flexibility may be predicted from the amino acid sequence using a sliding window averaging method based on Bhaskaran and Ponnuswamy[185] (BP) protein flexibility parameters (Table 6.5), which were derived from three-dimensional protein structure. We used the BP values to calculate average flexibility of the residues in the protein. The protein sequence can be read from a PDB file. The optimized sliding window size is nine and the weighting (exponential impact factor) of residues from left window to right window is 0.25, 0.4375, 0.625, 0.8125, 1, 0.8125, 0.625, 0.4375, and 0.25.[186] Such the flexibility of each residue is dependent on not only itself but also the nature of neighbouring residues. The average flexibility index (F) of the protein is calculated based on [186]:

$$F = \sum_{i=10}^{n-9} f_i /(n-10) \qquad [6.11.1]$$

where f_i is the average flexibility of each amino acid.

$$f_i = [B_{nc,i} + 0.8125(B_{nc,i-1} + B_{nc,i+1}) + 0.625(B_{nc,i-2} + B_{nc,i+2}) + 0.4375(B_{nc,i-3} + B_{nc,i+3}) + 0.25(B_{nc,i-4} + B_{nc,i+4})] / 5.25 \quad [6.11.2]$$

The calculated f_i values of individual amino acid of ubiquitin and cytochrome c using program protscale[187] are shown in Figure 6.7 and Figure 6.8. The average protein flexibility indexes (F) of ubiquitin and cytochrome c are respectively 0.602 and 0.556, listed in Table 6.6.

Table 6.5 The flexibility scale of 20 amino acids used in calculation[185].

Amino acid	Flexibility scales*[185]
ALA	0.36
ARG	0.53
ASN	0.46
ASP	0.51
CYS	0.35
GLN	0.49
GLU	0.50
GLY	0.54
HIS	0.32
ILE	0.46
IEU	0.37
LYS	0.47
MET	0.30
PHE	0.31
PRO	0.51
SER	0.51
THR	0.44
TRP	0.31
TYR	0.42
VAL	0.39

Amino acid sequence of Ubiquitin: MQIFVKTLTG(10) KTITLEVEPS(20) DTIENVKAKI(30) QDKEGIPPDQ(40) QRLIFAGKQL(50) EDGRTLSDYN(60) IQKESTLHLV(70) LRLRGG(76)

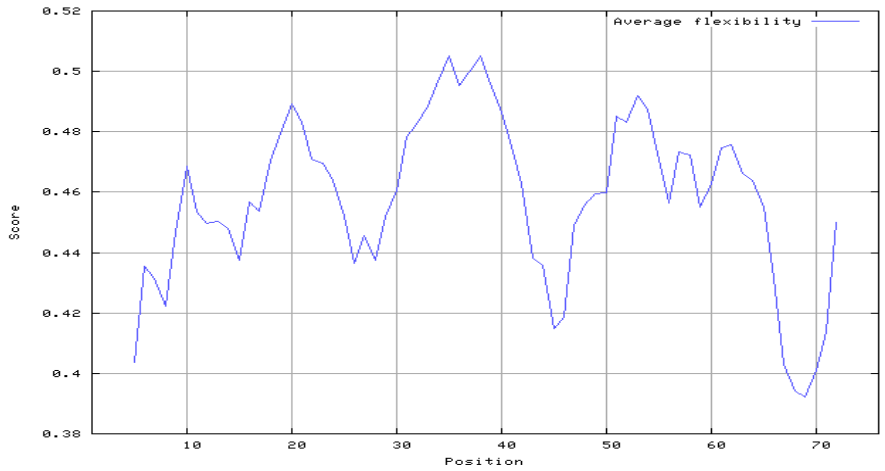

Figure 6.7 The amino acid sequence and the average flexibility of each amino acid of ubiquitin calculated by protscale.

Amino acid sequence of Cytochrome C: GDVEKGKKIF(10) VQKCAQCHTV(20) EKGGKHKTGP(30) NLHGLFGRKT(40) GQAPGFTYTD(50) ANKNKGITWK(60) EETLMEYLEN(70) PKKYIPGTKM(80) IFAGIKKKTE(90) REDLIAYLKK(100) ATNE(104)

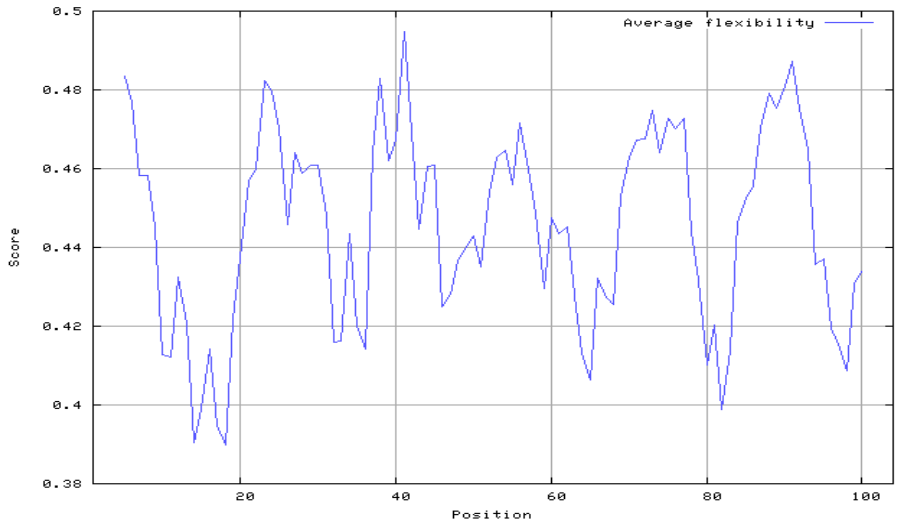

Figure 6.8 The amino acid sequence and the average flexibility of each amino acid of cytochrome c calculated by protscale.

Table 6.6 The calculation results of average superficial hydrophobicity and flexibility of Ubiquitin and Cytochrome C.

Protein	flexibility (9 windows)
ubiquitin	0.602
cyto c	0.556

6.12 Protein stability and adsorption

6.12.1 Some physiochemical properties of RNase A, Lysozyme C, Lactalbumin and Myoglobin

To study the relationship of protein stability and adsorption on the hydrophobic surfaces, we chose four proteins of similar size: RNase A, Lysozyme c, α-Lactalbumin and Myoglobin. Protein conformations are marginally stable and mainly affected by an interplay of H-bonding and hydrophobic effects. [188] Thus, proteins usually have a hydrophobic core and a surface containing a higher density of polar groups. The three-dimensional structures of the proteins studied here are known to high resolution from X-ray crystallography and were obtained from the Protein Data Bank. The 3D structure and surface of RNase A, Lysozyme c, α-Lactalbumin and Myoglobin are shown in Figure 6.9, generated using the program VMD [189] and structured data from the Protein Data Bank. Figure 6.9 also indicates the acid, base, polar and hydrophobic groups on the surfaces in different colours.

Proteins are large, amphipathic and intrinsically surface active molecules. Interactions between proteins and surfaces not only depend on chemical and physical properties of surface, and solution environment, but also depend on the properties of protein such as hydrophobity,

charge, stability, size and shape of protein.[190] Some physiochemical properties of RNase A, Lysozyme C, Lactalbumin and Myoglobin are listed in Table 6.7.

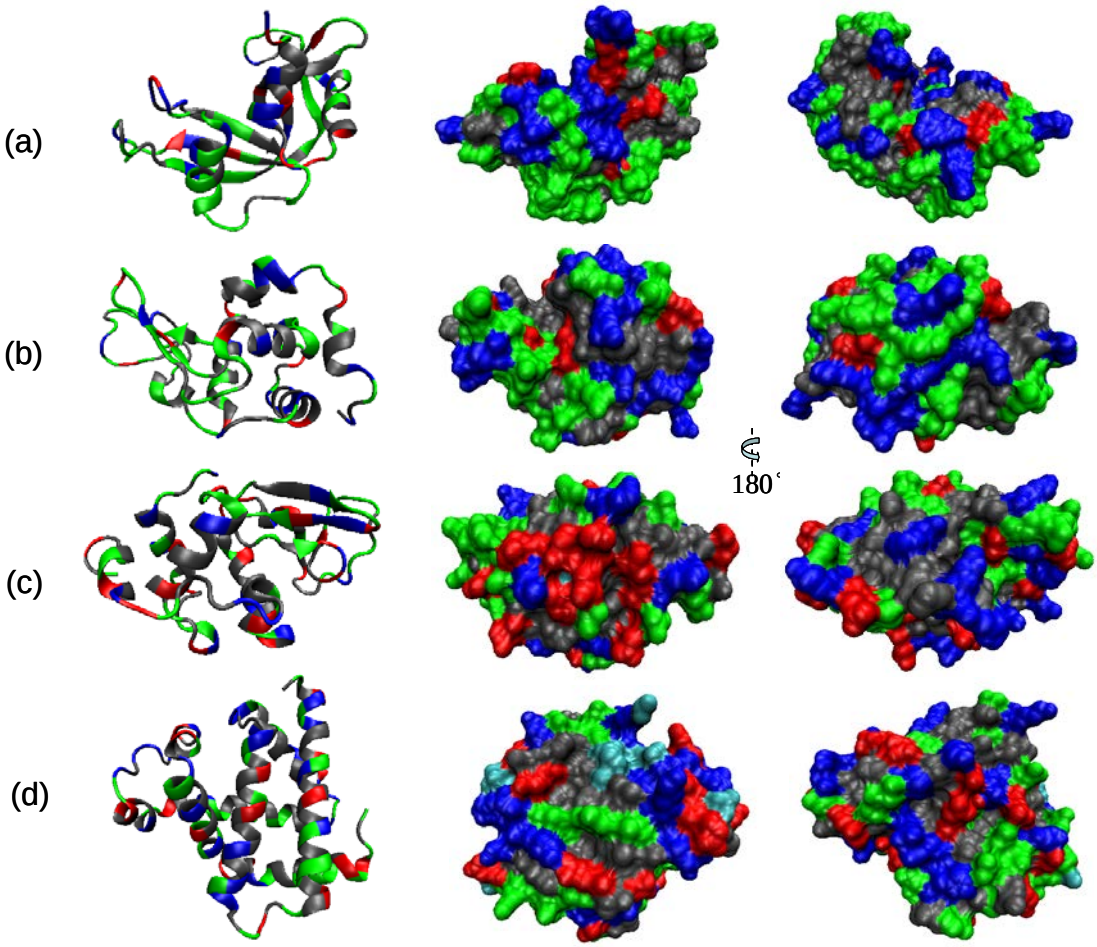

Figure 6.9 The interaction surfaces of proteins (a) RNase A (b) Lysozyme c (c) α-Lactalbumin and (d)Myoglobin ; Acid (red), basic (blue), polar (green), hydrophobic (grey) groups. All diagrams were generated by VMD.[189]

Proteins interact with surfaces structures by numerous intermolecular interactions such as hydrophobic, electrostatic, van der Waals and hydrogen-bond interactions.[188] Here we studied protein adsorption on two different surfaces: OT-Au and FOT-Au. Both the surfaces of OT-Au and FOT-Au are hydrophobic, with the FOT-Au surface more hydrophobic than OT-Au

as tested in contact angle measurements. Thus, the hydrophobic interaction should be the main interaction force controlling the adsorption process.

Table 6.7 Some physiochemical properties of the proteins: RNase A, Lysozyme C, Lactalbumin and Myoglobin.

Protein	α-Lactalbumin	Myoglobin	Lysozyme	RNase A
PDB ID	1HFX	3LR7	3AW6	5RSA
Molar mass (D)	14280	16950	14471	13803
Size (nm^3)	3.3 × 6.5 × 4.9	3.5 × 2.9 × 6.3	7.9 × 7.9 × 3.8	3.0 × 3.8 × 5.3
Isoelectric point (pH unit)	4.2-4.5	6.8,7.2	11.00	9.50
T_m (°C) (phosphate buffer 12.5 mM, pH 7.4)	55.6	83.3	72.6	63.8
Δ G (kcal/mol)	4.2, pH 7.0[191]	6.1[32]	8.9, pH 5.5[191]	7.5, pH 7.0 [191]

When in contact with a hydrophobic surface, many proteins undergo different degrees of conformational change, exposing more internal hydrophobic regions to strengthen the interaction. Thus, the thermodynamic stability of protein, one of intrinsic properties, has the greatest impact on the surface-induced protein conformational change.[190]

Arai and Norde first introduced the concept of "hard" and "soft" proteins. They observed that soft proteins can be adsorbed on hydrophilic surfaces even under electrostatic repulsion due to the significant gain of structural entropy while hard proteins only adsorbed on hydrophilic surfaces under electrostatic attraction. [192, 193] The correlation existing in the concept "soft" and "hard" protein and protein stability is that "soft" proteins have lower thermodynamic stability.

[194-196] "Soft" proteins are more likely to denature due to the lower thermodynamic stability and usually give greater conformational change adsorbed on the surface and rotational freedom due to the increase of entropy. [192] In the other words, the "hard" protein with greater stability is able to resist the surface induced conformation change. The adsorbed "hard" proteins often retained a large extended secondary structure and show disrupted tertiary structure with exposed hydrophobic patches. [197] Kondo et. al reported "soft" proteins such as albumin and hemoglobin undergo extensive loss of secondary structure during the adsorption on silica while "hard" proteins like RNase A exhibit different behavior [200,202].

The thermal stability of a given protein is often measured by the melting temperature T_m, which is the temperature at which proteins are half unfolded.[186] DSC scans to determine melting temperature of RNase A, Lysozyme C, Lactalbumin and Myoglobin in phosphate buffer (12.5 mmol, pH 7.4) are shown in Figure 6.10. However, the low T_m of one protein does not always mean that it is a "soft" protein since T_m is not directly related to the thermodynamic stability (ΔG). The thermodynamic stability (ΔG) of RNase A, Lysozyme C, Lactalbumin and Myoglobin are shown in Table 6.7. Table 6.7 shows that lactalbumin and myoglobin have lower thermodynamic stability (ΔG) than that of lysozyme C and RNase A. Some researchers, who focused on the study of protein stability and adsorption, have classified lysozyme C and RNase A as "hard" proteins, and lactalbumin and myoglobin as "soft" proteins. [198-201]

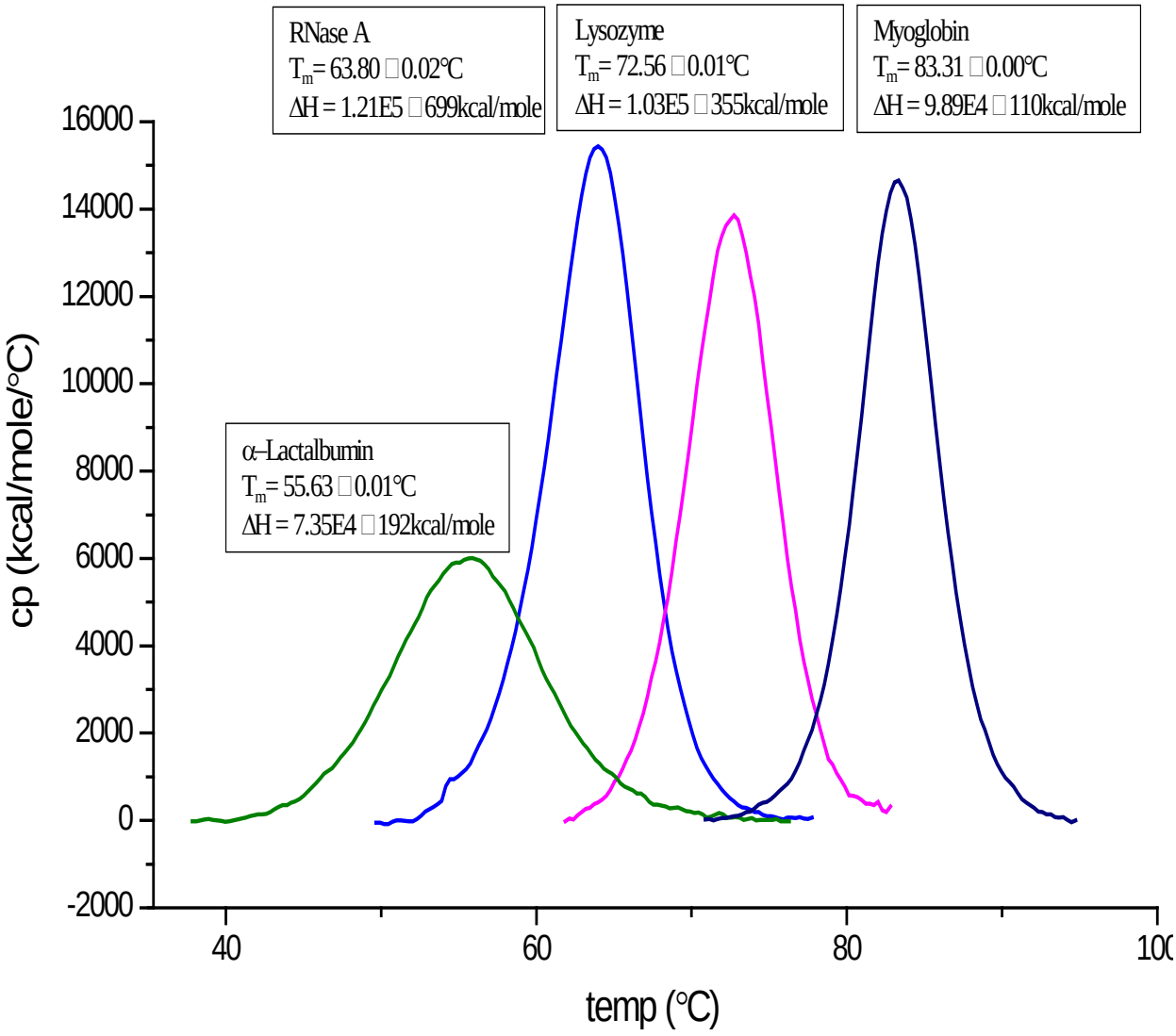

Figure 6.10 DSC transition curve of RNase A, Lysozyme C, Lactalbumin and Myoglobin in 12.5 mM phosphate buffer at pH 7.4

6.12.2 Proteins adsorption on OT, FOT SAMs at different concentrations

Figures 6.11 to 6.14 represent the SPR association and dissociation curves of lysozyme, RNase A, lactalbumin and myoglobin at different concentrations on the surfaces of OT- Au and FOT-Au. Each adsorption curve was fitted with BIAevalution software using kinetic fitting and a drifting baseline model using the following equation:

For the adsorption: A + B ⇌ AB

where A is analyte, B is the surface binding sites and AB is analyte – surface complex upon adsorption.

For association phase: $dR_{AB} / dt = k_a C(R_{\max} - R_{AB}) - k_d R_{AB}$ [6.12.2.1]

For dissociation phase: $dR_{AB} / dt = -k_d R_{AB}$ [6.12.2.2]

Total response (RU): $\Gamma = R_{AB} + RI + \text{Drift} \times (t\text{-}t_{on})$ [6.12.2.3]

Where dR_{AB} / dt is the rate of change of the SPR signal caused by the formation of AB, C is the concentration of analyte A, R_{max} is the maximum analyte binding capacity in response unit. RI is the bulk refractive index contribution in the total response (RU), which is simulated as an instantaneous shift in the sensor gram and does not affect the evaluation of kinetic constants. A significant bulk contribution usually impacts the SPR sensorgram for a few seconds.
.
The fitting curves for each SPR curve are also shown in Figures 6.11 to 6.14 to compare with the SPR curve. The adsorption rate constant k_a ($M^{-1}s^{-1}$) of lysozyme, RNase A, lactalbumin, myoglobin at different concentration on OT-Au and FOT-Au was calculated and respectively plotted in Figures 6.15 and 6.16.

The kinetics of protein adsorption is very complicated as protein may undergo conformation change and conformation change may affect the lateral interaction among adsorbed proteins.

We observed that higher protein concentration gave the higher protein adsorption density Here we consider that the protein adsorption occurs in two steps: reversible adsorption and the irreversible conformation change adsorption. As protein concentration increases, the surface is filled in a short time. Thus, the adsorbed protein has less time to spread and further spread will be blocked by the neighboring protein molecules. As a result, the adsorption on the hydrophobic surfaces has greater surface density of protein. In other words, the higher surface density coverage of protein will decrease the degree of protein structural changes in the adsorbed proteins as at higher surface coverage the area available for protein spreading is limited and reduced. [202-205] We observed that a positive relationship between the lower surface coverage of protein and an increased adsorption rate constant k_a on both surfaces of OT-Au and FOT-Au. This may be explained by considering that at higher concentration, the lateral interactions such as electrostatic repulsion among adsorbed protein molecules are stronger, thus the adsorption rate constant k_a is lower.

When adsorption rate constants are compared for protein adsorption on OT-Au and FOT-Au surface, at high concentrations the rate constants for protein adsorption on OT-Au and FOT-Au surfaces are similar. At low concentration, the protein adsorption rate constants on FOT-Au surfaces are less than for the same protein on OT-Au. Since at lower concentration, the lateral interactions are reduced, the adsorption rate and conformation change will be more dependent on the adsorption and spreading of individual protein molecule. This is presumably caused as the greater protein conformational change induced at low concentration by FOT-Au surface need longer times to take place, consequently reducing the adsorption rate as compared with OT-Au surface.

The protein adsorption rate constant (k_a) four proteins lysozyme, RNase A, lactalbumin and myoglobin on OT-Au and FOT-Au surfaces are compared in Figure 6.16. Figure 6.16 shows that

the hard proteins (lysozyme and RNase A) have greater k_a than soft proteins (lactalbumin and myoglobin) on both surfaces. It is presumably caused as the "soft" proteins have greater loss of conformation compared to "hard" protein during the adsorption process. Thus, "soft" proteins need a longer time to reach their denatured states. In addition, the calculated average superficial hydrophobicity of the "hard" proteins are greater than that of the "soft" proteins, which might be also contributed to the faster protein adsorption rate constant due to the stronger hydrophobic interactions before the next slower step of adsorption (protein denaturation) happens. In addition, for "hard" protein lysozyme C and RNase A, we observed an "overshooting" effect (the adsorption curve slight decreases as a function of time instead of increasing). This was presumably caused because the adsorption rate was faster than the proteins' denaturing and spreading rate. Thus, the adsorbed proteins have filled the surface before they have the opportunity to denature and spread.

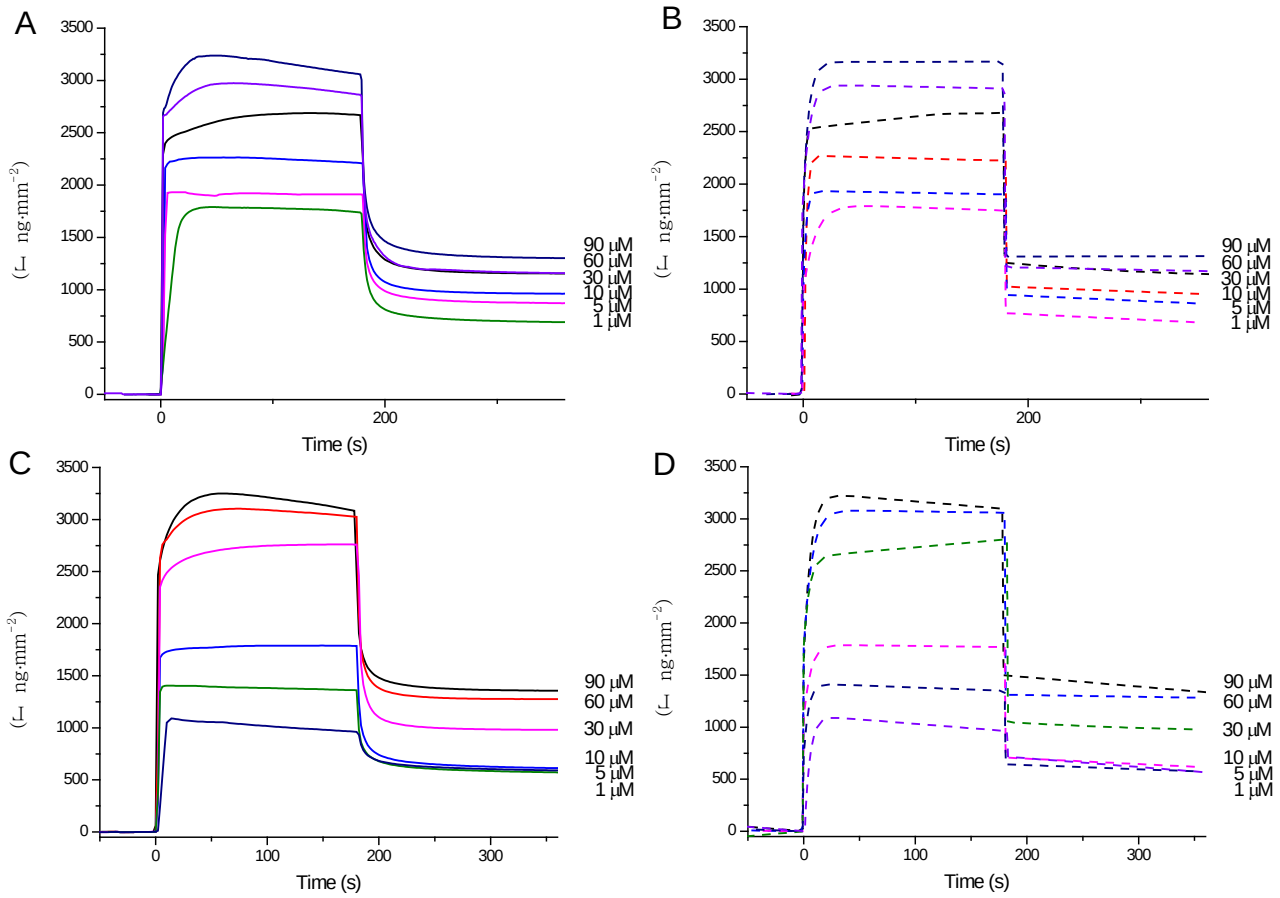

Figure 6.11 Adsorption (A) and kinetic fitting curve (B) for lysozyme on an OT-Au surface. (C) and (D) similarly on an FOT-Au surface.

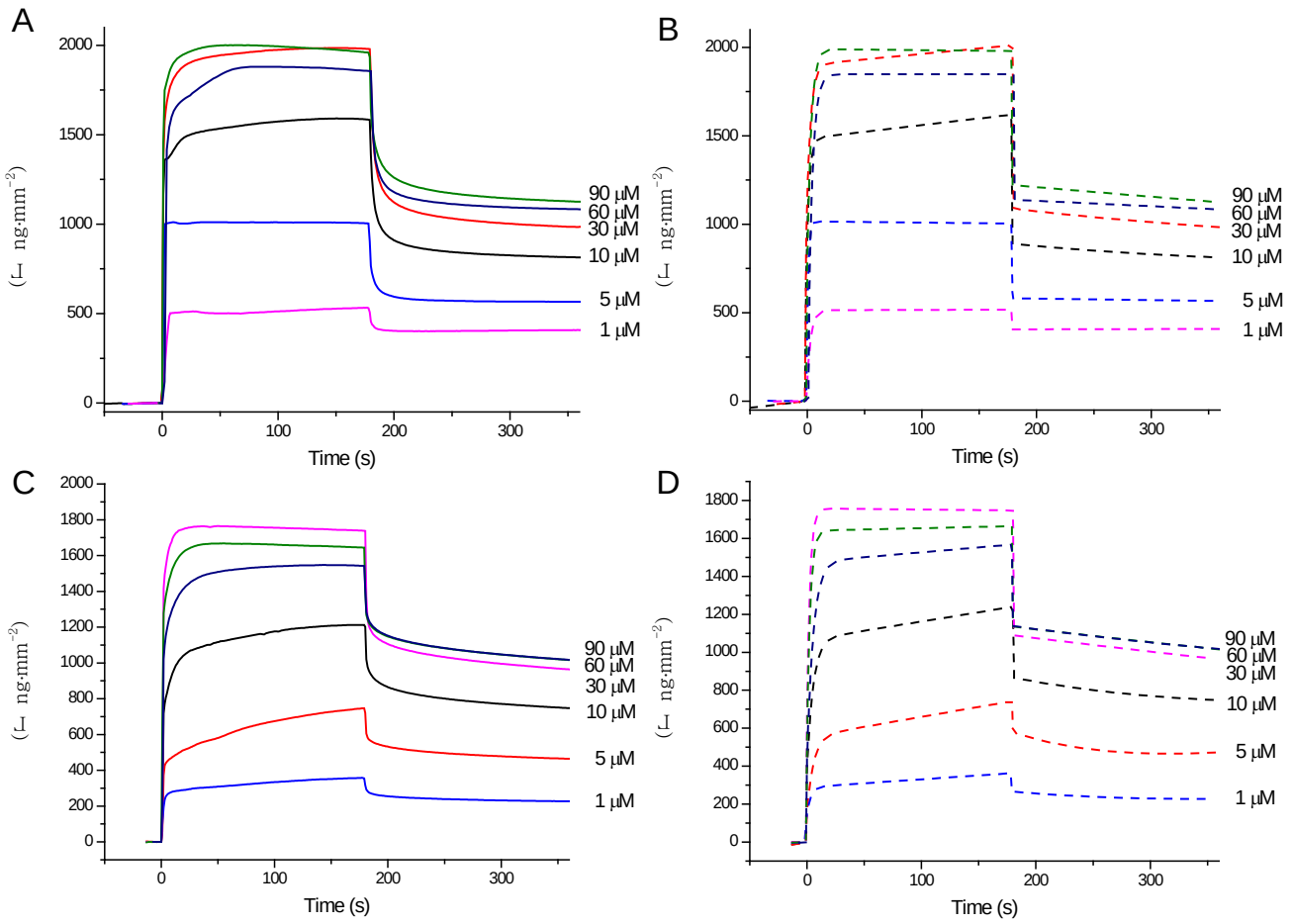

Figure 6.12 Adsorption (A) and kinetic fitting curve (B) for RNase A on an OT-Au surface. (C) and (D) similarly on an FOT-Au surface.

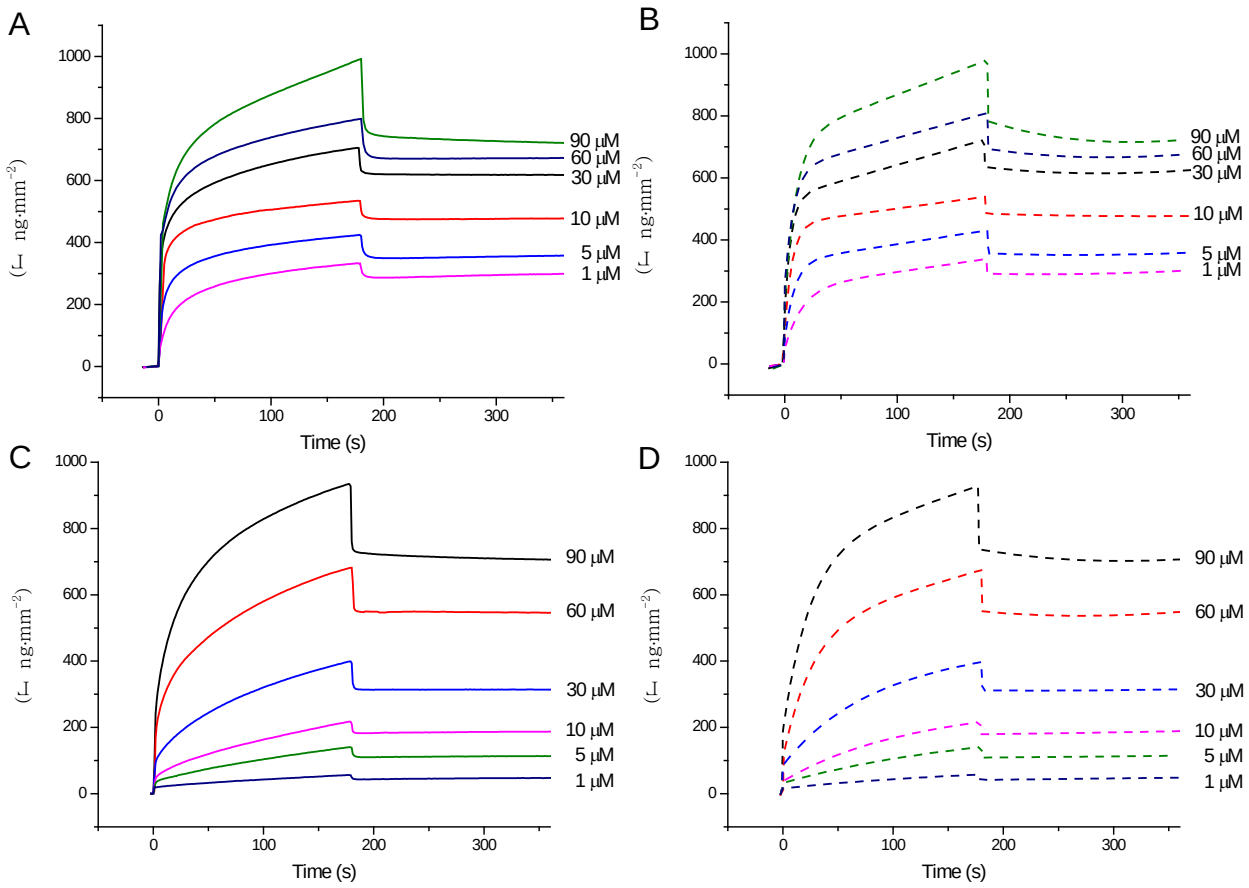

Figure 6.13 Adsorption (A) and kinetic fitting curve (B) for Lactalbumin on an OT-Au surface. (C) and (D) similarly on an FOT-Au surface.

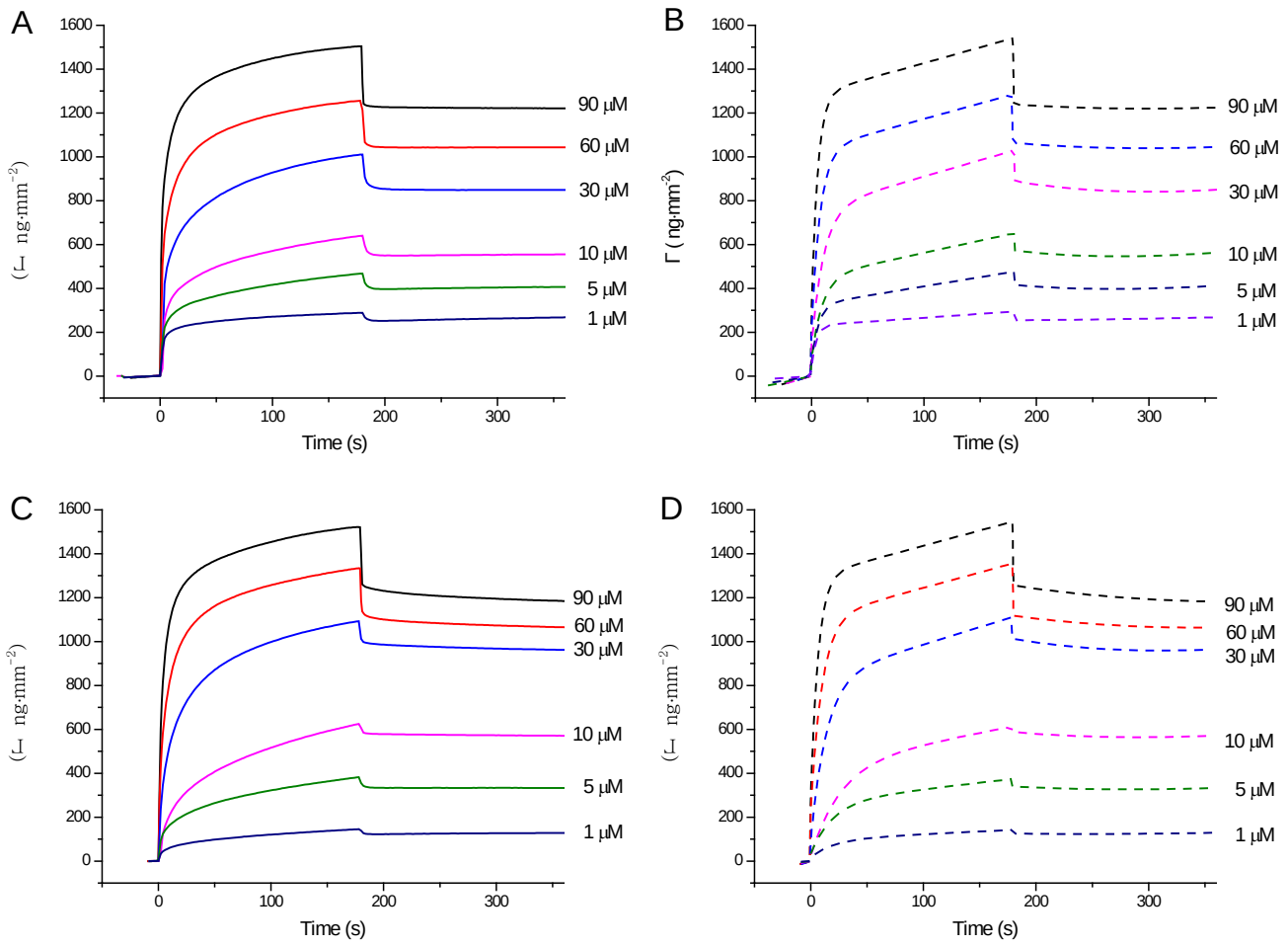

Figure 6.14 Adsorption (A) and kinetic fitting curve (B) for Myoglobin on an OT-Au surface. (C) and (D) similarly on an FOT-Au surface.

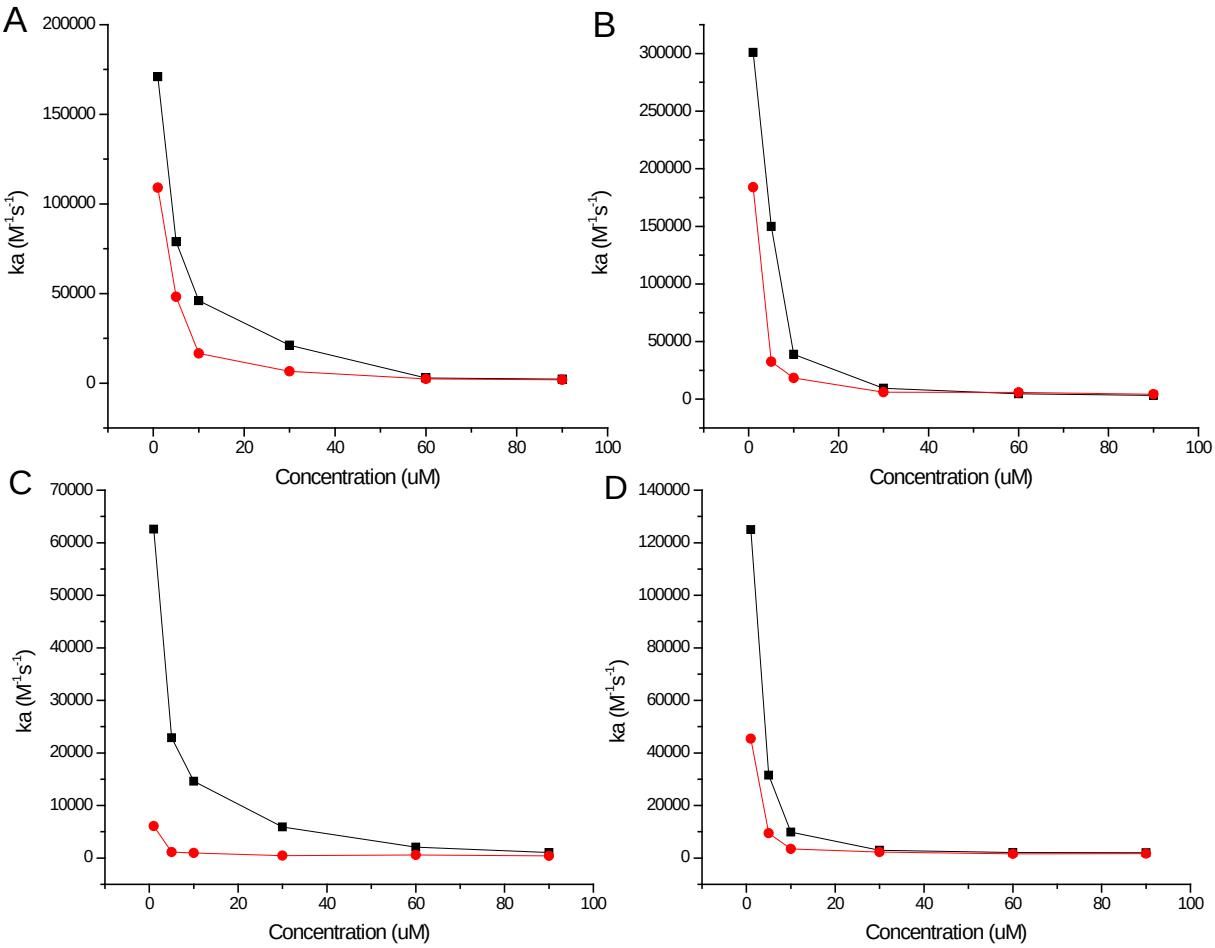

Figure 6.15 The adsorption rate constant of A) lysozyme, B) RNase, C) lactalbumin and D) myoglobin on OT-Au (■) and FOT-Au (●).

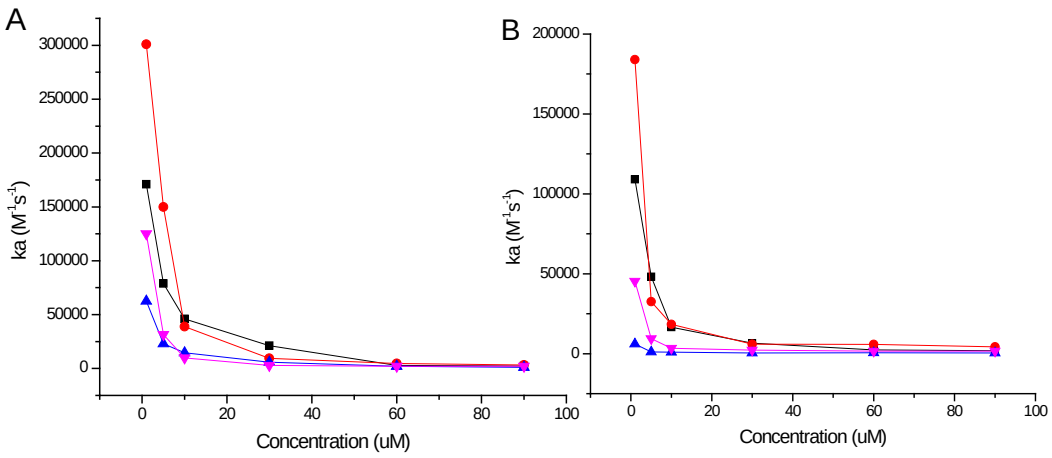

Figure 6.16 The adsorption rate constant of lysozyme (■), RNase A (●), lactalbumin (▲) and myoglobin (▼) on OT-Au (A) and FOT-Au (B).

6.13 pH effect on protein adsorption

6.13.1 Protein structure and the calculation of hydrophobicity and flexibility

Here we chose ubiquitin and cytochrome c to study the pH effect on different proteins as they have large differences in isoelectric point, amongst other properties. Some physiochemical properties of these species listed in Table 6.8. Cytochrome c is a small globular heme protein and serves as an electron carrier in the respiratory chain of mitochondria. It consists of 104 amino acid residues with molecular weight 12 kDa. Ubiquitin is a regulatory globular protein, consisting of 76 amino acid residues with molecular mass of about 8.5 kDa. It regulates a host of processes in eukaryotic cells through the covalent attachment to other proteins.[206]

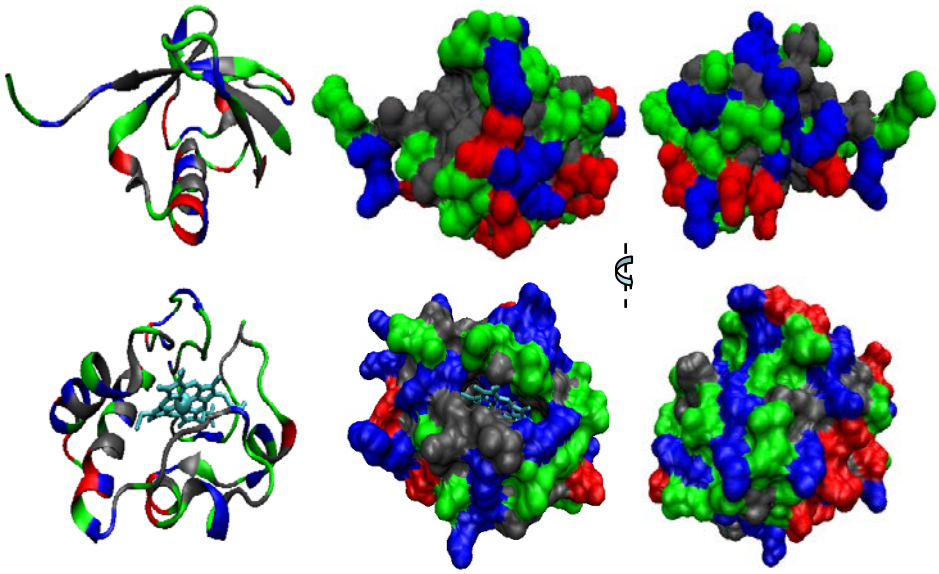

Figure 6.17 Proteins (a) Ubiquitin (1UBQ)[207] (b) Cytochrome c (1HRC)[208], its interaction surfaces ; Acid (red), basic (blue), polar (green), hydrophobic (grey) groups. All diagrams were generated by VMD.[189]

The three-dimensional structures of cytochrome c and ubiquitin are known to high resolution from X-ray crystallography and obtained from the Protein Data Bank. The 3D structure and surface properties of cytochrome c and ubiquitin are shown in Figure 6.17, which are generated by program VMD [189].

6.13.2 The properties of cytochrome c and ubiquitin.

In this study, we chose pH range 4.5-8.5 to study the pH effect on different protein adsorption. First, we measured protein conformation change in the same pH range. As shown in the CD spectra of ubiquitin and cytochrome c in 30μM phosphate buffer at pH 4.5, 5.5, 6.5, 7.5 and 8.5 (Figure 6.18), no protein conformation changes were observed over this pH range. Theorell and Akesson showed that five different conformations (Ⅰ to Ⅴ) of cytochrome c were observed between pH 0 and pH 14 with dissociation constants $pK_{\text{Ⅰ-Ⅱ}}$=0.42, $pK_{\text{Ⅱ-Ⅲ}}$=2.50, $pK_{\text{Ⅲ-Ⅳ}}$

=9.35, p$K_{\text{IV-V}}$=12.76. [209] Thus, over the pH range used here, the native conformation of cytochrome c (state Ⅲ) should be dominant.

Kondo *et al*. demonstrated that cytochrome c, like RNase A and lysozyme C undergo less protein conformation change upon the adsorption compared to the "soft" protein bovine serum albumin, which could be considered as a more stable "hard" protein [200,202]. Vihinen and Torkkila showed inverse correlation between thermal stability and structural flexibility by calculation. [210] Usually the residues within protein core are more tightly bound compared to surface residues as the latter lack stabilizing interactions. From the protein flexibility calculation, ubiquitin is "softer" than cytochrome c. But the calculated protein average superficial hydrophobicity shows that the surface of ubiquitin is more hydrophobic than that of cytochrome c.

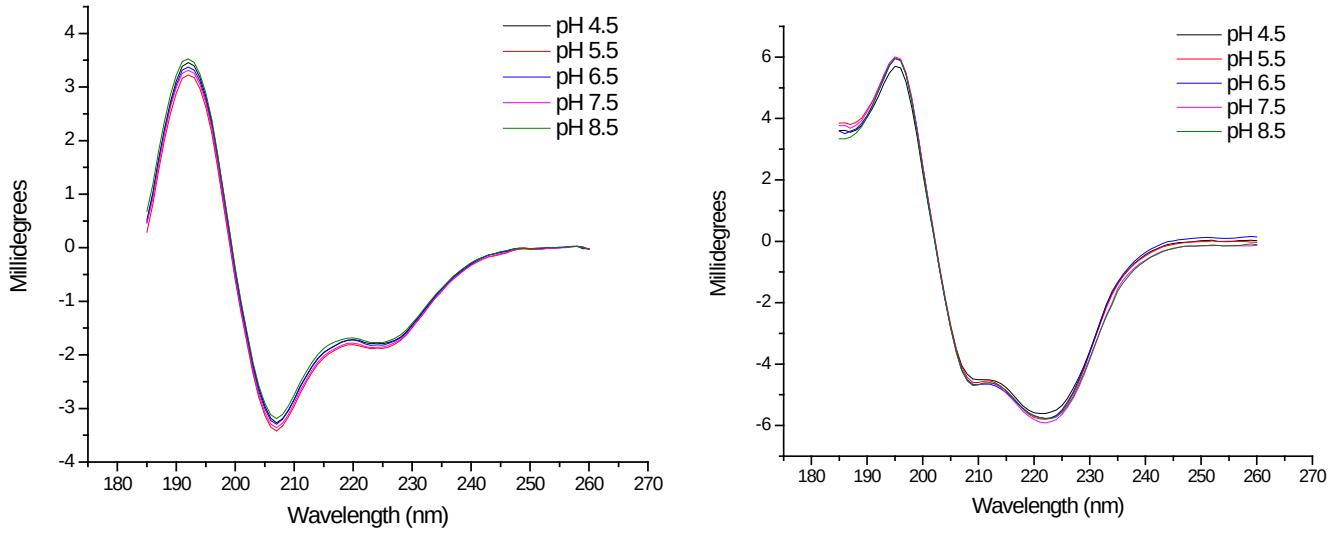

Figure 6.18 CD spectra of (a) ubiquitin and (b) cytochrome c in 30μM phosphate buffer at pH 4.5, 5.5, 6.5, 7.5 and 8.5

Table 6.8 Some properties of the proteins: ubiquitin and cytochrome c.

Protein	ubiquitin (from bovine red blood cells erythrocytes)	cytochrome c (from horse heart)
PDB ID	1UBQ	1HRC
Molar mass (D)	8565	12327
Size (nm^3)	5.1 × 4.3 × 2.9	5.8 × 5.8 × 4.2
Isoelectric point (pH unit)	6.5	10.0
T_m (°C)	95.6 pH 7.4	85.3 pH7.4
Δ G (kcal/mol)	6.0, pH 5.0 [211]	5.4, pH 7.0 [212]

6.13.3 protein conformation and adsorption on OT, FOT, MOT surface in the range of pH 4.5-8.5

We studied the pH effect on protein adsorption here on three kinds of surface: OT-Au, FOT-Au and MOT-Au. As discussed before, FOT-Au and OT-Au surface are both hydrophobic and FOT-Au is more hydrophobic than OT-Au surface. MOT surface is hydrophilic due to the surface hydroxyl groups.

pH has a critical effect on the adsorption as the protein net charge and stability are pH dependent. Thermal unfolding Gibbs energy changes depend strongly on pH, a result that may be attributed to the pH dependence of protein charge-charge interactions. [213] Some research has indicated that the maximum adsorption may occur at the isoelectric point (pI) due to the higher

stability of proteins and minimum electrostatic repulsion among the adsorbed proteins. [190, 214, 215]

For an MOT-Au surface, the surface hydrogen bonds could be formed between hydroxyl-carbonyl, hydroxyl-hydroxyl and hydroxyl-amide in protein adsorption. The pI of cytochrome c is around pH 10 and it has net positive charge of +5e to +6e at pH 7.[216] In the range of pH 8.5 to 4.5, the positive charge gradually increases. As shown in Figure 6.19, the quantity of cytochrome c adsorbed increased as pH increased from 4.5 to 8.5, which is consistent with the reduction of lateral electrostatic repulsion among the adsorbed proteins as the pH approaches the pI. However, we did not observe the maximum adsorption at pH 6.5 for ubiquitin (pI 6.5). Since the pI of protein only describe the average charge state of protein, and the local charge on the protein surface should also impact adsorbed protein lateral interactions, maximum adsorption does not always occur at pH=pI for all of proteins. The quantity of protein adsorbed as a function of pH may also change as the protein adsorption orientation is also pH dependent. [201]

As shown in Figure 6.19, the adsorptions of proteins on OT-Au and FOT-Au surfaces have same trend as a function of pH, but the quantity adsorbed on OT-Au is greater than on FOT-Au. Since proteins interact with these two surfaces through hydrophobic interactions and the surface of FOT-Au is of greater hydrophobicity, we assume that the proteins on FOT-Au are more strongly denatured and spread so that individual protein molecules occupies more surface area compared to protein molecules adsorbed on an OT-Au surface. A number of studies reported higher affinity and stronger denaturing effect on hydrophobic surfaces than hydrophilic surfaces. [204, 217, 218] We clearly observed in the pH range 4.5-8.5, the maximum quantity of ubiquitin adsorbed on MOT-Au is much less than on OT-Au surface, similarly for cytochrome c except at pH 7.5 and 8.5.

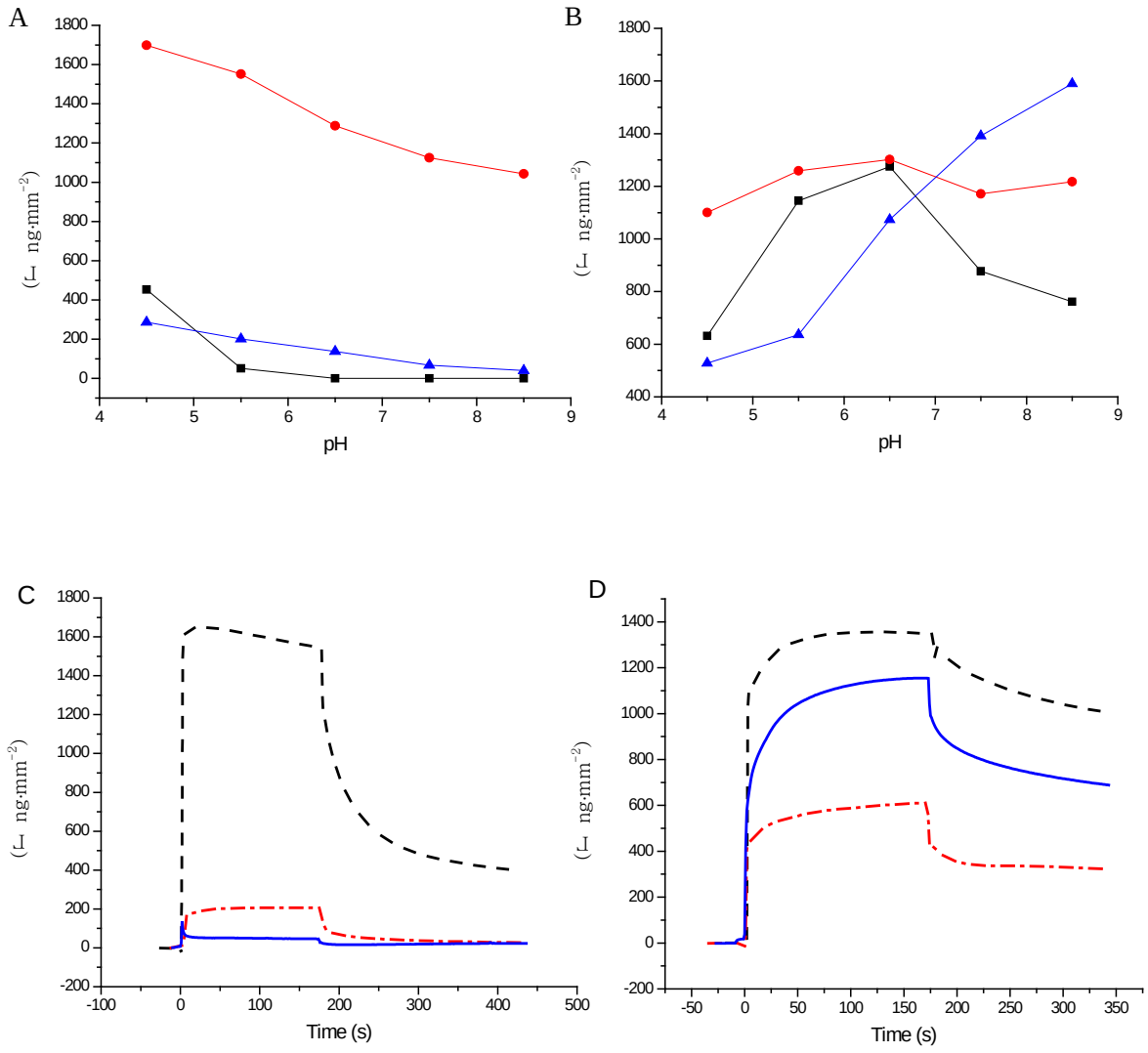

Figure 6.19 The maximum adsorption amount of (A) ubiquitin (B) cytochrome c on the surfaces of OT-Au (●), FOT-Au(■), MOT-Au(▲). Adsorption curve of Ubiquitin (C) and Cytochrome C (D) and the surfaces of OT-Au (dash), MOT-Au (dash dot) and FOT-Au (solid line) in 30mmol phosphate buffer at pH 5.5

In the pH range 4.5 to 8.5, the relative decrease of adsorption of ubiquitin on FOT-Au compared to OT-Au was greater than that observed for cytochrome c. Since ubiquitin is more flexible than cytochrome c, albeit of smaller size, we presume that after denaturation on FOT-Au

ubiquitin achieves a greater surface-protein contact area. For ubiquitin adsorption on the FOT-Au surface under pH 6.5, 7.5, or 8.5, we did not acquire the adsorption signal because it was under the detection limit. For mass loading measurement, the sensitivity of SPR is of a detection limit of about 10pg/mm^2, which corresponds to about seven hundred million ubiquitin molecules (8.5kDa) on a 1mm^2 sensing area.

In addition, we observed the "overshooting" effect for ubiquitin. Since the calculated average superficial hydrophobicity indicated that the surface of ubiquitin is more hydrophobic than that of cytochrome c, the "overshooting" may be caused as the adsorption rate of ubiquitin was faster than its denature and spreading rate, similar to the observations with lysozyme C and RNase A.

Conclusions

The kinetics of adsorption of two "hard" proteins (lysozyme C and RNase A) and two "soft" proteins (Lactalbumin and myoglobin) on OT-Au and FOT-Au surfaces were studied. The conclusions from this study are summarized as follows:

1. We observed that a positive relationship among the lower protein concentration, the lower surface coverage of protein and an increased adsorption rate constant k_a on both surfaces of OT-Au and FOT-Au. The lower protein concentration gives lower lateral protein electrostatic repulsion interaction, thus leading to an increased adsorption rate constant $k_{a.}$

2. We observed that at high concentration the protein adsorption rate constants on OT-Au and FOT-Au surface are similar. At low concentration, the protein adsorption rate constants on FOT-Au surface are less than for the same protein on OT-Au surface. This was presumably caused as the greater protein conformation change induced by the FOT-

Au surface needs a longer time to achieve, decreasing the overall adsorption rate.

3. Comparing the protein adsorption rate constant (k_a), four proteins lysozyme, RNase A, lactalbumin and myoglobin on OT-Au and FOT-Au surfaces show that the "hard" proteins (lysozyme and RNase A) have greater k_a than "soft" proteins (lactalbumin and myoglobin) for both surfaces. This occurs as the "soft" proteins lost more protein conformation compared to "hard" protein during the adsorption process, thus the "soft" proteins need a longer time to reach their denatured conformation. In addition, the calculated average superficial hydrophobicity of the "hard" proteins are greater than that of the "soft" proteins, which may lead to a higher protein adsorption rate constant (k_a) when interacting with the hydrophobic surfaces.

The adsorption of two proteins: cytochrome c and ubiquitin on the OT-Au, FOT-Au and MOT-Au surfaces were studied in the pH range 4.5 to 8.5. For an MOT-Au surface, the quantity of cytochrome c adsorbed increased as pH increased from 4.5 to 8.5, consistent with the reduction of lateral electrostatic repulsion among the adsorbed proteins as the pH approaches the protein pI . However, we did not observe the maximum adsorption at pH 6.5 for ubiquitin (pI=6.5). Adsorption of cytochrome c and ubiquitin on OT-Au and FOT-Au surfaces show a similar trend as a function of pH, but the adsorption of proteins on OT-Au is greater than FOT-Au due to stronger denaturation and spreading so that individual protein molecules occupy more surface area on FOT-Au. The adsorption decrease of ubiquitin on FOT-Au surface compared to it on OT-Au surface was larger than the decrease of cytochrome c on these surfaces due to the smaller size of ubiquitin and greater flexibility of its structure.

Chapter 7
Conclusions

In this thesis, I have described a study of the interactions between solution-phase macromolecules and a series of solid surfaces, focusing on metal oxide and perfluorinated interfaces. To understand these interactions at the solid-liquid interface, the surface properties were studied using a series of techniques, including zeta potential, atomic force microscopy, X-ray photoelectron spectroscopy, attenuated total reflection Fourier transform infrared spectroscopy, surface Plasmon resonance, and contact angle measurements. These methods probed surface charge, surface topography, surface composition, overlayer thickness and molecular orientation, and the relation between protein adsorption dynamics and suface hydrophobicity.

The interactions between molecules and solid surface at liquid-solid interface are both complex and diverse. The various interaction forces studied include hydrophobic effects, electrostatic repulsion, ionic hydrogen bonding, hydrogen bonding, and van der Waals forces. Specifc observations were as follows:

1. Chemical force titration was used to study the adhesion force between phenol-terminated AFM tip and various iron/aluminum hydr(oxide) colloidal particles which were modified by phosphate, GA or TA. The formation of strong ionic hydrogen bonding, between phenol and all oxo Fe-OH surface sites at higher pH and between phenol and protonated Fe-OH sites at lower pH dominate the adhesion force interactions of the phenol-terminated tip against the iron hydroxide colloid surface. Similarly, strong ionic hydrogen bonding between phenol and Al-OH surface sites in the pH range of 9 to 11 and 3 to 7 dominate the adhesion force interaction of the phenol-terminated tip against the surface of aluminum hydroxide colloid. Adsorption of

phosphate anions or TA blocks surface binding sites on both colloids to phenol groups. In addition, GA switches the adsorption functional geometry depending on precipitation methods.

2. We studied the surface modification of PDMS using overlayers of fluoroalkylsilane molecules (nonafluorohexyltriethoxysilane (PF6), 1H,1H,2H,2H-perfluorooctyltriethoxysilane (PF8), 1H,1H,2H,2H -perfluorodecyltriethoxysilane (PF10), or 1H,1H,2H,2H-perfluorododecyltriethoxysilane (PF12)), which have similar structure but different fluoroalkyl chain length. The experimental results showed the solvent compatibility has an important impact on the deposition process. PDMS covered with a flourous-terminated overlayer exhibits lower surface roughness compared to freshly-oxidized PDMS and, other than the short chain PF-6 species, have a similar fluoroalkylsilane molar density on the surface, regardless of chain length. The potential values of unmodified PDMS and various perfluorinated PDMS were quite independent of pH with the order of magnitude of potential PF-12 ≈ PF-10 > PF-8 > PF-6 > PDMS. This may be explained by a combination of changes in surface modifying molecule density, relative surface dipole moments and fluoroalkyl chain lengths.

3. The kinetics of adsorption of two "hard" proteins (lysozyme C and RNase A) and two "soft" proteins (Lactalbumin and myoglobin) on the self-assembled monolayers of 1H, 1H, 2H, 2H-perfluorooctyl-1-thiol (FOT) modified Au surface were studied. We observed that a positive relationship among the lower protein concentration, the lower surface coverage of protein and an increased adsorption rate constant k_a on both surfaces. We observed that at low concentration, the protein adsorption rate constants on FOT-Au surface are less than for the same protein on OT-Au surface. This was presumably caused as the greater protein conformation change induced by the FOT-Au surface needs a longer time to achieve, decreasing the overall adsorption rate. In addition, the "hard" proteins have greater k_a than "soft" proteins for both surfaces. This occurs as the "soft" proteins lost more protein conformation compared to "hard" protein during the

adsorption process, thus the “soft” proteins need a longer time to reach their denatured conformation.

With the advancing developments in miniaturization, the studies of properties of interfaces and molecular interactions at interfaces become more crucial in physics, materials science, chemistry, and biology due to the increasing surface-to-bulk ratio in miniaturization. The interaction forces are not only influenced by the chemical nature and physical properties of surfaces but also influenced by the interacting molecules and surrounding medium. Our work presented several examples in this research field and provided the basic understand of molecule-surface interactions. New techniques and new ways to characterize materials and test molecule-surface interaction will make tremendous contributions in this research field.

Reference

1. Grimal, J.Y., E. Frossard, and J.L. Morel, *Maize root mucilage decreases adsorption of phosphate on goethite.* Biology and Fertility of Soils, 2001. **33**(3): p. 226-230.
2. Liu, F., et al., *Competitive adsorption of sulfate and oxalate on goethite in the absence or presence of phosphate.* Soil Science, 1999. **164**(3): p. 180-189.
3. Borggaard, O.K. and A.L. Gimsing, *Fate of glyphosate in soil and the possibility of leaching to ground and surface waters: a review.* Pest Management Science, 2008. **64**(4): p. 441-456.
4. Violante, A., C. Colombo, and A. Buondonno, *Competitive adsorption of phosphate and oxalate by aluminum-oxides.* Soil Science Society of America Journal, 1991. **55**(1): p. 65-70.
5. Gimsing, A.L. and O.K. Borggaard, *Competitive adsorption and desorption of glyphosate and phosphate on clay silicates and oxides.* Clay Minerals, 2002. **37**(3): p. 509-515.
6. Borggaard, O.K., *Comparison of EDTA and oxalate as extractants for amorphous iron-oxides in soil.* Acta Agriculturae Scandinavica, 1984. **34**(2): p. 244-248.
7. Grafe, M., et al., *Adsorption of arsenate and arsenite on ferrihydrite in the presence and absence of dissolved organic carbon.* Journal of Environmental Quality, 2002. **31**(4): p. 1115-1123.
8. Hinsinger, P., *Bioavailability of soil inorganic P in the rhizosphere as affected by root-induced chemical changes: a review.* Plant and Soil, 2001. **237**(2): p. 173-195.
9. vanLoon, G.W. and S.J. Duffy, *Environmental chemistry: a global perspective* 2005, New York: Oxford University Press.
10. Guan, X.H., C. Shang, and G.H. Chen, *Competitive adsorption of organic matter with phosphate on aluminum hydroxide.* Journal of Colloid and Interface Science, 2006. **296**(1): p. 51-58.
11. Guan, X.H., et al., *Role of carboxylic and phenolic groups in NOM adsorption on minerals: a review.* Water Science & Technology: Water Supply, 2006. **6**(6): p. 155-164.
12. Johnson, S.B., et al., *Adsorption of organic matter at mineral/water interfaces. 2. Outer-sphere adsorption of maleate and implications for dissolution processes.* Langmuir, 2004. **20**(12): p. 4996-5006.

13. Chi, F.H. and G.L. Amy, *Kinetic study on the sorption of dissolved natural organic matter onto different aquifer materials: the effects of hydrophobicity and functional groups.* Journal of Colloid and Interface Science, 2004. **274**(2): p. 380-391.
14. Aiken, G.R., et al., *Humic substances in soil, sediment and water*. 1985, New York: John Wiley & Sons, Inc.
15. Noy, A., et al., *Chemical force microscopy - exploiting chemically-modified tips to quantify adhesion, friction, and functional-group distributions in molecular assemblies.* Journal of the American Chemical Society, 1995. **117**(30): p. 7943-7951.
16. Omoike, A.I. and G.W. Vanloon, *Removal of phosphorus and organic matter removal by alum during wastewater treatment.* Water Research, 1999. **33**(17): p. 3617-3627.
17. Cathalifaud, G., J. Ayele, and M. Mazet, *Aluminium ions organic molecules complexation: Formation constants and stoichiometry. Application to drinking water production.* Water Research, 1997. **31**(4): p. 689-698.
18. Smith, D.A., et al., *The effect of electrolyte concentration on the chemical force titration behavior of omega-functionalized SAMs: Evidence for the formation of strong ionic hydrogen bonds* J. Phys. Chem. B, 2000. **104**: p. 8862.
19. Feng, W.Y., Y. Ling, and C. Lifshitz, *Reactivity of mixed and neat proton bound dimers of acetonitrile and methyl acetate.* Journal of Physical Chemistry, 1996. **100**(1): p. 35-39.
20. Meotner, M. and L.W. Sieck, *The ionic hydrogen-bond and ion solvation .5. OH...O$^-$ bonds - gas-phase solvation and clustering of alkoxide and carboxylate anions.* Journal of the American Chemical Society, 1986. **108**(24): p. 7525-7529.
21. Douma, M., et al., *The adsorption of globular proteins onto a fluorinated PDMS surface*. Vol. 331. 2009: Elsevier Science. 90-97.
22. Wang, D., et al., *Surface modification of poly(dimethylsiloxane) with a perfluorinated alkoxysilane for selectivity toward fluorous tagged peptides.* Langmuir, 2008. **24**(15): p. 8395-8395.
23. Ostuni, E., et al., *Adsorption of proteins to hydrophobic sites on mixed self-assembled monolayers.* Langmuir, 2003. **19**(5): p. 1861-1872.
24. Mccarthy, J.F. and J.M. Zachara, *Subsurface transport of contaminants - mobile colloids in the subsurface environment may alter the transport of contaminants.* Environmental Science & Technology, 1989. **23**(5): p. 496-502.
25. Levine, *Physical Chemistry* 2001, Boston.

26. Schwertmann, U., *Relations between iron-oxides, soil color, and soil formation.* Soil Color, 1993. **31**: p. 51-&159.
27. Davydov, A.A. and C. Rochester, *Infrared spectroscopy of adsorbed species on the surface of transition metal oxides*. 1990, Chichester, UK Wiley.
28. Russell, J.D., et al., *Surface-structures of gibbsite goethite and phosphated goethite.* Nature, 1974. **248**(5445): p. 220-221.
29. Felmy, A.R. and J.R. Rustad, *Molecular statics calculations of proton binding to goethite surfaces: Thermodynamic modeling of the surface charging and protonation of goethite in aqueous solution.* Geochimica Et Cosmochimica Acta, 1998. **62**(1): p. 25-31.
30. Gastuche, M.C. and A. Herbillon, *Etude des gels dalumine-cristallisation en milieu desionise.* Bulletin De La Societe Chimique De France, 1962(7): p. 1404.
31. Parfitt, R.L., et al., *Adsorption on hydrous oxides .2. oxalate, benzoate and phosphate on gibbsite.* Journal of Soil Science, 1977. **28**(1): p. 40-47.
32. Sposito, G., *The surface chemistry of soils*. 1984, New York, Oxford: Oxford University Press, Clarendon Press.
33. Borggaard, O.K., *Soil chemistry in a pedological context (6th Edition)*. 2002, Frederiksberg: DSR Forlag.
34. Hiemstra, T. and W.H. Van Riemsdijk, *Surface structural ion adsorption modeling of competitive binding of oxyanions by metal (hydr)oxides.* Journal of Colloid and Interface Science, 1999. **210**(1): p. 182-193.
35. Auerswald, K., H. Stanjek, and J.M. Bigham, *Soil and environment-soil processes from mineral to landscape scale*, Reiskirchen: Catena-Verlag.
36. Hingston, F.J., et al., *Specific adsorption of anions.* Nature, 1967. **215**(5109): p. 1459
37. Hingston, F.J., A.M. Posner, and J.P. Quirk, *Competitive adsorption of negatively charged ligands on oxide surfaces.* Discussions of the Faraday Society, 1971(52): p. 334
38. Stevenson, F.J., *Humus chemistry: genesis, composition, reactions*. 2 nd ed ed. 1994, New York: John Wiley & Sons, Ltd.
39. Swift, R.S., *Macromolecular properties of soil humic substances: Fact, fiction, and opinion.* Soil Science, 1999. **164**(11): p. 790-802.
40. Buffle, J., F.L. Greter, and W. Haerdi, *Measurement of complexation properties of humic and fulvic acids in natural-waters with lead and copper ion-selective electrodes.* Analytical Chemistry, 1977. **49**(2): p. 216-222.

41. Haworth, R.D., *Chemical nature of humic acid.* Soil Science, 1971. **111**(1): p. 71
42. Schulten, H.R. and M. Schnitzer, *Chemical model structures for soil organic matter and soils.* Soil Science, 1997. **162**(2): p. 115-130.
43. Stein, L.T., et al., *Conformational modelling of a proposed building block of humic acid: Searching chirally undefined conformational space.* Polish Society of Humic Substances, 1997: p. 73-77.
44. Stevenson, I.L. and M. Schnitzer, *Transmission electron-microscopy of extracted fulvic and humic acids.* Soil Science, 1982. **133**(3): p. 179-185.
45. Burdon, J., *Are the traditional concepts of the structures of humic substances realistic?* Soil Science, 2001. **166**(11): p. 752-769.
46. Sutton, R. and G. Sposito, *Molecular structure in soil humic substances: The new view.* Environmental Science & Technology, 2005. **39**(23): p. 9009-9015.
47. Piccolo, A., *The supramolecular structure of humic substances.* Soil Science, 2001. **166**(11): p. 810-832.
48. Simpson, A.J., et al., *Molecular structures and associations of humic substances in the terrestrial environment.* Naturwissenschaften, 2002. **89**(2): p. 84-88.
49. Wershaw, R.L., *Molecular aggregation of humic substances.* Soil Science, 1999. **164**(11): p. 803-813.
50. Hayes, M.H.B. and C.E. Clapp, *Humic substances: Considerations of compositions, aspects of structure, and environmental influences.* Soil Science, 2001. **166**(11): p. 723-737.
51. McCarroll, M., K. Toerne, and R. von Wandruszka, *Micellar fluidity and preclouding in mixed surfactant solutions.* Langmuir, 1998. **14**(11): p. 2965-2969.
52. von Wandruszka, R., *The micellar model of humic acid: Evidence from pyrene fluorescence measurements.* Soil Science, 1998. **163**(12): p. 921-930.
53. Davis, J.A., *Adsorption of natural dissolved organic-matter at the oxide water interface.* Geochimica Et Cosmochimica Acta, 1982. **46**(11): p. 2381-2393.
54. Gu, B.H., et al., *Adsorption and desorption of natural organic-matter on iron-oxide - mechanisms and models.* Environmental Science & Technology, 1994. **28**(1): p. 38-46.
55. Ochs, M., B. Cosovic, and W. Stumm, *Coordinative and hydrophobic interaction of humic substances with hydrophilic Al_2O_3 and hydrophobic mercury surfaces.* Geochimica Et Cosmochimica Acta, 1994. **58**(2): p. 639-650.

56. Vermeer, A.W.P., W.H. van Riemsdijk, and L.K. Koopal, *Adsorption of humic acid to mineral particles. 1. Specific and electrostatic interactions.* Langmuir, 1998. **14**(10): p. 2810-2819.

57. Filius, J.D., et al., *Modeling the binding of fulvic acid by goethite: The speciation of adsorbed FA molecules.* Geochimica Et Cosmochimica Acta, 2003. **67**(8): p. 1463-1474.

58. Wang, L.L., Y.P. Chin, and S.J. Traina, *Adsorption of (poly)maleic acid and an aquatic fulvic acid by goethite.* Geochimica Et Cosmochimica Acta, 1997. **61**(24): p. 5313-5324.

59. Meier, M., et al., *Fractionation of aquatic natural organic matter upon sorption to goethite and kaolinite.* Chemical Geology, 1999. **157**(3-4): p. 275-284.

60. Benedetti, M.F., et al., *Metal-Ion binding to humic substances - Application of the nonideal competitive adsorption model.* Environmental Science & Technology, 1995. **29**(2): p. 446-457.

61. Bhatti, J.S., N.B. Comerford, and C.T. Johnston, *Influence of oxalate and soil organic matter on sorption and desorption of phosphate onto a spodic horizon.* Soil Science Society of America Journal, 1998. **62**(4): p. 1089-1095.

62. van den Brand, J., et al., *Interaction of anhydride and carboxylic acid compounds with aluminum oxide surfaces studied using infrared reflection absorption spectroscopy.* Langmuir, 2004. **20**(15): p. 6308-6317.

63. *IUPAC stability constants of metal-Ion complexes. Part B. organic ligands.* 1979, Oxford: Pergamon Press.

64. Verzele, M., P. Delahaye, and C. Dewaele, *A new structural formula for the polygalloyl glucose tannic acids.* Bulletin Des Societes Chimiques Belges, 1984. **93**(2): p. 151-152.

65. Julien, F., B. Gueroux, and M. Mazet, *Comparison of organic-compounds removal by coagulation-flocculation and by adsorption onto preformed hydroxide flogs.* Water Research, 1994. **28**(12): p. 2567-2574.

66. Dentel, S.K., et al., *Sorption of tannic-acid, phenol, and 2,4,5-trichlorophenol on organoclays.* Water Research, 1995. **29**(5): p. 1273-1280.

67. Meitl, M.A., et al., *Transfer printing by kinetic control of adhesion to an elastomeric stamp.* Nature Materials, 2006. **5**(1): p. 33-38.

68. Mukhopadhyay, R., *When PDMS isn't the best.* Analytical Chemistry, 2007. **79**(9): p. 3248-3253

69. Duffy, D.C., et al., *Rapid prototyping of microfluidic systems in poly(dimethylsiloxane).* Analytical Chemistry, 1998. **70**(23): p. 4974-4984.

70. Fritz, J.L. and M.J. Owen, *Hydrophobic recovery of plasma-treated polydimethylsiloxane.* Journal of Adhesion, 1995. **54**(1-2): p. 33-45.

71. Vickers, J.A., M.M. Caulum, and C.S. Henry, *Generation of hydrophilic poly(dimethylsiloxane) for high-performance microchip electrophoresis.* Analytical Chemistry, 2006. **78**(21): p. 7446-7452.

72. Wong, I. and C.M. Ho, *Surface molecular property modifications for poly(dimethylsiloxane) (PDMS) based microfluidic devices.* Microfluidics and Nanofluidics, 2009. **7**(3): p. 291-306.

73. Manz, A., N. Graber, and H.M. Widmer, *Miniaturized total chemical-analysis systems - a novel concept for chemical sensing.* Sensors and Actuators B-Chemical, 1990. **1**(1-6): p. 244-248.

74. Whitesides, G.M., *The origins and the future of microfluidics.* Nature, 2006. **442**(7101): p. 368-373.

75. Ajdari, A., *Generation of transverse fluid currents and forces by an electric field: Electro-osmosis on charge-modulated and undulated surfaces.* Physical Review E, 1996. **53**(5): p. 4996-5005.

76. Stroock, A.D., et al., *Patterning electro-osmotic flow with patterned surface charge.* Physical Review Letters, 2000. **84**(15): p. 3314-3317.

77. Li, D.Q., *Electrokinetics in microfluidics*, ed. A. Hubbard. 2004, San Diego: Elsevier Inc. 15.

78. Effenhauser, C.S., et al., *Integrated capillary electrophoresis on flexible silicone microdevices: Analysis of DNA restriction fragments and detection of single DNA molecules on microchips.* Analytical Chemistry, 1997. **69**(17): p. 3451-3457.

79. Ocvirk, G., et al., *Electrokinetic control of fluid flow in native poly(dimethylsiloxane) capillary electrophoresis devices.* Electrophoresis, 2000. **21**(1): p. 107-115.

80. McDonald, J.C., et al., *Fabrication of microfluidic systems in poly(dimethylsiloxane).* Electrophoresis, 2000. **21**(1): p. 27-40.

81. Mrksich, M. and G.M. Whitesides, *Using self-assembled monolayers to understand the interactions of man-made surfaces with proteins and cells.* Annual Review of Biophysics and Biomolecular Structure, 1996. **25**: p. 55-78.

82. Roach, L.S., H. Song, and R.F. Ismagilov, *Controlling nonspecific protein adsorption in a plug-based microfluidic system by controlling interfacial chemistry using fluorous-phase surfactants.* Analytical Chemistry, 2005. **77**(3): p. 785-796.

83. Prime, K.L. and G.M. Whitesides, *Adsorption of proteins onto surfaces containing end-attached oligo(ethylene oxide) - a model system using self-assembled monolayers.* Journal of the American Chemical Society, 1993. **115**(23): p. 10714-10721.

84. Lee, S. and J. Voros, *An aqueous-based surface modification of poly(dimethylsiloxane) with poly(ethylene glycol) to prevent biofouling.* Langmuir, 2005. **21**(25): p. 11957-11962.

85. Bhushan, B. and M. Cichomski, *Nanotribological characterization of vapor phase deposited fluorosilane self-assembled monolayers deposited on polydimethylsiloxane surfaces for biomedical micro-/nanodevices.* Journal of Vacuum Science & Technology A, 2007. **25**(4): p. 1285-1293.

86. Kawaguchi, T., et al., *Prevention of nonspecific adsorption onto a poly(dimethylsiloxane) microchannel in a microsensor chip by using a self-assembled monolayer.* Journal of Micro-Nanolithography Mems and Moems, 2010. **9**(1).

87. Onclin, S., B.J. Ravoo, and D.N. Reinhoudt, *Engineering silicon oxide surfaces using self-assembled monolayers.* Angewandte Chemie-International Edition, 2005. **44**(39): p. 6282-6304.

88. Troughton, E.B., et al., *Monolayer films prepared by the spontaneous self-assembly of symmetrical and unsymmetrical dialkyl sulfides from solution onto gold substrates - structure, properties, and reactivity of constituent functional-groups.* Langmuir, 1988. **4**(2): p. 365-385.

89. Bain, C.D. and G.M. Whitesides, *Molecular-level control over surface order in self-assembled monolayer films of thiols on gold.* Science, 1988. **240**(4848): p. 62-63.

90. Ulman, A., *Formation and structure of self-assembled monolayers.* Chemical Reviews, 1996. **96**(4): p. 1533-1554.

91. Schwartz, D.K., *Mechanisms and kinetics of self-assembled monolayer formation.* Annual Review of Physical Chemistry, 2001. **52**: p. 107-137.

92. Jiang, S., *Molecular simulation studies of self-assembled monolayers of alkanethiols on Au(111).* Molecular Physics, 2002. **100**(14): p. 2261-2275.

93. Bain, C.D., et al., *Formation of monolayer films by the spontaneous assembly of organic thiols from solution onto gold.* J. Am. Chem. Soc., 1989. **111**(1): p. 321-335.

94. Poirier, G.E. and E.D. Pylant, *The self-assembly mechanism of alkanethiols on Au(111).* Science, 1996. **272**(5265): p. 1145-1148.

95. Bain, C.D., H.A. Biebuyck, and G.M. Whitesides, *Comparison of self-assembled monolayers on gold: coadsorption of thiols and disulfides.* Langmuir, 1989. **5**(3): p. 723-727.

96. Zhuravlev, L.T., *Concentration of hydroxyl-groups on the surface of amorphous silicas.* Langmuir, 1987. **3**(3): p. 316-318.

97. Senaratne, W., L. Andruzzi, and C.K. Ober, *Self-assembled monolayers and polymer brushes in biotechnology: Current applications and future perspectives.* Biomacromolecules, 2005. **6**(5): p. 2427-2448.

98. Wang, R.W., G. Baran, and S.L. Wunder, *Packing and thermal stability of polyoctadecylsiloxane compared with octadecylsilane monolayers.* Langmuir, 2000. **16**(15): p. 6298-6305.

99. Wang, R.W. and S.L. Wunder, *Thermal stability of octadecylsilane monolayers on silica: Curvature and free volume effects.* Journal of Physical Chemistry B, 2001. **105**(1): p. 173-181.

100. Tillman, N., et al., *Incorporation of phenoxy groups in self-assembled monolayers of trichlorosilane derivatives-effects on film thickness, wettability, and molecular-orientation.* Journal of the American Chemical Society, 1988. **110**(18): p. 6136-6144.

101. Srinivasan, U., et al., *Alkyltrichlorosilane-based self-assembled monolayer films for stiction reduction in silicon micromachines.* Journal of Microelectromechanical Systems, 1998. **7**(2): p. 252-260.

102. Lennard-Jones, J.E. and B.M. Dent, *The change in lattice spacing at a crystal boundary.* Proceedings of the Royal Society of London Series a-Containing Papers of a Mathematical and Physical Character, 1928. **121**(787): p. 247-259.

103. Hunter, R.J., *Zeta potential in colloid science: principles and applications*. 1988, London: Academic Press.

104. Stern, O., *The theory of the electrolytic double shift* Zeitschrift für Elektrochemie, 1924. **30**(508).

105. WB, R., S. DA, and S. WR, *Colloidal dispersions*. 1989, Cambridge: Cambridge University Press.

106. Derjaguin, B., *A theory of interaction of particles in presence of electric double layers and the stability of lyophobe colloids and disperse systems.* Acta Physicochimica URSS 1939. **10**(3): p. 333-346.
107. Israelachvili, J., *Intermolecular and Surface Forces*. 1992, New York: Academic Press.
108. Liang, Y., et al., *Interaction forces between colloidal particles in liquid: Theory and experiment.* Advances in Colloid and Interface Science, 2007. **134-35**: p. 151-166.
109. de Boer, J.H., *The influence of van der waals' forces and primary bonds on binding energy, strength and orientation, with special reference to some artificial resins.* Transactions of the Faraday Society, 1936. **32**(1): p. 0010-0036.
110. Lifshitz, E.M., *The theory of molecular attractive forces between solids.* 1956. **2**(Soviet Physics JETP): p. 73-83.
111. Bell, G.M., S. Levine, and Mccartne.Ln, *Approximate methods of determining double-layer free energy of interaction between two charged colloidal spheres.* Journal of Colloid and Interface Science, 1970. **33**(3): p. 335-&.
112. Derjaguin, B., *Analysis of friction and adhesion IV The theory of the adhesion of small particles.* Kolloid-Zeitschrift, 1934. **69**(2): p. 155-164.
113. Bowen, W.R. and F. Jenner, *Dynamic ultrafiltration model for charged colloidal dispersions - a Wigner-Seitz cell approach.* Chemical Engineering Science, 1995. **50**(11): p. 1707-1736.
114. Kuwabara, S., *The forces experienced by a lattice of elliptic cylinders in a uniform flow at small reynolds numbers.* Journal of the Physical Society of Japan, 1959. **14**(4): p. 522-527.
115. Gruen, D.W.R. and S. Marcelja, *Spatially varying polarization in water - a model for the electric double-layer and the hydration force.* Journal of the Chemical Society-Faraday Transactions Ii, 1983. **79**: p. 225-242.
116. Jonsson, B., *Monte-Carlo simulations of liquid water between two rigid walls.* Chemical Physics Letters, 1981. **82**(3): p. 520-525.
117. Lin, Q., et al., *Measurement of the long- and short-range hydrophobic attraction between surfactant-coated surfaces.* Langmuir, 2005. **21**(1): p. 251-255.
118. Derjaguin, B.V., V.M. Muller, and Y.P. Toporov, *Effect of contact deformations on adhesion of particles.* Journal of Colloid and Interface Science, 1975. **53**(2): p. 314-326.

119. Johnson, K.L., K. Kendall, and A.D. Roberts, *Surface energy and contact of elastic solids.* Proceedings of the Royal Society of London Series a-Mathematical and Physical Sciences, 1971. **324**(1558): p. 301-&.

120. Muller, V.M., V.S. Yushchenko, and B.V. Derjaguin, *On the influence of molecular forces on the deformation of an elastic sphere and its sticking to a rigid plane.* Journal of Colloid and Interface Science, 1980. **77**(1): p. 91-101.

121. Vezenov, D.V., A. Noy, and P. Ashby, *Chemical force microscopy: probing chemical origin of interfacial forces and adhesion.* Journal of Adhesion Science and Technology, 2005. **19**(3-5): p. 313-364.

122. Evans, E. and P. Williams, *In physics of bio-molecules and cells*. Springer and EDP Sciences, ed. H. Flyvbjerg, Ju¨licher, F., Ormos, P. & David, F. Vol. 75. 2002, Heidelberg.

123. Meot-Ner, M., *The ionic hydrogen bond.* Chemical Reviews, 2005. **105**(1): p. 213-284.

124. Smith, D.A., et al., *Chemical force spectroscopy and imaging.* Reviews in Analytical Chemistry, 2001. **20**(1): p. 1-26.

125. Smith, D.A., et al., *The effect of electrolyte concentration on the chemical force titration behavior of omega-functionalized SAMs: Evidence for the formation of strong ionic hydrogen bonds.* Journal of Physical Chemistry B, 2000. **104**(37): p. 8862-8870.

126. Binnig, G. and H. Rohrer, *Scanning tunneling microscopy.* Helvetica Physica Acta, 1982. **55**(6): p. 726-35.

127. Noy, A., D.V. Vezenov, and C.M. Lieber, *Chemical force microscopy.* Annual Review of Materials Science, 1997. **27**: p. 381-421.

128. Lieber, C.M., et al., *Chemical force microscopy.* Abstracts of Papers of the American Chemical Society, 1998. **216**: p. U200-U200.

129. Zavala, G., *Atomic force microscopy, a tool for characterization, synthesis and chemical processes*. Vol. 286. 2008: Springer-Verlag, Berlin/Heidelberg. 85 - 95.

130. Maganov, S.N. and M.H. Whangbo, *Surface analysis with STM and AFM*. 1994, Weinheim: VCH.

131. Leite, F.L. and P.S.P. Herrmann, *Application of atomic force spectroscopy (AFS) to studies of adhesion phenomena: a review.* Journal of Adhesion Science and Technology, 2005. **19**(3-5): p. 365-405.

132. Cleveland, J.P., et al., *A nondestructive method for determining the spring constant of cantilevers for scanning force microscopy.* Review of Scientific Instruments, 1993. **64**(2): p. 403-405.
133. Sader, J.E., et al., *Method for the calibration of atomic-froce microscope cantilevers.* Review of Scientific Instruments, 1995. **66**(7): p. 3789-3798.
134. Hutter, J.L. and J. Bechhoefer, *Calibration of atomic-force microscope tips.* Review of Scientific Instruments, 1993. **64**(7): p. 1868-1873.
135. Vezenov, D.V., et al., *Force titrations and ionization state sensitive imaging of functional groups in aqueous solutions by chemical force microscopy.* Journal of the American Chemical Society, 1997. **119**(8): p. 2006-2015.
136. Smith, D.A., et al., *Chemical force microscopy: applications in surface characterisation of natural hydroxyapatite.* Analytica Chimica Acta, 2003. **479**(1): p. 39-57.
137. Oura, K., et al., *Surface Science: An Introduction.* 2003: Berlin: Springer.
138. Czanderna, A.W., *Method of surface analysis*. 1975, New York: American elsevier publishing company, Inc.
139. Watts, J.F., *X-ray photoelectron-spectroscopy.* Vacuum, 1994. **45**(6-7): p. 653-671.
140. Wagner, C.D., *Chemical-shifts of Auger lines, and Auger parameter.* Faraday Discussions, 1975: p. 291-300.
141. Linsmeier, C., *Auger-electron spectroscopy.* Vacuum, 1994. **45**(6-7): p. 673-690.
142. Briggs D, S.M., 2nd edn. Wiley, , *Practical surface analysis.* . 2nd ed. Vol. Auger and photoelectron spectroscopy. 1990, Chichester: Wiley.
143. Weightman, P., *X-ray-excited Auger and photo-electron spectroscopy.* Reports on Progress in Physics, 1982. **45**(7): p. 753-814.
144. *Surface and thin film analysis*. WILEY-VCH, ed. H. Bubert and H. Jenett. 2002, Weinheim. 13-14.
145. Tougaard, S. and H.S. Hansen, *Non-destructive depth profiling through quantitative-analysis of surface electron-spectra.* Surface and Interface Analysis, 1989. **14**(11): p. 730-738.
146. Tougaard, S., *Practical algorithm for background subtraction.* Surface Science, 1989. **216**(3): p. 343-360.
147. Tougaard, S., *Quantitative-analysis of the inelastic background in surface electron-spectroscopy.* Surface and Interface Analysis, 1988. **11**(9): p. 453-472.

148. Shirley, D.A., *Hign-resolution X-ray photoemission spectrum of valence bands of gold.* Physical Review B, 1972. **5**(12): p. 4709-&.

149. Proctor, A. and P.M.A. Sherwood, *Data-analysis techniques in X-ray photo-electron spectroscopy.* Analytical Chemistry, 1982. **54**(1): p. 13-19.

150. Chung, M.F. and L.H. Jenkins, *Auger electron energies of outer shell electrons.* Surface Science, 1970. **22**(2): p. 479-&.

151. Riviere, J.C., *Surface analytical thechniques*. 1975, Oxford Clarendon Press.

152. Wang, D., et al., *The adsorption of globular proteins onto a fluorinated PDMS surface.* Journal of Colloid and Interface Science, 2009. **331**(1): p. 90-97.

153. Welford, K., *Surface-plasmon polaritons and their uses.* Optical and Quantum Electronics, 1991. **23**(1): p. 1-27.

154. Piliarik, J.H.M., *Chem Sens Biosens*, in *Springer Ser*. 2006, Springer-Verlag: Berlin Heidelberg p. 45-67.

155. Cavadas, F. and M.R. Anderson, *Surface energy differences in monolayers prepared with the isomers 3-and 4-(12-mereaptododecyl)phenol.* Langmuir, 2003. **19**(23): p. 9724-9729.

156. Hu, J. and M.A. Fox, *A convenient trimethylsilylthioxy-dehalogenation reaction for the preparation of functionalized thiols.* Journal of Organic Chemistry, 1999. **64**(13): p. 4959-4961.

157. Pavia, D.L., G.M. Lampman, and G.S. Kriz, *Introduction to spectroscopy*. 2001, Washington Thomson Learning, Inc.

158. Silverstein, M.R. and X.F. Webster, *Spectrometric identification of organic compounds*. 1998, New York: John Wiley & Sons, Inc.

159. Liang, J. and J.H. Horton, *Interactions of benzoic acid and phosphates with iron oxide colloids using chemical force titration.* Langmuir, 2005. **21**(23): p. 10608-10614.

160. Kreller, D.I., et al., *Competitive adsorption of phosphate and carboxylate with natural organic matter on hydrous iron oxides as investigated by chemical force microscopy.* 2003. **212**: p. 249 - 264.

161. Kreller, D.I., et al., *Chemical force microscopy investigation of phosphate adsorption on the surfaces of iron(III) oxyhydroxide particles.* Journal of Colloid and Interface Science, 2002. **254**(2): p. 205-213.

162. Moulder, J.F., P.E. Stickle, and K.D. Sobol, *Handbook of X-ray photoelectron spectroscopy*. 1992, Eden Prairie, MN, 1992: Perkin-Elmer Co.,.

163. Wagner, C.D., et al., *Handbook of X-Ray photoelectron spectroscopy*. 1979, Eden, MN Perkin-Elmer Corp., Physical Electronics Division: .

164. Turner, N.H. and J.A. Schreifels, *Surface analysis: X ray photoelectron spectroscopy and Auger electron spectroscopy*. Analytical Chemistry, 1998. **70**(12): p. 229R-250R.

165. NIST X-ray photoelectron spectroscopy database (version 3.5).

166. Ebel, H., et al., *Calculation of escape depths from inelastic mean free paths.* 1990. **50**: p. 109-116.

167. Sinton, D., et al., *Direct and indirect electroosmotic flow velocity measurements in microchannels*. Journal of Colloid and Interface Science, 2002. **254**(1): p. 184-189.

168. Sze, A., et al., *Zeta-potential measurement using the Smoluchowski equation and the slope of the current-time relationship in electroosmotic flow*. Journal of Colloid and Interface Science, 2003. **261**(2): p. 402-410.

169. Lee, J.N., C. Park, and G.M. Whitesides, *Solvent compatibility of poly(dimethylsiloxane)-based microfluidic devices.* Analytical Chemistry, 2003. **75**(23): p. 6544-6554.

170. Tandon, V. and B.J. Kirby, *zeta potential and electroosmotic mobility in microfluidic devices fabricated from hydrophobic polymers: 2. Slip and interfacial water structure.* Electrophoresis, 2008. **29**(5): p. 1102-1114.

171. Tandon, V., et al., *zeta potential and electroosmotic mobility in microfluidic devices fabricated from hydrophobic polymers: 1. The origins of charge.* Electrophoresis, 2008. **29**(5): p. 1092-1101.

172. Ren, X.Q., et al., *Electroosmotic properties of microfluidic channels composed of poly(dimethylsiloxane).* Journal of Chromatography B-Analytical Technologies in the Biomedical and Life Sciences, 2001. **762**(2): p. 117-125.

173. Wheeler, A.R., et al., *Electroosmotic flow in a poly(dimethylsiloxane) channel does not depend on percent curing agent.* Electrophoresis, 2004. **25**(7-8): p. 1120-1124.

174. Petersen, P.B. and R.J. Saykally, *Confirmation of enhanced anion concentration at the liquid water surface.* Chemical Physics Letters, 2004. **397**(1-3): p. 51-55.

175. Green, R.J., et al., *Surface plasmon resonance analysis of dynamic biological interactions with biomaterials.* Biomaterials, 2000. **21**(18): p. 1823-1835.

176. Homola, J., *Surface plasmon resonance sensors for detection of chemical and biological species.* Chemical Reviews, 2008. **108**(2): p. 462-493.

177. Powell, C.J. and A. Jablonski, *Electron effective attenuation lengths for applications in Auger-electron spectroscopy and x-ray photoelectron spectroscopy.* Surface and Interface Analysis, 2002. **33**(3): p. 211-229.

178. Tanuma, S., *Calculations of electron inelastic free paths in Au-Cu and Au-Ag alloys.* Bunseki Kagaku, 1991. **40**(11): p. 667-672.

179. Dewar, M.J.S., et al., *The development and use of quantum-mechanical molecular-models .76. Am1 - a new general-purpose quantum-mechanical molecular-model.* Journal of the American Chemical Society, 1985. **107**(13): p. 3902-3909.

180. Biffinger, J.C., H.W. Kim, and S.G. DiMagno, *The polar hydrophobicity of fluorinated compounds.* Chembiochem, 2004. **5**(5): p. 622-627.

181. Salgado, J.C., I. Rapaport, and J.A. Asenjo, *Is it possible to predict the average surface hydrophobicity of a protein using only its amino acid composition?* Journal of Chromatography A, 2005. **1075**(1-2): p. 133-143.

182. Berggren, K., et al., *The surface exposed amino acid residues of monomeric proteins determine the partitioning in aqueous two-phase systems.* Biochimica Et Biophysica Acta-Protein Structure and Molecular Enzymology, 2002. **1596**(2): p. 253-268.

183. Frishman, D. and P. Argos, *Knowledge-based protein secondary structure assignment.* Proteins-Structure Function and Genetics, 1995. **23**(4): p. 566-579.

184. Cowan, R. and R. Whittaker, *Hydrophobicity indices for amino acid residues as determined by high-performance liquid chromatography.* Peptide Res, 1990. **3**: p. 75.

185. Bhaskaran, R. and P.K. Ponnuswamy, *Positional flexibilities of amino-acid residues in globular-proteins.* International Journal of Peptide and Protein Research, 1988. **32**(4): p. 241-255.

186. Vihinen, M., E. Torkkila, and P. Riikonen, *Accuracy of protein flexibility predictions.* Proteins-Structure Function and Genetics, 1994. **19**(2): p. 141-149.

187. E., G., et al., *Protein identification and analysis tools on the ExPASy server*. The Proteomics Protocols Handbook, ed. J.M. Walker. 2005: Humana Press.

188. Norde, W., *Driving forces for protein adsorption at solid surfaces.* Macromolecular Symposia, 1996. **103**: p. 5-18.

189. Humphrey, W., A. Dalke, and K. Schulten, *VMD: Visual molecular dynamics.* Journal of Molecular Graphics, 1996. **14**(1): p. 33-&.

190. Karlsson, M. and U. Carlsson, *Adsorption at liquid-solid interface: influence of protein stability on conformational changes.* Encyclopedia of surface and colloid Science, 2007. **1**(1): p. 1-16.

191. Ahmad, F. and C.C. Bigelow, *Estimation of the free-energy of stabilization of ribonuclease-a, lysozyme, alpha-lactalbumin, and myoglobin.* Journal of Biological Chemistry, 1982. **257**(21): p. 2935-2938.

192. Norde, W., *Adsorption of proteins from solution at the solid-liquid interface.* Advances in Colloid and Interface Science, 1986. **25**(4): p. 267-340.

193. Norde, W., *Driving forces for protein adsorption. In Biopolymers at Interfaces*. 1st ed, ed. M. Malmsten. 1998, New York: Marcel Dekker, Inc.

194. Arai, T. and W. Norde, *The behavior of some model proteins at solid liquid interfaces .1. Adsorption from single protein solutions.* Colloids and Surfaces, 1990. **51**: p. 1-15.

195. Arai, T. and W. Norde, *The behavior of some model proteins at solid liquid interfaces .2. Sequential and competitive adsorption.* Colloids and Surfaces, 1990. **51**: p. 17-28.

196. Nakanishi, K., T. Sakiyama, and K. Imamura, *On the adsorption of proteins on solid surfaces, a common but very complicated phenomenon.* Journal of Bioscience and Bioengineering, 2001. **91**(3): p. 233-244.

197. Ptitsyn, O.B., *Molten globule and protein folding.* Advances in Protein Chemistry, Vol 47, 1995. **47**: p. 83-229.

198. Gekko, K., A. Kimoto, and T. Kamiyama, *Effects of disulfide bonds on compactness of protein molecules revealed by volume, compressibility, and expansibility changes during reduction.* Biochemistry, 2003. **42**(46): p. 13746-13753.

199. Walsh, G., *Pharmaceutical biotechnology products approved within the European Union.* European Journal of Pharmaceutics and Biopharmaceutics, 2003. **55**(1): p. 3-10.

200. Kondo, A., F. Murakami, and K. Higashitani, *Circular-dichroism studies on conformational-changes in protein molecules upon adsorption on ultrafine polystyrene particles.* Biotechnology and Bioengineering, 1992. **40**(8): p. 889-894.

201. Karlsson, M. and U. Carlsson, *Protein adsorption orientation in the light of fluorescent probes: Mapping of the interaction between site-directly labeled human carbonic anhydrase II and silica nanoparticles.* Biophysical Journal, 2005. **88**(5): p. 3536-3544.

202. Kondo, A. and H. Fukuda, *Effects of adsorption conditions on kinetics of protein adsorption and conformational changes at ultrafine silica particles.* Journal of Colloid and Interface Science, 1998. **198**(1): p. 34-41.

203. Larsericsdotter, H., S. Oscarsson, and J. Buijs, *Thermodynamic analysis of lysozyme adsorbed to silica.* Journal of Colloid and Interface Science, 2004. **276**(2): p. 261-268.

204. Zoungrana, T., G.H. Findenegg, and W. Norde, *Structure, stability, and activity of adsorbed enzymes.* Journal of Colloid and Interface Science, 1997. **190**(2): p. 437-448.

205. Maste, M.C.L., W. Norde, and A.J.W.G. Visser, *Adsorption-induced conformational changes in the serine proteinase savinase: A tryptophan fluorescence and circular dichroism study.* Journal of Colloid and Interface Science, 1997. **196**(2): p. 224-230.

206. Pickart, C.M. and M.J. Eddins, *Ubiquitin: structures, functions, mechanisms.* Biochimica Et Biophysica Acta-Molecular Cell Research, 2004. **1695**(1-3): p. 55-72.

207. Vijaykumar, S., C.E. Bugg, and W.J. Cook, *Structure of ubiquitin refined at 1.8 a resolution.* Journal of Molecular Biology, 1987. **194**(3): p. 531-544.

208. Bushnell, G.W., G.V. Louie, and G.D. Brayer, *High-resolution 3-dimensional structure of horse heart cytochrome-c.* Journal of Molecular Biology, 1990. **214**(2): p. 585-595.

209. Theorell, H. and A. Akesson, *Studies on cytochrome c. II. The optical properties of pure cytochrome c and some of its derivatives.* Journal of the American Chemical Society, 1941. **63**: p. 1812-1818.

210. Vihinen, M., *Relationship of protein flexibility to thermostability.* Protein Engineering, 1987. **1**(6): p. 477-480.

211. Loladze, V.V., et al., *Engineering a thermostable protein via optimization of charge-charge interactions on the protein surface.* Biochemistry, 1999. **38**(50): p. 16419-16423.

212. Bagel'ova, J., M. Antalik, and Z. Tomori, *Effect of polyglutamate on the thermal stability of ferricytochrome c.* Biochemistry and Molecular Biology International, 1997. **43**(4): p. 891-900.

213. Graf, M. and H. Watzig, *Capillary isoelectric focusing - reproducibility and protein adsorption.* Electrophoresis, 2004. **25**(17): p. 2959-2964.

214. Lu, J.R., et al., *Effect of pH on the adsorption of bovine serum albumin at the silica water interface studied by neutron reflection.* Journal of Physical Chemistry B, 1999. **103**(18): p. 3727-3736.

215. Hook, F., et al., *Structural changes in hemoglobin during adsorption to solid surfaces: Effects of pH, ionic strength, and ligand binding.* Proceedings of the National Academy of Sciences of the United States of America, 1998. **95**(21): p. 12271-12276.

216. Wang, L. and D.H. Waldeck, *Denaturation of cytochrome c and its peroxidase activity when immobilized on SAM films.* Journal of Physical Chemistry C, 2008. **112**(5): p. 1351-1356.

217. Marsh, R.J., R.A.L. Jones, and M. Sferrazza, *Adsorption and displacement of a globular protein on hydrophilic and hydrophobic surfaces.* Colloids and Surfaces B-Biointerfaces, 2002. **23**(1): p. 31-42.

218. Roach, P., D. Farrar, and C.C. Perry, *Interpretation of protein adsorption: Surface-induced conformational changes.* Journal of the American Chemical Society, 2005. **127**(22): p. 8168-8173.